Numerical modelling of marine dunes in a shallow shelf sea in an offshore wind farm context

Noémie Durand

THÈSE DE DOCTORAT

de l'École nationale des ponts et chaussées

Numerical modelling of marine dunes in a shallow shelf sea in an offshore wind farm context

École doctorale N°531, Sciences, Ingénierie et Environnement (SIE)

Spécialité : Sciences de l'ingénieur

Thèse préparée au sein du Laboratoire d'Hydraulique Saint-Venant

Thèse soutenue le 24 octobre 2024, par

Noémie DURAND

Composition du jury:

Christian WINTER Professor, Kiel University, Germany	*Président*
Katrien VAN LANDEGHEM Professor, Bangor University, UK	*Rapporteure*
Pieter ROOS Associate professor, University of Twente, NL	*Rapporteur*
Rebekka KOPMANN BAW, Karlsruhe, Germany	*Examinatrice*
Richard WHITEHOUSE Professor, HR Wallingford, UK	*Examinateur*
Pablo TASSI EDF R&D and LHSV, France	*Directeur de thèse*
Alice LEFEBVRE MARUM, University of Bremen, Germany	*Co-encadrante*
Olivier BLANPAIN France Energies Marines, France	*Co-encadrant*

Numerical modelling of marine dunes in a shallow shelf sea in an offshore wind farm context

Ecole Doctorale Sciences, Ingénierie et Environnement (SIE)

Noémie Durand

December 5, 2024

PhD research

This dissertation has been approved by:

Dr. Pablo Tassi	supervisor
Dr. Alice Lefebvre	co-supervisor
Dr. Olivier Blanpain	co-supervisor

This research is part of the three-year MODULLES project: MOdelling of marine DUnes: Local and Large-scale EvolutionS in an OWF context, which is co-funded by the French National Research Agency as part of the France 2030 Investment Plan, under reference number ANR-10-IEED-0006-34, and by France Energies Marines (FEM) and its members. It was hosted by the Saint-Venant Hydraulics Laboratory (LHSV) in Chatou. Computer time was provided under the EDF R&D POWER project.

Edition date *December 5, 2024*

Abstract

Marine dunes, also known as sand waves, are large sedimentary bedforms found on the seabed of shallow shelf seas. They migrate under the combined influence of tidal currents, winds, and waves, moving at rates of up to tens of metres per year. This dynamic behaviour is relevant to human activities, such as renewable energy projects. However, the morphology and dynamics of dunes in open marine environments are not well understood. Most modelling research to date has relied on two-dimensional vertical representations, ignoring lateral variations along the dune crests. Previous studies have largely used simplified hydrometeorological forcing, such as representative tidal currents and winds.

The present research aims to extend our knowledge of marine dune dynamics and modelling over time and space scales ranging from days to years and metres to kilometres. It also seeks to advance our understanding of the interactions between marine dunes and Offshore Wind Farm (OWF) foundations. To achieve this, we have developed a three-dimensional (3D) coastal area model using the open**TELEMAC** system for an application offshore Dunkirk, France. The area, proposed site for a 600 MW offshore wind project, is characterised by large marine dunes.

Extensive site-specific surveys have been conducted, providing data to characterise the meteorological forcing, hydrodynamics, sedimentology, and morphodynamics of the area. The region is influenced by strong tidal flows, with near-bed currents up to 0.9 m/s, and winds predominantly from the southwest and, to a lesser extent, from the north. The seabed is mainly composed of reasonably well sorted gravelly sands with median grain sizes between 240 μm and 450 μm. There is little evidence of spatial or seasonal trends in the sediment data. The surveys document the evolution of large marine dunes with heights between 2 m and 3 m, travelling at a net rate of approximately 30 m/year.

Our 3D numerical model, validated with the in situ data, was shown to accurately simulate hydrodynamics and dune dynamics. Simplifying assumptions excluded wave effects and focused on bedload transport. Two sediment transport predictors were evaluated in detail: the Soulsby and van Rijn predictor (SvR97), which was noted for its robustness and suitability for long-term modelling, and the Soulsby and Damgaard predictor (SD05), which accurately reflected the morphology of the dune but produced instabilities in the long term. Therefore, the SvR97 predictor was used in our research.

To determine the contribution of wind-induced currents compared to tide-induced currents to the dynamics of large marine dunes, a 4-month period was simulated, with and without meteorological effects included in the numerical model. The results show that the migration of marine dunes is closely related to the amplitude and direction of the residual flow, which are influenced by wind conditions. Therefore, meteorological forcing is necessary to accurately represent seabed changes over time. Although deviations in wind direction from the prevailing pattern have the potential to temporarily reverse the general migration trend, they are too sporadic to fundamentally alter the sediment dynamics in the study area.

To understand the impact of OWF foundations on the dynamics of large marine dunes, exploratory scenarios with a single monopile were run for a period of 2 years. These scenarios were later extended to a realistic scenario consisting of 46 wind turbines within the proposed Dunkirk OWF footprint. Our results show that monopiles significantly affect their environment, causing dunes to converge towards them along the tidal flow axis, which we linked to the 'wake effect'. This effect accelerates dune propagation, highlighting the need for careful siting of wind turbines to mitigate impacts on dune fields. These findings bridge the gap between studies at the OWF level and those at the monopile level.

Résumé

Les dunes marines sont de grandes formes sédimentaires présentes au fond des mers épicontinentales peu profondes. Sous l'influence des courants de marée, vents et vagues, elles peuvent migrer jusqu'à des dizaines de mètres par an, et impacter les projets d'énergie renouvelable. Cependant, la morphologie et la dynamique des dunes dans les environnements marins ouverts ne sont pas bien comprises. Les recherches menées jusqu'à présent en modélisation se sont appuyées sur des représentations verticales bidimensionnelles, ignorant les variations latérales le long des crêtes de dunes, et utilisant des forçages hydrométéorologiques simplifiés.

Cette thèse vise à étendre notre connaissance de la dynamique et de la modélisation des dunes marines sur des échelles de temps de jours à années et d'espace de mètres à kilomètres, et à améliorer notre compréhension des interactions entre les dunes marines et les fondations de parcs éoliens en mer. Pour ce faire, nous avons développé un modèle tridimensionnel (3D) avec le système open**TELEMAC** pour une application dans le sud de la mer du Nord, au large de Dunkerque, France. Cette zone, proposée pour un projet éolien en mer de 600 MW, est caractérisée par de grandes dunes marines.

Le forçage météorologique, l'hydrodynamique, la sédimentologie et la morphodynamique de la zone ont été caractérisés grâce à des données spécifiques au site. La région est influencée par de forts courants de marée, pouvant atteindre 0,9 m/s près du fond, et des vents provenant principalement du sud-ouest et, dans une moindre mesure, du nord. Les fonds marins sont principalement composés de sables graveleux raisonnablement bien triés, dont la taille médiane des grains se situe entre 240 μm et 450 μm, sans tendances spatiales ou saisonnières. De grandes dunes marines d'une hauteur comprise entre 2 et 3 m se déplacent à une vitesse nette d'environ 30 m/an.

Notre modèle numérique 3D, validé avec ces données in situ, simule avec précision l'hydrodynamique et la dynamique des dunes. Les effets des vagues sont exclus. Deux prédicteurs de transport de sédiments ont été évalués en détail : le prédicteur de Soulsby et van Rijn (SvR97), qui a été noté pour sa robustesse et son aptitude à la modélisation à long terme, et le prédicteur de Soulsby et Damgaard (SD05), qui a reflété avec précision la morphologie des dunes mais provoque des instabilités à long terme. C'est donc le prédicteur SvR97 qui a été utilisé dans notre recherche.

Afin de déterminer la contribution à la dynamique des dunes marines des courants induits par le vent par rapport aux courants de marées, une période de 4 mois a été simulée, avec et sans effets météorologiques. Les résultats montrent que la migration des dunes est étroitement liée à l'amplitude et à la direction du courant résiduel, qui sont influencées par les conditions de vent. Par conséquent, le forçage météorologique est nécessaire pour représenter avec précision les changements du fond marin au fil du temps. Bien que des déviations de la direction du vent par rapport à la tendance dominante puissent temporairement inverser la direction de migration, elles sont trop sporadiques pour modifier fondamentalement la dynamique sédimentaire de la région.

Pour comprendre l'impact des fondations des éoliennes sur la dynamique des dunes marines, des scénarios exploratoires avec un seul monopieu ont été exécutés sur une période de 2 ans. Ces scénarios ont ensuite été étendus à un scénario réaliste comprenant 46 éoliennes dans le parc de Dunkerque. Nos résultats montrent que les monopieux ont un impact significatif sur leur environnement, provoquant la convergence des dunes le long de l'axe des courants de marée, ce que nous avons lié à l'« effet de sillage », qui accélère la propagation des dunes. Une implantation soigneusement étudiée des éoliennes est donc nécessaire pour atténuer les impacts sur les champs de dunes.

Acknowledgements

It was a combination of circumstances that led me to undertake this PhD project, after several years working as a consultant. I saw it as an opportunity to acquire knowledge in a field that was new to me, linked to my previous activities in hydrodynamic and wave modelling. It was inspiring, uplifting. I would like to thank France Energies Marines for the opportunity and for funding this research through the MODULLES project. Thanks to the Saint-Venant Hydraulics Laboratory (LHSV) and EDF R&D in Chatou for hosting me.

I am grateful to my supervisors Pablo, Alice and Olivier for the trust they have always shown in me and their pertinent comments during our discussions. Pablo in particular for his boundless optimism and enthusiasm. Thank you to my office colleague at LHSV, Frédérique, for down-to-earth conversations and her practical advice. And of course, my husband, Sébastien, for his unfailing support and re-evaluation of (life's) priorities when times were hard.

A special thought for my son, Baptistin, for whom I have not had enough time these past 3 years. As I write this, he is about to embark on his own journey at the University of British Columbia (UBC) in Canada.

My group manager at France Energies Marines, Florent, once reminded me that a PhD is training in research (and these 3 years have certainly been very formative!) and that you are not supposed to have all the answers. I came across a quote by George Box, a contemporary British statistician: 'Essentially all models are wrong, but some are useful'. I hope to have contributed in my small way to our knowledge of the numerical modelling of the dynamics of marine dunes in a shallow shelf sea in an offshore wind farm context.

Notation

β	angle of sloping bed relative to the horizontal [rad]
ϵ	amplitude of the disturbance in stability analysis [m]
κ	von Kármán constant [-]
λ_p	bed porosity [-]
ν	kinematic viscosity of water [m^2/s]
ϕ	angle between the current direction and the direction of wave travel [rad]
ϕ_r	angle of repose of sediment [rad]
ψ	solution to the stability analysis problem
ρ	water density [kg/m^3]
ρ_{air}	air density [kg/m^3]
ρ_s	sediment density [kg/m^3]
σ	wave angular frequency [rad]
τ_{cr}	critical (or threshold) bed shear-stress [N/m^2]
τ_c	bed shear-stress due to currents only [N/m^2]
τ_{eff}	effective bed shear-stress [N/m^2]
τ_{max}	maximum bed shear-stress [N/m^2]
τ_m	mean bed shear-stress [N/m^2]
τ_{wind}	wind stress [N/m^2]
τ_w	bed shear-stress due to waves only [N/m^2]
θ	current direction or wave propagation direction depending on context [rad]
Θ_{cr}	critical (or threshold) Shields parameter [-]
$\vec{c_g}$	wave group velocity [m/s]
$\vec{Q}_b$	mass sediment transport rate per unit width [kg/m/s]
$\vec{q}_b$	volumetric sediment transport rate per unit width [m^2/s]
$\vec{q}_t$	total volumetric sediment transport rate per unit width [m^2/s]
$\vec{U}$	flow velocity (u,v,w) [m/s]
$\vec{U}_{2D}$	depth-averaged flow velocity (u,v) [m/s]
$\vec{V}_{10m}$	wind velocity defined 10 m above sea level [m/s]

a, b, A	coefficients in various formulae [-]
A_s	marine dune asymmetry [-]
a_{wind}	dimensionless wind coefficient [-]
c	migration rate (or speed) [m/yr]
c_σ	propagation velocity component in the σ-space [rad/s]
c_θ	propagation velocity component in the θ-space [rad/s]
C_D	drag coefficient applicable to depth-averaged current [-]
D_*	dimensionless grain size [-]
d_{50}	median grain diameter [m]
d_n	grain diameter for which n% of the grains is finer, e.g., d_{10}, d_{90} [m]
E	energy density spectrum [m^2/Hz/rad]
f_w	wave friction factor [-]
g	acceleration due to gravity [m/s^2]
H	marine dune height [m]
h	water depth [m]
H_s	significant wave height [m]
k	wave number [m^{-1}]
k_s	Nikuradse sand grain roughness [m]
L	marine dune wavelength [m]
N	action density spectrum [m^2/Hz^2/rad]
P	Rouse number [-]
p	pressure [Pa]
p_{atm}	atmospheric pressure at sea level [Pa]
S	source and sink terms
s	relative density of the sediment [-]
T	wave period [s]
T_{m02}	mean wave period (spectral) [s]
T_p	peak wave period [s]
T_z	zero-crossing wave period [s]
u_*	friction velocity [m/s]
U_{cr}	critical (or threshold) depth-averaged flow velocity [m/s]
U_{rms}	root-mean-square wave orbital velocity [m/s]
w_s	sediment fall (or settling) velocity [m/s]
z_b	bed elevation [m]

Acronyms

ACC Anomaly Correlation Coefficient. 108, 119, 125, 135, 136
ADCP Acoustic Doppler Current Profiler. 57–59, 116
ADV Acoustic Doppler Velocimeter. 116
AHRS Attitude and Heading Reference System. 58
AST Acoustic Surface Tracking. 58, 62
AWAC Acoustic Wave and Current. 58, 62, 116

BSS Brier Skill Score. 108, 125, 135

CANDHIS Centre d'Archivage National des Données de Houle In Situ, National Archiving Centre for In Situ Wave Data. 63
CFD Computational Fluid Dynamics. 47, 163

DTM Digital Terrain Model. 63, 64, 72, 73, 98, 117, 121, 145

ECMWF European Centre for Medium-Range Weather Forecasts. 76
ECOWind Ecological Consequences of Offshore Wind. 164
EMD Eoliennes en Mer de Dunkerque. 55, 64, 73

FEM France Energies Marines. 4, 25, 63, 164

HAT Highest Astronomical Tide. 56
HPC High Performance Computers. 161

IHO International Hydrographic Organization. 31
IOS Institute of Oceanographic Sciences. 81

LAT Lowest Astronomical Tide. 56, 73
LiDAR Light Detection And Ranging. 55, 73, 75

MAE Mean Absolute Error. 78, 88
MBES Multibeam echosounder. 53
MFI Mobilisation Frequency Index. 22, 91–93
MHWN Mean High Water Neaps. 56
MHWS Mean High Water Springs. 56
MLWN Mean Low Water Neaps. 56
MLWS Mean Low Water Springs. 56
MODULLES MOdelling of marine DUnes: Local and Large-scale EvolutionS in an OWF context. 4, 9, 163, 164
MSL Mean Sea Level. 51, 53, 56, 58, 60, 72, 73, 116

OWF Offshore Wind Farm. 5, 19, 21–25, 27, 40, 42–49, 51, 53, 55, 57–59, 61–67, 70, 72, 73, 77, 78, 82, 87, 92, 111, 115–117, 136–138, 141–143, 148, 150, 155, 156, 159–161, 163, 164

PVD Progressive Vector Diagram. 82

RMAE Relative Mean Absolute Error. 19, 78, 81, 82, 88, 118

RMS Root Mean Square. 91
RMSE Root Mean Square Error. 19, 78, 81, 82, 88, 108, 125, 135

SAR Synthetic Aperture Radar. 44, 152
SD05 Soulsby and Damgaard bedload predictor. 5, 7, 23, 96, 97, 103–108, 110, 111, 162
Shom French Navy Hydrographic and Oceanographic Service. 56, 59, 63, 65, 66, 73
SMI Sediment Mobilisation Index. 22, 93, 94
SPM Suspended Particulate Matter. 46
SvR97 Soulsby and van Rijn total load predictor. 5, 7, 23, 96, 97, 100–104, 106, 108, 110, 111, 119, 129, 131, 141, 162

UTM Universal Transverse Mercator. 21, 52, 72, 73

VLIZ Flanders Marine Institute. 138

ZH Zéro Hydrographique. 56, 73

Table of Contents

List of Tables

List of Figures

Chapter 1

Introduction

There has been a convergence, in recent years, of worldwide efforts towards the decarbonisation of energy systems and the transition to renewable energies (hydropower, wind power, solar energy, bioenergy, geothermal energy, etc.). Offshore wind is poised to play an important role in this context, being the most mature of marine renewable energies.

Marine dunes are common occurrences on the bed of shallow shelf seas worldwide. They are present in the Irish Sea, the English Channel and in the North Sea, where most of the proposed European offshore wind farms (OWFs) will be located. Constantly remodelled by the combined action of tidal currents and waves, they pose a challenge to the design, implementation, safety, and maintenance of marine renewable energy systems.

Being able to predict the evolution and migration of marine dunes past OWF (elements) is, therefore, essential. At the same time, it is also paramount to understand the effects that the development of OWF projects might have on these areas of high ecological significance.

This is the context in which our research takes place, with a specific application to the future OWF project of Dunkirk in the north of France. It is part of a three-year industrial project, MODULLES: 'MOdelling of marine DUnes: Local and Large-scale EvolutionS in an OWF context', led by France Energies Marines.

1.1 Marine dunes in shallow shelf seas

Hydrodynamics in the coastal zone is driven by a combination of tides, winds and waves. Under their action, the seabed can be mobilised to form what is collectively known as 'bedforms'.

1.1.1 Bedforms in the marine environment

In the most general sense, bedforms are defined as sediment deposits, resulting from the interaction between a fluid and a mobile sediment bed. When the fluid is water, they are found in fluvial, estuarine, coastal, and marine environments. Bedforms can be composed of gravel, sand or mud of siliciclastic or carbonate origin. Many types are observed in nature. Their geometry, spatial scale and temporal dynamics cover a wide range, from a few centimetres to over 1 km in length; from centimetres to tens of meters in height; and time scales from seconds to decades and centuries (Knaapen, 2004). This large spectrum has encouraged attempts at classifying bedforms, based on morphological, sedimentological or hydrodynamic parameters such as wavelength, geometry, grain size, characteristic flow velocity (Allen, 1968; Ashley, 1990; Belderson et al., 1982; Boothroyd, 1978).

Bedforms often observed in sandy marine environments include:

- sand ripples: small bedforms whose heights are independent of water depth. They can be symmetrical, under wave action, or asymmetrical, oriented according to the prevailing flow direction;

- nearshore bars, also called breaker bars: submerged ridges formed by wave action in the breaker zone. They are separated from the beach face by a longshore trough;
- marine dunes: large-scale flow-transverse bedforms;
- sandbanks: relatively shallow, broad expanses of sand deposits along or off a coast, loosely in line with the tidal flow. They can be submerged at all states of the tide, or exposed at low tide; and
- sand ribbons: thin, elongated bands of sand overlying coarser sediment, which is exposed between them.

Our research focuses on marine dunes, examples of which are shown in Figure 1.1.

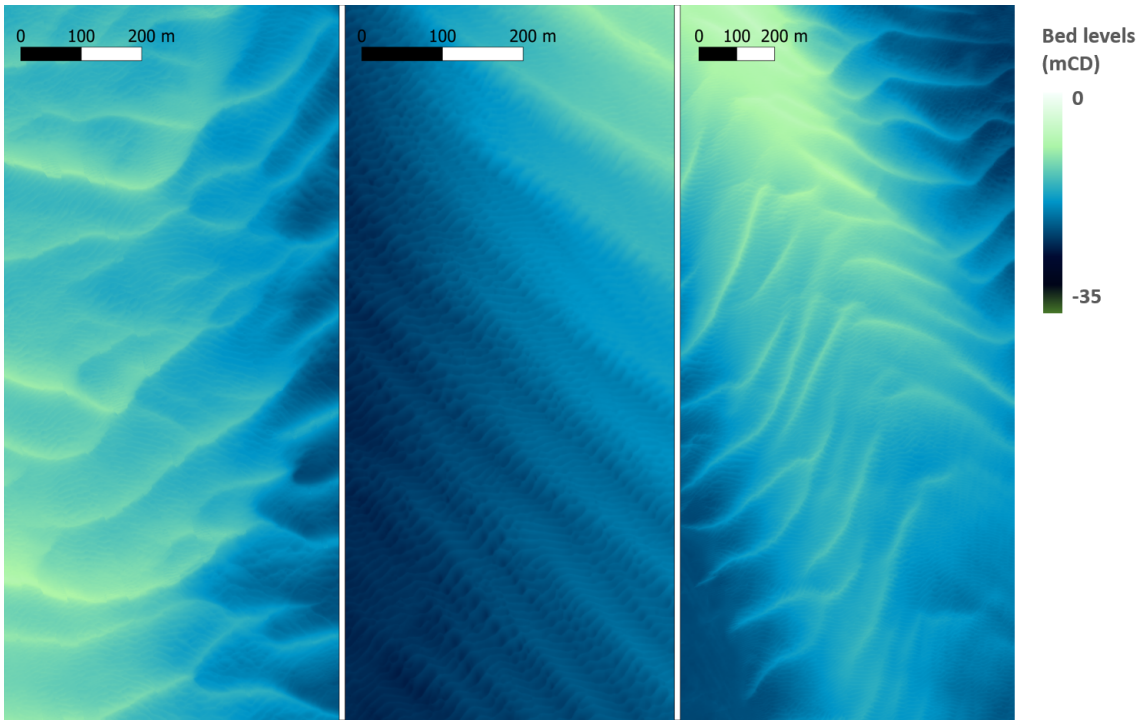

Figure 1.1: Example marine dune fields, observed offshore Dunkirk (Data source: EMD, 2021)

1.1.2 The place of marine dunes

Marine dunes are referred to in the literature as sand waves, megaripples, or, in keeping with the recommendations of the SEPM (Society of Economic Paleontologist and Mineralogists, now Society for Sedimentary Geology) (Ashley, 1990) as subaqueous dunes. A symposium was indeed convened in 1987, entitled 'Classification of Large-Scale Flow-Transverse Bedforms', with the intention to unify the terminology. The term 'dunes' was recommended, which is meant to be generic and encompass fluvial as well as coastal and shallow marine environments. It was suggested that the qualifier 'subaqueous' be used to distinguish them from aeolian dunes (Courrech du Pont et al., 2024). First order descriptors of size and shape and second/third order descriptors such as sediment size and bedforms superimposition were recommended to refine the description. This classification is reproduced from Ashley (1990) in Table 1.1. It is noteworthy that flow-transverse bedforms with spacing (wavelength) under 0.6 m are not catered for in Table 1.1: they belong to a different class of bedforms referred to as ripples.

In our research the above terminology is adopted and we call marine dunes large, harmonic, flow-transverse bedforms, characterised by wavelengths in hundreds of metres and heights of a few metres (commonly between 1 m and 15 m). The qualifier 'marine' is preferred to 'subaqueous' in our research, as is done elsewhere (e.g., Ferret et al., 2010; Garlan, 2007; Idier et al., 2002; Le Bot & Trentesaux, 2004; Lefebvre et al., 2016), to refer to coastal and open marine environments.

First Order Descriptors (necessary)					
Size:		small	medium	large	very large
	Spacing =	0.6 - 5 m	5 - 10 m	10 - 100 m	> 100 m
	Height* =	0.075 - 0.4 m	0.4 - 0.75 m	0.75 - 5 m	> 5 m
Shape:	2-Dimensional				
	3-Dimensional				
Second Order Descriptors (important)					
Superposition:	simple or compound (sizes and relative orientation)				
Sediment characteristics:	size, sorting				
Third Order Descriptors (useful)					
Bed form profile (stoss and lee slope lengths and angles)					
Fullbeddedness (fraction of bed covered by bed forms)					
Flow structure (time-velocity characteristics)					
Relative strengths of opposing flows					
Dune behaviour-migration history (vertical and horizontal accretion)					

* height H estimated from wavelength L using $H = 0.0677L^{0.8098}$ (Flemming, 1988)

Table 1.1: Classification scheme recommended by the 1987 SEPM Symposium on large-scale flow-transverse bedforms (Ashley, 1990)

Marine dunes develop almost exclusively on sandy seabeds (Besio et al., 2003; R. Bijker et al., 1998; Hulscher & van den Brink, 2001; Terwindt, 1971), where near-bed currents are energetic enough to erode, transport and deposit sands. Their formation depends not only on the hydrodynamic regime (tidal currents, storm-induced currents, oceanic currents, internal waves and eddies), but also on sedimentary characteristics (availability, sediment composition and grain size), and local topography.

They can occur on their own (in dune fields or in isolation when sediment availability is low), but it is not uncommon for a relatively shorter secondary bedform to ride on the back of a larger-scale primary bedform. For example, small secondary dunes have been observed in association with marine dunes (e.g., Barnard et al., 2011; Malikides et al., 1988; Terwindt, 1971); and marine dunes with sandbanks and shoals (e.g., Blunden et al., 2020; Garlan et al., 2008; Katoh et al., 1998; Lanckneus & de Moor, 1991).

In plan view, their crests can be straight, sinuous, or in the form of a crescent in sediment-starved environments (Belderson et al., 1982). They are approximately perpendicular to the mean current, hence their classification as flow-transverse bedforms. Hulscher (1996) has shown using linear stability analysis that deviations of up to 10° anti-clockwise from the principal current direction can be expected (in Németh et al., 2001). Le Bot (2001) indicates that deviations of up to 20° have been observed. It is noteworthy that the crest orientation of superimposed bedforms may largely differ from that of the dunes they coexist with (e.g., Barnard et al., 2011; Malikides et al., 1988, or Figure 1.1, central panel).

In cross-sectional view, the shape of the dunes is characteristic of the forcing mechanisms: symmetrical dunes essentially result from symmetrical tidal currents; whereas asymmetrical dunes occur under unidirectional currents (particularly relevant for river settings) or can reflect, for example, the predominance of a tidal phase over the other. Asymmetrical dunes exhibit a gentle side and a steep side (Figure 1.2). In unidirectional currents, the side sheltered from the flow (lee side) is steep, while the side facing the flow (stoss side) is gentle. The terms 'lee' and 'stoss' are sometimes used by extension for large bedforms in tidal flows, in relation to the residual current. For clarity, we use the terms 'steep' and 'gentle' in this dissertation. Berné et al. (1989) remark that average steep slopes are generally between 10° and 20° (in accordance with e.g. Langhorne (1982) in the South of England or Terwindt (1971) in the southern North Sea), but that it is not uncommon to observe dunes presenting, over the entire steep side, slopes between 25° and 35°. They further indicate that underwater measurements in

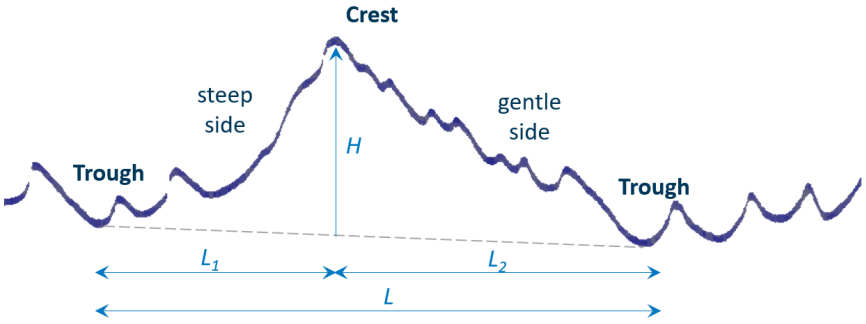

Figure 1.2: Sketch illustrating marine dune characteristics

Normandy, France, have confirmed these high values, with recorded angles of 28°. Belderson et al. (1982) have compiled observational data in the literature or available to the authors, and report steep side angles commonly in the range 20° to 35° for dune height under 2 m, 4° to 20° otherwise.

Several authors have described separation of the boundary layer flow in the lee of asymmetrical dunes with a steep (angle of repose) side (e.g., Best, 2005; Langhorne, 1977). Maximum velocity, hence bed shear stresses, occurs atop the crest. The sediment entrained as bedload is further transported by avalanching down the steep slope. Strong eddy recirculations result from the flow separation, downstream of the crest. The return flow is likely to erode and enhance the steep slope in turn. Aliotta and Perillo (1987) have suggested that this mechanism explained the development of secondary bedform fans in the lee of steep sided dunes, at the entrance to Bahía Blanca Estuary, Argentina. In contrast, Lefebvre and Cisneros (2023) indicate that flow separation is absent or intermittent with steep dune angles shallower than around 20°.

The water depth is a natural limiting factor for the height of the dune in shallow settings, since reduced depths over the crest result in higher current / wave activity, hence stronger bed shear stresses, eroding the crest away. Empirical formulae estimate marine dune heights to be approximately between 5% and 25% of the water depth (e.g., van Rijn, 1984b; Yalin, 1964, in Soulsby (1997)). In deeper settings, the same limitation does not apply and marine dunes stop growing when, for example, the currents are strong enough that suspended sediment transport becomes predominant, or when sediment supply becomes scarce.

Marine dunes are very active bedforms: growing, evolving and migrating. They migrate under the action of a residual current, which can originate from the tide (tidal asymmetry), or from the wind / waves impacting the background current to the point, for example, that current reversal is hindered. Idier et al. (2002) offer that the superimposition of secondary bedforms on the dunes can also contribute to their migration when the smaller bedforms avalanche on the lee side of the dunes. Marine dunes have been shown to migrate up to tens of metres per year (e.g., Daniell et al., 2008; Katoh et al., 1998; van Dijk et al., 2011). According to several authors, two-dimensional dunes (with linear crests) show slower migration rates than three-dimensional dunes (in Garlan, 2007), which can be explained by the stronger flows associated with the latter (Belderson et al., 1982). Other factors can also impact dune behaviour and van Landeghem et al. (2012), for example, indicated that the correlation between plan shape and migration rates is not universally observed. Berné et al. (1989) have analysed repeated bathymetric surveys of a very large crescent-shaped dune in the Dover Strait and estimated considerable migration speeds of 70 m/year on average.

1.1.3 Marine dunes in shallow shelf seas

Marine dunes have been observed worldwide in a variety of environments: from shallow shelf seas, straits and tidal inlets (e.g., Bartholdy et al., 2002; Bellec et al., 2019; Besio et al., 2004; Malikides et al., 1988; Terwindt, 1971; Zhou et al., 2020) to continental slopes (e.g., King et al., 2014; Valentine et al., 1984) and deep water (e.g., Kenyon et al., 2002; Viana et al., 1998; Wynn & Stow, 2002), as

a result of a variety of controlling agents: from waves, tides and wind-induced currents (e.g., Ferret et al., 2010; P. T. Harris, 1989; Le Bot et al., 2000; Porter-Smith et al., 2004; Terwindt, 1971) to oceanic and bottom currents (e.g., Kenyon et al., 2002; Wynn & Stow, 2002) and internal waves (e.g., Droghei et al., 2016; Reeder et al., 2011; Ribó et al., 2016). This diversity of environments is illustrated in Figure 1.3, which is by no means exhaustive.

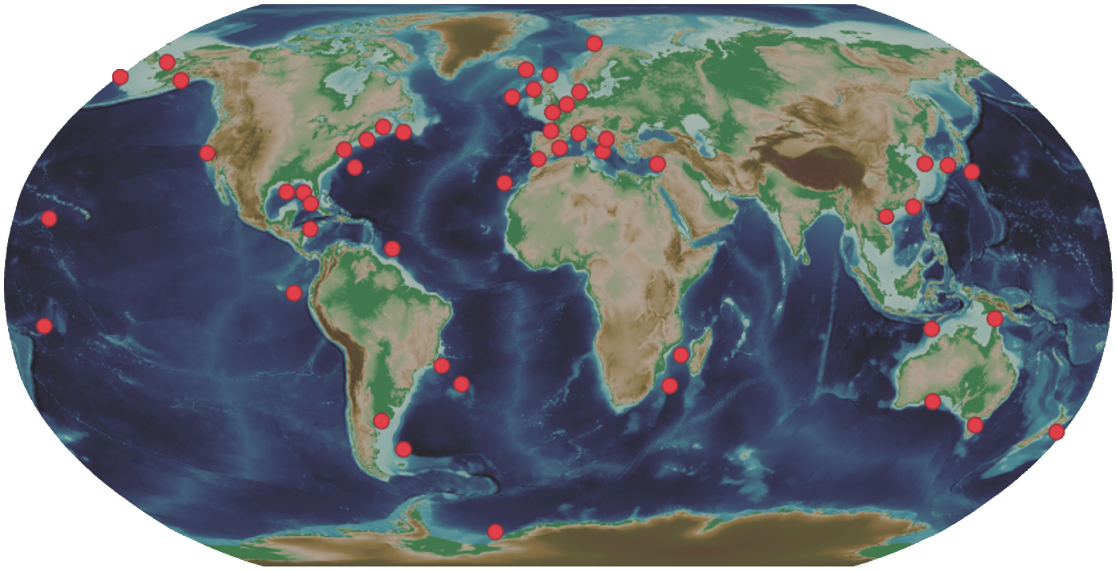

Figure 1.3: Distribution of marine dunes observed in the world (not an exhaustive list of locations). Shallow shelf seas are shown in light blue (Source of background imagery: GEBCO)

Our research focuses on marine dunes in shallow shelf seas. Shelf seas refer to the ocean waters on the continental shelf, defined by the International Hydrographic Organization (IHO) as 'a zone adjacent to a continent (or around an island), extending from the low water line to the depth at which there is usually a marked increase of slope to greater depth' (International Hydrographic Organization, Last accessed March 1, 2022). In practice, the depths of shallow shelf seas rarely exceed 200 m. They are indicated by light blue shades in Figure 1.3, which is based on the GEBCO 2021 bathymetric chart of the oceans.

Shelf seas cover almost 9% of Earth's ocean surface area according to P. T. Harris et al. (2014). Tides, wind forcing and river inflows are the principal mechanisms controlling shelf sea flows. Marine dunes are often associated with (macro) tidal environments. While these are not the only settings where dunes can form, they provide the relatively strong near-bed currents necessary for dune development. Elsewhere, achieving these conditions may require currents to be accelerated by local topographic constrictions or narrowing channels (Langhorne, 1977), for example.

Examples of shallow shelf seas include:

- in Europe, the North Sea and the English Channel;
- in North America, the Hudson Bay;
- in Southeast Asia, the South China Sea and the Gulf of Thailand;
- in Australia, the Bass Strait separating mainland from Tasmania;
- in South America, the Patagonian Sea;
- between Asia and the Arabian Peninsula, the Persian Gulf.

To the author's knowledge, the North Sea is one of the better studied shelf seas. Marine dunes abound there, but they have also been documented in the Barents Sea (Bellec et al., 2019), the Bisanseto Sea (Katoh et al., 1998), the South China Sea (Jiang & Lin, 2016), the Taiwan Strait (Zhou et al., 2018,

2020, 2022), the Bass Strait (Malikides et al., 1988), San Francisco Bay (Barnard et al., 2006), the Bay of Fundy (Dalrymple et al., 1978) or in the Race of Alderney (Blunden et al., 2020). Table 1.2 is a compilation of marine dune parameters: wavelength, height and migration rate for a range of environments, based on a selection of observational data reported in the literature. It is anticipated that, as mapping of the world's continental shelves progresses (Wölfl et al., 2019), we may find that marine dunes are recurrent shallow shelf sea features.

Focusing on the Dover Strait and the Southern Bight of the North Sea, Augris et al. (1990) characterise site conditions (nature, morphology and mobility of the seabed) in the North of France, differentiating the NS-oriented seaboard from the EW-oriented seaboard, from Cap Gris-Nez to Dunkirk. In the latter region, they highlight the presence of compound bedforms consisting of tidal sandbanks, in association with marine dunes and smaller dunes. Ripples have been universally observed, on video or while diving, alone or on the back of the larger bedforms. The general direction of sediment transport is east-northeast.

The Dover Strait, in particular where the South Falls and Sandettié sandbanks meet, has been under investigation by several authors (e.g., Idier et al., 2002; Le Bot et al., 2000). They describe what are very large marine dunes according to the SEPM classification (Ashley, 1990). Two distinct zones are identified by their morphology/behaviour. To the south of a SW-NE axis that corresponds to the major axis of the tidal current ellipse, are large isolated dunes; to the north are smaller dunes connected to a sandbank. On a decennial time scale, the migration of the dunes is mostly attributed to tidal influences with a clockwise migration about the tidal ellipse axis. On a much shorter time scale (that of a storm event, for example), the dynamics is said to be directly affected by the wind conditions either strengthening, slowing down, or even reversing the effect of tidal currents.

Closer to Dunkirk, Lanckneus and de Moor (1991) report on the northern Kwintebank, on the Belgian continental shelf, where marine dunes also coexist with tidal sandbanks and smaller superimposed bedforms. Survey data indicate that the dune crests are mostly linear and trend northeast. The dune profile is asymmetrical in all cases, dipping towards the northeast, being the peak flood direction. The dunes vary in size, notably with water depth (refer to Table 1.2).

Source	Location	Wavelength (m)	Height (m)	Migration rate (m/yr)
Barnard et al. (2006)	San Francisco Bay	30 – 220	6.0 *	7
Bartholdy et al. (2002)	Danish Wadden Sea	50 - 250	1.3 - 3.6	16 - 47
Bellec et al. (2019)	Barents Sea	300 – 700	4.0 – 19	–
Besio et al. (2004)	North Sea	120 – 500	2.0 – 10	1.5 – 8
Blunden et al. (2020)	Alderney Race	–	–	> 100 "
Bouma et al. (1980)	Lower Cook Inlet	75 - 500	2.0 - 9.0	–
Dalrymple et al. (1978)	Bay of Fundy	10 – 215	0.2 – 3.4	–
Harris (1988)	Torres Strait	80 - 750	2.0 - 6.0	–
Katoh et al. (1998)	Bisanseto Sea	80 - 180	2.0 - 6.0	up to 20
Knaapen (2004)	North Sea	220 *	1.5 *	5.0
Lanckneus and de Moor (1991)	North Sea	90 - 210 *	1.6 - 3.6 *	67 "
Malikides et al. (1988)	Bass strait	55 - 1730	2.0 - 12	–
Németh et al. (2007)	Gulf of Cadiz	50 - 350	1.0 - 5.0	–
Roos et al. (2007)	North Sea	145 – 760	1.5 – 7.3	–
Santoro et al. (2002)	Messina Strait	50 - 300	0.5 - 3.5	–
Terwindt (1971)	North Sea	125 - 1250	2.9 - 9.1	–
van Dijk et al. (2011)	North Sea	72 – 800	1.1 – 9.7	0 – 37
Zhou et al. (2018)	Taiwan Strait	50 *	1.5 *	1 - 5

Values marked by * correspond to average values;
Those marked by " to values extrapolated from short term measurements.

Table 1.2: Compilation of marine dune parameters from a selection of field observations in shallow shelf seas

1.2 Numerical modelling of marine dune dynamics

Roos (2019) presents a short overview of the approaches available to study marine dunes (what the author called tidal sandwaves). He differentiates data analysis and empirical (or conceptual) modelling, which are based solely on observations and do not describe physical processes, from process-based modelling that does describe physical processes and represents the morphodynamic feedback loop, thereby expressing the intimate relationship between the hydrodynamic conditions and the sediment transport mechanisms, hence bed evolution.

Process-based modelling itself encompasses two types of models: idealised and full, or complex, models, so-called because they include a detailed representation of the geometry and boundary conditions. While the former has typically been employed to qualitatively explore sensitivities to targeted parameters or processes on marine dune dynamics, the latter is usually reserved for in-situ applications. In the remainder of this document, we will adopt the term 'morphodynamic model(ling)' to refer to 'process-based model(ling)'.

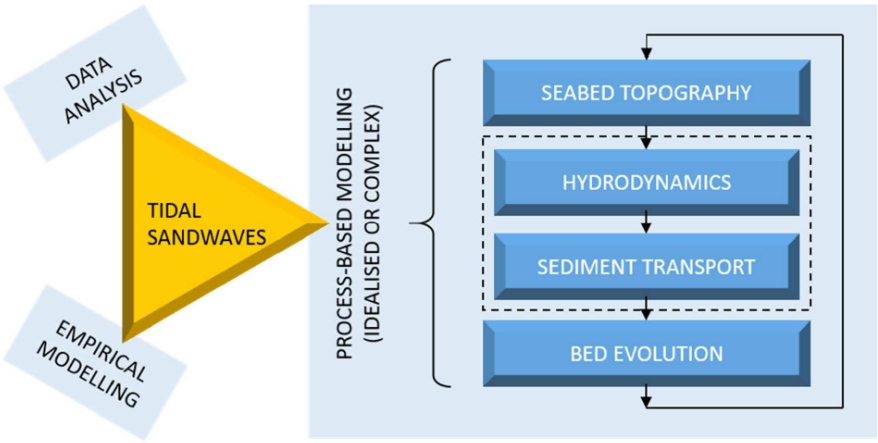

Figure 1.4: Overview of approaches available to study marine dunes, distinguishing data analysis and empirical modelling (left) from process-based modelling (right) (Roos, 2019)

As also noted by Idier et al. (2010) in the context of marine aggregate extraction, these approaches are not mutually exclusive and should ideally be used in conjunction for an optimal assessment. Separately, Anthony and Aagaard (2020) remarked that numerical modelling is increasingly relied upon to overcome spatial and temporal limitations in field observations. They warned that the reliability of the numerical models is closely related to the data from which they are developed.

1.2.1 Empirical models

The overarching principle of empirical models is to derive a general behaviour law that fits an extensive data set. As such, they do not include the description of physical processes. Examples of empirical models include simple shape predictors such as Allen (1968), Flemming (1988, Equation 1.1), van Rijn (1984b) or Yalin (1964). These usually take the form of power laws relating the dune characteristic wavelength and height, to the water depth (and the bed shear-stress in some cases). It is noteworthy that, owing to the wide range of environments in which marine dunes occur, a significant scatter is observed in the data and a generic relationship is thus difficult to establish.

$$H = 0.0677 L^{0.8098} \tag{1.1}$$

where H denotes the dune height and L its wavelength.

Another example is the geometry-based migration predictor developed by Knaapen (2005). This predictor relies on the observation that asymmetry often serves as an indicator of migration direction,

from gentle to steep dune sides. It expresses the migration rate of a dune, c, as a function of its median shape parameters: wavelength, length-to-height ratio, and asymmetry (Equation 1.2). The predictor was calibrated against survey data from nine areas in the Southern Bight of the North Sea, and validated against another three, after the migration rates were estimated from changes in the crest position (smaller bedforms filtered out, subject to inaccuracies in positional errors). Notably, while Knaapen (2005) dataset showed a strong correlation between dune migration rate and asymmetry, this relationship may not always hold true (e.g., van Landeghem et al., 2012).

$$c = \alpha L \frac{L}{H} A_s |A_s| \tag{1.2}$$

where H and L are defined in Figure 1.2; A_s is the dune asymmetry, defined as the ratio of the difference between gentle-side length ($L2$) and steep-side length ($L1$) to the total dune length L ($A_s = 0$ for symmetrical dunes). In Equation (1.2), α is a tuning parameter, with dimension yr^{-1}.

Knaapen et al. (2002; 2005) have also investigated the use of conceptual *Landau-type* models to characterise the evolution of the dune height over time. The Landau equation describes the growth of patterns to their equilibrium state. Knaapen and Hulscher (2002) have shown that it was suitable to describe marine dune development. Two parameters determine the solution, one controlling the linear growth and the other the non-linear effects, which in time limit undue growth:

$$\frac{\partial H}{\partial t} = a H + b H^3 \tag{1.3}$$

where H denotes the dune height (the original equations in Knaapen et al. (2002; 2005) were written in terms of dune amplitude, half the height). Parameters a and b describe the linear growth and the non-linear dampening, respectively. These parameters were tuned in Knaapen and Hulscher (2002) using data assimilation techniques and were shown to adequately reproduce the marine dune regeneration observed after dredging in Katoh et al. (1998). In an application to Rotterdam Harbour, Knaapen et al. (2005) indicated that a Landau approach was superior to a linear model in predicting marine dune recovery after dredging, in the context of a Decision Support System for navigation channels.

Empirical and/or conceptual models are only strictly valid for the range of environmental conditions for which they were originally derived. Some authors suggest adjusting the model parameters for site-specific applications. Failing that, extrapolation to different environments should be considered with caution.

1.2.2 Idealised morphodynamic models

Idealised morphodynamic models describe, in a simplified form, the hydrodynamic and sedimentary mechanisms related to sediment transport and bed evolution. The schematisation of physical processes and geometry makes these models computationally efficient and particularly suitable for exploratory sensitivity analyses, to gain generic insight into the role of certain parameters and / or processes.

To that effect, idealised models are often used in conjunction with stability analysis methods (whether linear or not) and solve the physical equations partly in the spectral space, and partly in the physical space.

Linear stability approach

Linear stability analysis refers to a method used to assess the response of a system to a disturbance. It is based on the linearisation of the mathematical problem. Under the assumption of infinitesimal disturbances, $\epsilon \ll 1$, the solution can be written as a power series as follows:

$$\psi = \psi_0 + \epsilon \psi_1 + \mathcal{O}(\epsilon^2) \tag{1.4}$$

where ψ_0 and ψ_1 denote the initial and disturbed states respectively and where higher order terms are neglected. When applied to the study of bedforms, the disturbance is a small topographic perturbation; ψ_0 refers to the state of the system for a flat seabed; and ϵ denotes the amplitude of the seabed disturbance with respect to the undisturbed water depth.

A range of disturbances with arbitrary wave numbers are modelled. Whilst the solution to the problem determines the flow and sediment transport conditions associated with a given disturbance, it is the resulting growth rate of the disturbance that is of interest in the study of bedforms. The initial state is stable if all disturbances decay (negative growth rate). If, however, some modes grow, the seabed is unstable, and the fastest growing mode (FGM) is assumed to determine the dominant bedforms.

Huthnance (1982) was the first to adopt a linear stability model with a coupled seawater / sandy seabed system to investigate the mechanisms responsible for the development of bedforms. Although this approach was capable of generating sandbanks, it could not initiate the formation of marine dunes. Hulscher (1996) attributed this to the lack of vertical circulation in Huthnance's model, based on depth-integrated shallow water equations. The author showed that, when vertical flow structures are represented, sand transport could indeed converge to the crest of a seabed disturbance and support the growth of dunes. The model predictions were said to be in line with observations in the southern North Sea and near the Dutch coast.

The influence of various physical processes was subsequently explored by improvements to Hulscher's original model, such as the effect of residual currents (Németh et al., 2002), grain size (Besio et al., 2003), sand pit geometry (Roos, 2004, in the context of marine aggregate extraction), suspended load transport (Besio et al., 2006), graded sediments (van Oyen & Blondeaux, 2009b), wind and wave climates (Campmans et al., 2018b), or benthic organisms (Damveld et al., 2019).

Non-linear stability approach

Strictly speaking, linear stability analysis models are only valid for infinitesimal disturbances, and as such are limited to short-term behaviour and the onset of dune development. They cannot describe the complete range of dune growth from generation to their final amplitude.

To reach equilibrium, growth needs to slow over time. This is done with the introduction of non-linear terms counteracting linear growth. Non-linear models are, therefore, required to investigate the marine dune long-term behaviour, equilibrium profile and interactions with anthropogenic activities (Besio et al., 2008).

Németh et al. (2007) have, for example, studied the formation and evolution of marine dunes over long time scales of 50 to 200 years; and van den Berg et al. (2012) over large domains following the observation that small domains (of hundreds of metres) are unable to reproduce variability in dune morphology. Campmans et al. (2018a) have explored the role of wind, wave and intermittent storms on finite-amplitude dunes.

The principal weakness of these models, as they stand, is that, although they are able to represent dune growth towards an equilibrium, they tend to significantly over-predict marine dune height compared to field observations (order of several metres).

1.2.3 Complex morphodynamic models

Complex morphodynamic models rely on the solution of mathematical equations expressing the governing laws of water and sediment motion, and using state-of-the-art process formulations. They require a detailed representation of the geometry and of initial and boundary conditions. Examples of such models are the Deltares Delft3D software suite (`https://oss.deltares.nl/web/delft3d`), the DHI Mike software suite (`https://www.dhigroup.com/technologies/mikepoweredbydhi`), and the open source community models, open**TELEMAC** (`https://opentelemac.org/`) and Croco (`https://www.croco-ocean.org/`).

The flow conditions are usually derived from the two-dimensional depth-averaged, horizontal shallow water (2DH) equations or the three-dimensional Reynolds-Averaged Navier-Stokes (3D) equations (Eqs. 3.1 and 3.2), taking into account external influences such as wind and atmospheric pressure. The wave conditions are derived from the spectral action density balance equation, taking into account transformation processes as the waves propagate into shallower waters, and interactions with the current field (Eq. 3.5). The sediment transport processes occurring as a result of these forcings

(suspended load and / or bedload) are modelled using advection-diffusion equations and transport rate predictors suited to a range of sediment types and transport mechanisms. Finally, the bed evolution is governed by the Exner equation that expresses sediment conservation (Eq. 3.13).

Complex models are, for the most part, reserved for in-situ and engineering applications. To the author's knowledge, they have not been widely used thus far to study the dynamics of marine dunes, other than in highly schematised settings (e.g., sinusoidal dunes or dune trains, limited number of tidal constituents, uniform grain distribution), which restricts their relevance to qualitative assessments. In addition, they rarely take account of all three dimensions and are rather often limited to two-dimensional width-averaged (2DV) representations (one horizontal and one vertical dimension), recognising the importance of vertical effects but ignoring lateral variability.

Tonnon et al. (2007) have, for example, applied an idealised 2DV approach to an isolated artificial dune offshore of Rotterdam Harbour, the Netherlands. Other studies have investigated the correlation between suspended sediment transport and the occurrence of marine dunes (Borsje et al., 2014); the role of turbulence (Borsje et al., 2013), or tidal forcing, sediment size and bed slope effects (Z. Wang et al., 2019) on the formation of marine dunes; the effect of suspended load transport and tidal asymmetry (van Gerwen et al., 2018), or grain sorting processes (Damveld et al., 2020) on finite-amplitude dunes.

More recently, efforts have been made to move away from idealised geometries (e.g., Krabbendam et al., 2019, 2021; Overes, 2021) and simplified forcing in studies related to marine dunes. For instance, Auguste et al. (2021) explored sensitivities of marine dunes to environmental parameters (in particular sediment properties and bed friction formulation) with an application to Banks Strait, Australia, using realistic wind and wave forcing based on climate reanalysis data. Similarly, Creane et al. (2023) investigated sediment transport pathways at Arklow Bank in the Irish Sea. Both studies used depth-averaged, horizontal (2DH) models.

Krabbendam et al. (2023) and Nnafie et al. (2023) were among the first to use a three-dimensional (3D) modelling approach in a coastal setting. They developed local-scale models (3 km × 3 km) for specific dune fields in the southern North Sea, examining their response to background topography and sediment availability. But tidal forcing was represented relatively simply (using just 4 constituents), and meteorological forcing was not considered. Pessanha et al. (2023) took a hybrid approach, using a depth-averaged model for a larger area to provide flow conditions for a very local 3D model (estimated around 500 m × 500 m) off Martha's Vineyard in the USA. The large-area model incorporated sea levels from a regional ocean tide model and wind / wave conditions from in situ observational data.

In a river setting, Goll (2016) suggested that the contribution of the turbulence should be included in the bed shear-stress calculations to improve the 3D numerical model predictions, in particular the shape (kurtosis and skewness) of the dunes.

1.2.4 Environmental controls

Observations, empirical and conceptual models, and morphodynamic models have all contributed to better our understanding of dunes in a marine environment. This section summarises some of the outcomes.

Currents

Using a linear stability model, Hulscher (1996) showed that marine dunes are generated by tidal movements. Migration was absent from her model, which was based on symmetrical tidal currents, but the author remarked that Fredsøe and Deigaard (1992) were able to model migration as a result of a steady current. Therefore, she suggested that both tidal and residual currents would be required to model marine dunes adequately.

If the growth of marine dunes has been explained by the presence of tide-averaged circulation cells (Hulscher, 1996, Figure 1.5) building up the crest by the convergence of sediment particles, the

presence of a residual current disrupts this mechanism: the convergence point is moved downstream of the crest. The bedforms are consequently shaped by the residual currents (with a gentler slope facing the residual flow and a steeper slope sheltered from the flow) and migrate in their direction (van Gerwen et al., 2018).

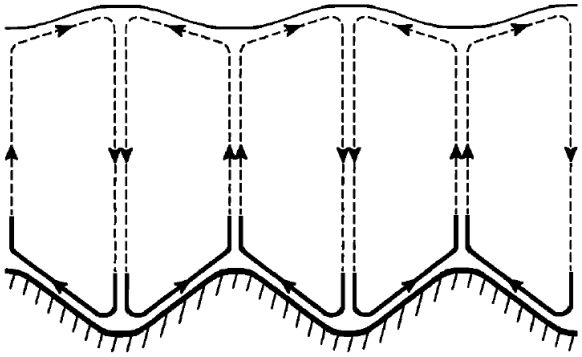

Figure 1.5: Sketch illustrating strong near-bed circulations supporting the growth of marine dunes (Hulscher, 1996)

Expanding from Hulscher (1996)'s model, Németh et al. (2002) explored two mechanisms able to generate a residual flow: wind and pressure gradients. The order of magnitude of the resulting migration rate was found to agree with the values reported in the literature for typical North Sea conditions. From the observation that dune migration is a direct result of bed shear-stress asymmetry, Németh et al. (2002) suggested that tidal asymmetry due to higher harmonics would also trigger dune movement, even if to a lesser extent.

This was corroborated by Besio et al. (2004) who considered the effect of a steady current superimposed on tidal components M2 and M4. In accordance with field observations, they showed that the direction of marine dune movements could differ from that of the steady residual current, and was rather controlled by the relative strength of the residual current with respect to the tidal currents and phase shift between the M2 and M4 components. They concluded that a detailed knowledge of the tidal constituents was essential to be able to satisfactorily reproduce dune migration.

Separately, van Gerwen et al. (2018) adopted the (2DV) Delft3D numerical model developed by Borsje et al. (2013, 2014) to investigate the growth of marine dunes towards equilibrium. They found that stronger residual flows resulted in higher migration rates and lower equilibrium dune heights.

Winds and waves

Several authors have highlighted the influence of wind and wave conditions on the dynamics of marine dunes. There is observational evidence that while the long-term migration of the dunes is mostly determined by the strength of the residual current, the short-term evolution is directly affected by synoptic-scale wind conditions. Depending on their direction relative to background currents, wind-induced currents have been shown to strengthen, slow down, or even reverse the effect of tidal currents on dune migration (e.g., P. T. Harris, 1989, 1991; Idier et al., 2002; Lanckneus & de Moor, 1991; Le Bot et al., 2000).

This is corroborated by the work of Campmans et al., who have studied at length the influence of storms on marine dune evolution using linear and non-linear stability analyses (Campmans et al., 2017, 2018a, 2018b, 2019). Based on model runs for a combination of wind and wave conditions derived from 20 years of data in the North Sea, they found that storms affected primarily the dune migration rate, and to a lesser extent its growth rate. Seasonal variability in the climate was mirrored by seasonal variability in the dune dynamics, and migration rates tended to be higher during the winter months, growth rates smaller than during the rest of the year (Campmans et al., 2018b). Comparison of the

model results against dune transects surveyed on several occasions between 1992 and 2010 in the North Sea (Menninga, 2012) was deemed encouraging.

Campmans et al. (2018b) have further estimated that average wind and wave conditions, present in their 20-year climate only a third of the time, accounted for two thirds of the migration, while extreme wind and wave conditions contributed only modestly.

Pessanha et al. (2023) also studied the impact of winds and waves on marine dune dynamics at Wasque Shoals (located in the southeast corner of Martha's Vineyard, USA, water depths < 7 metres). The model incorporated realistic hydrometeorological forcing. The authors found that the speed of dune migration was underestimated by more than 50%, compared with bathymetric survey data, if only tide- and wind-induced currents were taken into account. Good agreement required additional consideration of wave forcing.

If not directly on migration, waves have been shown to play a role on the morphology of marine dunes. Although oscillatory currents induced near the seabed may not generate net sediment transport, they do contribute to stirring up the sediment, which is then available for tidal and residual (even wind-induced) currents to transport. This mechanism is particularly relevant on the crest of marine dunes due to reduced water depths, and several modelling studies have identified the waves dampening effect on the dune growth rate and final equilibrium height in particular (e.g., Auguste et al., 2021; Campmans et al., 2018a, 2019; Tonnon et al., 2007). Interestingly, Tonnon et al. (2007) found that, when the wave contribution is taken into account, the crest alone may migrate in the direction of the low water currents, while the dune body as a whole migrates in the direction of the dominant current.

Field observations also indicate a marked reduction in dune height under severe wave conditions (e.g., Langhorne, 1982; Terwindt, 1971). Terwindt (1971) have for example observed that the dune height was controlled in some instances by the frequency of occurrence of strong events and the time lapsed between these energetic periods (Southern Bight of the North Sea). More recently, Bao et al. (2020) used data from multi-beam surveys performed pre-storm, post-storm and one year after a tropical storm in the South China Sea to quantify the morphodynamic impact on a marine dune field. They concluded that the marine dunes had migrated during the storm, their crests dramatically eroding. The marine dunes appeared to have only partially recovered one year after the storm had passed.

Sediment properties and transport processes

Several authors (e.g., Borsje et al., 2014; Damen et al., 2018) have correlated the absence of marine dune fields in certain regions of the Dutch continental shelf to the strength of the currents in relation to sediment size, or in other terms the prevalence of suspended load over bedload. Tonnon et al. (2007) have set up a 2DV Delft3D morphodynamic model, including both bedload and suspended transport, to study the evolution of an artificial marine dune created from material dredged from the Rotterdam navigation channel. The dune was shown to grow when the environmental conditions were such that sediment transport occurred predominantly as bedload. Conversely the dune decayed in conditions favourable for transport by suspended load.

Using a similar modelling approach, Borsje et al. (2014) and van Gerwen et al. (2018) have also demonstrated the dampening effect of suspended sediment transport. This meant that, for larger sediment grain sizes (350 μm), the dune height was predicted to be lower and its wavelength longer when transport by suspension was included; while for smaller grain sizes (200 μm) dune formation was prevented altogether as a result of counter-balancing effects. Separately, Borsje et al. (2014) have determined that marine dunes could only form when Rouse numbers were in excess of 2.0, which is characteristic of bedload dominant transport.

Damen et al. (2018) developed correlation matrices linking marine dune shape characteristics to a) environmental parameters and b) theory-based indicators such as Rouse number and Shields parameter, with the view to confirm that the wide range of marine dune morphologies observed on the Dutch continental shelf was attributed to differences in local bed composition and hydrodynamic conditions. They based their analysis on survey data and model data / databases that inform on

concomitant bed and hydrodynamic parameters. They concluded that suspended load transport is an important process controlling the shape of marine dunes (Figure 1.6).

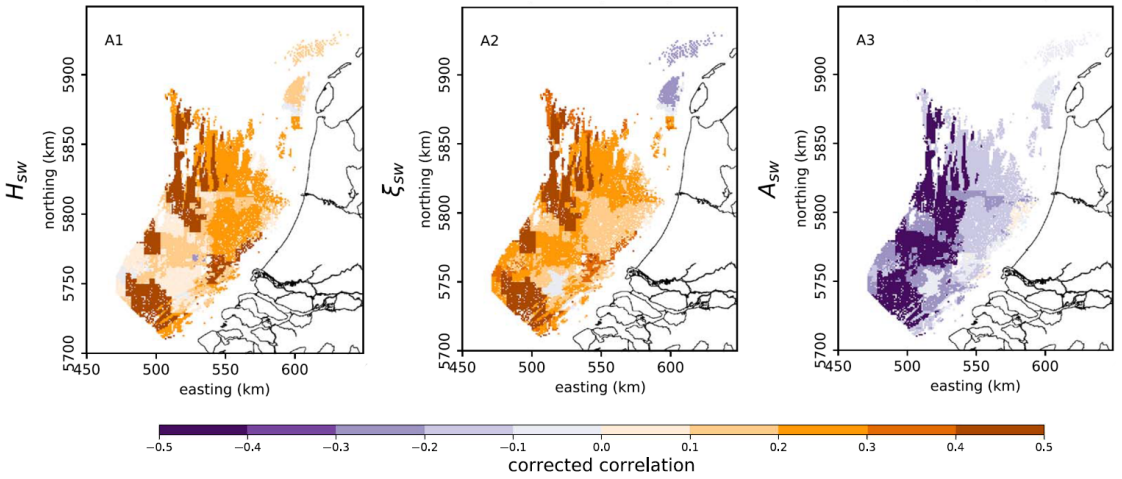

Figure 1.6: Correlation of marine dune characteristics (A1) height, (A2) spatial frequency and (A3) asymmetry with Rouse number (adapted from Damen et al., 2018)

In this context, any mechanism altering the balance between bedload and suspended load (e.g., weather and storms, turbulence, sediment properties) is likely to have an effect on marine dune dynamics.

Borsje et al. (2013) have specifically explored the influence of turbulence models on marine dune formation and evolution from bedload transport. Based on an idealised Delft3D model, the authors concluded that a $k-\epsilon$ turbulence model should be preferred over a constant vertical eddy viscosity model. The former was shown to reproduce more closely the marine dune wavelengths observed on the Dutch continental shelf, in relatively flat surroundings. In their study, Tonnon et al. (2007) had preferred the use of an algebraic turbulence model based on the parabolic–linear sediment mixing of Van Rijn (1993). They indicated that the use of a $k-\epsilon$ turbulence model resulted in a dip on the lee side of the dune, which they had no evidence to say was realistic.

From the linear stability analysis of a flat seabed subjected to oscillatory tidal currents, Besio et al. (2003) have indicated that marine dunes cannot form for critical grain size above ca. 1 mm. Marine dunes are, therefore, characteristic of sandy seabeds. van Oyen and Blondeaux (2009b, 2009a) have explored the influence of graded sediment and grain sorting processes on the formation of marine dunes. van Oyen and Blondeaux (2009a) have indicated that the distribution of the fine and coarse sediment fraction along the dune profile was the result of a balance between grain mobility and hiding / exposure effects. Depending on the strength of the tidal current, their model predicted an accumulation of fines at the crest (moderate currents) or conversely at the trough (stronger currents, with the caveat that suspended transport was not included in the model). This is reflected in apparently conflicting observational data, which the authors attributed to differences in local currents and seabed material.

van Oyen and Blondeaux (2009b) have also investigated the influence of graded suspended sediment transport. Their (linear stability analysis) model considered a bimodal sediment mixture (characterised by d_{33} and d_{66}, i.e. the diameter for which 33% (66%) of the sediment particles are finer) and included the effects of both bed and suspended load transport. It was concluded that, although fractional suspended load transport did not affect sediment-sorting processes, it did have an impact on the formation of marine dunes, which was found to be sensitive to the characteristics of the sediment mixture.

Damveld et al. (2020) have set up an idealised Delft3D model with four sediment classes and indicated that marine dunes were predicted to be lower and longer when the sediment was not well sorted. They

attributed this to the fine fraction being transported in suspension, resulting in the dampening effect also reported by others. Typically, the sediment at the crest of marine dunes was found to be coarser than that at the toe because of sorting processes by deposition. Separately, Auguste et al. (2021) have remarked that dune migration was accelerated when the sediment was not well sorted.

1.3 Offshore wind farm context

1.3.1 Climate neutrality by 2050

Thirty years ago, world leaders first came together to collectively address 'dangerous human interference with the climate system' (United Nations Conference on Environment and Development, Rio de Janeiro, June 1992). The United Nations then invited countries (parties) to sign an international environmental treaty by which each would commit to reducing, in particular, greenhouse gas emissions. 'Conference of the Parties' meetings have been held on an annual basis since 1995 to discuss progress and challenges with respect to the goals set out originally in the Kyoto Protocol, and then in the Paris Climate Accords. Dubaï recently hosted the 28th of these meetings (COP28) in December 2023. The signatory countries have pledged to phase out carbon-based energy sources 'in a just, orderly and equitable way' in order to mitigate the worst effects of climate change and achieve zero emissions by 2050.

In 2018, only a very small fraction (0.3%) of the world's electricity supply was provided by offshore wind (International Energy Agency, 2019). This number is expected to grow steadily in the coming decades to help meet climate neutrality.

In Europe, one of the proposals of the European Commission is to 'develop the full potential of Europe's offshore wind energy', thereby recognising the vast wind resource in Europe's sea basins and the technological leadership role it has played so far. The Offshore Renewable Energy Strategy (November 2020) aims to increase Europe's offshore wind capacity from its current level of ca. 12 GW to at least 60 GW (a fivefold increase) by 2030 and to 300 GW (another fivefold increase) by 2050.

1.3.2 Offshore wind industry

Offshore wind farms consist of an array of horizontal-axis turbines harnessing energy from the wind field. The appeal of offshore vs. onshore wind resides in a stronger and more consistent resource than over land, allowing for the use of larger turbines and yielding a more stable power generation. The turbines are typically arranged in a regular pattern, carefully designed to limit wind shadowing from upstream devices. The spacing between turbines is equivalent to 3–10 times the rotor diameter and depends on the prevailing wind direction (Bhattacharya, 2019).

As illustrated in Figure 1.7, wind turbines have steadily grown in size, hence in nameplate (or rated) capacity, since the first wind farm. This means that fewer turbines are required to achieve the desired capacity in a wind farm. For example, in Dunkirk, two scenarios are being investigated for an overall capacity of ca. 600 MW, depending on the availability of the technology at the time of implementation: 46 turbines of 220 m diameter and 13 MW capacity, or 35 turbines of 260 m diameter and 17 MW capacity.

Besides the turbines themselves, which convert wind flow into electrical power, several elements constitute an OWF (Figure 1.8):

- an offshore substation, which houses well above sea level the transformation hub raising the voltage to export levels;
- the foundations, which anchor the wind turbines and substation in the seabed;
- subsea intra-array cables, which transport the production of each turbine to the substation;
- subsea export cables, which connect the offshore substation to the mainland; and
- an onshore substation, which transmits and distributes the power generated by the OWF to the national grid.

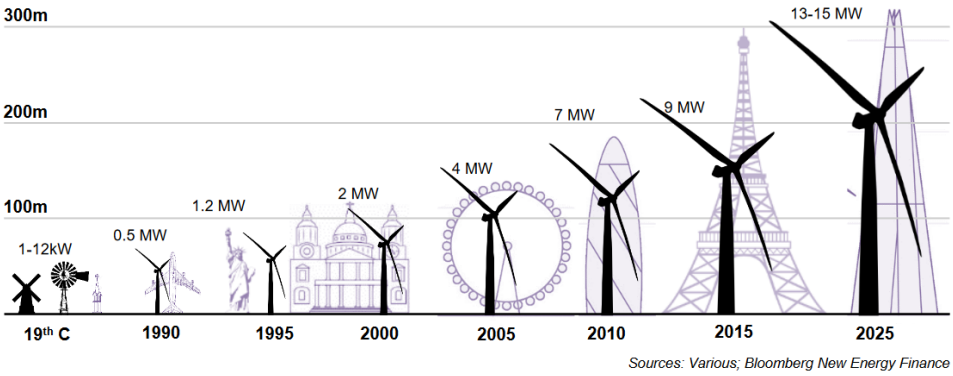

Figure 1.7: Evolution of wind turbine size and output (Liebreich, 2017)

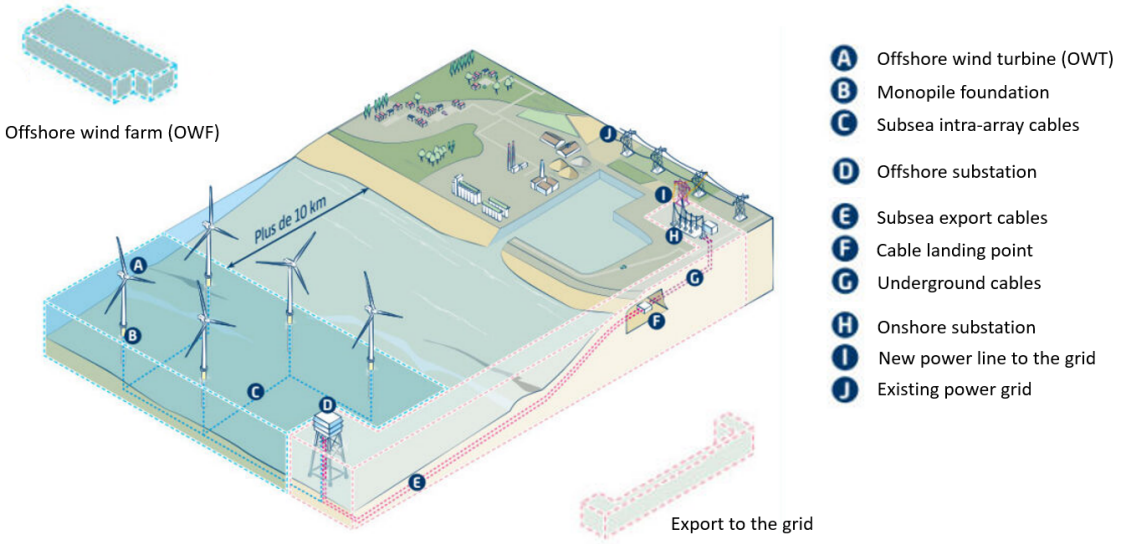

Figure 1.8: Overview of an offshore wind farm (adapted from Parc éolien en mer de Dunkerque website)

Monopile foundations are the most commonly used (accounting for about 80% in Europe, Pisanò, 2019) and will be used in Dunkirk. They consist of a pile of large diameter (5 m to 10 m) driven into the seabed (embedded length to diameter ratio in the range 3 to 6), noting that larger turbines require larger monopiles to cope with environmental loading from the wind and waves (Pisanò, 2019). Monopile foundations have traditionally been used in shallow waters (under 30 m depth) but their range is gradually extended to 50 m depth owing to their cost benefit compared to, for example, jacket foundations. In order to deploy offshore wind turbines in water depths exceeding 50-60 m, the industry is now investing in the development of floating technologies.

The offshore substation consists of a foundation propping up a topside, which houses the transformers well above sea level. Again, the foundations can be monopile or jacket, which is suited to transitional depths (20-80 m) and is said to make it safer to anchor. Jacket foundations use a lattice framework with several legs and anchors set on the seabed.

The intra-array and export cables are usually buried in the seabed to protect them from damage by fishing gear, (dropped or dragging) anchors or environmental conditions. In some cases the seabed can be prepared (dredged) prior to cable laying operations to reach, or at least, approach a stable seabed level. Several processes are available to then bury the cables (e.g., jet trenching or cutting, ploughing) depending on the geotechnical properties of the seabed. In cases where it is not practical to bury the cables, external protection works (e.g., rubble, concrete mattress) may be considered.

1.3.3 Impact of marine dunes on OWF projects

Current and future OWF projects are likely to be deployed in shallow shelf seas owing to the proximity to mainland and favourable depths. It is reasonable to consider the presence of marine dunes in these environments. The OWF elements would then experience additional pressures associated with dune dynamics and induced seabed level variations over the life cycle of the OWF project.

Starting at the implementation stage, trenches are often made to prepare the seabed for cable-laying operations for example. The rate of infilling of these trenches is an important consideration in the planning of operations, to determine the time window during which the trench will remain open, or if there is a need to mechanically backfill at the end.

During the life of the OWF, wind turbine foundations might be at risk of scouring (Whitehouse et al., 2011), which could weaken their structural integrity and stability, or, on the contrary, overburying, which could generate additional mechanical loads. Global scour, resulting in the general lowering of the seabed around a group of closely spaced structures (van der Tempel et al., 2004) could also be an element of concern.

The subsea power cables are buried in the seabed to protect them from damage by other seabed users (e.g., fishing and navigation activities Langhorne, 1977) and environmental conditions. In highly dynamic areas, the required burial depth may not be respected over time and there is a risk that the cables become exposed, making them vulnerable to damage (Langhorne, 1977). They could become suspended as a result of the dune mobility or change in shape (Németh et al., 2003), making them liable to breakages. In the Messina Strait, Italy, free spanning of a pipeline has been observed during a survey: the pipe was seen to hang between two successive dune crests (Santoro et al., 2002).

In contrast, power cables could be overburied, which would make it difficult to repair faulty cables without causing further damage on the one hand (Langhorne, 1977), but also modify their thermal environment on the other hand. Power cables are indeed sensitive to heat and designed to work within a certain range of internal temperatures, short of which they risk damage, specifically to the insulation component (Morvan et al., 2023).

Insofar as dune dynamics is still poorly understood in open marine environments, it is difficult to forecast when and where a cable is at risk of being exposed or overburied. Various strategies have been put forward (e.g., Roetert et al., 2017; Whitehouse et al., 2000) in an effort to support the choice of appropriate burial depths, quantify the risk of cable exposure, or optimise the cable route where avoidance of the dune field is not desirable nor practical.

However, offshore wind farm projects have been safely and successfully implemented in areas characterised by active marine dune fields, in the North Sea in particular. The challenge then resides in the monitoring and control of the impact of the mobile seabed on the OWF elements over time (typically the life of the project), for which a suitable (optimised) frequency must be determined (Games & Gordon, 2014).

1.3.4 Other industrial interests

Several authors (e.g., Langhorne, 1977; Whitehouse et al., 2000; Németh et al., 2003) have explored the relevance of marine dune dynamics in relation to subsea engineering challenges at large. In the same way that constant remodelling of the seabed due to the mobility of marine dunes can potentially overbury or expose intra-array and export cables, it is a potential hazard to the oil and gas pipelines, subsea communication and power cables that cross the seas.

Other renewable energy industries, such as floating wind or wave, rely on anchoring systems to ground the devices. Barrie and Conway (2014) have shown through examples along Canada's western coast that locations, which are promising in terms of their high tidal/wave/wind energy potential, are adversely affected by difficulties relating to the installation and connection to the electrical grid on the mainland, arising from the presence of large (mobile) marine dune fields. They conclude that these

examples illustrate the role that geosciences can play in supporting the safe deployment of marine renewable energy systems.

The mobility of marine dunes is also of concern for the safety of (recreational and commercial) navigation (e.g., Whitmeyer & FitzGerald, 2006). To avoid the risk of grounding, navigable depths must be maintained by the ports authorities in the approach channels for example. Where marine dunes are present and active, these depths risk being reduced to unacceptable levels. This leads to costly surveying and / or dredging campaigns. After dredging, the marine dunes gradually recover, all the faster if sand supply is readily available (Katoh et al., 1998). Several authors (e.g., Campmans et al., 2021; Knaapen & Hulscher, 2002; Knaapen et al., 2005) have taken an interest in the dune regeneration rate to help determine, via numerical modelling, the most efficient dredging strategies both in terms of frequency and volume.

The stability of sandbanks and larger dunes plays a role in protecting the coastline against wave attack for example, in that high events are likely to break over the reduced depths at the crests. Marine dune crests can offer suitable grounds for marine aggregate extraction in coastal waters (Roos, 2004), thus reducing this protection. Numerical modelling is useful for predicting the long-term morphodynamic effects of large-scale sand mining (e.g., Idier et al., 2010; Krabbendam et al., 2022; Roos, 2004).

Insight into marine dune dynamics might also prove of interest to study the burial and mobilisation of Unexploded Ordnance (UXO) and discarded military munitions, pollution, and other subsea hazards, which had previously been trapped in the sediment bed.

Ripples, dunes and sandbanks have been identified as part of the Habitats Directive. Although home to a limited number of species, these are unique and particularly adapted (restricted) to these dynamic ecosystems. The coast off Dunkirk in particular is a major spawning bed for numerous fish species, and therefore plays a key role in the renewal of fish stocks. The potential remodelling of the marine dune field may adversely impact these communities.

1.4 Numerical modelling of offshore wind farms

1.4.1 Representation of OWFs

Of the OWF elements identified in Section 1.3, the foundations are likely to have the greatest impact on the dynamics of marine dunes. Two distinct modelling approaches can be adopted to represent the presence of the turbine foundations:

- either implicitly through the use of proxies;
- or explicitly in the model mesh.

It is customary to use the implicit approach and to parameterise the foundations with a resistance term in large-scale coastal models (refer to guidance in Lambkin et al., 2009). This methodology has been widely used in simple and complex morphodynamic models alike (e.g., Christie et al., 2012; Margalit, 2017; Rivier et al., 2015, 2016; van der Veen & Hulscher, 2008). It has the advantage that it is straightforward to implement, but the drawback that complex flow-structure interactions yielding vortices and associated turbulence are not considered, which are likely to degrade the near-field model predictions.

In addition to this drag source term in the momentum equations, some authors have, therefore, investigated the use of a source term in the turbulence transport equations to represent the mixing effect of the obstruction (e.g., Rennau et al., 2012; Rivier et al., 2016). This approach is (said to be) common to assess the effect of vegetation on the flow field (e.g., van Velzen et al., 2002 in (van der Veen & Hulscher, 2008); Temmerman et al., 2005; Bouma et al., 2007; Baptist et al., 2007; in Rivier et al. (2016)) and is interesting.

In a 3D hydrodynamic and sediment transport model, Rivier et al. (2015, 2016) have explored the two different methodologies: implicit vs. explicit. They concluded that similar results were obtained in terms of near-field hydrodynamics and sediment transport. Separately, they discussed in more depth

the benefits and drawbacks of each technique. They indicated that although the explicit approach was more precise in principle, it required a relatively fine mesh to resolve the flow structure (which is usually not the object of a large-scale model) and that the discontinuity introduced with the obstacle generated an artificial asymmetry in the flow field. They went on to remark that the implicit (parameterised) approach could be adapted to coarser elements (e.g., of the pile dimensions) although the flow field was generally smoothed out as a result. They also noted that this methodology relies on the knowledge of the undisturbed velocity upstream of the structure, which can be difficult to assess, in particular with closely spaced turbines.

Christie et al. (2012) have chosen to break from the conventional approach of implicit parameterisation of the foundations, with the objective of achieving a more accurate representation of near-field processes. They have investigated the use of both 2D and 3D numerical models to simulate the impact of offshore wind farms on the hydrodynamics, and consequently on large-scale coastal processes. The 2D and 3D versions of the model were found to give comparable results in the far field, and the 3D model was said to be capable of representing intricate flow patterns around a monopile in the near field. However, while the flow and sediment erosion patterns compared favourably with the experimental results reported by Roulund et al. (2005) in front of the pile, the erosion occurring in its wake could not be replicated.

In addition to the foundations themselves, some authors have explored methods to model the forces exerted on the seabed as a result of enhanced, turbulent flow close to the turbine foundations. The conventional approach to compute bed shear-stresses relies on an estimate of the friction velocity. In different contexts, Goll (2016), Yiannoukos et al. (2020) and Couldrey et al. (2020) have modified the formulation close to the structure so that it is dependent on the turbulent kinetic energy near the seabed.

This follows the work of Pope et al. (2006) who explored the relationships between bed shear-stresses and current velocity in the field and in laboratory experiments. From the observation that bed shear-stresses derived by the log-profile method were marred by uncertainties, related to inaccuracies in the measure of vertical distances, they investigated an alternative prediction method based on the turbulent kinetic energy. Yiannoukos et al. (2020) have noted encouraging results compared to laboratory experiments aimed at investigating the hydrodynamic and morphodynamic impact of submerged obstacles (e.g., ship wreck).

Couldrey et al. (2020) have set up a local morphodynamic model where the turbine foundation was represented explicitly in the mesh (with ca. 10 nodes). They found that the high mesh resolution, combined with a $k-\epsilon$ turbulence model, provided a reasonable approximation of the turbulent processes generated in the presence of the monopile and computed the scour inducing bed shear-stresses in the immediate vicinity of the structure after Pope et al. (2006). When comparing the simulation results after four days (2 days of neap followed by two days of spring tides) to in-situ data, Couldrey et al. (2020) concluded that, although the direction of the scour was satisfactorily reproduced in the model, its extent was largely underestimated.

Finally, it is important to note that the effects of offshore wind turbines on hydrodynamics, and by extension on sediment transport processes, are generally limited to those resulting from the flow obstruction caused by their foundations. To our knowledge, morphodynamic models do not consider the reduction in wind speed caused by energy extraction downstream of a turbine (e.g., Frandsen et al., 2006). Although it is recognised that the atmospheric wake of large offshore wind farms can extend up to 20 km downstream (as observed from SAR imagery by M. B. Christiansen & Hasager, 2005), and that this wind speed deficit could potentially affect wave and surface current fields (N. Christiansen et al., 2022), these effects will not be considered in the present research.

1.4.2 Interactions with the seabed

Sediment transport patterns are affected both locally and further afield by the presence of an offshore wind farm. Near-field effects occur within the footprint of the OWF and might include scouring at the base of the turbine or suspended sediment plumes in its wake. Far-field effects extend beyond the

footprint of the OWF and might include shoreline erosion or changes in regional sediment transport patterns, for example (Clark et al., 2014).

Existing research indicates that most wind farm-induced changes occur within the wind farm footprint or are within natural variations. Cooper and Beiboer (2002) concluded that the presence of OWFs had limited impact in the near field, and unlikely significant impact in the far field. Their focus was particularly on first-round sites around the UK (small projects with a 10 km^2 footprint and with a maximum of 30 turbines), but the authors suggested that the results could be applied more widely to other scenarios. Clark et al. (2014) have commented on the potential impacts of offshore wind farms on the environment, for example in relation to turbulence and vertical mixing, changes in the wave field, sediment dynamics, currents and tides, atmosphere and biogeochemistry, with the same conclusions. Therefore, far-field effects are not addressed in this work.

Studies at wind farm sites usually concentrate on very near-field effects (within a few pile diameters), and the potential for scour hole formation at the base of the foundation. Indeed, wind turbine monopiles, like bridge piers, alter the hydrodynamics locally (e.g., Melville, 1988; Sumer & Fredsøe, 2002; Whitehouse, 1998) to generate a complex 3D flow structure. This is illustrated in Figure 1.9, reproduced from Melville (1988), representing in particular the horseshoe vortices developing near the seabed immediately upstream of the flow obstruction, and the vortex shedding in its wake. This added turbulence can result in the formation of a scour hole around the structure, for which scour protection works are sometimes envisaged.

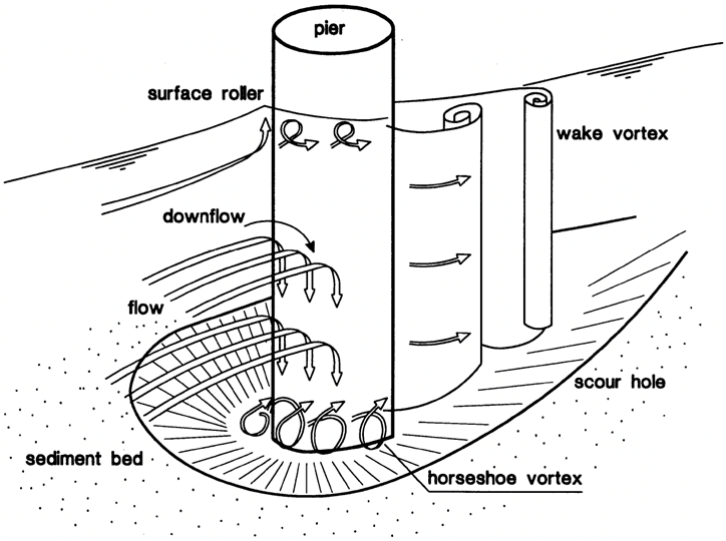

Figure 1.9: Sketch illustrating the flow and scour patterns near a vertical pier (Melville, 1988)

Whitehouse et al. (2011) have collated and analysed survey data typically collected every 6 months at existing offshore wind farms, located for the most part in the North Sea and in the Irish Sea. The data cover a variety of environments and designs. The authors concluded that the development of scour was intimately related to the seabed characteristics (e.g., sand vs. clay, depth of mobile sediment) and showed evidence of edge scour where protection works had been installed. Global scour, resulting in the general lowering of the seabed around a group of closely spaced structures, is observed around jacket foundations for example (van der Tempel et al., 2004) and could be of concern for the substation. However, this is unlikely to occur at the scale of a wind farm, where the turbines are arranged so that the resource is maximised, i.e., reasonably far apart.

While scouring is understandably of concern for the structural stability of the foundations, this is not something that can be fully investigated within the remit of our research, focused on larger scale effects. Little information is available, to the author's knowledge, on the impact observed at that scale on sediment transport patterns.

Vanhellemont and Ruddick (2014) have characterised the sediment plumes from satellite imagery of the southern North Sea. The turbid wake of individual turbines has been shown to be aligned with the general direction of the tidal currents locally; the extent of the fines plumes has been estimated between 30 m and 150 m wide and several kilometres long. In light of this, the authors have suggested that further studies should be conducted on the impact of increased concentration of suspended particulate matter (SPM) on sediment transport, for example.

Elsewhere, at the Scroby Sands wind farm, surveys have been conducted before, during and after construction to document and quantify (potential) changes in seabed levels, hydrodynamics and suspended sediment concentrations - bearing in mind that these in turn may alter sediment transport processes in the region. Scroby Sands was one of the pioneering UK Round 1 OWF projects, located on a shallow sandbank off the coast of Great Yarmouth, England. It consists of 30 wind turbines on monopile foundations. The environment is characterised by fast tidal currents. Waves are moderate but play a role in mobilising seabed sediment due to shallow water depths (combined bed shear-stresses are capable of resuspending 2 mm sand for prolonged periods). When granted, the project was considered a worst-case scenario in terms of potential impacts on coastal processes (Rees et al., 2006) and studies have been commissioned to assess these impacts, if any, in particular in relation to the stability of the sandbank on which the wind farm is built.

Rees et al. (2006) have reported on long scour tails, extending downstream as far as 95 turbine diameters (Figure 1.10), and characterised by larger bedforms than on the surrounding seabed (based on an analogy with experimental tests, J. Harris and Whitehouse (2014) hypothesise that sediment

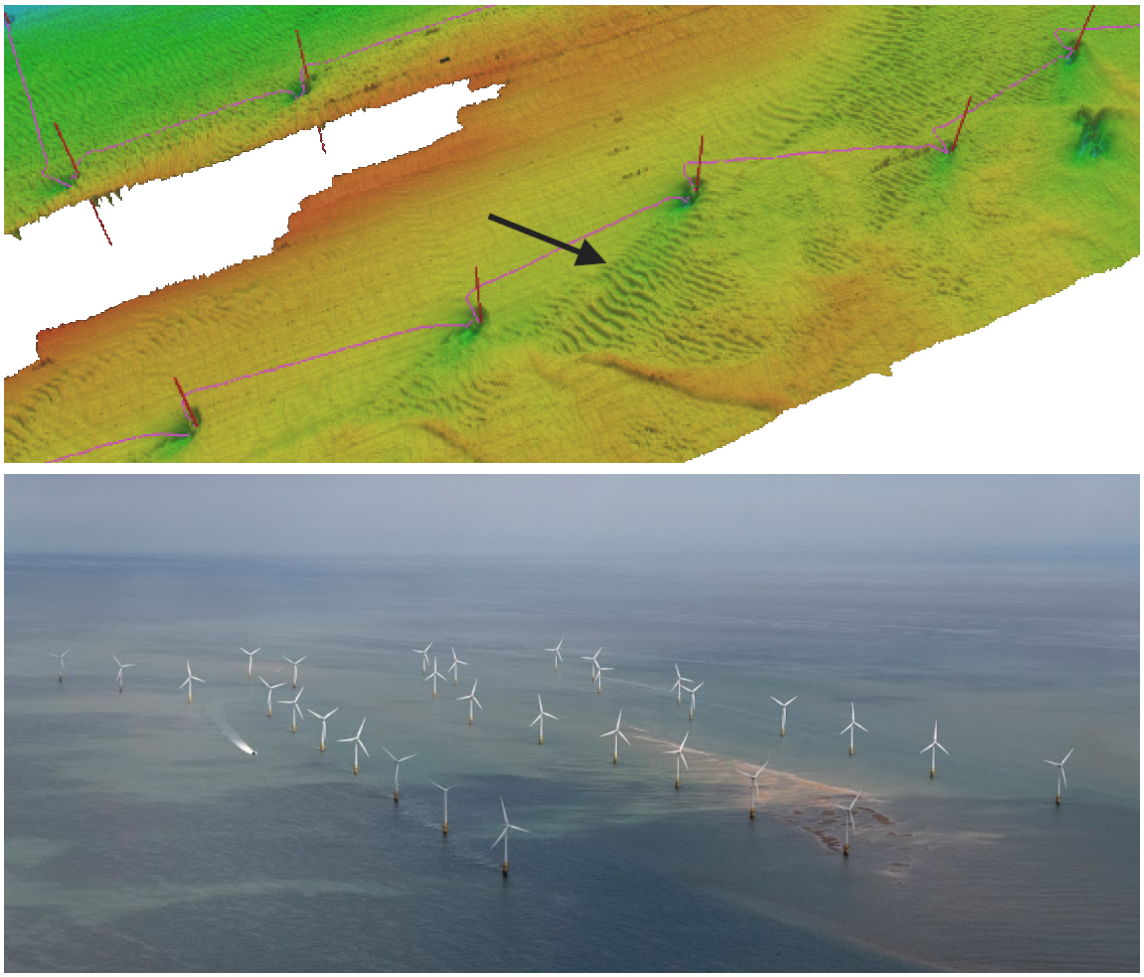

Figure 1.10: Top: scour tail at Scroby Sands wind farm, identified by the black arrow (Rees et al., 2006). Bottom: raised bed levels (Photo credit: John Fielding, July 2020)

accretion downstream of the scour hole formations modifies the flow to the extent that bedforms are initiated in the wake of the obstruction). Changes in the marine environment have also meant that the sandbank bed levels have risen over time, effectively stranding some of the turbines, as illustrated in Figure 1.10. This all suggests that OWFs may have an area of influence larger than the immediate vicinity of individual turbines.

To our knowledge, only one study observed an isolated (barchan) dune as it migrated past an offshore wind turbine foundation. Couldrey et al. (2020) explored the progression of the dune using multi-beam bathymetric data collected between 1995 and 2015. They found that the dune was temporarily stretched as it passed the monopile (because of the accelerated flows on either side of the obstacle) but that it rapidly recovered once it had moved away from the monopile. The impact of the passing of the dune on scour depths and on the natural frequency of the wind turbine and foundation assembly was also considered. It was concluded that the dune had had no significant effect on the stability (and consequently on the operational performance) of the structure.

Leaving aside small-scale near-field CFD-type models that study more precisely scour processes, little is available in the literature with regard to the numerical modelling of the interactions between marines dunes and OWF foundations. The model developed by Couldrey et al. (2020), although interesting, was very local (700 m × 1000 m) and focused on scour processes. It might benefit from extending to longer time scales to explore whether the model is able to reproduce the observed migration of the crescent-shaped dune over time.

Margalit (2017) has attempted to model the interactions between OWF foundations and the seabed, including, but not limited to scour formation. In a 3D configuration where the monopile was represented explicitly in the mesh, and a flat seabed was subjected to a uniform nominal current, he showed that, in the course of days, a dune formed from the sediments eroded around the pile, which travelled downstream. When a dune train was propagated across the domain over a longer time scale of ca. 6 years, the migration rate was said to slow as a result of the presence of the structure. These results should be taken with caution in our opinion noting that questions are raised with respect to the fitness of the model set-up.

Using different modelling tools, Blunden et al. (2020) and Auguste et al. (2021, 2022) have investigated the impact of *tidal energy converter devices* in the Race of Alderney, UK, and Banks Strait, Australia, respectively. Although the processes involved in tidal farms are distinct from those of offshore wind farms, tidal energy converters, like monopiles, modify the hydrodynamics in their wake, resulting in a downstream velocity deficit. Despite the presence of dunes in the area, Blunden et al. (2020) do not explicitly address their mobility. Instead, the authors focus on changes to residual velocities, residual transport rates and bed levels, with the objective of optimising the array location. In Banks Strait, the dunes are not within the boundaries of the tidal farm. However, Auguste et al. (2022) quantified the indirect impact of flow acceleration and redirection around the farm on the neighbouring dune field. They predicted that the larger the tidal farm, the faster the dunes travelled (for example, a 32% increase in migration rate was predicted over 3 months with 300 turbines). Both studies concluded that the placement and overall nameplate capacity of the farm should be carefully considered, since the hydrodynamics, hence the sediment dynamics, were found to be quite sensitive to these factors.

1.5 Knowledge gaps and research questions

1.5.1 Knowledge gaps

Although they may be present on large portions of the continental shelves, the morphology and dynamics of dunes are still not fully understood in open marine environments.

In a nature-based setting, marine dunes cannot be reduced to uniform, rhythmic dune trains with linear crests. The morphology of the dunes (e.g. sinuous crest lines, bifurcations, fans) reacts to spatial variations in the hydrodynamic conditions. However, much of the research work carried out so far with complex process-based models has been relying on a 2DV representation, whereby lateral variations along the dune crests are ignored.

Observational data indicate that meteorological events play a role in the evolution of marine dunes in shallow water environments. This is not surprising if we consider that weather conditions, in particular winds, influence the tidal current, and that currents are one of the driving forces behind sediment transport processes. However, previous research on marine dunes has largely been based on schematised hydrometeorological forcings (e.g., simplified tidal flow and/or representative winds).

Knowledge of how marine dunes evolve when they interact with offshore wind farms is scarce.

1.5.2 Research aim

The aim of our research is, therefore, to gain insight into the hydrodynamics, the sediment transport and morphological processes at play in a marine dune environment, at a coastal scale:

a) to improve our understanding of marine dune dynamics and modelling for time and space scales from days to years and from metres to kilometres, respectively;
b) to improve our understanding of the interactions between marine dunes and OWF elements.

This is considered critical in a context where the demand for renewable energy (and offshore wind) is expected to escalate in the coming years, involving wind farms with a larger footprint, an increased number of turbines, of larger dimensions.

Eventually, we hope that the outcome of our research may be able to support developers by providing some elements of response to the technical challenges they face when implementing offshore wind farms (cables, foundations) in a marine dune setting, as well as scientists by providing some elements of response to questions such as the resilience of marine dunes or the impact on marine species, habitats and ecosystem functioning.

1.5.3 Specific research questions

These knowledge gaps and research objectives motivate the following scientific questions.

RQ1. What are the environmental parameters controlling marine dune migration in shallow shelf seas?

Marine dunes are highly dynamic bedforms present in shallow shelf seas. They migrate because of residual currents that may arise from tidal asymmetry and are influenced by weather conditions (particularly wind). In extreme cases, these additional contributions can affect the background tidal current, hindering current reversal. To understand the development and evolution of marine dunes, it is essential to understand the underlying physical processes in shallow shelf seas. This Research Question aims to identify the role of meteorological influences on dune dynamics using a comprehensive morphodynamic model.

RQ2. How does a marine dune field evolve in space and time in shallow shelf seas?

Some studies suggest that, while long-term dune dynamics is influenced by the overall strength of residual currents, short-term evolution is more closely linked to meteorological influences. Consequently, inter-annual to decennial variability in weather patterns is expected to be reflected in the variability of dune evolution. This Research Question aims to determine which of the mild but frequent wind events or the extreme but rare wind events has a greater influence on shaping the dune field using a comprehensive morphodynamic model.

RQ3. To which extent does the presence of an offshore wind farm impact the marine dune field it was developed in?

The presence of offshore wind farms, specifically their foundations, is expected to modify the hydrodynamics within and around their footprint. Given that currents play a crucial role in sediment transport processes, these modifications are likely to influence dune dynamics. This Research Question aims to identify and understand the specific impacts resulting from these hydrodynamic changes.

1.6 Methodology

1.6.1 3D morphodynamic modelling, at a large scale, and with realistic forcings

It is important to use a complete representation of coupled hydrodynamics, sediment transport processes and bed evolution that can only be achieved with complex process-based modelling and so our research is based on the open**TELEMAC** system: a state-of-the-art free surface flow suite of solvers based on finite element methods and solving mathematical equations expressing the governing laws of water and sediment motion. We develop a 3D morphodynamic model, at a large scale, and with realistic hydro-meteorological forcings, for a specific application: the site of the future offshore wind farm project in Dunkirk, France, for which valuable in situ metocean and bathymetric data have been collected in recent years.

The methodology proposed to answer the specific research questions laid out in the previous section consists of two main parts:

I) Modelling marine dune dynamics in a shallow shelf sea: influence of hydro-meteorological conditions;
II) Modelling marine dune dynamics in an OWF context: interactions with foundations.

Dunes are not rigid bodies; they both deform and move. While their dynamics cannot be solely described by their migration (e.g., Ogor, 2018; Turki et al., 2021), this is our primary focus.

1.6.2 Modelling marine dune dynamics in a shallow shelf sea

The first part of the research focuses on the numerical modelling of marine dune dynamics in an undisturbed environment. The aim there is to provide elements of answers to research questions RQ1 and RQ2.

Following successful calibration and validation of the hydrodynamics and bed evolution with in situ data, we use the 3D morphodynamic model to explore the relationship between meteorological contributions and the dynamics of marine dunes. We simulate a one-year period, initially considering only tidal forcing in the model, and subsequently incorporating weather contributions through time- and space-varying wind and pressure fields.

By examining different time intervals throughout the year, we assess the impact of wind climate seasonality on dune propagation. To investigate specifically the influence of adverse meteorological events contrary to prevailing conditions, we focus our analysis on a 3-day storm originating from a direction opposite to the dominant sediment transport.

1.6.3 Modelling marine dune dynamics in an OWF context

The second part of the research focuses on the numerical modelling of marine dune dynamics within an offshore wind farm environment. The aim is to provide elements of answers to research question RQ3.

To achieve this, certain elements of the triangular finite element mesh are removed from the computation domain, to represent the wind turbine foundations explicitly in the validated 3D model. We then simulate a two-year period, including weather contributions, to evaluate any disturbances to the seabed caused by the foundations.

By positioning individual monopiles at various locations, we assess a range of responses. To specifically examine the group effect, we refine the mesh in the OWF area to model a realistic scenario consisting of 46 wind turbines.

1.7 Outline of the dissertation

This dissertation is organised as follows: Chapter 2 introduces the study area in the Southern Bight of the North Sea, including recent in situ metocean and bathymetric survey data. Chapter 3 delves into the controlling hydrodynamic and sediment transport processes, which inform our simplifying

modelling assumptions. This chapter also investigates the use of two sediment transport prediction formalisms, assessing their performance in predicting dune migration and their sensitivity to various parameters. Chapter 4 addresses the research questions RQ1 and RQ2 by quantifying the effects of tidal forcing alone or combined tidal and meteorological forcings in the natural (undisturbed) environment. Chapter 5 addresses the research question RQ3 by quantifying the impact of offshore wind farm foundations on the propagation of a dune field. Finally, Chapter 6 concludes this work, offering perspectives and insights for future research.

Chapter 2

Characterising the study area

Offshore wind farm (OWF) projects are rapidly developing around the world, in efforts to meet global environmental targets and ensure energy security. France is no exception. Three offshore wind farms are currently operational, while an additional four are being implemented for commissioning by 2027. One of them will be located in the Southern Bight of the North Sea, off the coast of Dunkirk, north of France, close to the Belgium border. The OWF will comprise a maximum of 46 wind turbines (depending on the technology available at the time of implementation) for a total power of ca. 600 MW. The area is known to be home to an intricate network of sandbanks, marine dunes, smaller dunes and ripples.

This chapter provides a comprehensive introduction to the study area, informed in part by a large data set collected over the last few years (2016-2022) in support of the Dunkirk OWF project and for research purposes. We focus on environmental factors, including winds (Section 2.1.1), sea levels (Section 2.1.2), currents (Section 2.1.3), and waves (Section 2.1.4). The seabed characteristics, specifically bathymetry (Sections 2.2.1 and 2.2.2), and sediment types (Section 2.2.3), complete this description.

The measurement locations are shown in Figure 2.1, coloured by data source. Table 2.1 provides a summary of the available parameters, with some parameters greyed out due to unavailability for our research. Specific details on each parameter can be found in the subsequent sections.

2.1 Environmental parameters

Site-specific meteorological and hydrodynamic campaigns provide recent data on wind speed, atmospheric pressure, water level, current speed and direction, and wave conditions. A wider search showed that long-term open-sea observations are available at the Westhinder measurement station, approximately 25 km north of the study area, in Belgian waters. All these elements complement the information reported by others (for example Latapy, 2020; Tresca, 2013) to qualify the environmental conditions offshore Dunkirk, offering valuable data for calibrating and validating hydrodynamic and wave models.

2.1.1 Winds

Wind climate

Meteorological parameters are recorded at the Westhinder platform (51°23.300' N 2°26.267' E, shown as a dark blue diamond in Figure 2.1(a)). The platform is located on the crest of the Westhinder sandbank, at a depth of approximately 13 m MSL (based on Shom, 2015, data). This open-sea location is exposed from all directions, close to the proposed OWF site, and is therefore considered representative of conditions in this part of the Southern Bight of the North Sea.

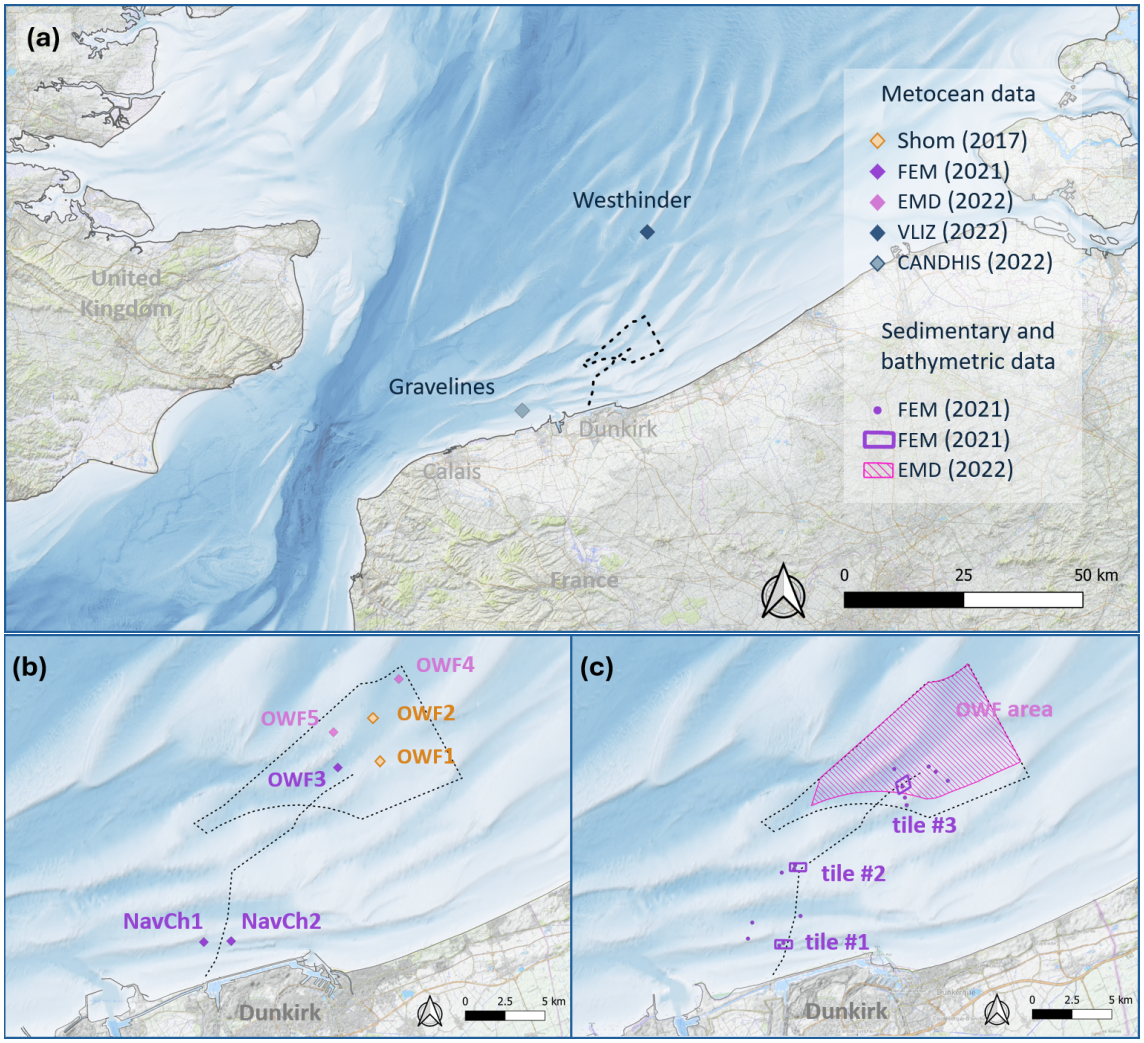

Figure 2.1: General location maps (UTM Zone 31N, EPSG 32631) showing where site-specific meteorological, hydrodynamic, sedimentary and bathymetric data are available (Table 2.1). The geographical footprint of the proposed offshore wind farm is marked by a dashed black line (Source of the background data: Shom (2015), OpenTopoMap, and European Environment Agency (EEA) coastline)

Wind data are collected since 1997, at 10-minute intervals, using a Vaisala Wind Set WA15 (WAA151 anemometer and WAV151 wind vane). The accuracy of these instruments is between 0.2 and 0.5 m/s depending on the wind speed measured, and less than 3° for directions (Vaisala, Last accessed May 10, 2024). Measurements of average wind speed and average wind direction at an altitude of 10 metres above sea level were obtained from the Flanders Marine Institute (VLIZ, 2022a).

The wind climate is depicted in Figure 2.2 in the form of a wind rose. A wind rose is a visual representation of the frequency of occurrence of certain conditions, grouped into directional sectors and wind speed intervals. In this analysis, we used 30° directional sectors and aligned the speed intervals on the Beaufort scale (Table 2.2; winds above 10 on the Beaufort scale are combined). The width of the colour bars indicates the percentage of occurrence for winds from a specific directional sector and speed range. The annual wind rose is based on data from complete years (25) to eliminate seasonal bias. In Figure 2.2, spring covers March to May, summer June to August, autumn September to November, and winter extends from December to February.

The winds offshore Dunkirk have a very distinct seasonality (Guerber et al., 2008). In the summer

Table 2.1: Meteorological, hydrodynamic, sedimentary and bathymetric data measured offshore Dunkirk

Location	Source	Latitude	Longitude	Approx. depth	Period obtained	Available data
OWF1	Shom (2017c, 2017d)	51°10.118' N	2°24.633' E	11 m MSL *	01-Sep-2016 to 23-Sep-2016	Currents, waves
OWF2	Shom (2017c, 2017d)	51°11.581' N	2°24.244' E	25 m MSL *	07-Sep-2016 to 08-Oct-2016	Currents, waves
NavCh1	FEM (2021b)	51°03.925' N	2°15.245' E	19 m MSL *	19-May-2021 to 30-Jun-2021	Levels, currents, waves
NavCh2	FEM (2021b)	51°03.969' N	2°16.714' E	14 m MSL *	19-May-2021 to 02-Jul-2021	Levels, currents, waves
OWF3	FEM (2021b)	51°09.883' N	2°22.372' E	27 m MSL *	19-May-2021 to 02-Jul-2021	Levels, currents, waves
OWF4	EMD (2022)	51°12.900' N	2°25.619' E	26 m MSL *	23-Oct-2020 to 06-May-2021	Weather, levels, currents, waves
OWF5	EMD (2022)	51°11.081' N	2°22.120' E	16 m MSL *	06-May-2021 to 28-Feb-2022	Weather, levels, currents, waves
Westhinder platform	VLIZ (2022a)	51°23.300' N	2°26.267' E	13 m MSL "	01-Jan-1997 to 02-Apr-2022	Weather
Westhinder platform	VLIZ (2022a)	51°23.300' N	2°26.267' E	13 m MSL "	21-Sep-2000 to 02-Apr-2022	Levels
Westhinder buoy	VLIZ (2022b)	51°22.850' N	2°26.133' E	23 m MSL "	01-Jan-1997 to 02-Apr-2022	Waves
Gravelines	CANDHIS (2022)	51°02.560' N	2°03.960' E	20 m MSL *	29-Sep-2020 to 31-Dec-2021	Waves
Cable route and OWF area	FEM (2020)	–	–	N/A	22/3-Oct-2019, 16/7-May-2020	Bed samples
OWF area	Shom (2017b)	BL: 51°08' N TR: 51°13' N	2°15' E 2°29' E	N/A	2016-17	MBES bed levels
OWF area	Shom (2017e)	BL: 51°08' N TR: 51°13' N	2°15' E 2°29' E	N/A	2016-17	Bed types
Tile #1	FEM (2021a)	51°04' N	2°16' E	N/A	17-Nov-2019 to 03-Jul-2021	MBES bed levels
Tile #2	FEM (2021a)	51°06' N	2°16' E	N/A	17-Nov-2019 to 09-Jul-2021	MBES bed levels
Tile #3	FEM (2021a)	51°09' N	2°22' E	N/A	17-Nov-2019 to 11-Jul-2021	MBES bed levels

* depths estimated from Shom (2016)
" depths estimated from Shom (2015)
BL (bottom left) and TR (top right) corners provide the approximate extent of the OWF area. If not specified, the approximate centre of the tile is given

Force	Wind type	Wind speed (m/s)
0	Calm	0 - 0.3
1	Light air	0.3 - 1.4
2	Light breeze	1.4 - 3.1
3	Gentle breeze	3.1 - 5.3
4	Mod. breeze	5.3 - 7.8
5	Fresh breeze	7.8 - 10.6
6	Strong breeze	10.6 - 13.6
7	Near gale	13.6 - 16.9
8	Gale	16.9 - 20.6
9	Strong gale	20.6 - 24.4
10	Storm	24.4 - 28.3
11	Violent storm	28.3 - 32.5
12	Hurricane	> 32.5

Table 2.2: Beaufort wind scale

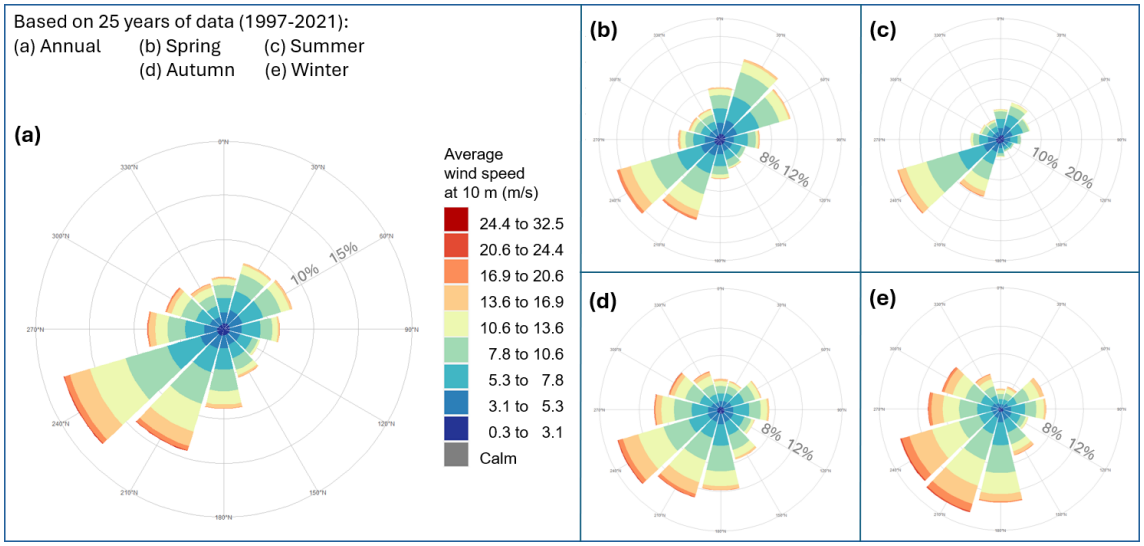

Figure 2.2: Open-sea wind climate at the Westhinder platform, 51°23.300' N 2°26.267' E (Data source: VLIZ, 2022a, period obtained: 1997-2021)

months (June through August), light winds prevail, occurring approximately 33.2% of the time. Strong winds, equivalent to Beaufort force 7 and over (exceeding 13.6 m/s), are rare, happening only about 4.1% of the time. In contrast, in winter, strong winds are as frequent as light winds, with 16.9% and 15.8% of observations falling into each category.

The prevailing wind direction is southwesterly, in line with the general atmospheric circulation and the Atlantic pressure fronts moving up the English Channel. These winds are strengthened by the channelling effect of the Dover Strait (Bertier, 2009). They blow parallel to the general orientation of the coastline at Dunkirk. However, in spring, there is a high proportion of cold northeasterly winds, fed by high pressure over Scandinavia (Figure 2.2(b)).

Further analysis of the data shows that gales (defined by speed > 13.6 m/s) come mainly from the southwest (50.8%, maximum of 30.3 m/s), and only marginally from the northeast (4.5%, maximum of 22.4 m/s). The strongest wind in the 25-year period was 30.3 m/s from 240°N, corresponding to a Beaufort force 11.

Site-specific wind data

Additional open-sea measurements of meteorological parameters are available that are directly relevant to the study area. Eoliennes en Mer de Dunkerque (EMD) deployed a NortekMed Alizé buoy (Figure 2.3) to characterise the metocean conditions in real time at the project site (EMD, 2022). The buoy was fitted with a weather station that recorded wind speeds and directions at 10-minute intervals. These measurements were taken 3.3 m above the water surface. The directions are provided relative to True North, with adjustments made for magnetic declination to account for measurements relative to Magnetic North.

Figure 2.3: NortekMed Alizé demonstration buoy installed off the coast of Carqueiranne, France (Photo credit: `https://www.alize-ocean.com`)

The buoy was moored between 23-Oct-2020 and 6-May-2021 in the channel between the Binnen Ratel and the Dyck Oriental sandbanks, in the northernmost corner of the OWF area (OWF4, 51°12.900' N 2°25.619' E). It was moved after a period of approximately 6 months to a different location to determine spatial variability in the metocean conditions (OWF5, 51°11.081' N 2°22.120' E, 6-May-21 to 28-Feb-22). These locations (OWF4 and OWF5) are indicated by pink diamonds in Figure 2.1(b).

The available period for OWF4 and OWF5 measurements is insufficient to be representative of long-term conditions to characterise the study area. However, these in situ measurements are useful to validate the forecast wind data used in the modelling (Sections 3.3 and 3.4).

For completeness, we should mention that LiDAR wind data have also been collected within the OWF footprint (EMD). LiDAR technology measures the speed of particles moving through the air column at various elevations up to several hundred metres, enabling wind speeds to be calculated accurately. EMD used these data to characterise the wind resource on a fine scale and could not share them.

Atmospheric pressure above mean sea level is also recorded both at the Westhinder platform and with the Alizé metocean buoy. These data are not discussed here.

2.1.2 Sea levels

Long-term sea levels

There are two main components to sea level: the astronomical tidal component that is caused by variations in the orbits and relative positions of the Sun, Moon and Earth, among other factors; and

the surge component that is related to weather conditions (noting that the term 'surge' is often associated with specific storm events rather than used to describe the continuous non-tidal component, Pugh, 1996).

The astronomical tidal component can be predicted for any point in the past or future using harmonic analysis of historical tide gauge records. Tides are categorised as semi-diurnal, diurnal, or mixed based on the prevalence of semi-diurnal or diurnal oscillations. This classification is often expressed with a Form Factor (e.g., $F = (H_{K1} + H_{O1})/(H_{M2} + H_{S2})$, H_* the amplitude of the K1, O1, M2 and S2 tidal constituents in Pugh, 1996).

In contrast, the surge component is predictable no more than a few days in advance. The most significant surges occur when strong winds persist over large shallow water areas. Extreme high or low sea levels result from the combination of tides and extreme positive or negative surges. Estimates can be derived from historical observations in the region.

The southern North Sea experiences semi-diurnal tides, similar to the oceans and most shallow shelf seas. The French Navy Hydrographic and Oceanographic Service (Service hydrographique et océanographique de la Marine, Shom) have determined astronomical tidal levels at standard ports along the French coast, including Dunkirk (51°03' N, 2°22' E Shom, 2020). Table 2.3 reproduces tidal levels relative to the Zéro Hydrographique (ZH), or Chart Datum. Spring tides are predicted to reach approximately 5.5 m (qualifying as macro-tidal according to J. L. Davies (1964) classification), while neap tides have a range of 3.5 m.

	HAT	MHWS	MHWN	MSL	MLWN	MLWS	LAT
Dunkirk	6.48 m	6.05 m	5.00 m	3.24 m	1.50 m	0.60 m	-0.01 m

Table 2.3: Astronomical tidal levels predicted inside the port of Dunkirk, 51°03' N, 2°22' E (Shom, 2020)

Long-term sea level measurements were obtained at the Westhinder platform (dark blue diamond in Figure 2.1(a)) (VLIZ, 2022a). The instrument (a directional wave radar, Figure 2.4) records water levels at 5-minute intervals since September 2000. The measurements are referenced relative to TAW (Tweede Algemene Waterpassing), which is a horizontal water level reference system used exclusively in Belgium. The Vlaamse Hydrographie of the Flemish government provides the necessary conversion factors to MSL (Mean Sea Level).

These data are not exempt of meteorological effects and include both the astronomical and surge components aforementioned (Figure 2.5). Preliminary analysis indicates, as mentioned by e.g., Bertier (2009), that the tidal curve is asymmetrical, with the tide rising more rapidly than it falls. We performed tidal harmonic analysis on sea levels observed during complete years in 2016 and 2021. This gives a Form Factor F = 0.07, which is significantly smaller than the threshold of 0.25 below which tides are classified as semi-diurnal (Pugh, 1996). The M2 lunar constituent dominates (87.2%), modulated by weaker constituents (approximately 7.5% for S2 and 2.7% for N2) and weather-related contributions.

Mean sea level is expected to rise in the future. The analysis of SONEL (Système d'Observation du Niveau des Eaux Littorales) long-term monthly means data at Dunkirk suggests an allowance for future sea level rise of the order of 1.7 mm/year. This is in keeping with Wahl et al. (2013) and the University of Colorado sea level trends (Last accessed January 24, 2022) for the southern North Sea. Projecting forward 30 years (the lifetime of the project), this corresponds to a 51 mm sea level rise, keeping in mind that the trend has been shown to accelerate in recent years (Frederikse et al., 2020). Future sea level rise was not allowed for in our work.

Through tidal harmonic analysis, we can isolate the surge component. Using surge data spanning 21 years (with 4% missing data), we calculated extreme surge levels via an extreme value analysis (marginal Generalised Pareto Distribution (GPD) fitted to the peak surge events with ASTEX, Bousquet &

Figure 2.4: Left: Westhinder platform located at 51°23.300' N 2°26.267' E (Photo credit: Alain Norro, Royal Belgian Institute for Natural Sciences). Right: Radac WaveGuide radar (Photo credit: Flemish Agency for Maritime and Coastal Services)

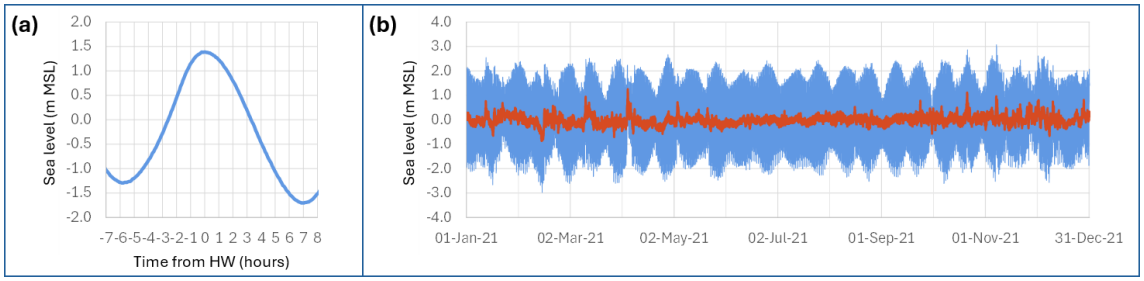

Figure 2.5: Sea levels at the Westhinder platform. (a) Close-up view of one tidal cycle, emphasising its asymmetry. (b) Observed sea level (blue) and surge component (red) predicted from tidal harmonic analysis for 2021

Bernardara, 2018). The predicted 50-year return positive surge elevation is estimated at +2.22 m, and the corresponding negative surge elevation at -1.72 m. The HSE Environmental Considerations report (HSE, 2002) offers positive surge estimates derived from a numerical storm surge model, which has been calibrated using observational data from seven UK reference ports. Our calculated estimate of 2.22 m is notably lower than the 2.75 m indicated in their Figure 5. This discrepancy is surprising, given reports that storm surge extreme trends in Europe match sea level rise trends (Calafat et al., 2022). However, it could be explained by the limited sample of simulated surge events in HSE (2002) or the fact that the analysis was concentrated on UK waters, rather than specifically on Dunkirk.

Site-specific sea level data

Site-specific sea level data are available that were collected:

- at 5-minute intervals, on the side of the navigation channel leading to the port of Dunkirk (NavCh1 and NavCh2) and in the OWF area (OWF3) using moored Acoustic Doppler Current Profilers (ADCP) (FEM, 2021b). These locations are marked by purple diamonds in Figure 2.1(b).
- at 10-minute intervals, at OWF4 (pink diamond, EMD, 2021), using a pressure sensor installed on the NortekMed Alizé buoy introduced in Section 2.1.1. Sea levels were also recorded at the second buoy location (OWF5) but were not made available to us.

The NavCh1 mooring was deployed in approximately 19 m water depth on 19-May-2021 and recovered on 30-Jun-2021. The NavCh2 and OWF3 moorings were installed in 14 m and 27 m water depths respectively, between 19-May-2021 and 02-Jul-2021. The instruments were mounted on rigid bed frames lowered on the sandy seabed (Figure 2.6). There were no interruptions in the records.

The data were obtained in raw format, which allowed us to perform basic quality checks. We observed clock drift at the NavCh2 mooring, which led us to exclude these data from processing due to the proximity to the NavCh1 mooring. Examination of the attitude parameters (pitch and roll) at the NavCh1 and OWF3 moorings give confidence in the reliability of the data. Pitch angles drifted over time by 9° and 1° at NavCh1 and OWF3, respectively, while roll angles drifted by 6° and 2° at the same locations. These values are well within the accepted range (20°). The heading of the instruments was stable (within 2°), which confirms that there were no interferences during the deployments, as expected for seabed-mounted devices.

We compared sea levels inferred from both pressure and Acoustic Surface Tracking (AST) recordings. At the NavCh1 mooring, differences ranged from -0.08 m to 0.37 m. At the OWF3 mooring, the results were noisier, with differences generally falling between -0.25 m and 0.10 m, but peak values reaching -1.39 m and 0.68 m. The AST technology is based on echo-ranging with a vertically oriented acoustic beam, avoiding attenuation issues present in velocity and pressure signals. Consequently, it provides a superior definition of the free surface. To calculate sea levels relative to MSL, we subtracted the time-averaged AST distance above the transducer from the instantaneous distances.

The OWF4 and OWF5 moorings are described in Section 2.1.1. While sea level data were provided in pre-processed form, the attitude parameters were accessible. These parameters exhibit semi-diurnal oscillations, characteristic of tidal effects. This is expected because metocean buoys are designed to adjust their orientation in response to environmental conditions (ocean currents, tides, wind and waves). The instrument being equipped with an Attitude and Heading Reference System (AHRS) module, it corrects buoy movements using the bin mapping technique.

The available periods of measurements are insufficient to characterise sea level trends in the study area. However, these in situ records are useful to validate the hydrodynamic modelling (Section 3.3).

2.1.3 Currents

Site-specific current data

Current data were collected on several occasions to inform the environmental conditions in and around the OWF site, with particular emphasis where local features may influence the hydrodynamics (e.g. depth-induced breaking in the shallows on top of the sandbanks, or funnelling of the currents in the channels between sandbanks). The deployments are summarised in Table 2.1. Their locations are marked by diamonds in Figure 2.1(b): beige for the 2016 campaign (Shom, 2017c), purple for the 2021 campaign (FEM, 2021b) and pink for the 2020-2022 campaign (EMD, 2022).

In September 2016, Nortek Acoustic Wave and Current (AWAC) devices were deployed on rigid bed frames lowered on the seabed. Typically, near-bed currents cannot be measured due to deployment setup and the instrument blanking zone. However, in these deployments, single-point Nortek Aquadopp current meters were strategically positioned approximately 1 metre above the seabed. The u- and v-velocity components were measured every 10 minutes and several positions in the vertical to characterise the current profile. Specifically, at OWF1, measurements were taken every metre at 7 depths ranging from 2.5 m to 8.5 m. Velocities were also measured at 8.8 m depth. At OWF2, measurements were taken every 2 metres at 8 depths from 7 m to 23 m. Supplementary measurements were collected at 24 m depth.

Between May and June 2021, Nortek Signature instruments were deployed (Figure 2.6). The ADCP devices were configured to measure current characteristics every 50 cm throughout the water column, at a very high resolution (4 Hz at locations NavCh1 and NavCh2, 2 Hz at OWF3). This setup was intended to capture flow turbulence but turbulence was not a specific focus during data processing. A Nortek Vector device was rigged on the OWF3 mooring to measure currents 10 cm above the seabed.

Figure 2.6: ADCP frame before deployment (left) and after deployment (right) (Photo credit: CERES)

Unfortunately, the Vector data became unreliable shortly after deployment, as evidenced by attitude parameters that drifted beyond acceptable values, leading us to exclude these data from our analysis.

In 2016, sand accretion was observed around the frame when the instruments were retrieved. In 2021, significant biofouling was noted (Figure 2.6). However, survey reports indicate that neither the reliability nor the accuracy of the measured data was affected as a result.

ADCP data were also collected within the OWF footprint, using a downward-looking Nortek Signature500 device mounted on the Alizé metocean buoy, between October 2020 and February 2022 (Table 2.1, OWF4 and OWF5). The u- and v-velocity components were measured every 10 minutes at one-metre intervals in the vertical, starting from 2.6 m below the sea surface.

The flood current generally sets in a longshore east-northeasterly direction and the ebb in a west-southwesterly direction. The local bathymetry channels the current, resulting in spatially variable ebb and flood directions. This is illustrated in Figure 2.7, which presents current ellipses for NavCh1 and OWF3. These scatter plots show depth-averaged and near-bed velocities (0.95 m and 1.35 m above the seabed, respectively), offering a detailed view of directional spread. The depth-averaged velocities were calculated as vector averages of all reliable bins in each profile. Notably, current reversal does not take place at high or low tide but is delayed by two to three hours, meaning that peak flood currents typically occur just before high water, while peak ebb currents nearly coincide with low water.

At OWF1 and OWF2, the near-bed current speed (approximately 1 m above the bed) reached a maximum of 0.7-0.8 m/s during spring tides, with an average value of around 0.3 m/s over the measurement period. No clear evidence of a well-established residual current was observed at either location (Shom, 2017), nor at OWF5. At the other 4 locations, the tidal currents mirror the asymmetry observed in the tidal curve discussed in Section 2.1.2. Specifically, at NavCh1, NavCh2 and OWF4, the flood current is stronger than the ebb current (Figure 2.7(a) and (b)). Conversely, at OWF3, the ebb current dominates (Figure 2.7(c) and (d)). This observation aligns with Vicaire (1991), who identifies the boundary between flood-dominated and ebb-dominated regions between the sandbanks of In Ratel and Dyck Central. Near-bed current speeds, extracted from the last reliable bin in the profile, can exceed 0.75 m/s. This is consistent with values recorded in 2016.

It is reminded that the measured data include meteorological effects. These field measurements are valuable for validating the hydrodynamic modelling (Section 3.3).

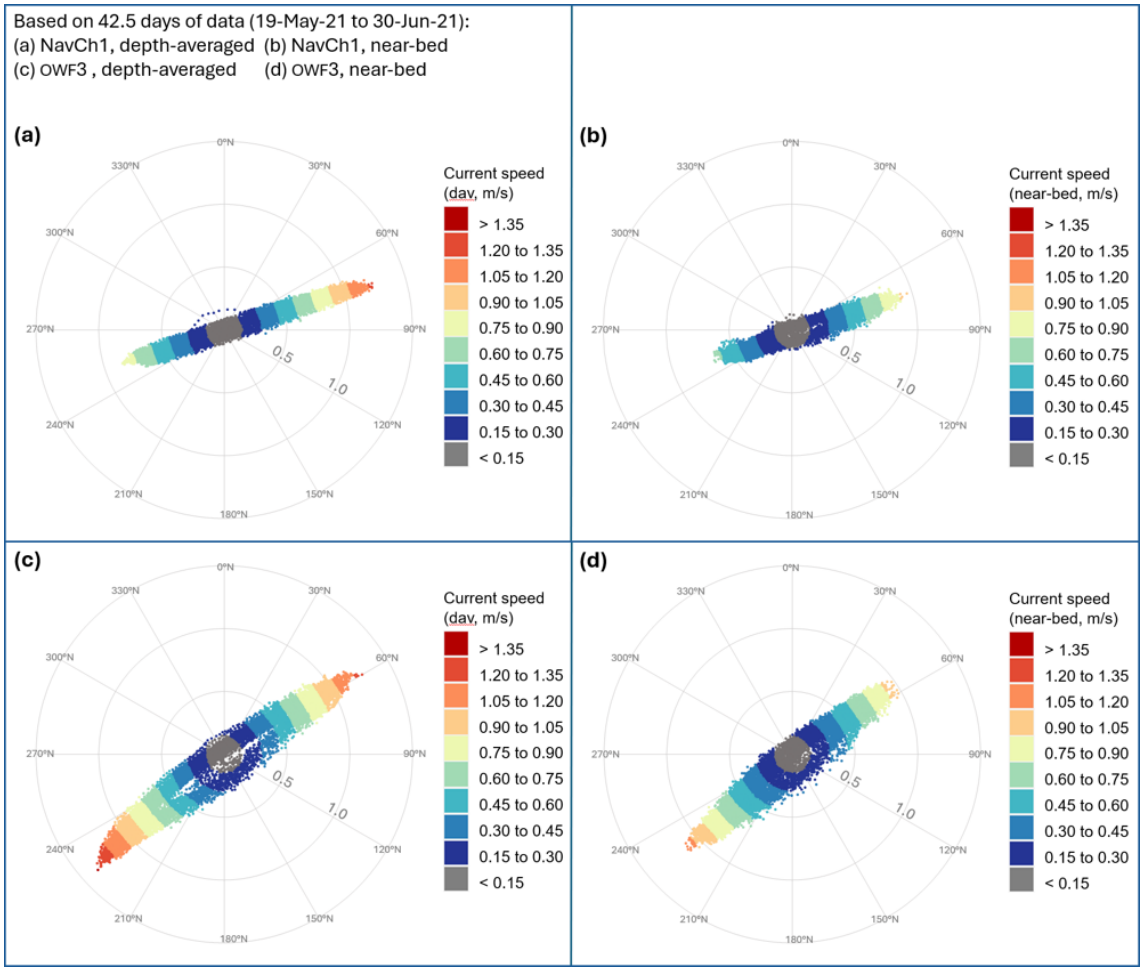

Figure 2.7: Current ellipses at NavCh1, 51°03.925' N 2°15.245' E, and at OWF3, 51°09.883' N 2°22.372' E (Data source: FEM, 2021b, Period: 19-May-2021 to 30-Jun-2021)

2.1.4 Waves

Long-term waves

Long-term wave measurements are available on the Westhinder sandbank, at 51°22.850' N 2°26.133' E, in the vicinity of the measurement platform. Historically, wave measurements had been collected from the Westhinder lightship (1950-1993). After retirement of the light and observation ship, they were obtained from directional wave buoys. The table hereafter summarises the various deployments (personal communication, Flemish Agency for Maritime and Coastal Services).

Start time	End time	Equipment
19-Jul-1990 14:00	30-Nov-2010 23:59	Datawell Wavec buoy (Figure 2.8, left)
01-Dec-2010 00:00	06-Feb-2016 01:59	Datawell Directional Waverider buoy (Figure 2.8, right)
06-Feb-2016 02:00	23-Mar-2016 14:59	Radac WaveGuide (Figure 2.4, right)
23-Mar-2016 15:00	–	Datawell Directional Waverider buoy

Table 2.4: History of wave buoy deployments on the Westhinder sandbank

The buoys are deployed above the southern slope of the sandbank, in approximately 23 m depth relative to MSL (based on Shom, 2015, data). The parameters recorded include, but are not limited to, wave height, average wave period, and direction for the swell and wind-sea components. Approximately 25 years of data were downloaded from the Flanders Marine Institute (VLIZ, 2022b), spanning from

January 1997 to April 2022. We estimate that about 12% of the data records are missing, with significantly fewer gaps starting in 2010 (coinciding with the introduction of the Datawell Directional Waverider buoy). These data records are available at half-hourly intervals, providing valuable insights into long-term wave conditions. The annual wave climate is depicted in Figure 2.9(a) as a wave rose. Seasonal wave roses are also presented in Figure 2.9 to inform about the seasonal variability in wave conditions.

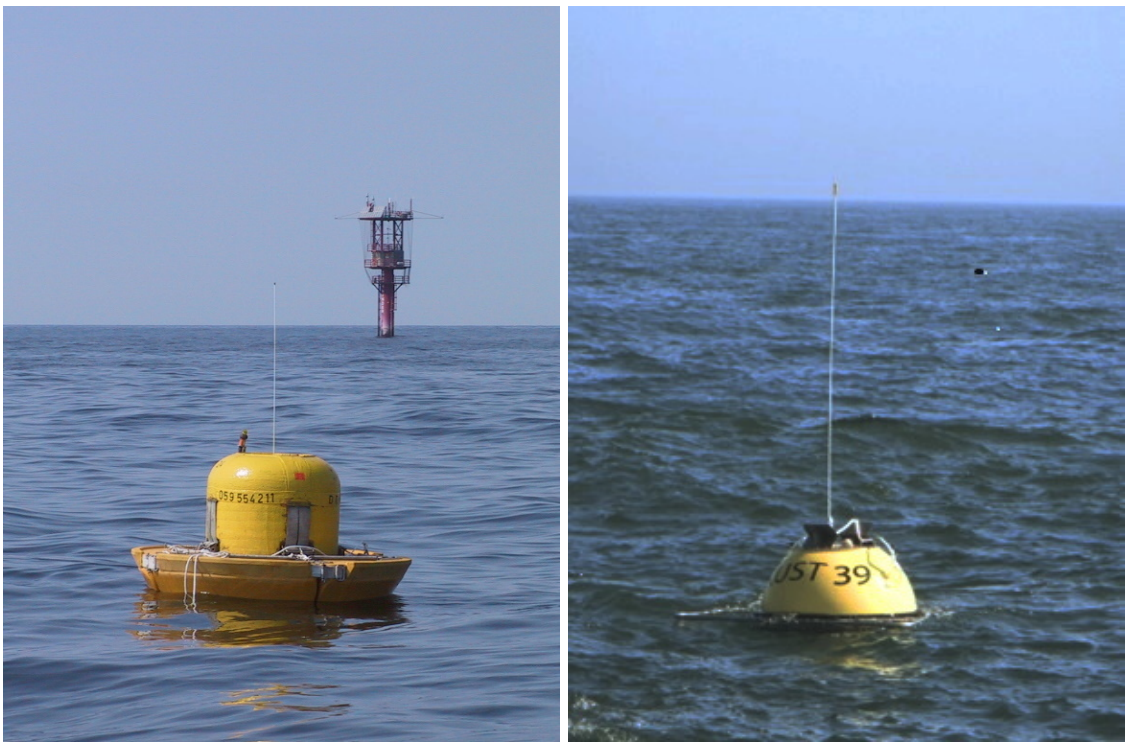

Figure 2.8: Directional buoys deployed on the Westhinder sandbank at 51°22.850' N 2°26.133' E. Left: Datawell Wavec buoy between July 1990 and December 2010. Right: Datawell Directional Waverider buoy from December 2010 (Photo credits: Flemish Agency for Maritime and Coastal Services)

Overall the directional distribution of the offshore waves is strongly dominated by southwesterly waves. Ebb and flood currents will respectively counter and follow these waves. In a simple setting, opposing currents tend to steepen waves, increasing their heights, while following currents typically reduce wave heights. However, the presence of numerous sandbanks and marine dunes in this area alters refraction patterns and complicates the interaction between currents and waves. Notably, high wave events also occur from the northwest to the northeast, generated in the North Sea. A large proportion of long-period swells originates from these directions (not shown in Figure 2.9).

At the Westhinder buoy, located approximately 30 km from the coast, 56% of the waves are less than 1 m high. The maximum significant wave height on record is 5.6 m. From the 25-year data set, we computed the 1-year condition (considering all directions) with a significant wave height of H_s = 4.4 m and a mean period of T_z = 6.6 s, and the 10-year condition at H_s = 5.1 m and T_z = 7.0 s. Offshore Calais, just south of the Sandettié sandbank, Cerema (2021) provide lower estimates for wave heights in similar depths: H_s = 4.0 m and H_s = 4.6 m, respectively (data point 05901-05902). However, we advise caution when interpreting these predictions, as they are based on extrapolation from short-term observations with an effective duration of 2.63 years. Based on data collected for the construction of the outer West Harbour of Dunkirk (Bonnefille et al., 1971), Bertier (2009) suggested a significant wave height of H_s = 5.7 m for a 10-year event and H_s = 7.4 m for a 100-year event. As waves travel into shallower depths, refraction effects and depth-induced breaking come into play, significantly reducing the wave height within the OWF footprint and closer to the shore.

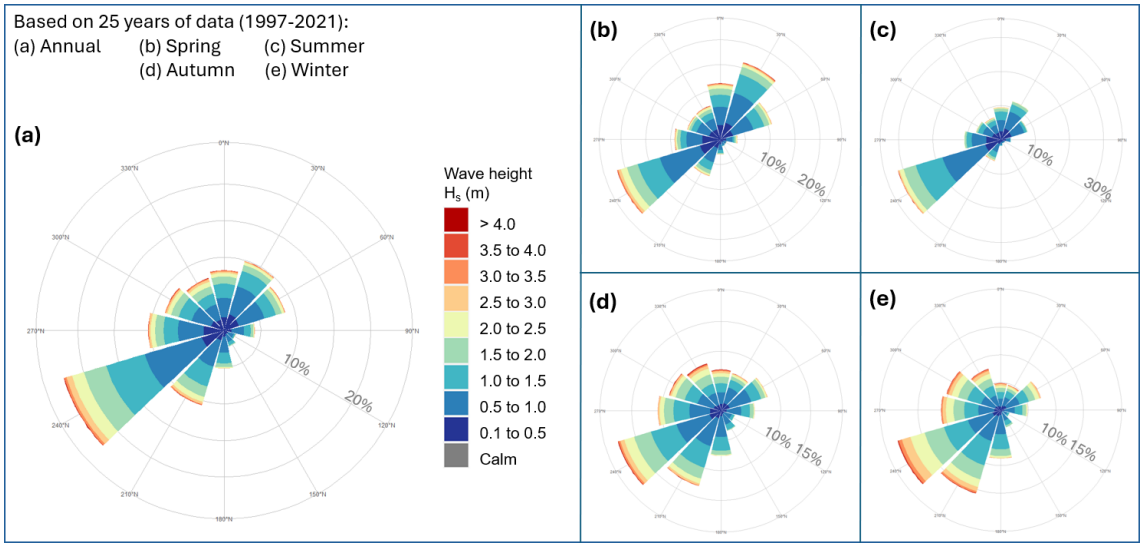

Figure 2.9: Open-sea wave climate at the Westhinder buoy, 51°22.850' N 2°26.133' E (Data source: VLIZ, 2022b, Period obtained: 1997-2021)

Site-specific wave data

Wave data were collected concurrently with velocity data (Table 2.1):

- on the side of the navigation channel to Dunkirk using moored Nortek Signature1000 devices (FEM, 2021b). These locations, NavCh1 and NavCh2, are marked by purple diamonds in Figure 2.1(b).
- within the OWF footprint using moored Nortek AWAC profilers (Shom, 2017d, OWF1 and OWF2, beige diamonds in Figure 2.1(b)), using a moored Nortek Signature500 device (FEM, 2021b, OWF3, purple diamond in Figure 2.1(b)), and using a 3DM-GX-25 MicroStrain inertial sensor installed on the NortekMed Alizé buoy (EMD, 2022, OWF4 and OWF5, pink diamonds in Figure 2.1(b))

The moorings have been described in previous sections.

Integrated wave parameters can be inferred from statistical or spectral analysis of the free surface elevation and velocity data. Typically, the data providers performed this analysis using the manufacturer processing software. However, in the case of the FEM (2021b) data set, a decision was made to carry out the analysis in-house. This was unsuccessful. As a result, wave data collected at NavCh1, NavCh2 and OWF3 are unavailable for our research.

A comprehensive data set of wave parameters, including significant wave height (H_s), peak period (T_p), and mean direction, are available at half-hourly intervals in September 2016 from Shom (2017d). These parameters rely on AST technology, which overcomes the depth limitations associated with pressure-based measurement methods (where wave periods shorter than 4-5 s are poorly captured in relatively deep water). Notably, the OWF1 and OWF2 instruments can capture wave periods as short as 2 s and 3 s, respectively. However, it is important to recognise that in very short, low-energy wave conditions — such as those observed during the measurement campaign in the Dunkirk area — the absence of directional distribution for high frequencies can significantly impact the calculation of mean directions.

Integrated spectral and statistical wave parameters are also available from EMD (2022), at 20-minute intervals, in the channel between the Binnen Ratel and the Dyck Oriental sandbanks (OWF4) and on top of the Dyck Oriental sandbank (OWF5). These cover longer periods of 6.5 months and a little under 10 months, respectively.

These in situ records are useful to validate the wave modelling (Section 3.4). They were supplemented

by wave parameters collected in 2021 and downloaded from the CANDHIS database (CANDHIS, 2022, data point 05903).

2.2 Seabed parameters

2.2.1 Bathymetry

The shoreface of the northern French coastline is characterised by numerous shore-parallel sandbanks, as is common in the southern North Sea. They are apparent in Figure 2.1. At Dunkirk, these are the Braek, the Snouw, and the Hills sandbanks separated from the coast by a navigation channel running along the coastline and serving the West and East harbours. Further offshore the Smal, the Breedt, In Ratel and Binnen Ratel, the Dyck and Ruytingen sandbanks. Flow-transverse marine dunes are also present. They typically have wavelengths in the hundreds of metres and heights ranging from 1 m to 15 m. Figure 1.1 in Chapter 1 showed examples offshore Dunkirk.

This complex system evolves in response to the tidal currents and the currents induced by winds and storms, at varying rates and time scales. While sandbanks tend to migrate (slowly) towards the coastline, marine dunes migrate longitudinally, consistently with the asymmetry of tidal currents noted in previous sections.

Seabed levels in the proposed OWF area and along the cable route are generally between -9m LAT and -33 m LAT (high resolution TANDEM bathymetric data Shom, 2016). Importantly the offshore sandbanks exhibit crest elevations as high as -9m LAT. Recurrent and detailed bathymetric surveys were conducted, in support of the OWF project, to provide a better representation of the seabed and of the dunes morphological dynamics. These recent sources of data are summarised in Table 2.5.

Source	Survey dates	Survey area
Shom (2017b)	28-Aug-2016 to 28-Oct-2016 *	OWF footprint
Shom (2017b)	9-Jun-2017 to 17-Jul-2017 *	OWF footprint
Shom (2017b)	15-Sep-2017 to 23-Sep-2017	cable route
FEM (2021a)	17-Nov-2019 (S1)	tiles #1 to 3
FEM (2021a)	17 & 18-Mar-2020 (S2)	tiles #1 to 3
FEM (2021a)	16-Apr-2020 (S3)	tiles #1 to 3
FEM (2021a)	31-Aug-2020 (S4)	tiles #1 to 3
FEM (2021a)	5 & 6-Dec-2020 (S5)	tiles #1 to 3
FEM (2021a)	22 & 23-Jan-2021 (S6)	tiles #1 to 3
FEM (2021a)	27 & 28-May-2021 (S7)	tiles #1 to 3
FEM (2021a)	3-Jul-2021 (S8)	tile #1
FEM (2021a)	9-Jul-2021 (S8)	tile #2
FEM (2021a)	11-Jul-2021 (S8)	tile #3
EMD (2021)	10-Jun-2021 to 27-Jun-2021 *	OWF footprint

* including weather or logistical unavailabilities

Table 2.5: Site-specific bathymetric surveys near the Dunkirk OWF area

High resolution multi-beam bathymetry data was collected by Shom in 2016-2017 over the entire area of the offshore wind farm and the cable route as part of a complete oceanographic / geophysical survey in support of the project. These data were acquired at a high resolution to enable the production of a 0.5 m resolution Digital Terrain Model (DTM) (Shom, 2017b).

Eight bathymetric surveys (S1 to S8) were carried out between 2019 and 2021, by GEOxyz on behalf of France Energies Marines (FEM), to refine the characterisation of the marine dunes in the proposed OWF area: their morphology, their migration speeds, and associated sedimentary flows (project DUNES). The surveys were conducted using an R2 Sonic 2024 broadband multi-beam echo sounder

supplemented by a Trimble BD982/960 GNSS receiver module (positioning system). They covered three predefined areas selected from the 2016-2017 survey data to include a variety of bedforms:

- tile #1, in the navigation channel to Dunkirk between buoys DW24 and DW26 (1000×500 m^2, extended to 1900×500 m^2 for S7 and S8),
- tile #2, immediately north of the Breedt sandbank in the cable route bend (1000×500 m^2), and
- tile #3, in the OWF area, at the top of the Binnen Ratel sandbank (850×750 m^2).

The general location of the three survey tiles is shown in Figure 2.1(c) and in Figure 2.10. The area is very dynamic and significant movements of some secondary bedforms and dune crests had sometimes been noticed in the 2016-2017 campaign, from one survey to the next (resumption of the previous day for example). Therefore, the extent of tiles #1, 2 and 3 was selected such that they could be surveyed within a day.

The elevation data were processed by GEOxyz to give DTMs for each data set at a resolution of 0.5 m. The horizontal and vertical accuracy is stated as 0.05 m. The DTMs document the evolution of the dune field off Dunkirk over successive periods ranging from 1 month to 4.5 months. The dunes exhibit different behaviours over time. Sometimes, they maintain their shape and move as a whole (e.g., from S1 to S2), while at other times, the steep slopes of the dunes become gentler (e.g., from S2 to S3), leading to an apparent migration of the dune crest.

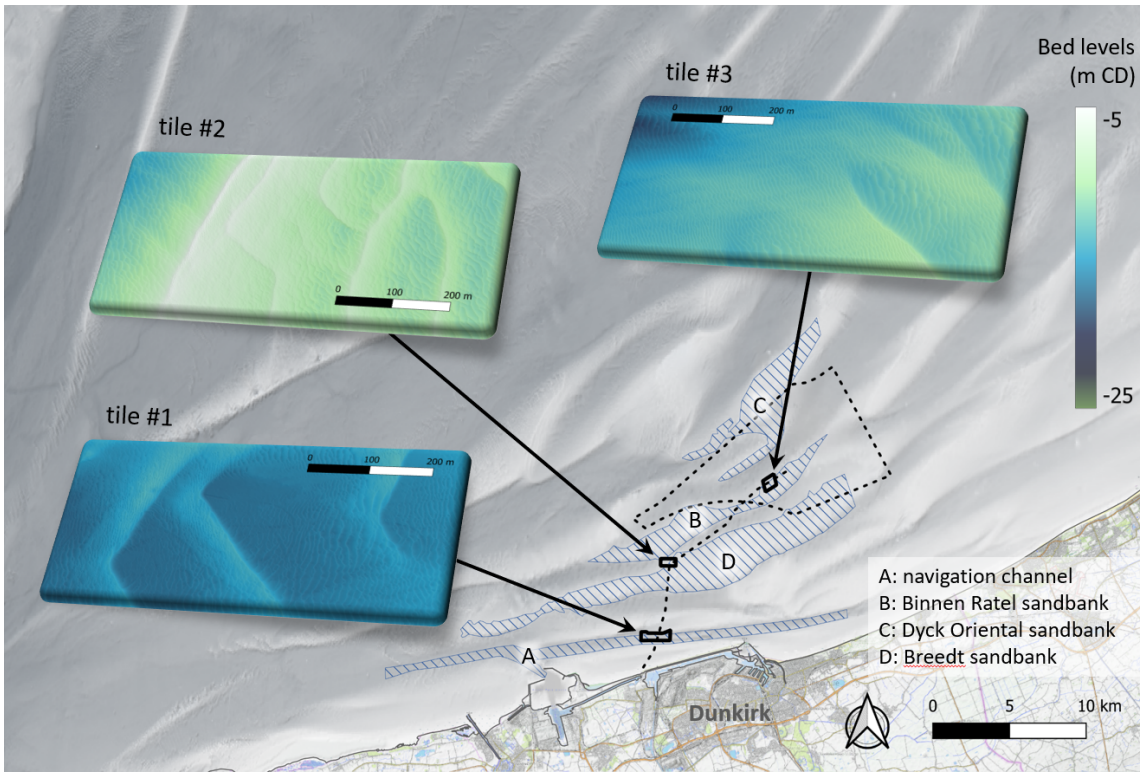

Figure 2.10: Seabed offshore Dunkirk, illustrating the range of bedforms observed during the GEOxyz surveys (Source of the background data: Shom (2015), OpenTopoMap, and EEA coastline)

In June 2021, G-Tec performed a marine geophysical survey of the OWF area on behalf of Eoliennes en Mer de Dunkerque (EMD) (area hatched in pink in Figure 2.1(c)). The campaign included concurrent multi-beam bathymetry, side scan sonar, sub-bottom profiler and ultra-high seismic data acquisition. The bathymetric data were processed and provided in the form a 0.5 m resolution DTM.

These field measurements are valuable for validating the morphodynamic modelling (Section 3.7).

2.2.2 Focus on tile #1

The recurrent bathymetric surveys conducted between November 2019 and July 2021 allow the characterisation of the dune morphology. Here we concentrate our analysis on tile #1, where we call Dunes 1, 2 and 3 the three crescent-shaped dunes starting from the western side (Figure 2.10). In accordance with the sketch shown in Figure 1.2:

- Dune height refers to the vertical elevation (distinct from inclined or average height).
- Dune length is the horizontal distance between successive troughs (local minima), excluding small secondary bedforms.
- The ratio of steep-side length to gentle-side length (ranging from 0 to 1) serves as a proxy for dune asymmetry. A value of 1 indicates symmetrical dunes, while a lower ratio signifies greater asymmetry. Thus, the closer the ratio is to 0, the more asymmetrical the dune.

Scheiber and Lefebvre (2023) established that the difference between horizontal and trough-to-trough distances is actually minimal due to the small baseline inclination of natural dunes. The same argument applies to vertical or inclined (orthogonal) dune height but the authors found that the average dune height, calculated as the average of upstream and downstream heights, can significantly differ for asymmetric dunes.

Dunes 1, 2 and 3 are strongly asymmetrical, featuring a gentler side and a steeper side, related to the predominant current direction. We determined representative angles for the gentle and steep sides of the dunes. Notably, a section of the steep face often approaches the angle of repose (observed between 27° and 36°), in line with the findings reported by Berné et al. (1989).

Using these definitions, the dune characteristics in survey tile #1 are summarised in Table 2.6, taking account of the variability across different survey times.

	Dune height	**Dune length**	**Asymmetry**	**Gentle slope**	**Steep slope**
Dune 1	2.2-2.8 m	130-190 m	0.19-0.57	2 °	9-20 °
Dune 2	3.0-3.4 m	175-200 m	0.14-0.39	2-3 °	11-21 °
Dune 3	1.6-2.0 m	190-210 m	0.05-0.11	1-2 °	9-18 °

Table 2.6: Dune morphology observed in tile #1 during recurrent bathymetric surveys (November 2019 - July 2021)

Considering their height, these dunes fall into the category of large dunes according to Ashley (1990) classification reproduced in Table 1.1 (and even qualify as very large if we consider their wavelength). The dune height is constrained by water depth, in the sense that reduced water depths over the dune crests leads to more pronounced hydrodynamic forces eroding the crest. We estimated dune heights to be typically 7% to 20% of the total water depth (depending on specific dune characteristics and state of the tide). This range agrees with empirical formulae reported by Soulsby (1997).

Le Bot et al. (2023) assessed the migration distances of dune crests along 20-m spaced profiles oriented from west to east. Between S1 and S8, Dunes 1, 2 and 3 consistently travel eastward at rates ranging from 25.94 metres per year (with a standard deviation of 18.59) to 37.20 metres per year (with a standard deviation of 11.69). These migration rates are said to be similar to those observed for dunes in the Dover Strait, located tens of kilometers away (Le Bot et al., 2000).

2.2.3 Sediment type and bed samples

In support of the OWF project, the Shom was commissioned to assess sediment depths above the non-erodable bed (Figure 2.11), and surficial sediment types in the development area and along the cable route (Shom, 2017e). Bed sample data were collated offshore Dunkirk (Shom, 2017a). These data go back to before 2000 in some cases and were supplemented by fourty-seven (47) new samples in 2016 to update and complete the sediment characterisation. The median grain diameter, d_{50},

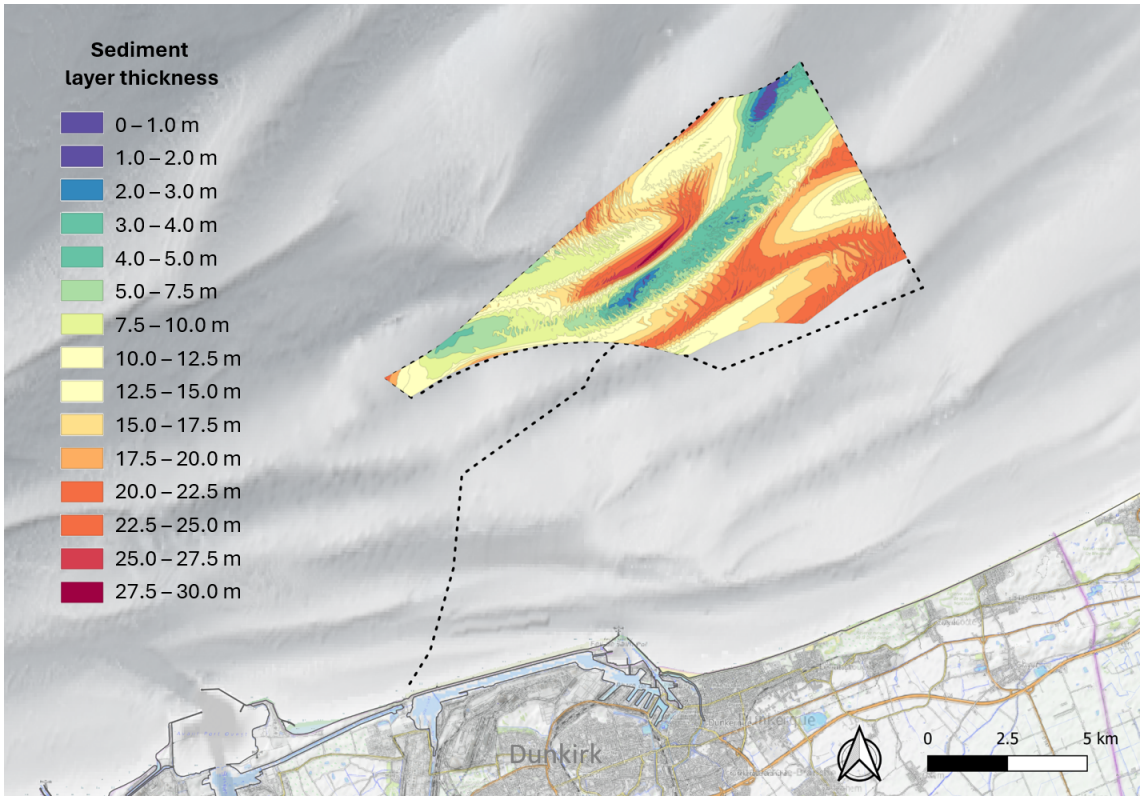

Figure 2.11: Sediment depths above the non-erodable bed in the OWF area (Source of the background data: Shom (2015), OpenTopoMap, and EEA coastline)

predominantly ranged from 125 μm to 500 μm. Observations made during the survey suggest that the surficial sediment mainly consists of sands and broken shells.

More recently, twenty-three (23) bed samples were collected at selected locations with a Shipek sediment grab sampler. The sampling occurred on two occasions: on 22 & 23-Oct-2019 and on 16 & 17-May-2020 (FEM, 2020). These locations primarily fall within the three bathymetric survey tiles, as indicated by filled circles in Figure 2.1(c). The samples were analysed by sieving, with opening diameters ranging from 63 μm to 12.5 mm. This provides valuable information about the distribution of surficial grain sizes.

The sediments predominantly consist of sand (over 90%), with minimal gravel and silt content (less than 5%). Based on Folk (1954) classification, the sampled sediments fall into the textural group of Slightly Gravelly Sands (79%) or Gravelly Sands (21%), in line with previous findings by Shom (2017e). Additionally, less than 1% of the sediment passes through the N°200 sieve, indicating a low content of fines. The average d_{10} is estimated at 210 μm, suggesting that the sediments are unlikely to exhibit cohesive properties (Soulsby, 1997).

The sediment distributions across the dunes and seasons (from autumn to spring) exhibit little variability within and between dunes. Sediment samples are considered well-sorted when they contain a narrow range of grain sizes. As a rough guideline, a geometric standard deviation $d_{90}/d_{10} < 2.4$ indicates good sorting (Soulsby, 1997). The majority of samples (89%) have a unimodal distribution, and three mode values are observed: 357.5 μm for 18 out of 38 samples, 282.5 μm for 14 out of 38 samples, and 225 μm for 5 out of 38 samples. The median grain sizes d_{50} range from 240 μm to 450 μm. These grain size parameters are in general agreement with those collected by the Shom at various times in past years. There is no clear evidence of a trend in the size of the sediment depending on the position on the dunes.

2.2.4 Shipwrecks

Shipwrecks dot the seabed off the coast of Dunkirk, notably following 'Operation Dynamo', the mission to evacuate Allied soldiers from Dunkirk during the Second World War. While some wrecks have been destroyed or buried, others have been preserved and are now visited by diving enthusiasts.

Shom (2022) lists wrecks and obstructions in the French exclusive economic zone. Obstructions are defined as artificial objects other than wrecks, such as a container or a lost anchor. Floating and drifting objects are not included in this inventory as their position changes rapidly. The data come from bathymetric surveys carried out by the Shom, supplemented by external sources of information, such as the Department of Underwater Archaeological Research (DRASSM) or divers' associations. They were obtained in shapefile format. The positions of the wrecks are georeferenced in the WGS84 system (EPSG: 4326).

Figure 2.12 shows the wrecks listed in Shom (2022). Of particular interest are the shipwrecks along the cable route and in the OWF area. They are marked with orange symbols. The wrecks in the OWF area could not be detected in the bathymetric data. However, the one located in the northeast corner of bathymetric survey tile #1 (at 51°4'0" N 2°16'30" E) is clearly identifiable from Shom (2016) with levels up to 6 metres above the surrounding seabed (Figure 2.12(c)).

The Sperrbrecher 174 (formerly Tindefjell, nicknamed the Fred before being formally identified by local French divers in 2012) was an 80 m long Norwegian cargo ship. She was seized by the Germans during the Second World War and converted into a sperrbrecher, whose mission was to precede convoys through minefields and to protect them from air attacks. She struck a mine on 28 May 1942 and sank west of buoy DW26 in the Dunkirk approach channel. She rests on her keel, with the bow higher than the stern (Everaert & Marquise, Last accessed December 7, 2023).

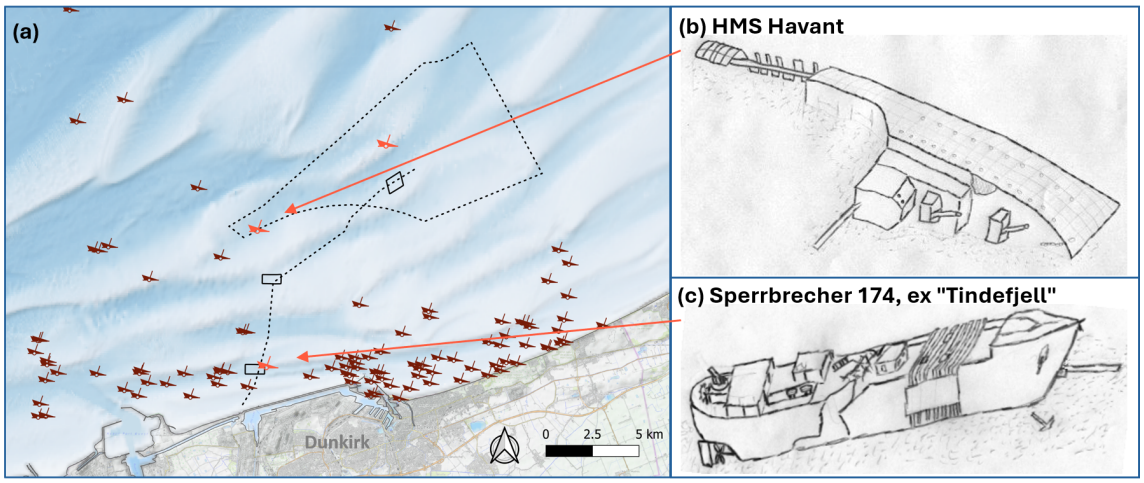

Figure 2.12: (a) Location of known shipwrecks in the French exclusive economic zone (Data source: Shom, 2022). (b) and (c) Sketch of the remains of HMS Havant and Sperrbrecher 174, formerly Tindefjell (Credit: Epaves au large de Dunkerque)

Chapter 3

Characterising hydrodynamic and sediment processes in 3D

3.1 Introduction

Our research relies on the development of a coastal area model near Dunkirk (Section 3.2). The model considers the interactions between tidal flows, winds, (waves,) sediment transport processes, and bed evolution to address the Research Questions laid out in Chapter 1.

In shallow shelf seas, coastal hydrodynamics (tides, winds and waves) governs sediment transport. An accurate description of the wave and current fields is, therefore, essential for a reliable description of the morphodynamic processes. It follows that our modelling exercise begins with the calibration and validation of the flow model (Section 3.3) and wave model (Section 3.4) against independently observed in situ data.

Next, we conduct preliminary analyses based on oceanographic considerations, drawing from the results of a two-year, coupled, hydrodynamic and wave simulation. These analyses allow us to identify the dominant processes shaping sediment transport in the study area (Sections 3.5 and 3.6), and inform our simplifying modelling assumptions.

A subsequent step consists in the calibration and validation of the morphodynamic model (Section 3.7) against recent bathymetric surveys, illustrating the evolution of a diverse range of marine dunes. We compare two sediment transport prediction formalisms: one is energy-based and is expressed in terms of depth-averaged velocities, while the other is expressed in terms of bed shear-stresses. Their behaviour and performance are assessed in comparison with in situ bathymetric data, highlighting their strengths and weaknesses.

This chapter is based on the following conference proceedings:

Durand, N., Tassi, P., Blanpain, O., & Lefebvre, A. (2022a). Towards numerical modelling of marine dunes in a shallow shelf sea. In *Actes des XVIIèmes Journées Nationales Génie Côtier - Génie Civil* (p. 337-346). October 11-13, 2022. Chatou, France. https://doi.org/10.5150/jngcgc.2022.035

Durand, N., Tassi, P., Blanpain, O., & Lefebvre, A. (2022b). Hydrodynamic modelling as a first step to assess marine dune dynamics: Influence of waves. In *XXVIIIth Telemac-Mascaret user conference* (p. 79-86). October 18-19, 2022. Paris-Saclay, France. https://hdl.handle.net/20.500.11970/110839

Durand, N., Tassi, P., Blanpain, O., & Lefebvre, A. (2023a). Understanding marine dune dynamics in a shallow shelf sea using sediment mobility indices. In *Marine and River Dune Dynamics VII Book of Proceedings* (p. 109-116). April 1-3, 2023. Rennes, France. https://maridnet.files.wordpress.com/2023/06/maridvii-durand-noemie.pdf

Durand, N., Tassi, P., Blanpain, O., & Lefebvre, A. (2023b). GAIA can model large marine dunes: Results from a sensitivity study in the southern North Sea. In *XXIXth Telemac-Mascaret user conference* (p. 190-197). October 12-13, 2023. Karlsruhe, Germany. https://hdl.handle.net/20.500.11970/112839

The chapter concludes by summarising the key points of our findings in Section 3.8.

3.2 Model development

3.2.1 The openTELEMAC system

To model marine dune dynamics at a large scale with realistic forcings, it is crucial to use a comprehensive representation of coupled hydrodynamics, sediment transport processes, and bed evolution. This can only be achieved through complex process-based modelling. Our research is based on the open**TELEMAC** system, a state-of-the-art suite of solvers for free surface flow based on the finite element method and unstructured grids. Originally developed by Electricité de France R&D (Hervouet & Watrin, 1987; Daubert et al., 1989), the open**TELEMAC** system now benefits from contributions from a large, worldwide community of users and developers.

The system is distributed as a version-controlled open-source software. The source code (a large set of Fortran 90 subroutines and Python 3 scripts; stable releases and development versions) and documentation are available on openTELEMAC gitlab (Last accessed February 24, 2022). In our research, we used the most recent version available at the onset (v8p3r1), incorporating new functionalities as necessary.

open**TELEMAC** comprises several modules, each describing different physical processes, of which TELEMAC-3D is the three-dimensional hydrodynamic module (Hervouet, 2007), TOMAWAC is the wave generation and transformation module (Benoit et al., 1996), and GAIA is the sediment transport and bed evolution module (Tassi et al., 2023).

3.2.2 Model extent and mesh resolution

The model was set up to cover the area from the port of Calais in the west to Ostend in Belgium in the east, i.e. approximately 80 km of coastline. Its offshore extent varies between 15 km in the Dover Strait and 75 km in the east. The full extent of the model is shown in Figure 3.1(a) superimposed on Shom (2015) and OpenTopoMap data.

We used an unstructured finite element mesh made of triangles with spatially varying resolution to represent the model domain. The main advantage of this discretisation technique is that it is very flexible: the mesh resolution can be adapted to the complexity of the coastline, bathymetric features or oceanic circulation for example, while becoming coarser away from areas of interest (in this case, a maximum of 2930 m at the open-sea boundary).

The finer the mesh resolution, the higher the computational cost. For this reason, tests were carried out to determine the optimum mesh size that would best capture variations in the seabed for a wide range of bedforms while limiting run times. A horizontal resolution of 10 m was deemed adequate to represent marine dunes (this is illustrated in Figure 3.2(b)) and was used in bathymetric survey tiles #1 and 3, where we aim to reproduce the evolution of the dune field. However, a finer resolution is expected to be required for more detailed analyses.

Outside these bathymetric survey tiles, we adopted a mesh resolution of 25 m to represent tile #2 (of lesser focus for our research), 75 m around the instrument locations in the OWF footprint (OWF1 to OWF5), 150 m along the proposed cable route, at Gravelines and Westhinder deployments, and 200 m along the shoreline (see Figure 2.1 for point locations). The mesh was constrained to follow the crests of the sandbank crests as far as possible, with a growth rate of 8%.

Overall, the model area comprises approximately 64,000 nodes and 128,000 elements. This configuration is the result of a comprehensive optimisation and mesh refinement testing process. Figure 3.1(a) shows the full extent of the model. A close-up view of the variable mesh resolution is shown in Figure 3.1(b).

The horizontal mesh is extruded vertically into layers of prisms to generate a 3D model domain. Within this domain, one of the surfaces represents the time-varying water surface, while another corresponds

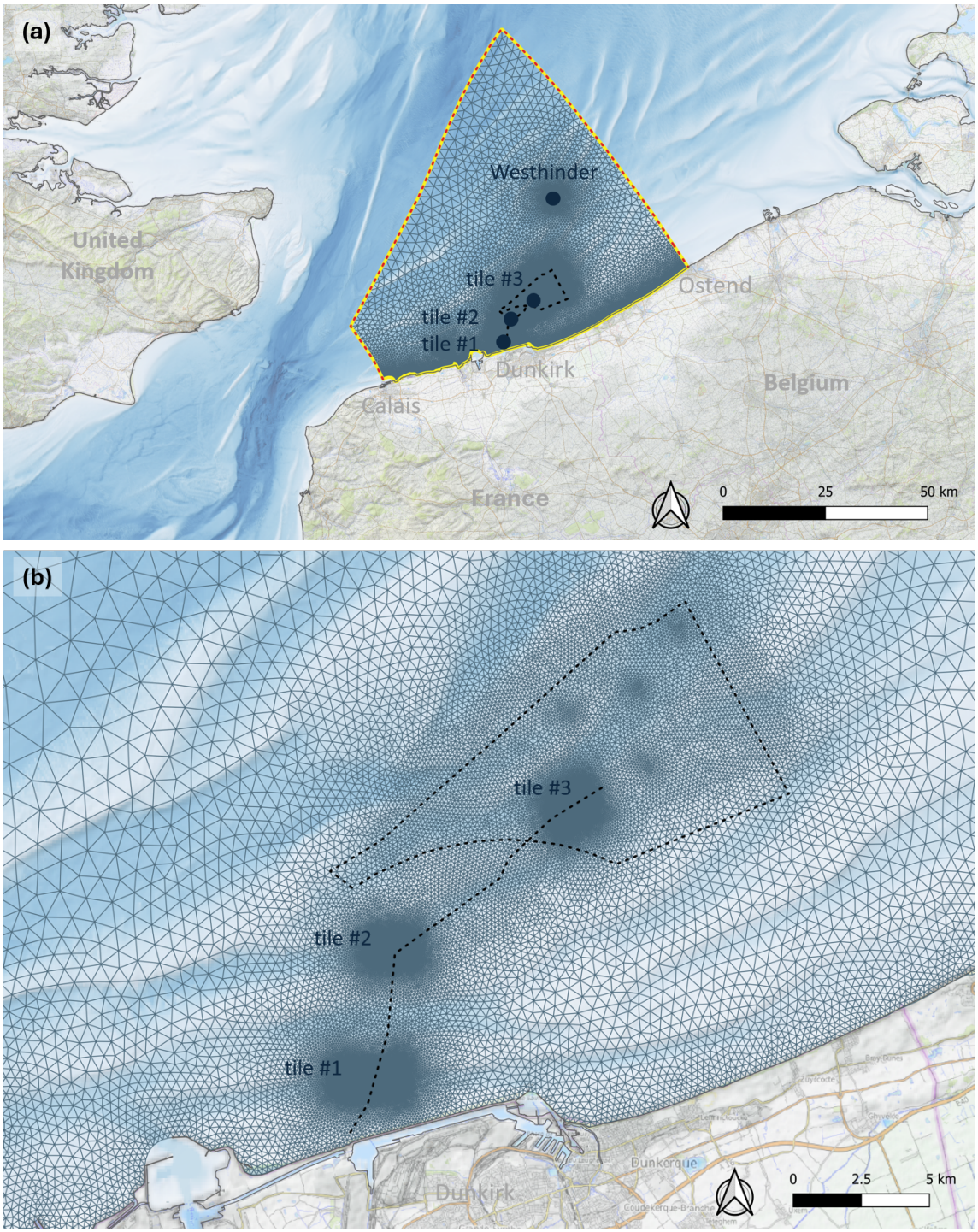

Figure 3.1: (a) Full model extent and mesh in relation to the geographical footprint of the proposed offshore wind farm (dashed black line). (b) Close-up view off Dunkirk showing increased resolution in the three bathymetric survey tiles, and mesh alignment with the crests of the sandbanks (Source of the background data: Shom (2015), OpenTopoMap, and EEA coastline)

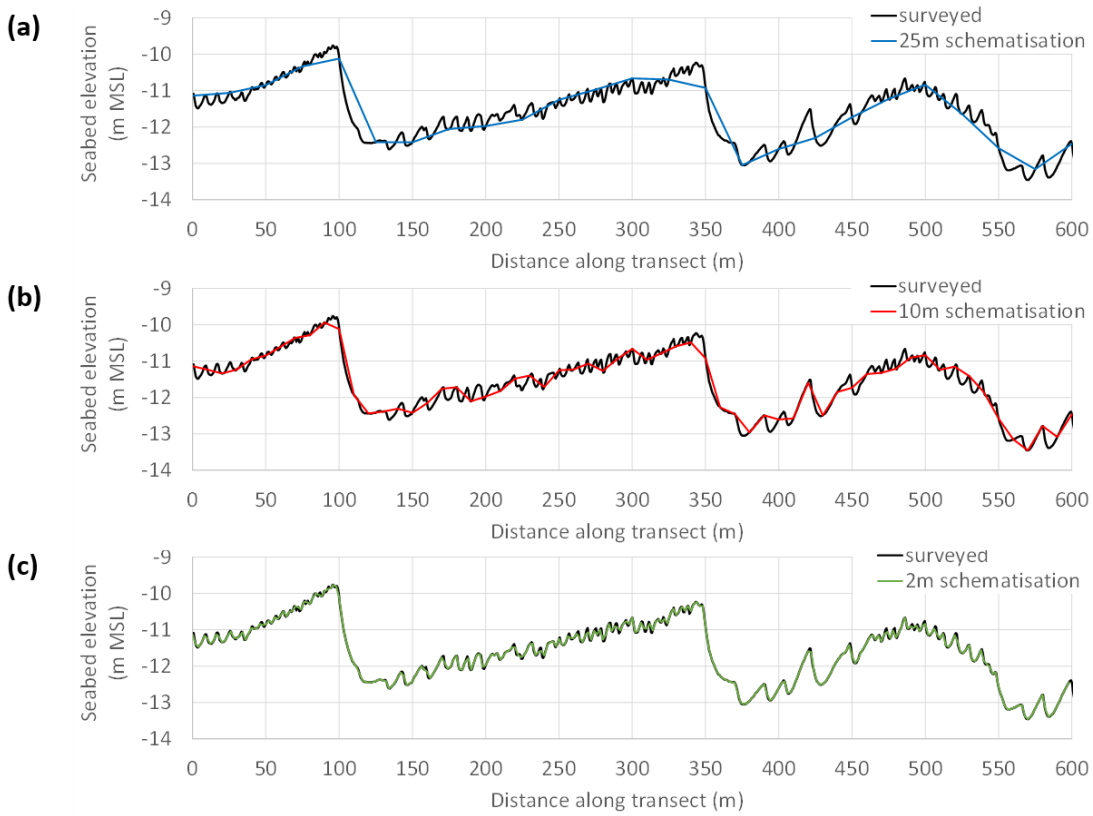

Figure 3.2: Model representation of bedforms at various horizontal resolutions: (a) 25 m, (b) 10 m and (c) 2 m. Results are shown for one test transect in tile #3 within the OWF footprint. Results for other test transects are not shown. The vertical scale is exaggerated by a factor of 25

to the time-varying seabed. The intermediate surfaces are customised to optimise the representation of relevant physical processes. Balancing model accuracy and computational costs, we opted for five vertical planes between the free surface and the seabed. Further details on vertical resolution can be found in Section 3.7.

In the following, where the coordinate system is not explicitly mentioned, it will be assumed to be Universal Transverse Mercator (UTM) Zone 31N (EPSG 32631). It follows that all directions are predicted to grid North. Where not explicitly mentioned, vertical levels are related to Mean Sea Level (MSL).

3.2.3 Seabed maps

The performance of a numerical model is closely related to a number of factors. Model resolution is one. An accurate representation of the seabed is another. As the area is highly dynamic, we constructed distinct seabed maps for specific time periods where in situ data are available to assess the model performance (Table 2.1). Accordingly, one map was developed to represent autumn 2016 conditions and another summer 2021 conditions. We used these maps to calibrate the hydrodynamic model. Additionally, a separate map was developed to represent November 2019 conditions, which we used to calibrate the morphodynamic model.

Several suitable sources of bathymetry data were identified, obtained in the form of Digital Terrain Models (DTM), and compiled to construct the model seabed maps. They are summarised in Table 3.1. Their geographical coverage is shown, colour-coded by source, in Figures 3.3 and 3.4 for 2016 and 2021 respectively.

Source of the DTM	CRS	Vertical datum	Resolution	Survey dates (if known)
HOMONIM (Shom, 2015)	WGS84	MSL	111 m	
TANDEM (Shom, 2016)	WGS84	MSL	20 m	
Litto3D® NHDF (Shom - ROLNHDF, 2022)	RGF93	IGN69	1 m and 5 m	2016-17
Dunkirk OWF area (Shom, 2017b)	WGS84	ZH	0.5 m and 1 m	2016-17
DUNES (FEM, 2021a)	RGF93	ZH	0.5 m	17-Nov-2019 (S1)
Dunkirk OWF area (EMD, 2021)	UTM 31N	LAT	0.5 m	Jun-2021
BCP (Flemish Hydrography, 2022)	UTM 31N	LAT	20 m	2017-22

Table 3.1: Bathymetry data sources

The HOMONIM DTM covers the southern North Sea, the English Channel and the Bay of Biscay (northern limit = 52°54.030' N; western limit = 6°0.030' W). It was produced by the Shom at a spatial resolution of 1/1000° (ca. 110 m) from a compilation of publicly available bathymetric soundings, data available in international databases, and existing DTMs (e.g. GEBCO, EMODnet) (Shom, 2015).

The TANDEM DTM was also produced by the Shom. It covers the eastern English Channel and the southern North Sea (upper left corner = 51°20.010' N, 0°50.018' E; lower right corner = 50°29.994' N, 2°32.606' E), including the French coastline of Nord-Pas-de-Calais and part of the UK coastline, with a finer spatial resolution of 1/5000° (ca. 20 m) (Shom, 2016). Maspataud et al. (2016) present the challenges faced in generating this high-resolution coastal DTM, elaborating on the sources and types of data used in its development.

The Litto3D® NHDF dataset is the result of a 'strategy for homogeneous, recurrent and sustainable monitoring of the eastern English Channel and southern North Sea coastline' (Shom - ROLNHDF, 2022). Data were acquired by airborne topographic, topo-bathymetric and bathymetric Light Detection And Ranging (LiDAR). DTMs have been developed from surveys carried out between 29-Sep-2016 and 20-Oct-2016 and between 5-May-2017 and 26-Jun-2017 covering the geographical area from Calais in the west to the border with Belgium in the east. The DTMs are available in two resolutions: 1 m or 5 m, on 1x1 km tiles for easier handling. We adopted the 1 m resolution product inside the OWF footprint, and the 5 m product outside.

BCP is a composite DTM of the Belgian continental shelf extending at least 60 km offshore. It was first generated by the Flemish Hydrography on September 1, 2016. The DTM undergoes regular updates to incorporate the latest (single-beam and multi-beam echo sounder) surveys. The current version primarily relies on surveys conducted between 2019 and 2021 by the Flemish Ministry of Mobility and Public Works, Maritime Services and Coast Agency, Coastal Division. Importantly, the data within the model area is no older than 2017. The grid resolution is 20 m × 20 m.

The data sets from Shom (2017b), FEM (2021a) and EMD (2021) are project specific and have been described in Chapter 2, Section 2.2.1.

We manually merged the different data sources into a common horizontal system (UTM Zone 31N, EPSG 32631) and vertical datum. While Zéro Hydrographique (ZH), and the Lowest Astronomical Tide (LAT) are relevant vertical references for nautical charts, MSL is preferred for hydrodynamic modelling applications. Where required, depths were converted to MSL based on the information published in Shom (2020) (in the case of data related to ZH Dunkerque), from BathyElli v2.0 ZH/ell (2018) (in the case of the EMD data, for consistency) or derived from products.

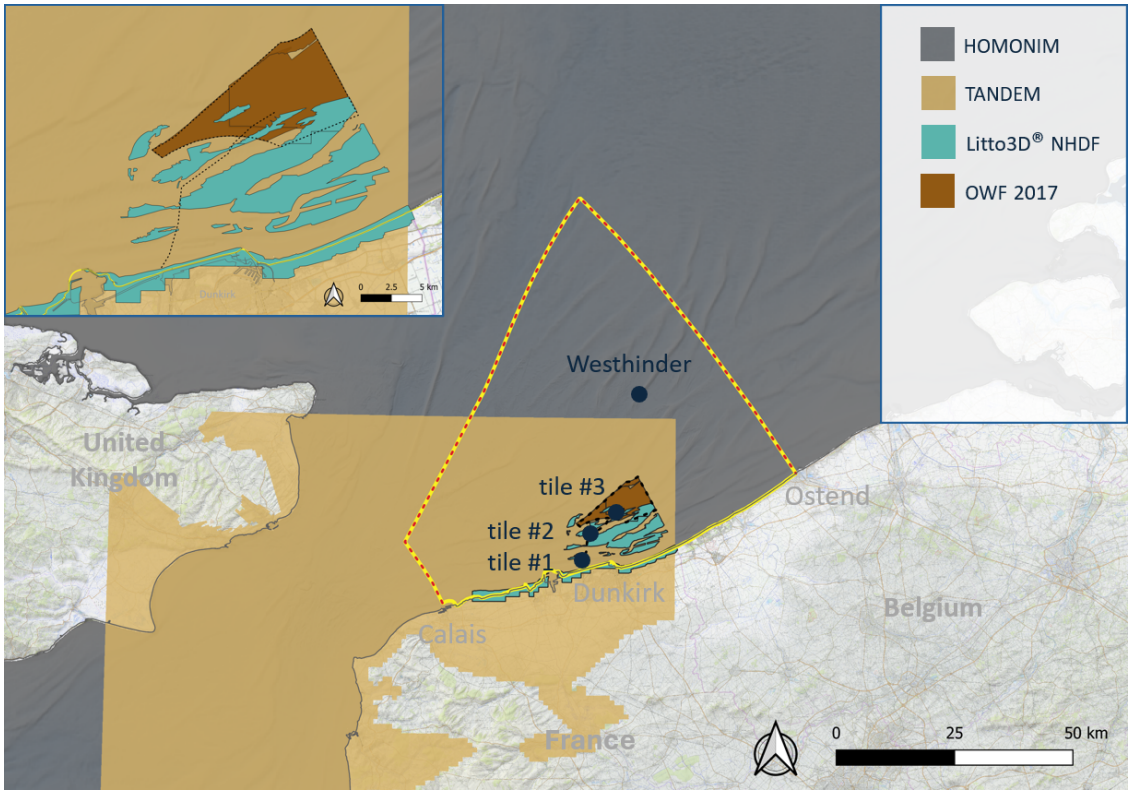

Figure 3.3: Source and coverage of the bathymetric data sets selected to develop the autumn 2016 model seabed map

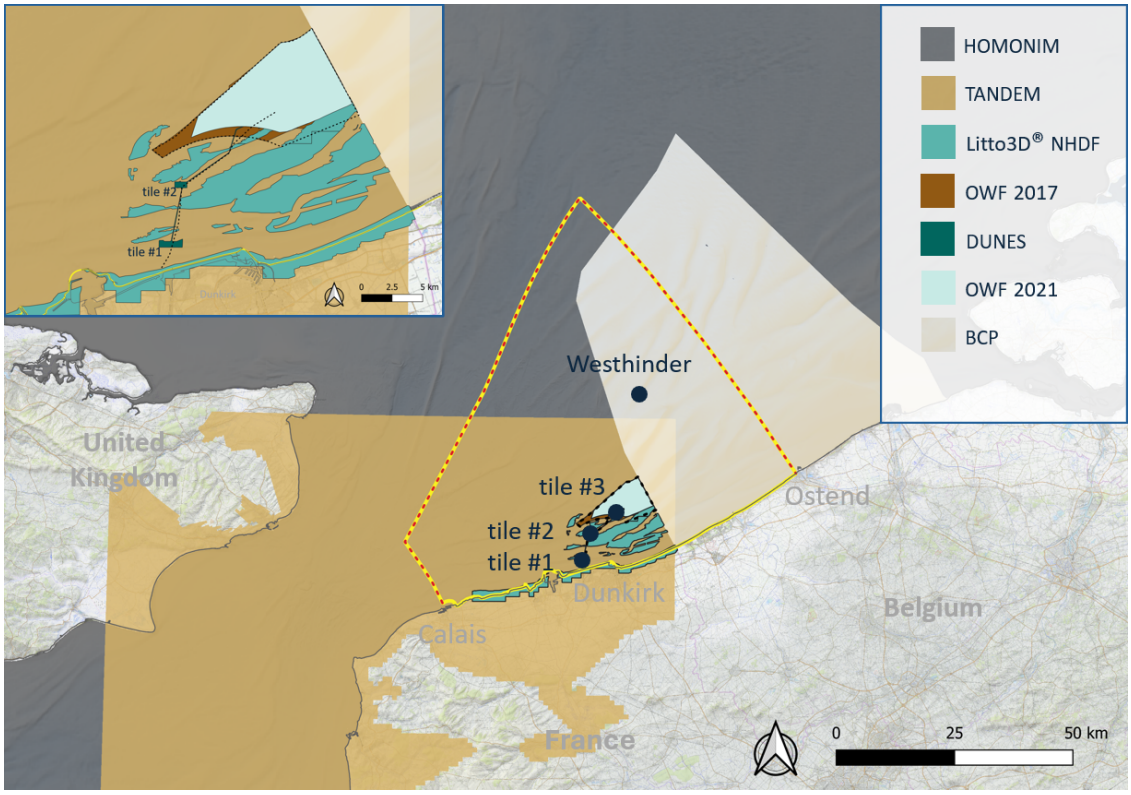

Figure 3.4: Source and coverage of the bathymetric data sets selected to develop the summer 2021 model seabed map

Data of higher quality were preferred to data of lower quality or resolution. For example, LiDAR data took precedence over data acquired by multi-beam echo sounder in shallow waters; site- and period-specific data took precedence over global data sets. We used best judgement to integrate these data as seamlessly as possible in a highly dynamic environment, for example by introducing buffer zones.

3.3 Hydrodynamic modelling

3.3.1 TELEMAC-3D

TELEMAC-3D (Hervouet, 2007) is the three-dimensional hydrodynamic module from the open**TELEMAC** system. It solves the 3D Reynolds-Averaged Navier-Stokes equations. We use the so-called 'non-hydrostatic' form, with no assumption on the pressure. Together with the continuity equation (Eq. 3.1), the Navier-Stokes equations are written in Cartesian coordinates as:

$$\vec{\nabla} \cdot \vec{U} = S_h \tag{3.1}$$

$$\partial_t \vec{U} + (\vec{U} \cdot \vec{\nabla})\vec{U} = -\frac{1}{\rho}\vec{\nabla} p + \upsilon \Delta \vec{U} + \vec{g} + \vec{S} \tag{3.2}$$

where t denotes the time (s); ρ the density of the fluid (kg/m^3); υ the kinematic viscosity of the fluid (m^2/s); and $\vec{g}$ the gravitational acceleration (m/s^2). The S terms are source and sink terms in the different equations: S_h (1/s) represents a flux of water such as rain, evaporation or discharges ($S_h = 0$ for this work); $\vec{S}$ (m/s^2) represents external forces (e.g., Coriolis acceleration), which are applied directly to the water body, as well as contact forces (e.g., wind or bottom friction), which are applied to its surface. The pressure p (Pa) and the three velocity components along the x, y, z Cartesian coordinate directions $\vec{U}$ = (u,v,w) (m/s) are the unknowns in these equations, computed at each node and layer of the computational domain.

Wind forcing appears in Equation 3.2 through the two-dimensional condition at the surface:

$$\upsilon \, \partial_n \vec{U}_H = \frac{\vec{\tau}_{wind}}{\rho} = \frac{\rho_{air}}{\rho} \, a_{wind} \, \|\vec{V}_{10m}\| \vec{V}_{10m} \tag{3.3}$$

where $\vec{U}_H$ denotes the horizontal velocity at the surface and $\vec{\tau}_{wind}$ the wind stress, expressed in Heaps (1965) and Flather (1979) in terms of a quadratic function of the wind velocity, $\vec{V}_{10m}$, commonly defined 10 m above sea level. a_{wind} is a dimensionless drag coefficient dependent on the wind velocity, and hiding complex phenomena (e.g., sea surface roughness, wind speed, fetch). In Equation 3.3, ρ_{air} is the air density (kg/m^3).

Atmospheric pressure gradients are integrated with the source terms:

$$\vec{S}_{atm} = -\frac{1}{\rho}\vec{\nabla} p_{atm} \tag{3.4}$$

where p_{atm} denotes the atmospheric pressure at sea level.

3.3.2 Tidal forcing

Tidal levels are applied along the open water boundaries of the model (dashed coloured line in Figure 3.1(a)). They are computed at each boundary node and for each time step from a global model of ocean tides.

In a preliminary version of the hydrodynamic model, we used the OSU TPXO9 atlas (Egbert & Erofeeva, 2002), which includes 15 tidal constituents: eight primary (M2, S2, N2, K2, K1, O1, P1, Q1), two long-period (Mf, Mm), three shallow-water (M4, MS4, MN4) and two small-amplitude (2N2, S1) constituents. TPXO9 is the latest in a series of regional and global models of ocean tides that

best fit the Laplace tidal equations and altimetry data. TPXO9 data are provided at a 1/30° global resolution.

The hydrodynamic model performed satisfactorily with these boundary conditions (Durand et al., 2022a), particularly in reproducing the residual currents. However, upon closer examination, we found that the model did not accurately capture the variations in the amplitude of the spring tides. When the in situ sea levels were subjected to tidal harmonic analysis to filter out non-tidal influences (see following section), a pattern emerged showing that the spring tidal range fluctuated with a period of around 30 days. For example, the spring tidal range calculated at the Westhinder platform was 4.78 m on 27-May-2021, then decreased to 4.24 m on 12-Jun-2021, and rose gain to 4.73 m on 26-Jun-2021. This pattern was not accurately reproduced in the model, suggesting that an important tidal constituent may not be included in the TPXO9 atlas.

FES2014 (Lyard et al., 2021; Noveltis, Legos and CLS, 2019) is another database for global model tide data, enhanced by the assimilation of long-term in situ and remote sensing data. It includes more harmonic constituents (34), with a spatial resolution of 1/16°: linear constituents (K1, M2, N2, O1, P1, Q1, S1, S2, K2, 2N2, EPS2, J1, L2, T2, La2, Mu, Nu2, R2), non-linear constituents (M3, M4, M6, M8, MKS2, MN4, MS4, N4, S4) and long-period constituents (MSf, Mf, Mm, MSqm, Mtm, Sa, Ssa). FES2014 was produced by NOVELTIS, LEGOS, CLS Space Oceanography Division and CNES.

It is important to note that sea levels derived from either of these databases are astronomical levels devoid from other influences (e.g., weather or oceanic currents). They are therefore corrected for the 'inverted barometer' effect caused by variations in atmospheric pressure relative to 1 atm when weather effects are considered.

3.3.3 Meteorological forcing

In addition to tidal forcing at the open boundaries, wind and pressure fields are applied over the computational domain to account for wind-induced set-up and surface currents, as well as the 'inverted barometer' effect. Long-term meteorological parameters are available from the Westhinder platform, and to a lesser extent at OWF4 and OWF5 (Section 2.1.1, Figure 2.1). Although these data are site-specific and representative of open-sea conditions, they are taken at discrete locations. Since it is important to capture both temporal and spatial variations, we evaluated two sources of offshore model wind and pressure data: the ERA5 reanalysis data set and the AROME database.

ERA5 (Hersbach et al., 2020) is a climate reanalysis data set produced by the Copernicus Climate Change Service (C3S) at the European Centre for Medium-Range Weather Forecasts (ECMWF). The name refers to the fifth major global reanalysis. It provides high-quality medium-resolution estimates of atmospheric parameters, with a horizontal resolution of 1/4°. Data are archived hourly and were obtained over the entire model area.

AROME (Bouttier, 2007) is an operational forecast from Météo-France, designed specifically to improve the short-term prediction of hazardous phenomena such as heavy rains, violent storms, fog or urban heat pockets. The initial model conditions are derived from assimilation of radar network data (precipitation and Doppler winds), with an hourly frequency. AROME offers predictions up to 42 hours ahead at a high resolution of 1/40°. Data are also archived hourly and were obtained from the 30-hour forecast throughout the model area.

To validate these sources, we compared them with long-term open-sea records from the Westhinder instrumented platform (positioned at 51°23.300' N 2°26.267' E, described in Section 2.1.1). Although AROME provides finer gridded data (tenfold), we extracted model winds from both ERA5 and AROME for the same location (51.45° N, 2.5° E) to ensure consistency in the comparisons. On the one hand, the ERA5 hindcast consistently underestimates wind speeds (by an average of 11% over one year, not shown). On the other hand, the AROME forecast agrees closely with the measurements, deviating by only 1% on average (Figure 3.5) - even extreme events are satisfactorily reproduced. This result is somewhat unexpected, as forecast models are generally perceived to be less precise than

hindcasts. However, in this instance, we believe that the superior spatial resolution of AROME offsets any potential inaccuracies.

Further validation was performed using wind records specific to the OWF area. The measurements at OWF4 and OWF5 were standardised to 1 hour average at 10 m elevation, following the recommended practice in DNV GL AS (2021). The ERA5 hindcast wind speeds require scaling up by approximately 25% to match the observed data. In contrast, the AROME forecast wind speeds exhibit a strong correlation without any adjustment.

We conducted a similar analysis to qualify the atmospheric pressure predictions against in situ observations. Both sources of data proved equally satisfactory. As a result, we selected AROME for our application and the spatially varying wind and pressure fields are linearly interpolated on the model mesh for each time step.

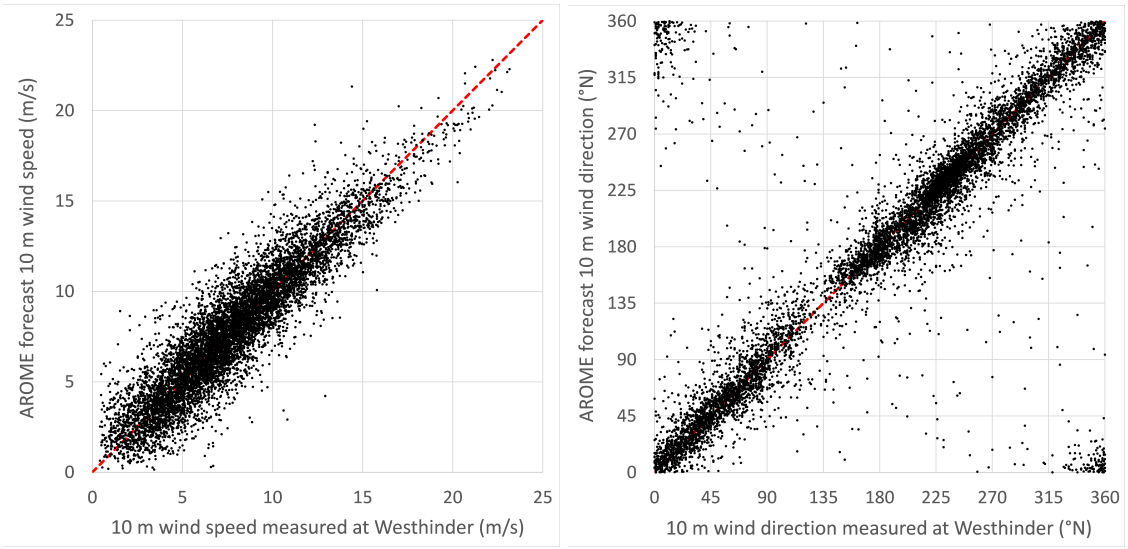

Figure 3.5: AROME forecast wind data (left: speed; right: direction) compared to open-sea wind measurements at the Westhinder platform for 2021

3.3.4 Calibration and validation of the hydrodynamics

The calibration and validation of the hydrodynamics is performed in two steps. The first step demonstrates the ability of the model to simulate the astronomical tide. The second step demonstrates the ability of the model to reproduce the non-tidal effects. To achieve this, we compared the model predictions over complete 14.5-day spring-neap tidal cycles with site-specific sea levels and depth-averaged currents.

Astronomical tide

It is essential to acknowledge that observations include effects other than the tide alone. Consequently, in the first step, the model predictions are compared with synthesised data obtained by tidal harmonic analysis (UTide, Codiga, 2011) of the observed sea level and current velocity records described in Sections 2.1.2 and 2.1.3.

Tidal harmonic analysis seeks to isolate the non-tidal components by breaking the overall tide into the summation of several simple and quasi-independent oscillations of varying periods, each corresponding to the cycle of an astronomical force or tidal harmonic constituent. The amplitude and phase of a tidal constituent are defined by harmonic constants that are unique to a given location. The derivation of these constants by harmonic analysis enables the prediction of the overall astronomical tide at any time in the future or past (Foreman, 2004b, 2004a).

The lunar and solar tides align for certain synodic periods. These periods (and their multiples) are useful for tidal harmonic analysis, for example the 29.53-day synodic month (Proudman Oceanographic Laboratory, UK, 1986). Therefore, our tidal analysis of the observed sea level and current data was carried out over periods of one, three, or six synodic months, depending on the length of the data record. Adjacent constituents cannot necessarily be separated for short time periods. To remedy this, we have established appropriate relationships to infer minor constituents based on data from the Westhinder platform, for which an analysis of a year is possible for sea levels. While the relationships between constituents have some regional stability, this does not apply to shallow-water constituents that are very dependent upon local conditions and cannot be extrapolated. Separately, there were frequent interruptions in the current record at OWF4 and OWF5, which constrained the period that could effectively be used. In general, between 15 (at OWF1) and 65 (at Westhinder) tidal harmonic constituents were identified.

Bed friction is parameterised with a Nikuradse roughness. To assess sensitivity to friction, we varied the roughness length by ±50% around the baseline value of $k_s = 2.5 \times d_{50} = 862.5$ μm (Soulsby, 1997), based on a grain size representative of the region. The hydrodynamics changed only marginally in response to variations in the friction coefficient. It is important to note that these values specifically represent skin friction, while total frictional forces (those associated with sediment grains and those associated with bedforms on the seabed) are relevant to hydrodynamics.

We lack information on secondary bedforms across the computational domain. Evidence suggests that they are present within tile #1 (FEM, 2021a); however, they are not found within certain areas of the OWF footprint (EMD, 2021). For completeness, we conducted a simulation with a higher roughness length of 0.1 m to account for form drag effects. No significant changes in water levels were observed. For velocities, the agreement is visually closer at OWF1, although the discrepancy with resynthesised data is comparable to that observed when considering only skin friction, due to a slight phase shift. The agreement deteriorates at all other locations where current speeds are excessively reduced. Furthermore, the predicted directions during the turning of the tide deviate from resynthesised data. Therefore, we have opted to continue using only skin friction in the hydrodynamic modelling.

As anticipated, the hydrodynamics are most sensitive to boundary conditions. The selection of the tidal database was discussed in Section 3.3.2. Initial tests highlighted the need for a more complete representation of the tides. The FES2014 database includes 34 harmonic constituents. The North-East Atlantic (NEA) atlas developed by CNES, NOVELTIS and LEGOS (`https://sirocco.obs-mip.fr/`) holds an impressive 47 harmonic constituents and has been integrated into other regional models along the French coastline (e.g., Raoult et al., 2018). Unfortunately, we were unable to obtain permission to use this database for our research. Instead, we opted for the FES2014 database, which demonstrated good agreement with the in situ current and level data, as illustrated in Figure 3.6 for 2016 and in Figure 3.7 for 2021.

In these figures, the flow characteristics are satisfactorily predicted by the model. The turning of the tide is well reproduced even if the model can be slightly ahead or behind on occasions, which reflects on the model statistics. The predicted current directions also compare favourably with observations. Differences are typically less than 5° for ebb and flood flows, noting that we did not adjust the observed directions for grid convergence, which is only half a degree in the study area.

While time histories give an immediate visual impression of the agreement between model and observations, the quality of the calibration / validation exercise is typically measured using statistical metrics such as the Root Mean Square Error (RMSE) or Mean Absolute Error (MAE). Sutherland et al. (2004) suggest a classification system based on normalised MAE (RMAE) to evaluate the performance of numerical models. An RMAE value of 20% (or less) is deemed to reflect excellent model calibration, while a value of 40% (or less) indicates good model calibration. Here, tidal levels are normalised against the mean tidal range, taken to be 4.4 m, and current speeds are normalised against the average synthesised speed. These statistics are summarised in Table 3.2, both in terms of RMSE and RMAE in brackets.

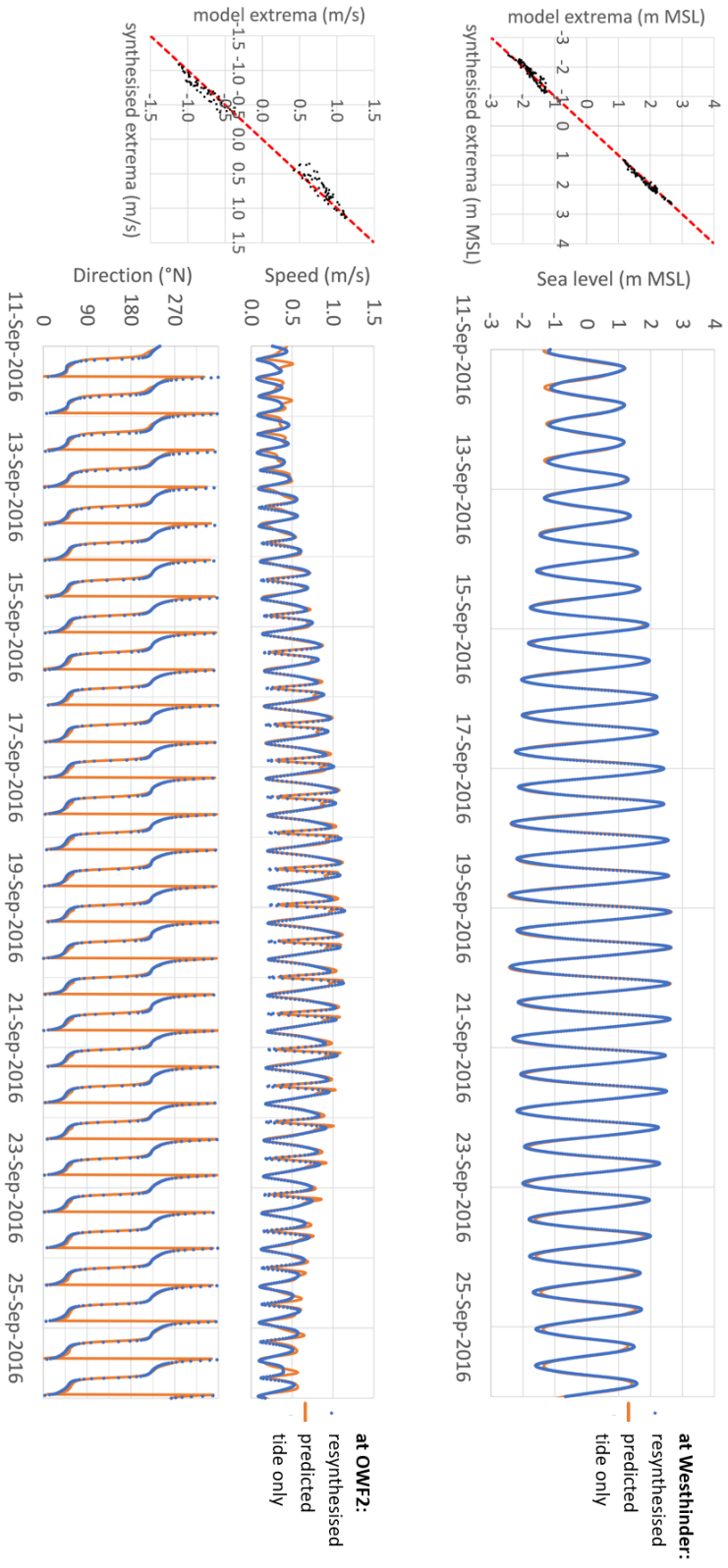

Figure 3.6: Comparison of model predictions (tide only) against resynthesised tidal levels at the Westhinder platform (right), and current magnitude and direction at OWF2 (centre and left) for a 15-day period in 2016

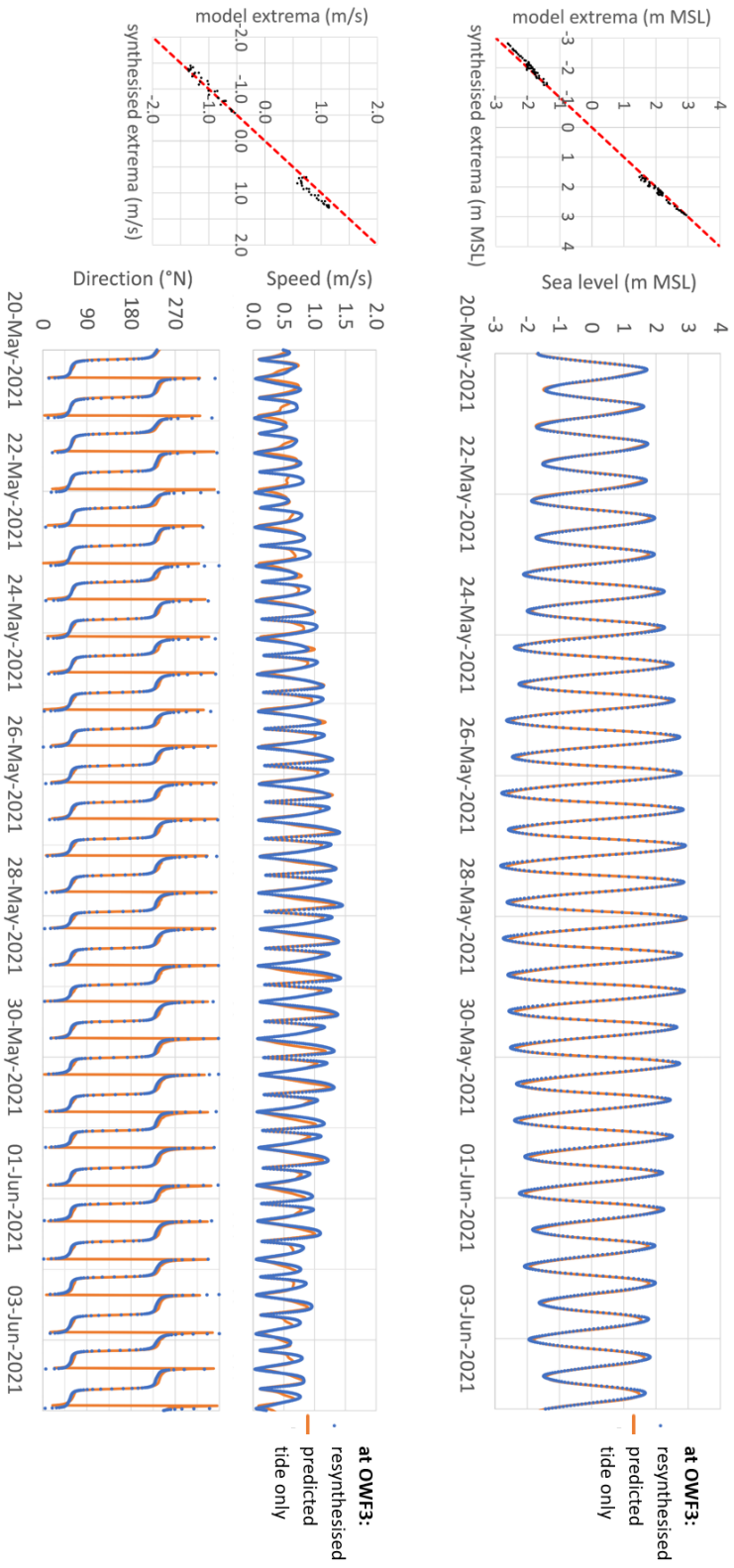

Figure 3.7: Comparison of model predictions (tide only) against resynthesised tidal levels (right), current magnitude (centre) and direction (left) for a 15-day period in 2021 at OWF3

The results from the 3D hydrodynamic model consistently meet the 'excellent' classification criteria, with the RMAE being less than 20% at each of the eight calibration and validation locations.

Location	Tidal levels	Current speeds
Westhinder (2016)	0.10 m (2%)	–
OWF1	–	0.12 m/s (19%)
OWF2	–	0.09 m/s (13%)
Westhinder (2021)	0.08 m (1%)	–
NavCh1	0.13 m (3%)	0.10 m/s (17%)
OWF3	0.11 m (2%)	0.10 m/s (14%)
OWF4	0.15 m (3%)	–
OWF5	–	0.10 m/s (13%)

Table 3.2: Performance of the 3D hydrodynamic model against resynthesised data for a complete spring-neap cycle, expressed in terms of RMSE values (with RMAE values in brackets)

Weather effects

The second step demonstrates the ability of the hydrodynamic model to reproduce the non-tidal effects. Using the same approach as in the first step, the model predictions, which now include atmospheric effects, are directly compared with observations. Model calibration focused on two processes: the hydrodynamic turbulence and the influence of wind in the 3D hydrodynamic model.

In three-dimensional environmental hydraulic applications, it is standard practice to differentiate between horizontal and vertical turbulence scales, as they typically relate to distinct physical processes. This is the approach adopted in TELEMAC-3D and a range of formulations is available to parameterise turbulent diffusion in both directions separately. For horizontal diffusion, we used a constant kinematic viscosity of 10^{-6} m^2/s. We performed initial simulations with a Prandtl mixing length model for vertical diffusion (`MIXING LENGTH MODEL = 1`), but the results were unsatisfactory. The agreement of predicted sea levels and current velocities with measured data was poor, with a notable phase lag in the velocities. The Tsanis mixing length model (`MIXING LENGTH MODEL = 6`, Tsanis, 1989) includes a more accurate representation of wind drift. Subsequent tests with this model for vertical diffusion corrected the phase discrepancies. Tests were also conducted with the k-ϵ turbulence model. Little changes were noted, but the use of this model significantly increased the computational cost. Consequently, we opted for the Tsanis model in the remainder.

The effect of wind comes into play in the momentum equations (Eq. 3.2). This term implicitly accounts for the distance over which the wind blows and the roughness of the sea surface. This influence is encapsulated by a dimensionless wind coefficient: α_{wind} in Equation 3.3. Various relationships have been suggested to calculate the wind drag coefficient (Shankar & Behera, 2021). TELEMAC-3D adopts the Heaps (1965) approach, which uses a stepwise function, capping the wind effect for speeds over 19.22 m/s with the Charnock and Crease (1957) coefficient (Figure 3.8). This approach is also used by the Institute of Oceanographic Sciences (IOS) in the UK.

Zijlema et al. (2012) recommended a quadratic function that reduces the wind drag with increasing wind speeds. This relationship was derived from fitting a regression curve to field observations. Another widely used relationship is that proposed by Wu (1982). We implemented both these functions in TELEMAC-3D (subroutine `prosou.f`) as alternatives to the default approach. For Wu (1982), a lower threshold is applied for wind speeds below 7.5 m/s, similar to its application in the SWAN wave model. These modifications are most noticeable during energetic events, when wind speeds are in excess of 15 m/s (e.g., 21 to 23-May-2021). Outside of these energetic periods, the wind drag modifications do not significantly affect water levels or current velocities. Visually, the Heaps (1965) approach gives the closest agreement for current velocities, in both magnitude and direction (turning of the tide).

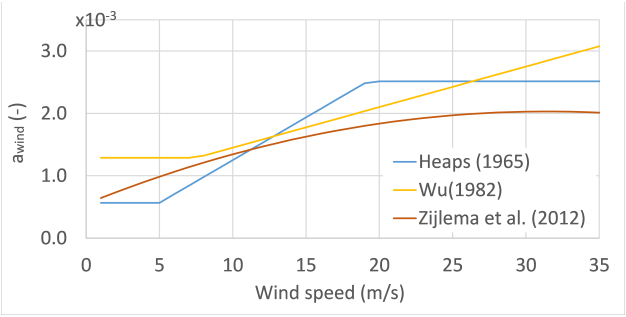

Figure 3.8: Representation of wind drag coefficient

The counterparts of Figures 3.6 and 3.7 are presented in Figures 3.9 and 3.10, respectively, which include weather effects. Notably, there is good visual agreement, particularly in the suppression of the ebb flows on 21-22 May 2021. The statistical metrics are summarised in Table 3.3, demonstrating that the results from the 3D hydrodynamic model consistently meet the 'excellent' classification criteria outlined by Sutherland et al. (2004). The RMAE remains below 20% at each of the seven calibration and validation locations.

Location	Tidal levels	Current speeds
Westhinder (2016)	0.18 m (3%)	–
OWF1	–	0.12 m/s (18%)
OWF2	–	0.09 m/s (15%)
Westhinder (2021)	0.15 m (3%)	–
NavCh1	0.16 m (3%)	0.09 m/s (15%)
OWF3	0.15 m (3%)	0.12 m/s (15%)
OWF5	–	0.10 m/s (13%)

Table 3.3: Performance of the 3D hydrodynamic model including weather against observed data for a complete spring-neap cycle, expressed in terms of RMSE values (with RMAE values in brackets)

Residual currents have been shown to play an important role in the dynamics of marine dunes (Németh et al., 2002). These currents are usefully represented by Progressive Vector Diagrams (PVD), which are constructed from the time histories of u- and v- velocity components at specific locations. Although the pattern and orientation of the predicted trace generally match those observed, there can be a discrepancy in magnitude. This difference is reflected in the values reported in Table 3.4. In particular, both the strength and orientation of the residual currents are satisfactorily reproduced in NavCh1 (Durand et al., 2022a). This is not always the case within the OWF footprint. It is important to recognise that this analysis is sensitive to the chosen time period, leading to different agreements based on alternative periods (see, for example, OWF3 in Table 3.4).

Location	Observed residual	Predicted residual
OWF1	0.015 m/s	0.004 m/s
OWF2	0.003 m/s	0.041 m/s
NavCh1	0.058 m/s	0.055 m/s
OWF3	0.043 m/s	0.025-0.041 m/s
OWF5	0.115 m/s	0.020 m/s

Table 3.4: Performance of the 3D hydrodynamic model including weather against observed data for a complete spring-neap cycle, expressed in terms of residual current

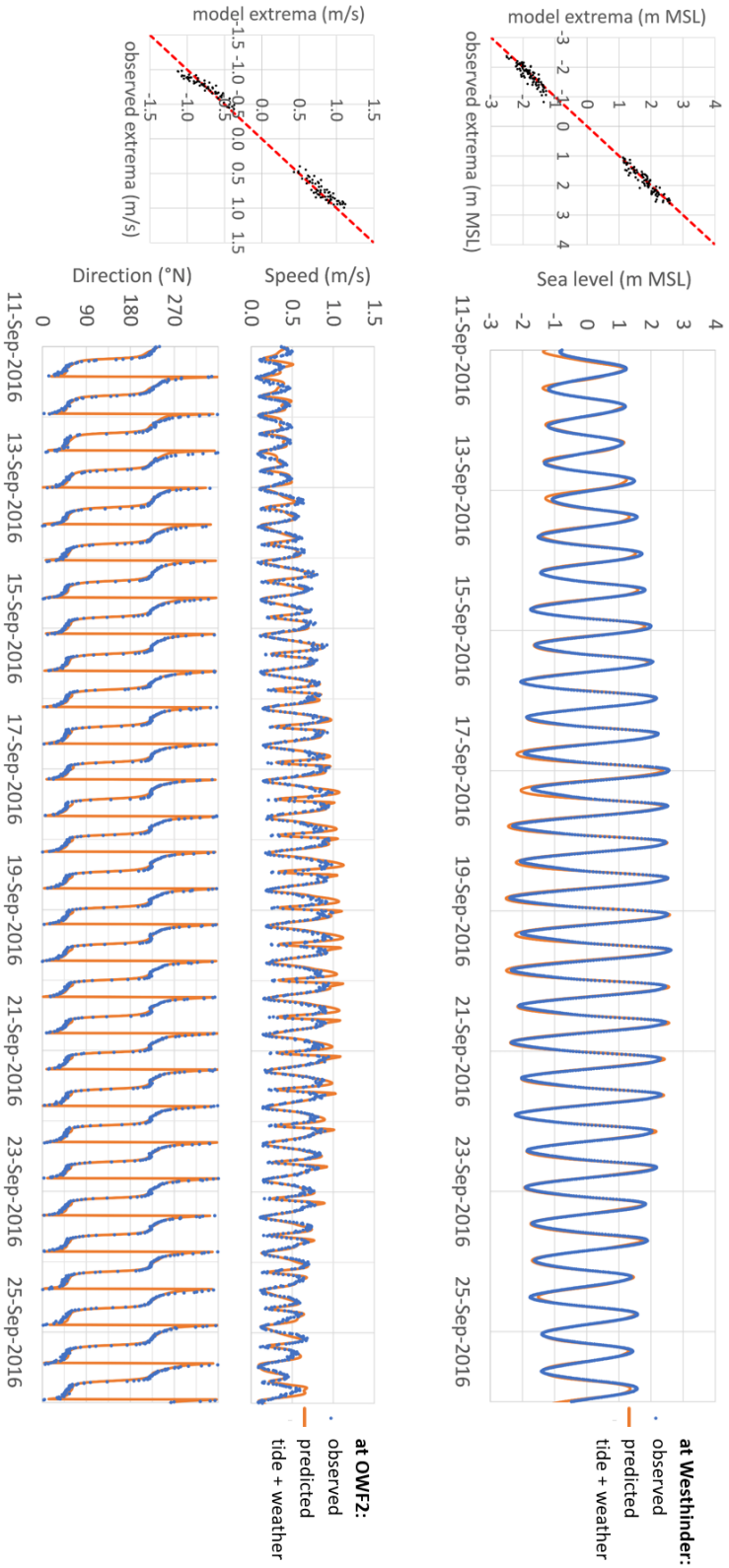

Figure 3.9: Comparison of model predictions against measured sea levels at the Westhinder platform (right), and current magnitude and direction at OWF2 (centre and left) for a 15-day period in 2016

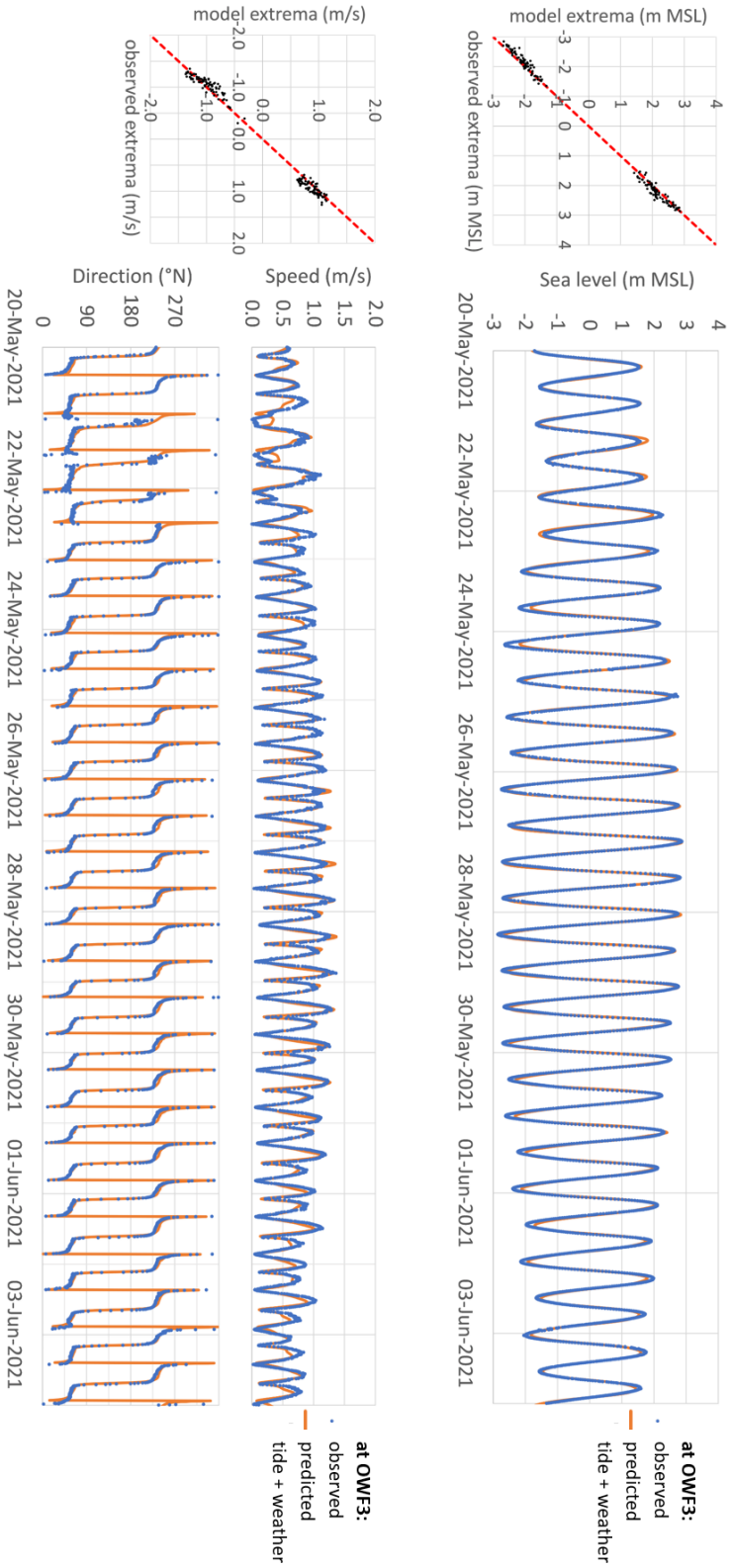

Figure 3.10: Comparison of model predictions against measured sea levels (right), current magnitude (centre) and direction (left) for a 15-day period in 2021 at OWF3

3.4 Wave modelling

3.4.1 TOMAWAC

TOMAWAC (Benoit et al., 1996) is the wave generation and transformation module from the open**TELEMAC** system. It is a time-stepping, phase-averaged, third-generation spectral wave model. These models, considered state-of-the-art for coastal wave modelling, solve the spectral action density balance equation, accounting for sources and sinks, without imposing constraints on the spectral shape or evolution:

$$\frac{\partial N}{\partial t} + \vec{\nabla}_x \cdot [(\vec{c_g} + \vec{U})N] + \frac{\partial c_\sigma N}{\partial \sigma} + \frac{\partial c_\theta N}{\partial \theta} = \frac{S}{\sigma} \tag{3.5}$$

where t denotes the time and x the two-dimensional geographical space; σ denotes the angular frequency (rad) and θ the propagation direction (rad); $\vec{c_g}$ is the group velocity in the geographical space, following from the dispersion relation. The propagation velocities in the spectral space (σ, θ) are noted c_σ and c_θ; and the ambient current field $\vec{U}$. S encompasses various physical processes responsible for generating, dissipating, or redistributing energy in the spectral space.

On the left-hand side of Equation 3.5, the second term represents the propagation of wave energy across geographical space, accounting for phenomena like wave shoaling. As waves travel from deep to shallow water, their energy distribution changes. The third and fourth terms correspond to frequency shifting and refraction processes respectively. These adjustments in frequencies and directions occur due to spatial variations in the seabed or ambient currents. In shallow water, S includes non-linear three-wave and four-wave interactions, and energy dissipation due to white-capping, bottom friction and depth-induced breaking. Wave generation by the local winds is also included, which makes the model especially suited for regions where waves may be equally comprised of offshore waves and those raised by local winds.

The wave action density spectrum N is the unknown ($m^2/Hz^2/rad$), computed at each node of the computational domain. Unlike the energy density spectrum $E(\sigma,\theta) = N\sigma$, which is not conserved in the presence of an ambient current (Whitham, 1974), N is conserved and wave models are commonly expressed in terms of the wave action density spectrum. Analysis and integration of the wave spectrum eventually yield wave parameters such as significant wave height, mean and peak wave periods and directions.

3.4.2 Wave forcing

TOMAWAC is driven by wave conditions specified at the open boundaries. Long-term wave measurements are available from the Westhinder buoy, and to a lesser extent, at OWF4 and OWF5 (Section 2.1.4, Figure 2.1). These measurements are site-specific but taken at discrete locations. Since it is important to capture both temporal and spatial variations, we assessed two sources of model wave data: the ERA5 reanalysis data set and the ANEMOC-3 hindcast database.

We introduced the ERA5 data set (Hersbach et al., 2020) in Section 3.3. In addition to atmospheric parameters, ERA5 provides high-quality but relatively coarse-resolution (1/2°) estimates of surface wave parameters. These data are archived on an hourly basis, covering the entire model area.

ANEMOC-3 (Raoult et al., 2018; Teles et al., 2022) is the third version of the ANEMOC database, originally developed by EDF R&D and Cerema. Its purpose is to hindcast sea states along the French coast (ANEMOC stands for Atlas Numérique d'Etats de Mer Océanique et Côtier). The database covers the Atlantic, English Channel, and North Sea French coast, down to a horizontal resolution of 1/100°. ANEMOC-3 is built upon the TOMAWAC third-generation wave model, where tidal effects are accounted for through water level and current maps predicted using a TELEMAC-2D hydrodynamic model of the same geographical area. Recently, the ANEMOC-3 database has been updated to include data up to 2021 (Teles et al., 2022).

The suitability of these two data sources (ERA5 reanalysis and ANEMOC-3 hindcast) was assessed by comparing their output with buoy measurements. The Westhinder directional waverider buoy is

located on the Westhinder sandbank, in approximately 23 m water depth (51°22.850' N 2°26.133' E, Section 2.1.4). The buoy records wave data, with predominant directions from the west-southwest, noting that significant wave events also occur from the northwest to the northeast. In these comparisons, we consider the entire year 2021 to eliminate any seasonal bias. The highest recorded wave in 2021 reached 4.4 m from the southwest, while waves originating from the north remained below 4.0 m.

Wave parameters (significant wave height, mean wave period and direction) were extracted from the ANEMOC-3 database near the buoy location at 51°22.866' N 2°26.148' E. The comparison with the observed data, on a direct time-for-time basis, is visualised in a scatter plot (Figure 3.11 left). ANEMOC-3 tends to underestimate wave heights above 1.5 m at Westhinder by approximately 7%. Similarly, the analysis for the mean wave period (Figure 3.11 right) indicates that the mean periods are under-predicted by 0.5 s on average. The repository from which we obtained the Westhinder wave data does not record the mean wave direction, only the swell and wind-sea wave directions separately. To estimate an average wave direction, we considered the proportion of energy associated with long periods. However, this analysis revealed a significant spread in the results (not shown).

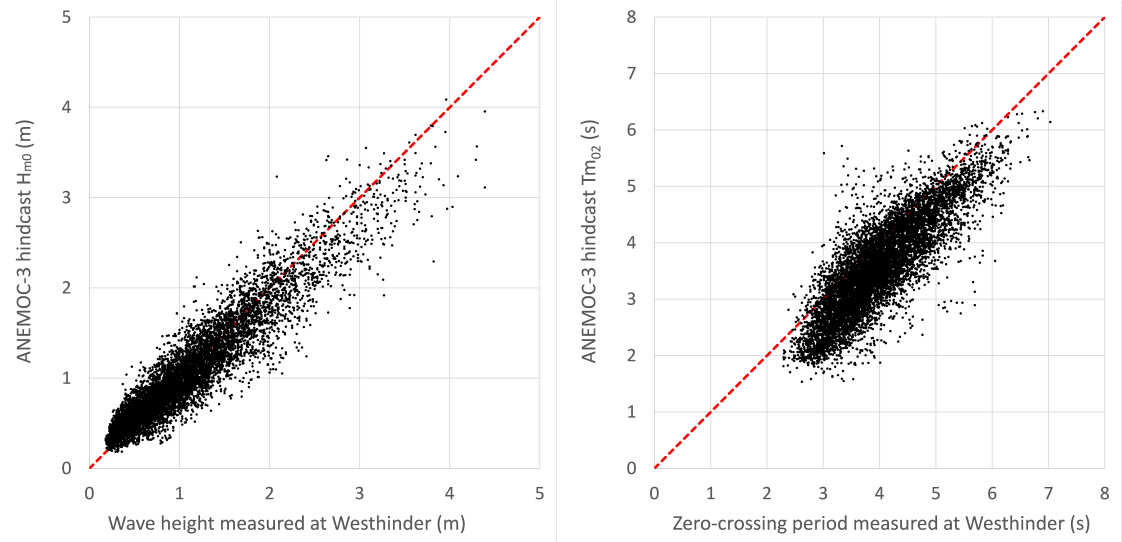

Figure 3.11: ANEMOC-3 hindcast wave data (left: height; right: mean period) compared to wave measurements at the Westhinder buoy for 2021

The horizontal resolution of the ERA5 dataset (1/2°, approximately 35 km from east to west by 56 km from north to south) did not allow for a similar comparison. The data point is either much further offshore than the buoy (51°42' N 2°30' E) or in shallower waters close to the coastline (51°12' N 2°30' E). As a result, the model wave heights are higher (by approximately 6%) or lower (by approximately 15%) than the measured values. Additionally, due to its relatively coarse resolution, the ERA5 data set cannot adequately describe fine spatial variations in wave conditions along our model boundaries.

Instead, we obtained time-varying wave spectra from ANEMOC-3 at 56 locations along the open boundaries of our wave model. These spectra are discretised with 32 frequencies and 36 directions. The use of spectral data is preferred over integrated sea states because it minimises information loss at the interface between the hindcast database and our wave model. The agreement shown in Figure 3.11 is considered satisfactory, leading us to use the ANEMOC-3 wave spectra directly as input for the wave model, without adjustments.

3.4.3 Meteorological forcing

In addition to wave forcing at the open boundaries, TOMAWAC is driven by winds that generate local waves. This process is accounted for using the WAM cycle 3 formulation and linear wave growth

as described by (Cavaleri & Rizzoli, 1981). In line with the analysis in Section 3.3.3, we adopt the AROME database for this purpose.

3.4.4 Hydrodynamic forcing

In shallow shelf seas, tidal effects significantly influence wave propagation and transformation. The currents cause wave refraction, Doppler shifting, and in cases of strong opposing currents, blocking of the wave propagation. In simple environments, opposing currents are expected to steepen waves, enhancing their height while reducing their wavelength. Conversely, following currents would dampen wave heights and increase wavelengths.

To account for these effects, the wave model is dynamically coupled with the calibrated hydrodynamic TELEMAC-3D model of the same geographical area. This ensures that spatial and temporal variations in sea levels and currents are automatically considered in the wave model (update frequency of 30 minutes).

3.4.5 Calibration of the waves

Given the location of the study area, it is crucial that the wave model be able to accurately predict the tidal modulations (that is, changes in wave height, period, and direction throughout the tidal cycle). If it can be shown that the model results agree with in situ measurements, then it gives confidence in the wave predictions for both normal and extreme events.

To achieve this, we simulated two energetic periods: one in autumn 2016 and the other in spring 2021, for which observed data are available in the OWF area and at the Westhinder buoy (Section 2.1.4). We then compared the model predictions with the mooring data, bearing in mind that defining wave parameters in either the time or frequency domain can yield different estimates. The model provides spectral parameters. These parameters are generally recorded by the instruments, allowing a direct comparison. However, there is uncertainty for the Westhinder buoy data. In the following, as per the file nomenclature, we assume that what is informally labelled as 'wave height' corresponds to $\boldsymbol{H_{m0}}$, while the 'average wave period' refers to the zero-crossing wave period ($\boldsymbol{T_z}$), best approximated by the spectral period $\boldsymbol{T_{m02}}$.

Calibration is carried out by tuning a number of physical processes (ambient current influence, wind generation, wave dissipation) until a good overall agreement is reached against the observed wave data. The results of the wave model are particularly sensitive to the choice of formulation used to account for the tidal modulations. `DISSIPATION BY STRONG CURRENT = 0` seemed to exaggerate the impact of currents on wave periods and directions. Reasonable results were obtained by introducing a dissipative term into the spectral action density balance equation (Eq. 3.5), as outlined in the work by van der Westhuysen (2012) (option 2). This approach worked well, provided that the dissipation coefficient was appropriately tuned. However, the most favourable results were obtained by limiting the wave spectra using a Phillips (1977) shape, as described in Hedges et al. (1985) (option 1).

We explored both wind generation and wave dissipation to improve storm peak predictions. In the TOMAWAC model, three wind generation models are available. Although no significant difference was observed between Janssen's model (`WIND GENERATION = 1`, Janssen, 1989, 1991) and Snyder's model (`WIND GENERATION = 2`, Snyder. et al., 1981), wind generation based on Yan (1987) (option 3) resulted in higher peaks, improving predictions at the Westhinder buoy but degrading results within the OWF footprint. Additionally, we tested various parameterisations for depth-induced breaking following the work of Pezerat et al. (2021), but the impact was minimal. In fact, the height of the storm peaks decreased, contrary to our desired outcome. Finally, we investigated whitecapping dissipation. The parameterisation proposed by Ardhuin et al. (2010) was thought to improve model performance, especially for easterly wind events with short fetches. This parameterisation was being implemented in the TOMAWAC model at the time and was tested, with mixed results. In light of these sensitivity tests, we decided to retain the default approaches and parameter values for wind generation and wave dissipation processes.

The comparison between model predictions and measurements (Figures 3.12 and 3.13) shows favourable agreement in terms of significant wave height, mean wave period and mean wave direction (all of which have an impact on sediment transport). The tidal effects are apparent in these figures, in particular Doppler shifting and refraction by the currents. These effects are reasonably well reproduced by the wave model but we note certain discrepancies. Despite our efforts to tune the generation and dissipation processes, there is a tendency to under-predict storm waves in autumn 2016. These differences could stem from limitations in the offshore wave data, inaccuracies in the wave model, errors in the measured values, or possibly a combination of the three. For example, there is noise in the observed wave directions for short wave periods (<3 s) at OWF2, likely due to limitations in the directional wave spectra data. These data are identified by a lighter shade of blue.

The Root Mean Square Error (RMSE) quantifies these differences, as summarised in Table 3.5 for the entire simulation period. The performance of the wave model is not as strong as that of the 3D hydrodynamic model if we follow Sutherland et al. (2004) classification system. While the RMAE values (obtained by normalising the MAE by the average wave height / period) remain below 20% at most of the calibration and validation locations, the values are relatively high, and Gravelines is only classified as 'good'.

Location	H_{m0}	T_{m02}
Westhinder (2016)	0.18 m (15%)	0.6 s (14%)
OWF1	0.13 m (18%)	0.5 s (16%)
OWF2	0.15 m (15%)	0.4 s (10%)
Westhinder (2021)	0.18 m (17%)	0.6 s (12%)
Gravelines	0.17 m (25%)	0.7 s (15%)
OWF5	0.16 m (20%)	0.6 s (14%)

Table 3.5: Performance of the wave model against observed data, expressed in terms of RMSE values (with RMAE values in brackets)

3.5 Relative influence of currents and waves on sediment mobility

Water particles in a wave follow an orbital motion, which diameter corresponds to the wave height near the surface. Closer to the seabed, in intermediate and shallow water, this motion induces oscillatory currents, whose strength depends on water depth, wave height and period. While these currents may not necessarily cause net sediment transport, they are susceptible to mobilise sediment particles at greater depths for higher waves and longer periods or smaller sediment grain sizes. The sediment grains are then available to be transported, for example by the tidal currents (University, 1999).

Owing to the location and depth of the study area, it is expected that wave effects reach the seabed during storm events. To verify this assumption and decide whether wave contributions should be included in the sediment transport modelling, we conducted a preliminary analysis of sediment mobility based on oceanographic considerations. For this, a two-year period (from January 2020 to December 2021) was run using the validated hydrodynamic and wave models described in previous sections. Considering complete years removes any seasonal bias, although it is recognised that a more robust approach would consist in using a longer period, which is not done because of computational time constraints. In these simulations, the seabed is static and based on the summer 2021 model seabed map (Section 3.2).

3.5.1 Sediment mobilisation

Seabed sediment is mobilised by either current, wave, or combined wave and current action. The dominant processes will vary in space and in time. To help assess the dynamics of marine dunes in particular, Whitehouse et al. (2000) have suggested drafting what they call seabed mobility maps, from available information on wave climate, current speeds and seabed sediment composition. The authors have not expanded on their definition of such maps. It is our understanding that they should

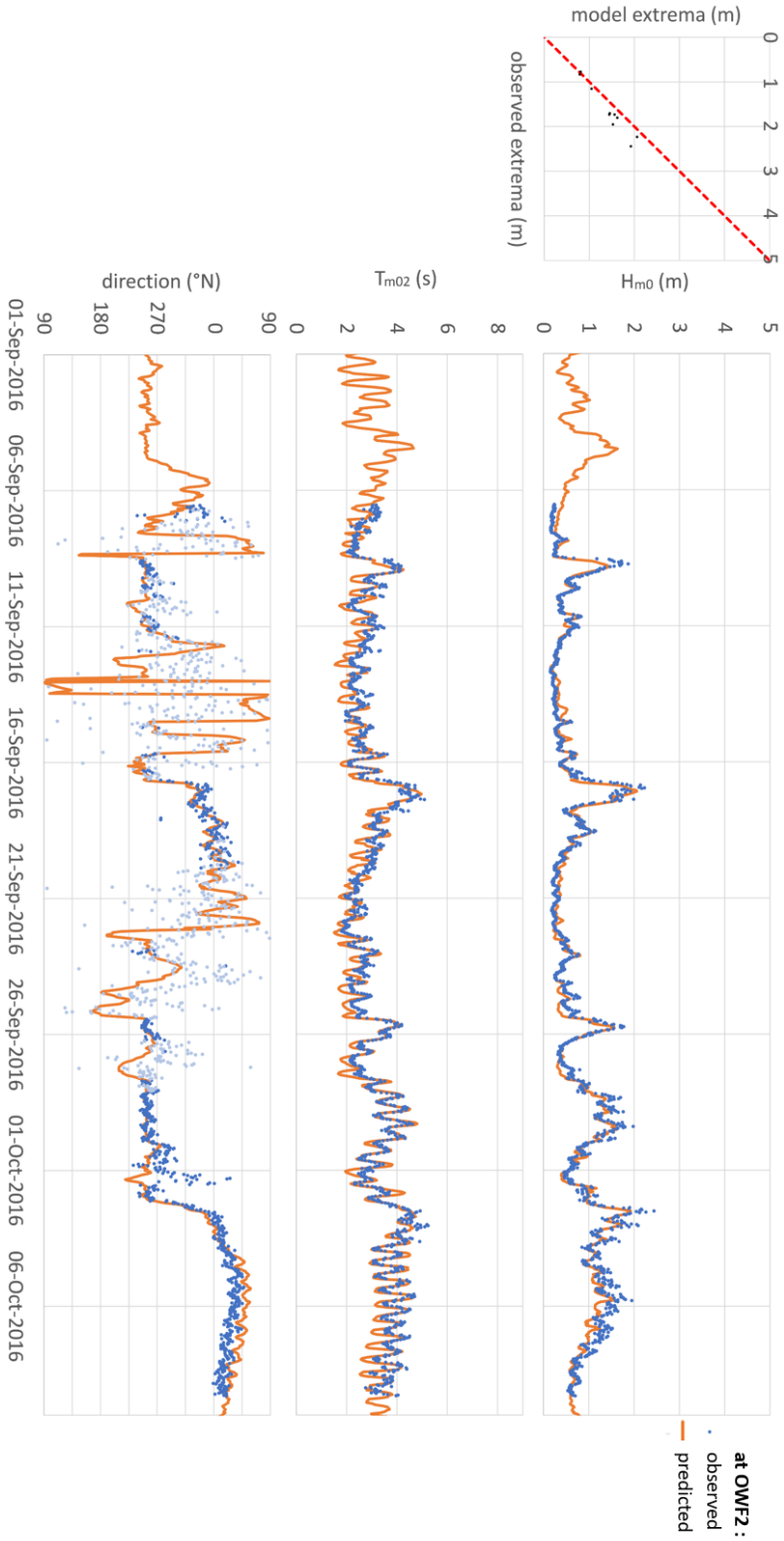

Figure 3.12: Comparison of model predictions against measured significant wave height H_{m0} (right), mean wave period T_{m02} (centre) and mean wave direction (left) between 01-Sep-2016 and 10-Oct-2016 at OWF2

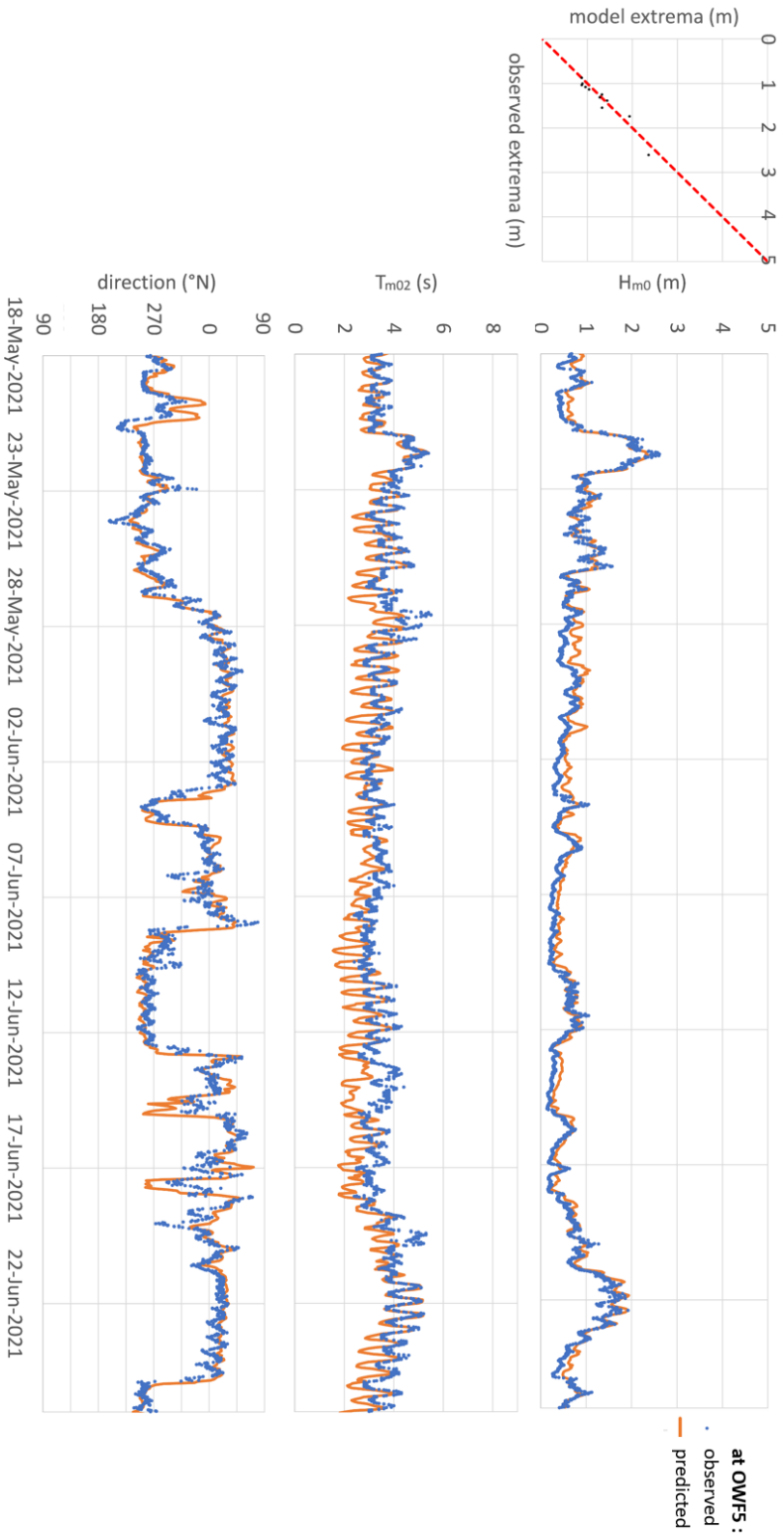

Figure 3.13: Comparison of model predictions against measured significant wave height H_{m0} (right), mean wave period T_{m02} (centre) and mean wave direction (left) between 15-May-2021 and 26-Jun-2021 at OWF5

express the proportion of the time that the threshold bed shear-stress for onset of motion is exceeded (referred to as the Mobilisation Frequency Index in Coughlan et al., 2021). For the Australian continental shelf, Porter-Smith et al. (2004) have compiled such exceedance maps, for swell waves and tidal currents separately. These maps were derived for the observed mean grain size distribution, from predictions of long-term (3 years) wave data and tidal current speed over a spring-neap cycle. They inform on the likelihood of sediment transport in response to environmental conditions, and perhaps more interestingly, allow a regionalisation of the predominance of wave or current processes around Australia, based on the ratio of wave and tidal exceedance estimates (their Figure 9).

3.5.2 Bed shear-stress

To estimate sediment mobilisation, grain shear-stresses induced by currents and those induced by waves were computed independently. The shear-stresses generated by currents alone, τ_c, are computed from the water density ρ = 1027 kg/m^3, the dimensionless drag coefficient C_D (a function of the friction coefficient) and the depth-averaged current velocity $\|\vec{U}_{2D}\|$ as a first approximation:

$$\tau_c = \rho C_D \|\vec{U}_{2D}\|^2 \tag{3.6}$$

The shear-stresses generated by waves alone, τ_w, are computed from the water density, the RMS orbital velocity near the seabed U_{rms} (small-amplitude linear wave theory, in the absence of a current), and the dimensionless wave friction factor f_w defined in Swart (1976):

$$\tau_w = \rho f_w U_{rms}^2 \tag{3.7}$$

In most coastal and shelf sea environments, hydrodynamic conditions comprise equally of currents and waves. The formulation of the bed shear-stress is, therefore, modified accordingly, to take account of both influences. Because currents and waves interact with each other, their individual contributions cannot merely be added. The mean and maximum bed shear-stresses during a wave cycle are computed from Soulsby (1997):

$$\tau_m = \tau_c \left[1 + 1.2 \left(\frac{\tau_w}{\tau_c + \tau_w}\right)^{3.2}\right] \tag{3.8}$$

$$\tau_{max} = \sqrt{((\tau_m + \tau_w cos\phi)^2 + (\tau_w sin\phi)^2)} \tag{3.9}$$

where ϕ denotes the angle between the current and wave directions.

The threshold bed shear-stress for onset of motion is computed for a sediment with median grain diameter d_{50} of 345 μm representative of the region:

$$\tau_{cr} = \Theta_{cr}[g(\rho_s - \rho)d_{50}] \tag{3.10}$$

where g = 9.81 m/s^2 is the acceleration due to gravity; ρ_s = 2650 kg/m^3 is the sediment density; and Θ_{cr} is the threshold Shields parameter estimated from Soulsby (1997).

3.5.3 Maps of sediment mobility

By computing the percentage of time when the threshold bed shear-stress, τ_{cr} (Eq. 3.10), is exceeded by the tide-induced bed shear-stress, τ_c (Eq. 3.6), and by the wave-induced bed shear-stress, τ_w (Eq. 3.7), considered separately, a spatial assessment of the relative importance of current and wave processes in mobilising seabed sediment was carried out. We adapted the classification scheme used in Porter-Smith et al. (2004) for the Australian Shelf and a region is categorised as:

- 'tide-dominated' when the percentage of time of tidal mobilisation is greater than 3 times that of wave mobilisation,
- 'wave-dominated' when the percentage of time of wave mobilisation is greater than 3 times that of tidal mobilisation,
- 'mixed' in between.

The result of this analysis is shown in Figure 3.14. It follows that sediment in the study area is predominantly mobilised by the strong tidal current (at least 3 times more than by waves) in relatively deep waters. Over the sandbanks (an area broadly delineated by the -15 mMSL contour) the role of waves in stirring the sediments is enhanced and these areas are designated as 'mixed' in accordance with Porter-Smith et al. (2004) classification. Wave-dominated disturbance occurs in very localised areas, only close to the shore, where tidal currents are weakened, and wave orbital velocities stronger owing to reduced water depths. While this corroborates our working hypothesis that wave action should not be discarded altogether as a mechanism for sediment mobilisation (Durand et al., 2022b), we note that, with this scheme, the bathymetric tiles and most of the OWF area (north of the Binnen Ratel sandbank where turbines will be installed as part of the Dunkirk OWF project) are classified as 'tide-dominated'.

It is recognised that this regionalisation is the result of an average over a two-year period and does not mean to say that wave contribution to sediment mobilisation is minimal in 'tide-dominated' areas. Indeed, during storms for example, the wave action can be stronger than that of the currents in stirring the seabed sediment as illustrated in Durand et al. (2022b). But these results give us grounds to consider wave processes as being of second order in the areas of interest for our research.

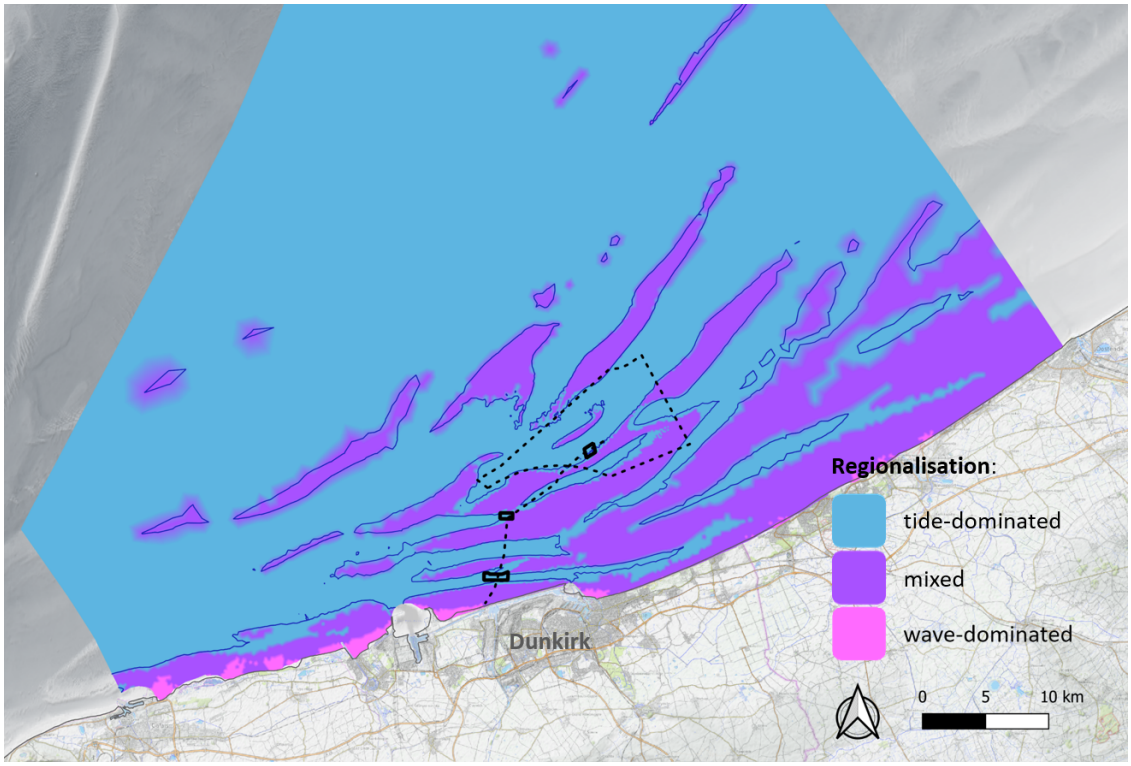

Figure 3.14: Regionalisation of seabed mobilisation by different dominant processes, also showing the -15 m MSL isobath (Source of the background data: Shom (2015), OpenTopoMap, and EEA coastline)

Another useful indicator of sediment mobility is the Mobilisation Frequency Index (MFI) (Coughlan et al., 2021), defined as the percentage of time the threshold bed shear-stress for the chosen grain size, τ_{cr}, is exceeded by the maximum bed shear-stress under combined wave and current action, τ_{max} (Eq. 3.9). MFI therefore gives some indication on how often the seabed sediment is mobilised. This is illustrated in Figure 3.15. MFI values range from 0 to 96%. High levels of exceedance (> 70%) are largely correlated to sandbank crests (water depths shallower than 15 m) and the 'mixed' disturbance areas highlighted in Figure 3.14. Focusing on tile #1 (location in Figure 2.1(c)), the seabed sediment is mobilised 60% of the time on average, with higher rates (up to 67%) on top of the dune crests, in the navigation channel.

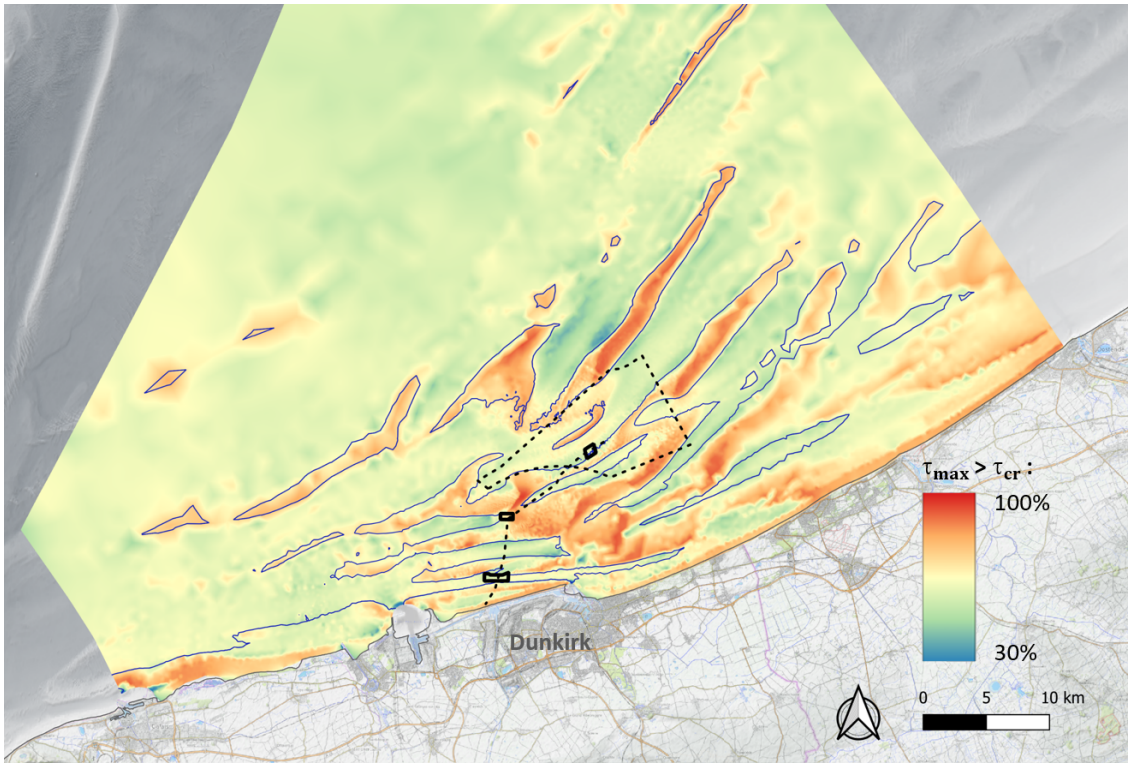

Figure 3.15: Spatial distribution of Mobilisation Frequency Index (MFI) calculated from two years of model results, also showing the -15 m MSL isobath (Source of the background data: Shom (2015), OpenTopoMap, and EEA coastline)

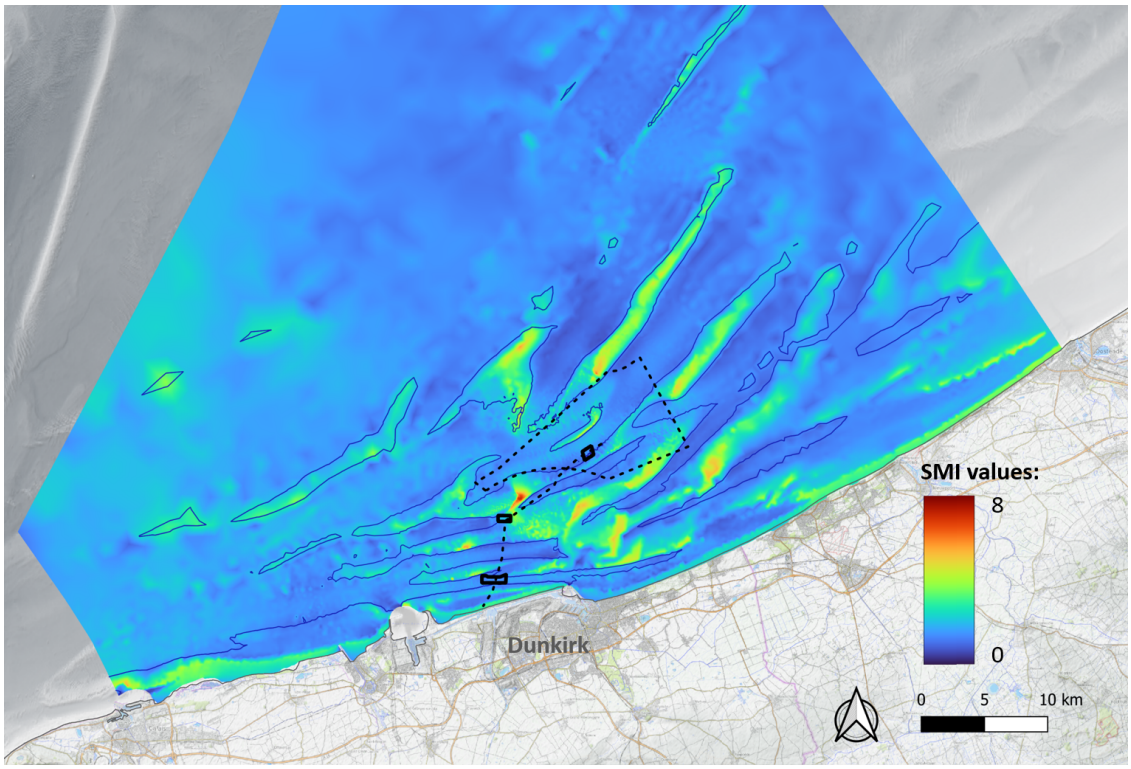

Figure 3.16: Spatial distribution of Sediment Mobilisation Index (SMI) calculated from two years of model results, also showing the -15 m MSL isobath (Source of the background data: Shom (2015), OpenTopoMap, and EEA coastline)

Coughlan et al. (2021) noted that while the above approaches are good indicators of the frequency of mobilisation of the sediment, they do not inform on its strength. They offer the use of additional parameters, adopted from M. Z. Li et al. (2015) in the Bay of Fundy, such as the Sediment Mobilisation Index (SMI) that integrates both the magnitude and frequency of sediment mobilisation. SMI is calculated as the mean ratio of the maximum combined bed shear-stress, τ_{max}, by the threshold bed shear-stress, τ_{cr} (only for those times when the threshold of motion is exceeded) times the percentage time exceedance (M. Z. Li et al., 2009).

Figure 3.16 presents the spatial distribution of the Sediment Mobilisation Index. SMI values typically range between 0 and 2.5 in 'tide-dominated' areas. These values are comparable to those reported by Coughlan et al. (2021) in the Irish Sea, and generally higher than those reported by M. Z. Li et al. (2015) in the Bay of Fundy. Higher SMI values (typically reaching 5.0) are computed in 'mixed' areas, in particular along the coast and atop the sandbanks (associated reduced water depths). These values are indicative of intense sediment mobilisation due to the combined wave and current action. Focusing on tile #1, SMI values range between 1.2 and 2.0. Recall that the seabed sediment there is mobilised about 60% of the time, the threshold of motion is then exceeded between 2 and 3 times, on average over a two-year period. It can be expected that tile #1 be more active during storm events.

3.6 Relative influence of bedload and suspended load

3.6.1 Rouse number

The Rouse number (P) is a dimensionless parameter that defines the shape of the suspended sediment concentration profile. By extension, it is often used to determine the predominant mode of sediment transport. It is widely accepted that P values greater than 2.5 are characteristic of bedload dominant transport, and values between 0.8 and 1.2 of suspended load dominant transport (Fredsøe & Deigaard, 1992).

The Rouse number is expressed as the ratio between the sediment fall velocity and the shear velocity acting on the grain:

$$P = \frac{w_s}{\kappa u_*} \tag{3.11}$$

where κ is the von Kármán constant; w_s the sediment fall (or settling) velocity (m/s); and u_* the friction velocity (m/s). The sediment fall velocity can be determined experimentally from in situ bed samples. Alternatively, there exist formulations for w_s, based on the dimensionless grain size D_*, which are appropriate for natural sands (e.g., Hallermeier, 1981; van Rijn, 1984c; Soulsby, 1997).

3.6.2 Map of sediment transport mechanism

Several authors have relied on an analysis of the Rouse number to determine the prevailing sediment transport processes. Borsje et al. (2014), for example, have correlated the absence of marine dune fields in certain regions of the Dutch continental shelf to the predominance of suspended sediment transport in these areas (as estimated from the Rouse number). They have tested their working hypothesis with a morphological model and have shown that marine dunes could only form when the Rouse numbers were in excess of 2.0, in line with observations on the Dutch continental shelf.

We calculated the Rouse number from Equation 3.11. In these calculations, w_s is estimated by Equation 3.12 (Soulsby, 1997) in the absence of in situ measurements, and u_* is replaced by $\sqrt{\tau_m/\rho}$ (τ_m given by Eq. 3.8) to consider the effect of wave action on seabed sediment mobilisation.

$$w_s = \frac{\nu}{d_{50}} \left[\left(10.36^2 + 1.049 D_*^3 \right)^{1/2} \right) - 10.36 \right] \tag{3.12}$$

The results are averaged at each point over the two-year period between 2020 and 2021 and depicted as a map in Figure 3.17. The average Rouse number is significantly higher than 2.5 throughout the computational domain, exceeding 5. This gives some indication that bedload is the dominant sediment

transport mechanism in the study area (Fredsøe & Deigaard, 1992) and is consistent with the findings of Borsje et al. (2014) and Damen et al. (2018) on the Dutch continental shelf.

Bed shear-stresses are understandably at their highest in shallow areas, especially at the top of sandbanks, reaching values of 3.0 N/m^2. Focusing on tile #1, the maximum predicted value is 2.3 N/m^2, which corresponds to a Shields parameter of 0.42.

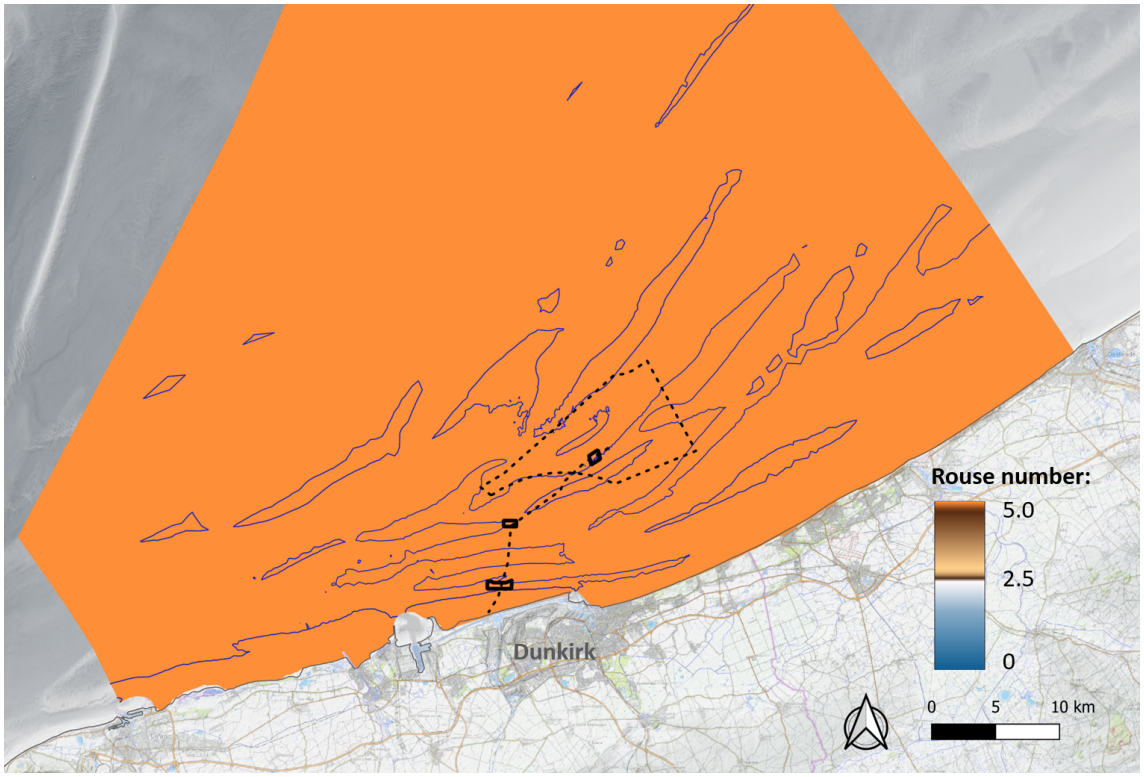

Figure 3.17: Spatial distribution of the Rouse number calculated from two years of model results, also showing the -15 m MSL isobath. (Source of the background data: Shom (2015), OpenTopoMap, and EEA coastline)

3.7 Morphodynamic modelling

The next step is to consider the calibration and validation of the morphodynamics. To do this, we started with a smaller configuration than the large-area model to gain insight into dune modelling. Our focus was on selecting a suitable transport predictor that could accurately reproduce the bed evolutions observed in situ, as well as identifying the parameters to which it might be sensitive. These findings were subsequently transferred to the large-area morphodynamic model.

3.7.1 GAIA

GAIA (Tassi et al., 2023) is the sediment transport and bed evolution module from the open**TELEMAC** system. GAIA is able to model complex sediment and morphodynamic processes in coastal areas, estuaries, rivers and lakes, accounting for spatial and temporal variability in sediment size classes (uniform, graded or mixed), in sediment properties (cohesive and non-cohesive) and transport mechanisms (suspended load, bedload and both simultaneously).

GAIA is internally coupled with the hydrodynamic and/or wave transformation modules to provide the conditions that drive the sediment transport and bed evolution processes. The coupling strategy

adopted in the open**TELEMAC** system is based on synchronous-decoupled techniques. TELEMAC-3D, for example, computes the hydrodynamic solution for a given (fixed) bed map. GAIA is then called to update the bed map according to the revised hydrodynamics. The revised bed map is fed back into TELEMAC-3D. This loop is repeated at each model time step, ensuring a conservative computation of the sediment transport mass and bed level changes.

The change in bed level is computed by solving the sediment mass conservation equation, also known as the Exner equation. This equation expresses the fact that bed levels rise in proportion to the amount of sediment that is no longer transported, and conversely, lower in proportion to the amount of sediment that is entrained by the flow. In its simplest form (bedload transport of one class of non-cohesive sediment), this equation reads:

$$(1-\lambda_p)\partial_t(\rho_s z_b)+\vec{\nabla}\cdot\vec{Q}_b=0 \tag{3.13}$$

where z_b denotes the bed elevation (m) and λ_p the bed porosity (= 0.40 for this work in the absence of site-specific value). The bedload mass transport rate, $\vec{Q}_b = (Q_{b,x}, Q_{b,y})$, is related to the volumetric transport rate, $\vec{q}_b$, by $\vec{Q}_b = \rho_s \vec{q}_b$ (kg/m/s), with ρ_s the sediment density (kg/m^3).

Total sediment transport can be divided into suspended sediment transport, where sediment put in suspension by the turbulence of the flowing water is transported by the ambient current, and bedload transport, where sediment is transported in almost continuous contact with the bed, by rolling, sliding or being carried by saltation. Suspended sediment transport is not explicitly considered in this work, in keeping with the findings of Section 3.6, Durand et al. (2023a), and will not be expanded upon here. Bedload transport is taken into account by computing bedload fluxes in accordance with predictors published in the literature and introduced hereafter.

3.7.2 Sediment transport predictors for the marine environment

Various transport rate predictors have been proposed. We only consider those applicable to coastal areas owing to the site location. These predictors are largely based on parameterisation of physical processes and have been calibrated by their authors with experimental or field data. It should be emphasised that the majority of predictors are designed for use with a flat, horizontal seabed. Should the seabed have a slope, gravity will play an additional role, either increasing or decreasing the rate of sediment transport.

Two formalisms emerge and are explored in this work:

- predictors based on current velocities (of all nature, tidal or not). In GAIA, they are Soulsby and van Rijn (1997) (hereafter SvR97), Bailard (1981), and Dibajnia and Watanabe (1992) (revisited by da Silva et al. (2001)); and
- those based on bed shear-stresses. In GAIA, this is E. W. Bijker (1968). The excess shear predictor proposed by Soulsby and Damgaard (2005) (hereafter SD05) was implemented in GAIA as part of this work.

Bailard predictor is said to perform best in wave-dominated environments (Soulsby, 1995). Because of its formulation, the question arises whether the Dibajnia and Watanabe predictor is suitable without waves. Soulsby and Damgaard predictor is preferred over Bijker's as it incorporates the notion of threshold of motion. Therefore, we will focus on the SvR97 and SD05 sediment transport predictors in the following.

Soulsby and van Rijn (1997) predictor

The SvR97 predictor provides an estimate of the total transport rate (bedload + suspended load) by currents and waves. It was adapted from van Rijn (1984b) sand transport predictor for currents only, to include the wave contribution (turbulent kinetic energy produced by the combined wave and current boundary layers over rippled bed) following the methodology introduced by Grass (1981). It does not include complex wave processes such as velocity asymmetry, acceleration asymmetry, or boundary layer streaming. It is only valid for non-breaking waves.

In this work, wave processes are considered to be of second order as discussed in Section 3.5 and discarded as a first approximation. In this case, the SvR97 predictor reduces to:

$$\vec{q}_t = (A_{sb}+A_{ss})\,\vec{U}_{2D}\left[\|\vec{U}_{2D}\| - U_{cr}\right]^{2.4} \tag{3.14}$$

where $\vec{q}_t$ is the total volumetric transport rate per unit width (m^2/s). $\vec{U}_{2D}$ is the depth-averaged current velocity (m/s) and $\|\vec{U}_{2D}\|$ its norm; $U_{cr} = f\left(d_{50}, h/d_{90}\right)$ the threshold depth-averaged velocity defined by Equation 3.15 (van Rijn, 1984b). $A_{sb} = f\left(h^{-0.2}\right)$ denotes the bedload coefficient (h the water depth), $A_{ss} = f\left(d_{50}^{-0.8}\right)$ the suspended load coefficient. These coefficients had originally been derived for rivers, both from physical and empirical considerations (van Rijn, 1984b). They are valid for water depths between 1 and 20 m, depth-averaged velocities of between 0.5 and 5 m/s and sediment grains between 0.1 and 2 mm.

$$U_{cr} = \begin{cases} 0.19(d_{50})^{0.1}\log_{10}(4h/d_{90}) & \text{for } 0.1 \text{ mm} \le d_{50} \le 0.5 \text{ mm} \\ 8.5(d_{50})^{0.6}\log_{10}(4h/d_{90}) & \text{for } 0.5 \text{ mm} \le d_{50} \le 2 \text{ mm} \end{cases} \tag{3.15}$$

$$A_{sb} = \frac{0.005\,h}{[(s-1)g\,d_{50}]^{1.2}}\left(\frac{d_{50}}{h}\right)^{1.2}, \quad A_{ss} = \frac{0.012\,h}{[(s-1)g\,d_{50}]^{1.2}}\left(\frac{d_{50}}{h}\right)(D_*)^{-0.6} \tag{3.16}$$

where s is the relative density of the sediment $= \rho_s/\rho$ (ρ the water density, ρ_s the sediment density); g the acceleration due to gravity (m/s^2); and D_* the dimensionless grain size defined as $d_{50}\left(g(s-1)/\nu^2\right)^{1/3}$, with ν the kinematic viscosity (m^2/s).

Soulsby and Damgaard (2005) predictor

The SD05 predictor provides an estimate of bedload transport rate, which is appropriate in our context as we have demonstrated that sediment transport occurs primarily as bedload. Currents and sinusoidal or asymmetric waves can be considered, including velocity asymmetry as waves shoal and become increasingly skewed. The contribution of currents alone is derived from sheet flow theory. Sediment concentration and velocity profiles are defined in the sheet flow layer, whose thickness is determined by Coulomb friction. Integration of sediment flux through the sheet flow layer gives the dimensionless transport rate. It is interesting to note that the same formula was independently obtained by fitting a curve to bedload transport data (Nielsen, 1992).

The SD05 predictor is an excess shear-stress formula. In that sense, it is consistent with the physical intuition that sediment grains can only be mobilised when the shear-induced forces exceed the resisting forces (e.g., friction). It is only for bedload transport, which is justified in the region offshore Dunkirk (Section 3.6), and more widely on the Dutch continental shelf (Borsje et al., 2014).

In the absence of waves, the SD05 transport predictor simplifies to:

$$\vec{q}_b = 12\sqrt{\frac{\|\vec{\tau}\|}{\rho}}\left(\frac{\|\vec{\tau}\| - \tau_{cr}}{g\left(\rho_s - \rho\right)}\right)\frac{\vec{U}_{2D}}{\|\vec{U}_{2D}\|} \tag{3.17}$$

where $\vec{q}_b$ is the volumetric bedload transport rate per unit width (m^2/s); τ the bed shear-stress; and τ_{cr} the threshold bed shear-stress for onset of motion (Eq. 3.10). $\vec{U}_{2D}$ denotes the depth-averaged current velocity (m/s).

3.7.3 Development of a simplified configuration

Rather than performing our sensitivity analysis with the large-area model, we opted to develop a streamlined, flume-like configuration. This simplified model is designed to effectively represent the primary sediment transport processes, while also minimising computational costs. Tile #1 is particularly suited for this exercise (location indicated in Figure 2.1(c)). The currents there are mostly bidirectional,

switching direction with the tidal phase, constrained by the orientation of the navigation channel (approximately trending 80°N during the flood; 260°N during the ebb).

The mesh is based on the *bosse* test case provided in the GAIA examples folder (openTELEMAC, December 2022), where dimensions have been scaled so that the mesh resolution is approximately 10 m in both x- and y- directions (consistent with the large-area model). This gives an 800-m-long by 110-m-wide computational domain comprising 891 nodes and 1600 elements (Figure 3.18).

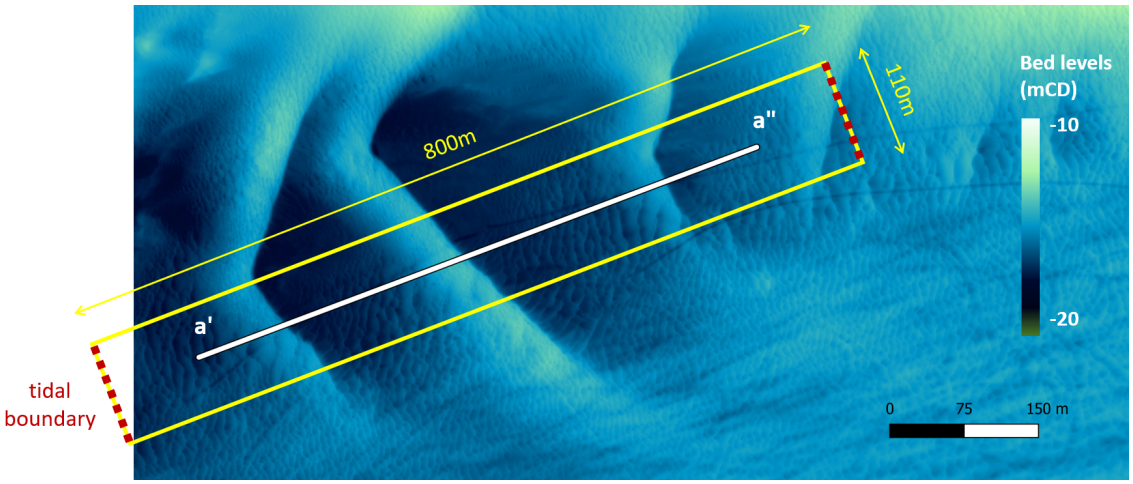

Figure 3.18: Extent of the flume-like model of tile #1, showing the boundary types. Wall boundaries are marked by a solid yellow line, tidal boundaries by a dashed coloured line (Source of the background data: FEM, 2021a)

The digital elevation model of the seabed has been constructed from a dune profile extracted from the November 2019 bathymetric survey data (FEM, 2021a), taken in the predominant direction of the flow, approximately perpendicular to the dune crests (section a'-a" in Figure 3.18). This profile is duplicated across the domain so that the elevation of the bed does not vary laterally. This representation is deemed appropriate as a first instance, given the strong directionality of currents in the navigation channel to the port of Dunkirk.

3.7.4 Hydrodynamic forcing

We have chosen to model the four-month period between S1 and S2 (from 17-Nov-2019 to 17-Mar-2020). Examination of the seabed profiles extracted from DTMs of the local survey data (FEM, 2021a) indicates that dune evolution is not uniform over time (Figure 3.19). Specifically, the dunes were very mobile during the S1-S2 period (compared with S3-S4 and S6-S7 with similar duration). In that period, they migrated approximately 15 m northeast while maintaining their overall shape. If our model performs well under high hydrodynamic stresses (S1-S2), then it gives confidence in the predictions for other time periods.

Although the southern North Sea is open to waves from the Atlantic Ocean and the North Sea, they are relatively short. Due to the large water depth in the navigation channel compared to wavelength ($kh > 0.5$, k the wave number and h the water depth), wave activity is a second-order process for sediment transport at depths > 15 mMSL as described in Section 3.5, Durand et al. (2023a). Therefore, wave processes are not included in this exploratory work, and numerical simulations are performed by internally coupling TELEMAC-3D with the sediment transport and bed evolution module GAIA.

Time-varying water discharges and free surface elevations are applied at both ends of the flume. For that purpose, time histories of velocities and levels have been extracted from a long-term simulation of the calibrated, large area, 3D hydrodynamic model (Section 3.5) in the middle of section a'-a".

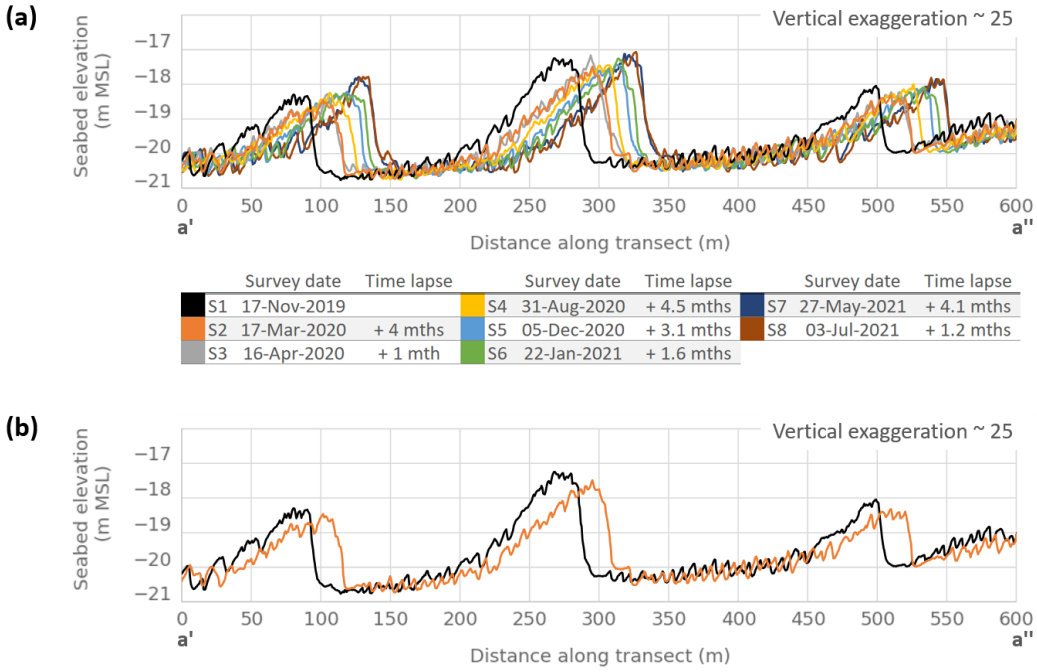

Figure 3.19: (a) Dune profiles along section a'-a", in tile #1, showing the evolution from S1, 17-Nov-2019 to S8, 3-Jul-2021. The predominant flow direction is from left to right. (b) Focus on the period simulated in the model

Water fluxes are calculated as the product of the instantaneous magnitude of the current by the instantaneous water depth, integrated across the width of the flume (Figure 3.20).

Larger peak fluxes are predicted during the flood cycle (positive values) than during the ebb cycle (negative values). The resulting easterly residual (obtained from a rolling average of the instantaneous water flux values) is shown in black in Figure 3.20. Day-to-day oscillations are apparent, which occur because the averaging window does not align exactly with a full tidal cycle. The dark red circles indicate times when the net water flux was directed opposite the dominant easterly direction.

Negative net water fluxes are associated with sustained wind events from the North-West; strong positive net water fluxes (in excess of 500 m^3/s) with energetic events from the South-West. In light of these results, it is anticipated that the preferred direction of sediment transport is towards the East. This is supported by the morphology of the dunes, which exhibits a gentler side facing west and a steeper side facing east (Figure 3.19), typical of bedforms subjected to a prevailing flow direction.

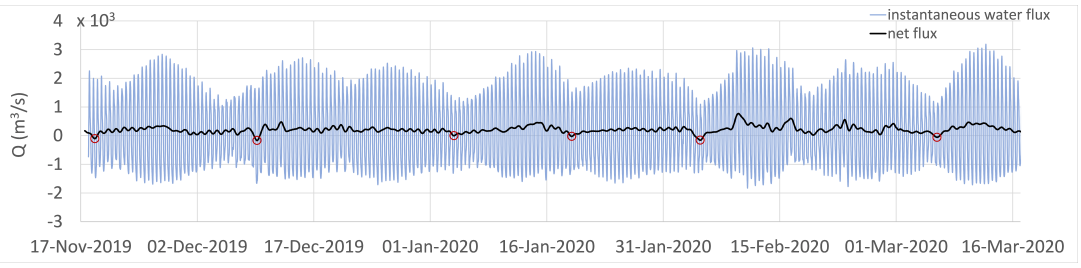

Figure 3.20: Instantaneous water flow predicted by the coastal area model. Positive values correspond to the flood cycle, trending eastward

In this simplified configuration, we retained the settings that resulted in good performance of the large area 3D hydrodynamic model (Section 3.3). Bed friction is expressed in the form of a Nikuradse roughness (taken as 862.5 μm, based on a grain size representative of the region). Turbulent diffusion is defined by a constant eddy viscosity (taken as 10^{-6} m^2/s) in the horizontal direction, and by the Tsanis mixing length model along the vertical direction.

3.7.5 Evaluation of the SvR97 total load predictor

An extensive range of simulations was performed to assess the behaviour of the SvR97 sediment transport predictor, and identify its sensitivities to parameters such as temporal and spatial resolution, vertical discretisation, friction, sediment grain size, slope effect, and consideration of dynamic pressure. Some conclusions from these simulations are presented hereafter.

Influence of vertical plane distribution

Five irregularly spaced sigma planes were used in the vertical for the SvR97 model runs. These were defined at approximately 1/6th, 1/3rd and 2/3rd of the water column, the first plane representing the seabed and the last the free surface. No sensitivity to the distribution of the vertical planes was performed on the grounds that the SvR97 sediment transport predictor is based on depth-averaged velocities.

Influence of friction

Simulations were performed in which undulations were filtered from the bed profile (corresponding to secondary bedforms that are not well resolved in the model, with heights of 0.2-0.6 m and lengths of 5-10 m). A Nikuradse roughness length of 0.1 m, and then 0.2 m, was used as a proxy to account for bedform drag.

A very limited effect was observed with this configuration compared to the original (raw) bed profile. This is attributed to the fact that only hydrodynamics are directly affected by a smoother bed and greater friction (`SKIN FRICTION CORRECTION = 1` in GAIA), and only a marginal reduction of the depth-averaged velocity is predicted.

Influence of grain size

For the purpose of the modelling, we adopted a unimodal distribution. A median grain diameter of d_{50} = 345 μm, and d_{90} = 1 mm, was used, informed by recent sediment grab samples collected offshore Dunkirk (FEM, 2020). The sensitivity to sediment grain size was investigated by varying the median grain diameter within the observed range, i.e. ± 30% about the representative value of 345 μm used elsewhere.

Changes in d_{50} affect not only U_{cr} but also the suspended load coefficient A_{ss} in Equation 3.14. The finer sediments are slightly easier to mobilise (indicated by a 4% reduction in U_{cr} for d_{50} = 230 μm compared to 345 μm), while the coarser sediments are slightly harder to mobilise (3% increase for d_{50} = 450 μm compared to 345 μm). At the same time, the transport rate associated with suspended load is 34% higher with d_{50} = 230 μm and 19% lower with d_{50} = 450 μm. This means that, although the morphology of the dunes is not significantly modified, they move at a noticeably faster rate with finer sediments (ca. +50% for d_{50} = 230 μm compared to 345 μm). With coarser sediments, the crests are levelled, and the migration rate is reduced (ca. -25% for d_{50} = 450 μm compared to 345 μm). The range in predicted bed evolution about that obtained with d_{50} = 345 μm (solid line) is represented by a shaded area in Figure 3.21.

Separately, a larger d_{90} (all other things being the same) means a smaller threshold velocity, hence more frequent stirring of the seabed sediment, and higher transport rates. Using a d_{90} 10 times larger than estimated from recent bed samples gave U_{cr} values approximately 20% lower than with the original d_{90}, and a migration rate increased by ca. 20%.

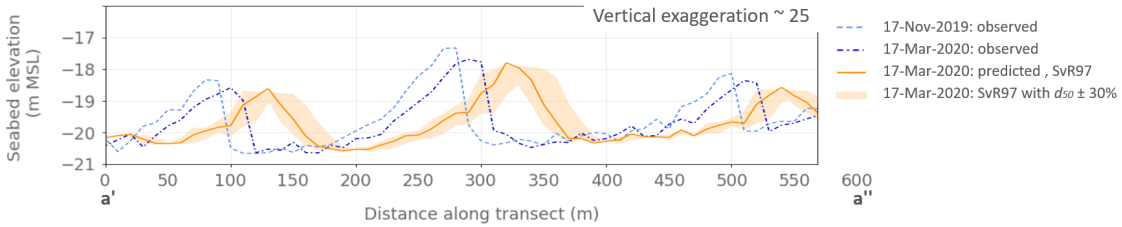

Figure 3.21: Influence of sediment grain size on bed evolution with the SvR97 predictor

Influence of slope effect correction

When the seabed has a slope, the bed shear-stress required to transport sediment grains is affected by gravity. This effect varies depending on whether the flow is uphill or downhill (Soulsby, 1997) and influences both the magnitude and the direction of bedload transport. The transport rate can be corrected accordingly.

The correction proposed by Koch and Flokstra (1980) (`FORMULA FOR SLOPE EFFECT = 1`, Equation 3.18) directly modifies the magnitude of the bedload transport rate to account for the streamwise bed slope effect. Unlike other corrections, it does not modify the critical shear-stress, making it the only slope effect parameterisation in GAIA that is consistent with the use of the SvR97 sediment transport predictor. The direction of transport is also modified by the van Bendegon relation, for which Koch and Flokstra (1980) have devised a specific sediment shape function dependent on the dimensionless shear stress (`FORMULA FOR DEVIATION = 1`, not detailed here).

$$\|\vec{q}_t\| = \|\vec{q}_t\| \left[1 - b \left(\frac{\partial z_b}{\partial x} \cos\theta + \frac{\partial z_b}{\partial y} \sin\theta \right) \right] \tag{3.18}$$

where $\vec{q}_t$ is the total transport rate estimated by the SvR97 predictor. The terms $\partial z_b/\partial x$ and $\partial z_b/\partial y$ represent the transverse and longitudinal slopes respectively; θ is angle between the flow direction and the Cartesian coordinate direction $\vec{x}$; and b an empirical factor.

By its form (a 2nd order derivative of the bed elevation), the correction acts as a diffusion term in the bed evolution equation (Eq. 3.13). A simulation run with this correction and the default β value of 1.3 was not satisfactory: the dunes slumped and decayed with time.

Influence of dynamic pressure

Including or not including the dynamic pressure in the simulation has a noticeable but slight effect. It is noteworthy that the run time is halved when only the hydrostatic pressure is considered.

Bed evolution and crest migration

The threshold velocity, U_{cr}, is in the range 0.41 - 0.43 m/s (for the water depth and sediment conditions at the site) and is exceeded between 60% and 69% of the time over the four-month period.

Early runs with SvR97 revealed an overestimation of the dune migration rate. This is consistent with the general experience that the predictor tends to overestimate the sediment transport rate. The steep slopes become too shallow. After an initial phase of migration, the dunes flatten. If we consider only the bedload component in Equation 3.14, the transport rate becomes much lower. This is in line with the observation that suspended load transport accounts for approximately 85% of the total transport in Equation 3.14. There is an indication, over a period of one year, that the dunes are not migrating as much as changing shape (to become more symmetrical).

The performance of sediment transport predictors is known to vary considerably (Part II Section C, van Rijn et al., 2001) and it is generally accepted that estimates of sediment transport rates are valid within a factor of 2 to 5, particularly in coastal environments. In this context, it is legitimate to calibrate the parameters of a predictor to improve its performance when site-specific data are available

(Soulsby, 1997). In our application, a factor of 1/3 was applied to the original total load predictor (dark red lines in Figure 3.22), which agreed surprisingly well with the dune profile observed at the end of 4 months.

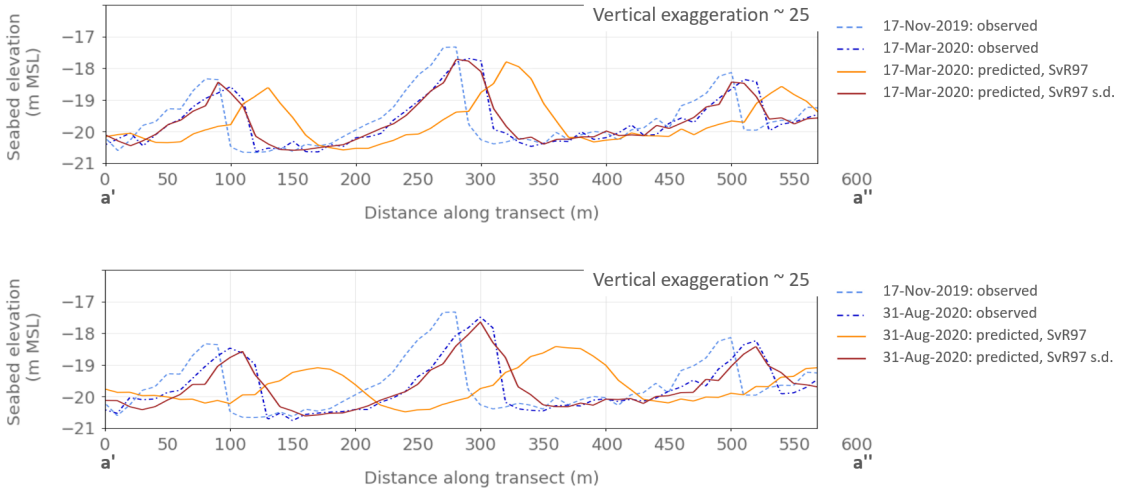

Figure 3.22: Comparison of SvR97 model predictions against observed dune migration for the period S1, 17-Nov-2019 to S2, 17-Mar-2020 (top) and for the period S1 to S4, 31-Aug-2020 (bottom), including results from scaled down (s.d.) transport rates

Of course, there is room for improvement. Lee slopes are not as steep as observed, and the crests tend to hang back compared to the steep face (Figure 3.22). Over time, a tendency was noted for crest heights to lower and for dunes to become more symmetrical in shape (Figure 3.22, bottom). This could be attributed to the form of the SvR97 predictor.

The speed of migration of the central and larger dune crest is plotted in Figure 3.23 as a function of excess velocity $U - U_{cr}$. For this, a spline is fitted to the bed levels predicted by the model to add the resolution lacking from the local model mesh (from 10 m to 1 cm resolution). The crest is taken to be the highest bed level, and its displacement is divided by the model output time step to give an hourly migration speed expressed in cm/day. There seems to be a trend towards a quadratic relationship between crest migration and excess velocity. However, there is significant variability, with a scatter of

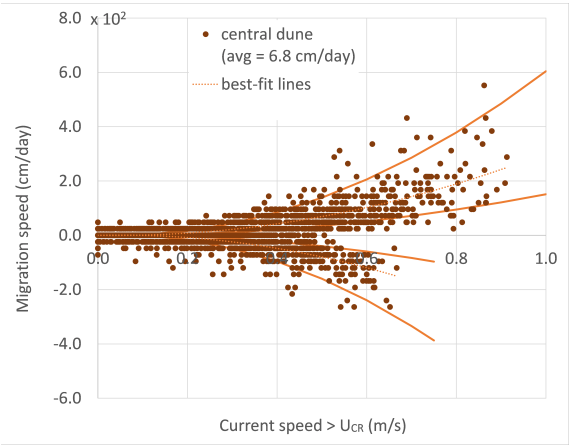

Figure 3.23: Relationship between crest migration speed and excess velocity predicted with the SvR97 (scaled down) predictor, with factor 2 solid lines around the dotted best-fit line

more than a factor of 2 indicated by the solid lines around the dotted best-fit line. Overall, the crest migrates towards the East (the positive values associated with the flood cycle trending East are higher than the negative values associated with the ebb cycle trending West).

The net migration speed is equal to 6.8 cm/day or 25 m/yr over the four-month period between S1 and S2. This is in line with Le Bot's estimate of 37.2 m/yr (Le Bot et al., 2023) considering that the crest tends to hold back (i.e., does not move as fast as the body of the dune) with the SvR97 predictor.

Strengths and weaknesses

With the default model configuration (5 irregularly spaced sigma planes, dt = 5s) and the use of the SvR97 total sediment transport predictor, it takes just over 8 hours to simulate a full year (without using a morphological factor to accelerate the simulation) on 10 cores of an Intel® Xeon® Platinum 8260 processor. This makes the SvR97 predictor highly efficient for our objectives.

Although it may not be immediately intuitive to use depth-averaged flows as predictors for modelling marine dune migration (we expect bedload to be closely related to near-bed processes), empirical evidence suggests the reliability of the SvR97 total load predictor.

It is the foundation of energy-based predictors, such as those proposed by Bagnold (1966) or van Rijn (1984a), that bedload transport rates are directly proportional to the kinetic energy in the flow field. This premise was demonstrated in a different context by Wengrove et al. (2019). In fact, without waves, the SvR97 predictor reduces to van Rijn's parameterisation of his full method (van Rijn, 1984a, 1984b) taking into account the logarithmic scaling of the boundary layer.

The spatial variability of depth-averaged currents is reflected in the spatial variability of the sediment transport rates, with a maximum value above the crest, resulting in the propagation of the dunes without deformation (growth or decay). In a fluvial environment, Lokin et al. (2023) compared the performance of 4 sediment transport predictors with in situ data and concluded that 'a sediment transport model based on mean flow velocity is able to simulate dune propagation'. Our results support this point of view and indicate a correct representation of the migration speed of marine dunes overall, as well as a reasonable prediction of dune shape.

However, it is important to recognise that the ratio of suspended load to bedload contributions (expressed as A_{sb}/A_{ss} in Eq. 3.14) depends solely on the grain size relative to water depth (d_{50}/h) and dimensionless grain size (D_*). In our specific configuration, this ratio significantly favours suspended load, which contradicts the current understanding of marine dune environments (typically bedload-dominated). Consequently, it is advisable to treat the predictor as a total load predictor, avoiding the use of separate terms to differentiate bedload from suspended load.

Additionally, while the dune heights are reasonably predicted, we notice what we describe as a 'softening' of the leading face. This softening manifests itself as a shallower angle of inclination. This effect is identified as a limitation of the SvR97 predictor when compared to alternatives like the SD05 predictor. Over time, this tendency towards more symmetrical dune shapes becomes more pronounced.

3.7.6 Evaluation of the SD05 bedload predictor

The same simulations were performed with the SD05 sediment transport predictor to identify its sensitivities to parameters such as temporal and spatial resolution, vertical discretisation, friction, sediment grain size, slope effect, and consideration of dynamic pressure. Some conclusions from these simulations are presented hereafter.

Influence of vertical plane distribution

The SD05 predictor is expressed in terms of bed shear-stresses. In TELEMAC-3D, the shear-velocity, hence the shear-stress, is computed from the flow velocity at the second plane (with the first plane coinciding with the seabed) under the assumption that the vertical profile close to the seabed is

logarithmic. If that assumption held true, then the distribution of the vertical planes in a 3D model would not be an issue: the velocity at any position in the water column would give the (same) near-bed shear-velocity. Goll et al. (2011) have shown that this was not the case over dunes. Therefore, some attention was paid to the computation of the grain bed shear-stress, and to the vertical discretisation.

Alternative methods were explored to compute the shear-velocity: based on a Chézy coefficient, assuming different profiles, or calculated from the velocity at a reference level (akin to van Rijn (2007) approach). None of these alternatives proved entirely satisfactory, so the original shear-velocity formulation was retained. Several tests with different vertical distributions were then carried out: (i) a limited number of 5 planes carefully selected at 0%, 0.3%, 2.3% 15% and 100% of the water column (this meant a near-bed resolution of about 5 cm); (ii) 5 planes; (iii) 11 planes; and (iv) 16 planes distributed logarithmically with a growth ratio of 1.3 (as was done for SvR97).

As expected, the bed shear-stresses predicted by the model, and the resulting bed evolution, are found to be quite sensitive to the vertical plane distribution. The more planes in the vertical from (ii) to (iv) (hence the finer the near-bed resolution, from approximately 3 m to 40 cm to 11 cm), the more the dunes move as a whole. With 5 planes (ii), only the lower section of the dunes moves. A drawback of finer near-bed resolution, however, is that the crests tend to be exaggerated and the troughs eroded. This is illustrated in Figure 3.24, where the envelop of the bed evolutions predicted using log-distributed planes (ii), (iii) or (iv) is represented as a shaded area.

The refined 5-plane distribution (i) seems like a good compromise (solid line in Figure 3.24): it captures the bed evolution as well as (iv) (arguably closer to observations near the crest, albeit further eroding the troughs). Importantly, the run time is approximately halved (1 day and 2 hours with (i) versus 2 days and 8 hours with (iv) to model 121 days).

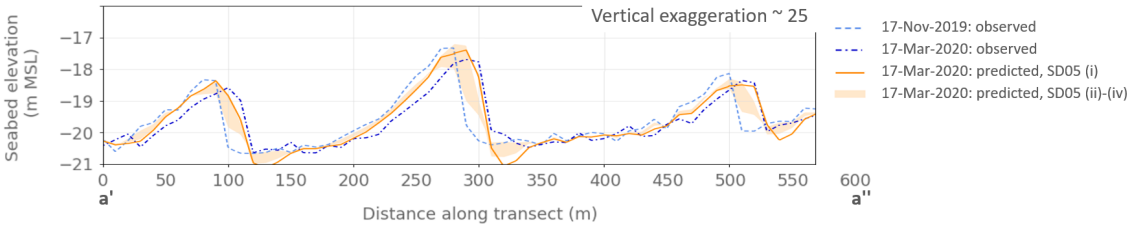

Figure 3.24: Influence of vertical plane distribution on bed evolution with the SD05 predictor

Influence of friction

Simulations with a filtered bed profile and a longer roughness parameter of 0.1 m or 0.2 m to account for bedform drag did not complete and so no conclusions can be drawn as to the influence of friction in the SD05 sediment transport predictor.

Influence of grain size

Bed evolution is shown to be relatively insensitive to grain size with the SD05 sediment transport predictor. Varying the median grain diameter d_{50} in the range ± 30% leads to a ± 10% difference in the transport rate, but the dune migration rate does not change in the same proportions and the effect is hardly noticeable.

Influence of slope effect correction

Without correction for slope effect, the SD05 predictor tends to be unstable: the crests accrete, the troughs erode, and the dunes eventually become too high to be sustainable. Adding the slope effect to the model proved useful for controlling dune growth.

Koch and Flokstra (1980) correction (FORMULA FOR SLOPE EFFECT = 1, Eq. 3.18) was used in the first instance, with default coefficient $b = 1.3$. The results are encouraging in terms of migration rate, dune height, and slopes (Figure 3.25), but the steep face migrates faster than the gentle face, meaning that the dunes become wider over time.

Soulsby's Equation 80a (Soulsby, 1997) (FORMULA FOR SLOPE EFFECT = 2 and FRICTION ANGLE OF THE SEDIMENT = 32°) was subsequently tested. This formulation adjusts the value of the threshold shear-stress τ_{cr} according to the angle between the flow and the slope direction, the angle of the bed slope, and the angle of repose. Deviations from τ_{cr} are the largest on the steep slope (± 14-21% compared to 6-7% on the gentle slope; $\tau_{cr} \sim 0.22$ N/m^2). The steep slopes are better conserved with Soulsby's correction, now close to those observed (Figure 3.25). On the other hand, the dune heights being less dampened than with Koch and Flokstra's correction are high compared to observations.

The formulation by Apsley and Stansby (2008) (FORMULA FOR SLOPE EFFECT = 3), recently integrated into the open**TELEMAC** system, was also tested together with an improved representation of avalanching (SEDIMENT SLIDE = 2, also recently available). This formulation is based on the concept of an effective shear-stress ($\vec{\tau}_{eff}$, Equation 3.19), which includes the down-slope component of the sediment particle weight. The threshold shear-stress is adjusted accordingly (Equation 3.20), in proportion to the gravity component normal to the slope. The correction to the direction of transport is not detailed hereafter.

$$\vec{\tau}_{eff} = \vec{\tau} + \frac{\tau_{cr}}{\tan\phi_r} \sin\beta\vec{b}, \qquad \text{with } \sin\beta\vec{b} = \frac{1}{1+\|\vec{\nabla} z_b\|^2}\left(-\frac{\partial z_b}{\partial x}, -\frac{\partial z_b}{\partial y}\right) \tag{3.19}$$

$$\tau_{eff,cr} = \tau_{cr}\cos\beta = \frac{\tau_{cr}}{\sqrt{1+\|\vec{\nabla} z_b\|^2}} \tag{3.20}$$

where $\vec{\tau}$ is the bed shear-stress used by the SD05 predictor; ϕ_r is the angle of repose of sediment, i.e. the angle at which sediment particles avalanche in the absence of flow; β is the angle made by the sloping bed with the horizontal; and $\vec{b}$ is a unit vector down the line of maximum slope.

The agreement of the predicted dune profile with measured data is generally improved, especially for the last dune in the transect, which now follows quite closely the observed steep face. By and large, the dunes are more forward inclined than they were with Soulsby's correction, where the crests were previously held back; the erosion of the trough is accentuated (Figure 3.25).

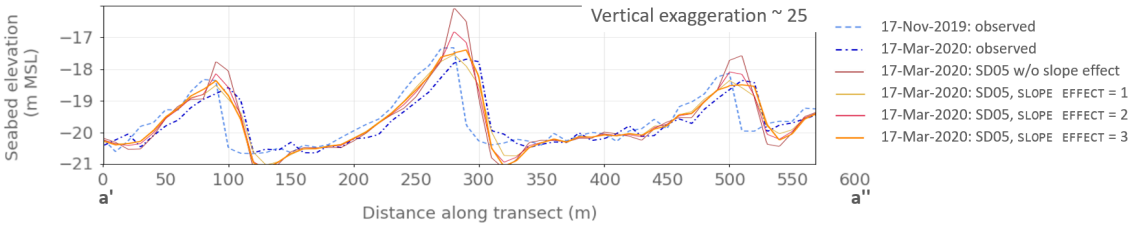

Figure 3.25: Influence of slope effect correction on bed evolution with the SD05 predictor

Influence of dynamic pressure

Dynamic pressure is also critical to the good performance of the SD05 predictor, as illustrated in Figure 3.26. Without it, the dunes hardly move; the crests remain at the same location while the troughs fill in to some extent, resulting in a shallower steep slope than initially or observed at the end of the period. This result is not unrelated to the findings of several authors (for example Hulscher, 1996) that vertical flow structures are an important process to support dune development.

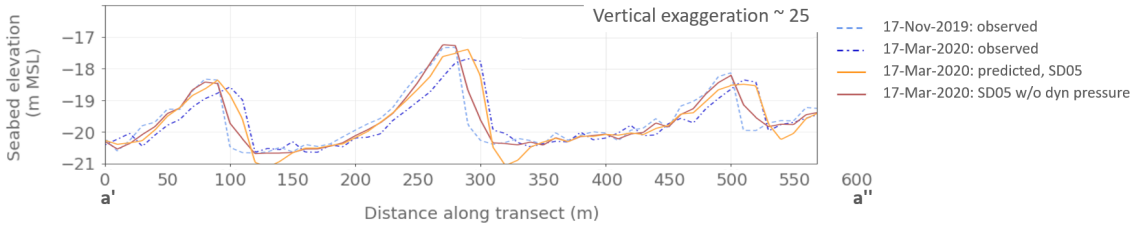

Figure 3.26: Influence of dynamic pressure on bed evolution with the SD05 predictor

Bed evolution and crest migration

The threshold shear-stress τ_{cr} is about 0.22 N/m^2 at the site (uniform in space and time since it depends only on D_*, hence d_{50}). It is exceeded between 42% and 79% of the time over the four-month period (the lower values are associated with the troughs, and the higher values with the more active crests). Good agreement is obtained with this sediment transport predictor at the end of the period (Figure 3.27, top). In particular, the slopes of the dunes are correctly predicted. However, it should be noted that the simulation shows signs of divergence (exacerbation of crests and troughs) and that, over a longer period (S1, 17-Nov-2019 to S4, 31-Aug-2020, (Figure 3.27, bottom), the agreement with observations is not as satisfactory as that obtained after 4 months.

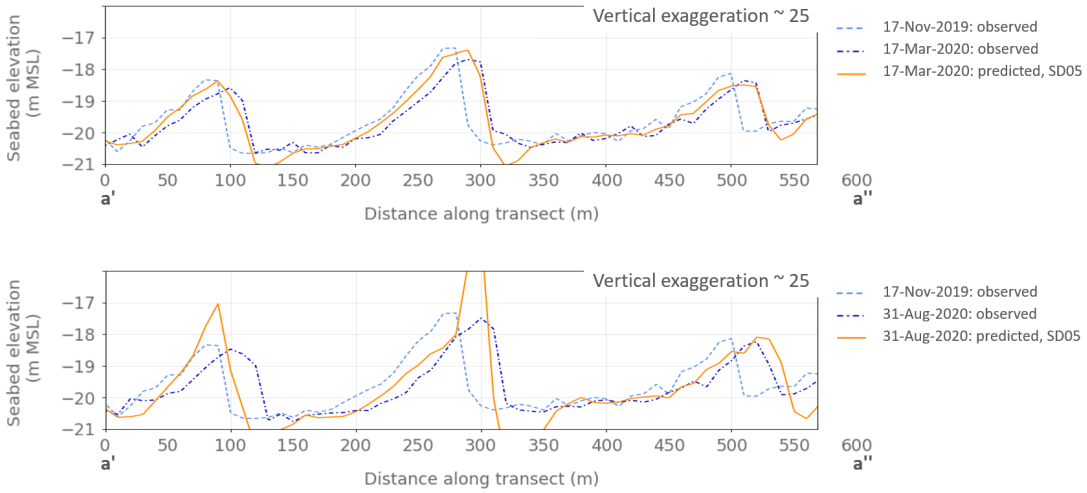

Figure 3.27: Comparison of SD05 model predictions against observed dune migration for the period S1, 17-Nov-2019 to S2, 17-Mar-2020 (top) and for the period S1 to S4, 31-Aug-2020 (bottom)

The speed of migration of the central dune crest is plotted in Figure 3.28 as a function of excess shear-stress. The correlation is less clear than it was for the SvR97 predictor: there is quite some spread in the data. The net migration speed is 8.7 cm/day or 32.0 m/yr over the four-month period. This is comparable to Le Bot's estimate of 37.2 m/yr (Le Bot et al., 2023) and ties in with the observations that the SD05 predictor is able to closely predict the dune morphology (in particular the slopes).

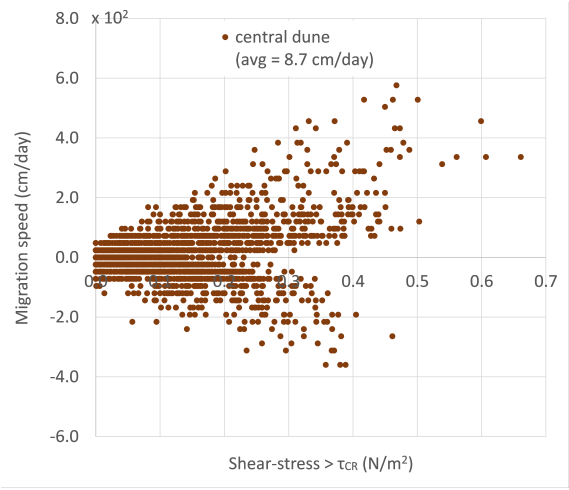

Figure 3.28: Relationship between crest migration speed and excess shear-stress predicted with the SD05 predictor

Strengths and weaknesses

With the default model configuration ((i) vertical discretisation, dt = 1s, slope effect correction) and the use of the SD05 bedload sediment transport predictor, one year does not run to completion on 10 cores of an Intel® Xeon® Platinum 8260 processor with a 3-day wall-time restriction (without morphological factor). The simulation is stopped after 338 days. This makes the SD05 predictor computer-intensive (which we attribute to the computation of the hydrodynamics rather than to the predictor itself).

Sediment transport predictors heavily rely on expressions that include bed shear-stress. Their appeal lies in the fact that bed shear-stress is a physical parameter that represents the frictional force exerted on unit area of seabed by the current flowing over it. Notably, this formalism is able to replicate the morphology of the dunes (including asymmetry and steep fronts), as demonstrated in preliminary tests using predictors like those proposed by E. W. Bijker (1968) and Engelund and Hansen (1967), as well as findings reported in earlier sections.

These predictors are understandably sensitive to the definition of bed shear-stress, which is not universal. Different approaches exist, based on depth-averaged velocity or near-bed velocity, and assuming various velocity profiles (such as the Law of the Wall, relying on a logarithmic profile). Our investigations revealed significant differences in bed shear-stress estimates, hence sediment transport rates.

In TELEMAC-3D, bed shear-stress is calculated assuming a logarithmic profile between the seabed and the first mesh plane along the vertical axis. However, Goll (2016) cautioned that this log profile does not hold well in dune environments, particularly in the troughs. Thus, careful consideration is necessary when determining an appropriate vertical distribution.

Separately, this family of predictors is prone to instabilities (e.g., Hudson et al., 2005; Stadler & Utz, 2023). Adopting a finite volume scheme to solve the Exner equation (Eq. 3.13) was overly diffusive and compromised the edge τ-based predictors in replicating the dune morphology. Recent developments in GAIA to introduce a mixed approach (Stadler & Utz, 2023) did not help either. These oscillations presently make the predictors less reliable over periods longer than a few months, even when accounting for all relevant physical processes.

3.7.7 Calibration of the morphodynamics

These findings were transferred to the large-area morphodynamic model. The model is calibrated by comparing its predictions after 4 months with bed levels extracted in tile #1 from the 2nd bathymetric survey S2 along section a'-a" (see Figure 3.18 for location). The model is validated by comparing its

predictions to a greater spatial extent than that of the transect: in bathymetric survey tile #1 and tile #3. Its performance is also assessed for longer time scales of the order of one year (up to S5).

In line with earlier results, the original SvR97 predictor tends to overestimate the speed of dune migration in the large-area model. To address this, we had introduced a scaling factor during the flume configuration tests. There could be an argument for this scaling factor to vary spatially to take into account the range of hydrodynamic processes experienced over the relatively large extent of the model. However, as a first approximation, the factor remained constant in space. No attempt was made to fine-tune it. Values of 1 (default), 1/3 (obtained by Durand et al., 2023b), and 1/4 were tested to calibrate the morphodynamic model. The migration of the dune profile observed along section a'-a" is satisfactorily reproduced with a scaling factor equal to 1/4. We emphasise that this scaling factor should be treated as a calibration parameter, and by no means as a correction to the original predictor that would be applicable everywhere.

Figure 3.29 presents the results of the calibration. In this figure, the initial bed profile surveyed on 17-Nov-2019 (S1) along section a'-a" is represented by a dashed black line, and that surveyed on 17-Mar-2020 (S2) by a dashed orange line. The bed profile predicted by the model is shown as a solid orange line. During this four-month period, the dunes migrate eastwards (to the right) by approximately 15 m. Their aspect is largely unchanged in the surveys. The model can reproduce the dune height and migration speed satisfactorily. The agreement between predictions and observations is quantified along the length of the transect in terms of bias = 0.01 m, RMSE = 0.23 m, Anomaly Correlation Coefficient (ACC) = 95% and Brier Skill Score (BSS) = 0.89. These metrics confirm the good performance of the model along section a'-a".

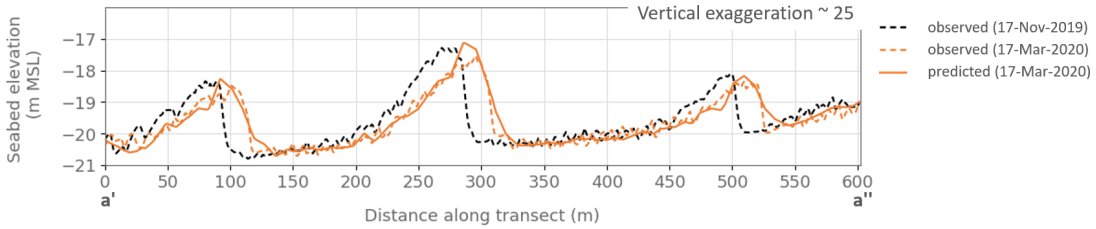

Figure 3.29: Comparison of coastal area model predictions against observed bed profile extracted along section a'-a", in tile #1, after 4 months (S2, 17-Mar-2020). The predominant flow direction is from left to right

However, the predicted shape of the dunes could be improved. Figure 3.29 clearly shows that the steep slopes are shallower in the model than in the observations, and that the crests tend to remain further back rather than dipping forward, resulting in a more symmetrical shape in the model than observed in situ. A formalism based on shear-stresses is likely to reproduce the morphology of the dune more closely (Durand et al., 2023b, and earlier sections). Unfortunately, using such a predictor (for example Soulsby & Damgaard, 2005) is impractical for large-scale applications since it is prone to instabilities (Hudson et al., 2005; Stadler & Utz, 2023). Despite our efforts, various strategies - including time-discretisation, vertical and horizontal space-discretisation, mesh aspect, numerical schemes, and stabilising physical processes such as slope effect and avalanching - did not yield successful results. Although promising, the use of the SD05 predictor was abandoned.

The performance of the morphodynamic model is validated in tile #1 (Figure 3.30) and in tile #3 (Figure 3.31). The evolution patterns of the marine dunes are closely predicted, including the slower dynamics observed in tile #3 compared with tile #1. The footprint of the changes is larger, to some extent, in the model than in the observations. This is attributed in part to the resolution of the model, but also to the softening of the steep slopes already observed in Figure 3.29.

Small secondary bedforms are present in both tile #1 (lower diagonal in Figure 3.30(a)) and tile #3 (between dunes in Figure 3.31(a)). The dimensions of these sedimentary bedforms (heights of 0.2-0.6 m

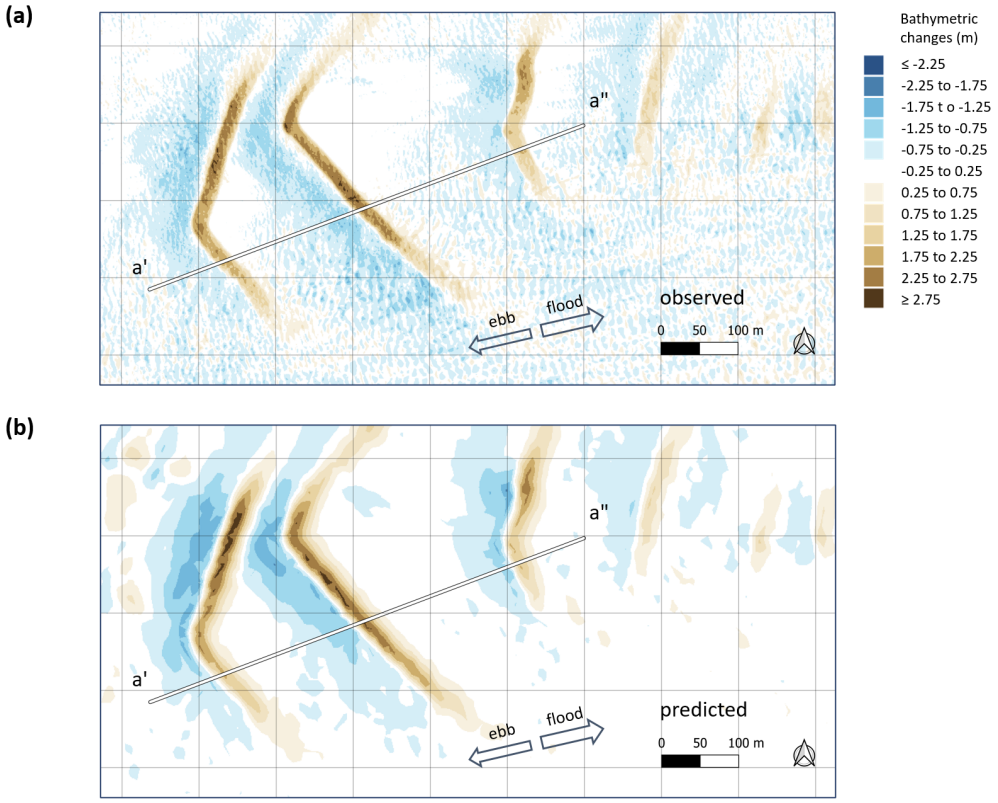

Figure 3.30: Comparison of model against observed bathymetric changes, calculated as the difference between final seabed levels (S2, 17-Mar-2020) and initial seabed levels (S1, 17-Nov-2019) in tile #1

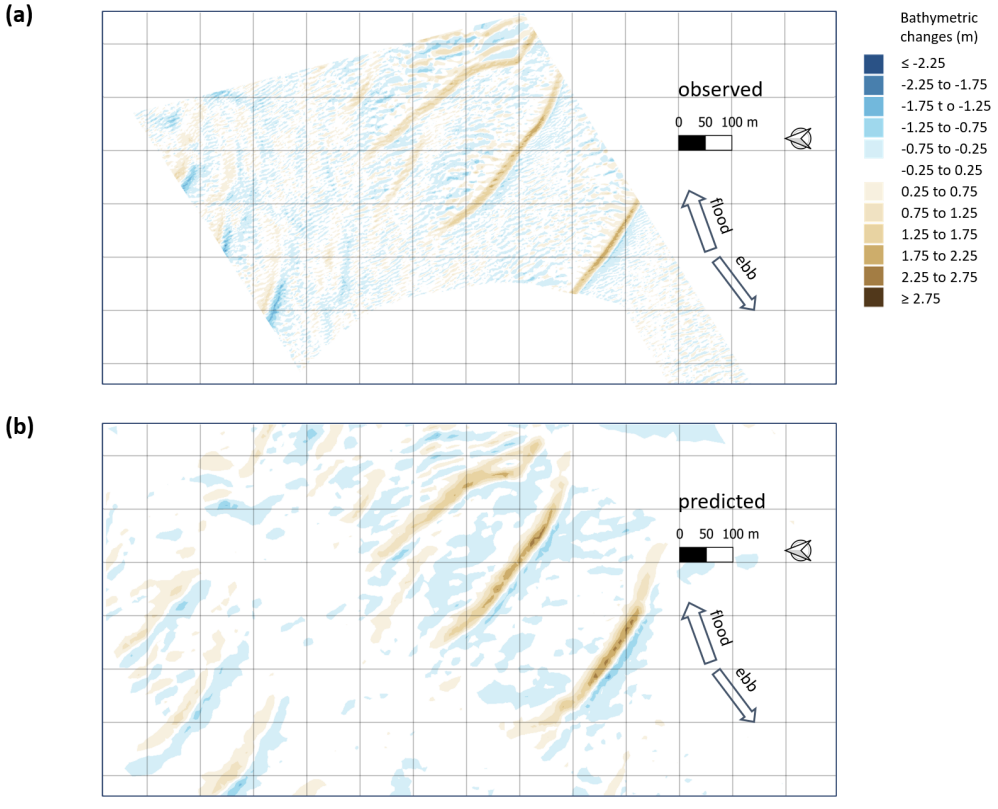

Figure 3.31: Comparison of model against observed bathymetric changes, calculated as the difference between final seabed levels (S2, 17-Mar-2020) and initial seabed levels (S1, 17-Nov-2019) in tile #3

and lengths of 5-10 m) do not allow them to be adequately resolved in our model, resulting in an apparent absence of movement in these regions. We do not interpret this result as a reflection of the model skill but rather of the model spatial resolution.

The seabed had also been surveyed in tile #2, immediately to the north of the Breedt sandbank (Figure 2.10). Tile #2 is extremely complex, in part due to the configuration of the dunes there (sinuous with multiple bifurcations) and in part due to the area being so dynamic that integration in the numerical model of these recent bathymetric data with older data sets is hazardous at best (seabed level differences at the interface between 2 and 4 m). For this reason, it was not considered in this work.

3.8 Closing remarks

We have developed a coastal area model with the complex process-based open**TELEMAC** system to study the dynamics of large marine dunes offshore Dunkirk.

The 3D hydrodynamic and wave models were rigorously calibrated and validated using in situ data for sea levels, currents, and waves. They demonstrated 'excellent' performance across a range of tidal currents and offshore wave and wind conditions, according to the classification scheme by Sutherland et al. (2004). These successful comparisons give confidence in the capabilities of the model to accurately simulate the hydrodynamics of the region, which is essential for future morphodynamic simulations.

Following from the hydrodynamic calibration exercise, a Nikuradse roughness was adopted to represent skin friction, guided by recent sediment samples. Turbulent diffusion is defined with a constant eddy viscosity (taken as 10^{-6} m^2/s) in the horizontal direction, and by the Tsanis mixing length model along the vertical direction.

Following from the wave calibration exercise, we retained the default methods and parameter values for wind generation and wave dissipation processes. Tidal modulations are best accounted for when limiting the wave spectra using a Phillips (1977) shape.

Calibrated numerical models can be used to overcome the spatial and temporal constraints of field observations. Therefore, the coupled hydrodynamic and wave models were run for a two-year period. The results served to determine controlling hydrodynamic processes, suggesting that sediments are predominantly mobilised by strong tidal currents in our areas of interest (depths > 15 mMSL). The results were also used to inform the controlling sediment transport processes. Sediment transport occurs primarily by bedload, consistent with the presence of marine dunes in the region.

This site analysis based on oceanographic considerations enables us to adopt simplifying modelling assumptions. Waves being a secondary process, we exclude their effects. Instead, GAIA is internally coupled with TELEMAC-3D alone to provide the hydrodynamic conditions that drive the sediment transport processes. The suspended load is not explicitly accounted for in this model.

We developed a simplified flume-like model of tile #1 to evaluate the behaviour of two sediment transport predictors pertinent to coastal settings, one based on velocities and the other on bed shear-stresses; and to identify their sensitivities and optimal parameters to replicate in situ data.

The Soulsby and van Rijn (SvR97) predictor stands out for its simplicity, robustness, and efficiency. The predictor is sensitive to grain size. Attempts to integrate the slope effect were seen to cause dune decay, which is not a desirable outcome. Despite some limitations in the SvR97 approach, we found that it is able to model the seabed evolution satisfactorily after applying a scaling factor. The stability and robustness of this predictor make it particularly well-suited for modelling extended time periods.

On the other hand, the Soulsby and Damgaard (SD05) predictor is a promising predictor that accurately reflects the morphology of the dune once an adequate vertical plane distribution is adopted. We found that dynamic pressure is crucial to the good performance of the predictor. However, it tends to

exaggerate the elevations of the dune crests and troughs. This makes the model liable to instabilities over long periods, although correcting for the slope effect does help. The SD05 predictor is therefore better suited for shorter time periods, where an accurate representation of dune morphology is important.

These findings were transferred to the large area TELEMAC-3D+GAIA model to consider 3D effects on large-scale morphological processes. A good representation of the evolution of the dunes was obtained with the SvR97 predictor across the computational domain.

This comprehensive coastal area model can now be used as a research tool to better understand marine dune dynamics in the Dunkirk area and their interaction with OWF elements.

Chapter 4

Modelling marine dune dynamics in a shallow shelf sea: influence of hydro-meteorological conditions

4.1 Introduction

Large dynamic sedimentary bedforms are common on the seabed of shallow shelf seas around the world. The North Sea is one of the better studied shelf seas (Besio et al., 2004; Games & Gordon, 2014; Terwindt, 1971), but these bedforms have also been documented in the Irish Sea (Creane et al., 2022; van Landeghem et al., 2009), the Bisanseto Sea in Japan (Katoh et al., 1998), the Taiwan Strait (Zhou et al., 2020), the Banks Strait north of Australia (Auguste et al., 2021), or south of Martha's Vineyard in Massachusetts (Pessanha et al., 2023) to name but a few. They are sometimes referred to in the literature as sand waves. We call them large marine dunes according to Ashley (1990)'s classification, reproduced in Table 1.1, and in opposition to fluvial or even aeolian dunes (Courrech du Pont et al., 2024). Large marine dunes are present in areas where many European offshore wind farms are currently located, or are planned to be located (`https://map.4coffshore.com/offshorewind/`). Constantly reshaped by flow, they present a challenge for the design (Whitehouse et al., 2000), implementation (Barrie & Conway, 2014), safety and maintenance (Games & Gordon, 2014; Langhorne, 1977; Németh et al., 2003) of marine renewable energy systems. Therefore, it is essential to understand the controlling environmental parameters and to predict the large-scale evolution and migration of marine dunes.

Large marine dunes develop almost exclusively on sandy seabeds (Besio et al., 2003; R. Bijker et al., 1998; Hulscher & van den Brink, 2001; Terwindt, 1971), where near-bed currents are sufficiently strong to entrain, transport and deposit sediment particles. They form and grow as a result of tidal movements (Hulscher, 1996) in conjunction with the composition and availability of sediments and local topography. They migrate as a result of tidal asymmetry and/or a residual flow (Fredsøe & Deigaard, 1992; Németh et al., 2002; van Gerwen et al., 2018).

The role of residual flows in the formation and evolution of marine dunes has been studied numerically using idealised models for the most part. Németh et al. (2002) developed the linear stability model of Hulscher (1996) to explore two mechanisms capable of generating a residual flow: wind, and pressure gradient. They found that, for an equivalent residual flow (0.1 m/s in their Figure 3), a higher migration speed was obtained from a pressure gradient than from a surface wind stress. They suggested that

This chapter is based on the following journal article:

Durand, N., Tassi, P., Blanpain, O., & Lefebvre, A. (2024). Meteorological Conditions Influence the Migration of a Marine Dune Field in the Southern North Sea. *Accepted for publication in Journal of Geophysical Research - Earth Surface*

The Appendix and Supporting Information have been omitted as they pertain to elements discussed in Chapter 3.

tidal asymmetry due to higher harmonics would also trigger dune movement, but to a lesser extent. Besio et al. (2004) superimposed a steady current on a tidal current, considering only the M2 and M4 tidal constituents. They showed that the direction of movement of the marine dunes was controlled by the relative strength of the two components of the current and by the phase difference between the tidal constituents. In this respect, it could differ from the direction of the steady current. van Gerwen et al. (2018) adopted the idealised two-dimensional, vertical (2DV) model developed by Borsje et al. (2013, 2014) to study the growth of marine dunes towards equilibrium. They found that the bedforms are shaped by residual flows and travel in their direction. Stronger residual flows resulted in higher migration speeds and lower equilibrium dune heights.

Campmans and co-authors specifically studied the influence of wind (and wave) climate(s) on the evolution of marine dunes using linear and non-linear idealised models. They identified that even a small proportion of storms in the year had a noticeable impact (Campmans et al., 2018a) and that the seasonal variability of the climate was reflected in the seasonal variability of dune dynamics. Migration speeds tend to be higher (and growth rates lower) during the winter months than during the rest of the year (Campmans et al., 2018b). With a lookup table approach, they further estimated that average wind and wave conditions accounted for 2/3 of the migration, while extreme wind and wave conditions made a modest contribution. More recently, Overes et al. (2024) have investigated the role of time-varying, non-tidal currents in a process-based 2DV model and concluded that these types of currents can substantially increase sediment erosion and accretion patterns, used as an indicator of dune migration. These conclusions are corroborated by field observations, which indicate that the long-term migration of dunes is primarily determined by the strength of the residual flow. However, meteorological events directly affect their short-term evolution. Depending on their direction relative to the background currents, wind-induced currents have been shown to deflect (Krewinkel, 2017), increase, slow down (Le Bot & Trentesaux, 2004), or even reverse the effect of tidal currents on dune migration (P. T. Harris, 1989, 1991; Lanckneus & de Moor, 1991).

These numerical studies are insightful but do not represent real-life settings. In nature, marine dune fields are not always regular trains of dunes with linear crests (Figure 4.1). Their morphology and evolution react to spatial and temporal variations in hydrodynamic conditions. For these reasons, attempts have been made in recent years to move away from idealised geometries (e.g., sinusoidal dunes, transects) and schematised forcing (e.g., simplified tidal flow and/or representative winds). Auguste et al. (2021) explored sensitivities of very large marine dunes to environmental parameters in Banks Strait, Australia. Creane et al. (2023) studied sediment transport pathways at Arklow Bank in the Irish Sea. Both used climate reanalysis data to provide realistic wind and wave forcing. Both used a depth-averaged, horizontal (2DH) modelling approach. Krabbendam et al. (2023) and Nnafie et al. (2023) were among the first to use a three-dimensional (3D) modelling approach. They developed local-scale models (3 km × 3 km) of specific dune fields in the southern North Sea to examine their response to background topography and sediment availability. The representation of tidal forcing is still relatively simple (4 constituents) and meteorological forcing is not taken into account. Pessanha et al. (2023) used a hybrid approach, in which a depth-averaged model of a larger area provided flow conditions for a very local 3D model (estimated around 500 m × 500 m, not specified by the authors) off Martha's Vineyard in the USA. The large-area model is driven by sea levels extracted from a regional ocean tide model and by wind and wave conditions derived from in situ observational data.

The modelling of marine dunes in three dimensions is still at an early stage, all the more if the aim is to model the evolution of dunes on a large scale, with input data that accurately simulate the conditions experienced in situ. We have developed and validated a complex process-based 3D model with real(istic) input for an area offshore Dunkirk, in the Southern Bight of the North Sea (Figure 4.1), where large marine dunes are present. Recent metocean and bathymetric data are available. The observations reveal that the dunes behave differently for periods of (approximately) the same duration. Their evolution is irregular over time, which we hypothesise is due to the influence of meteorological forcing on tidal forcing. Therefore, the model is used to explore the link between meteorological contributions and the migration of large marine dunes (for time scales of the order of months and space scales of the order of metres to kilometres).

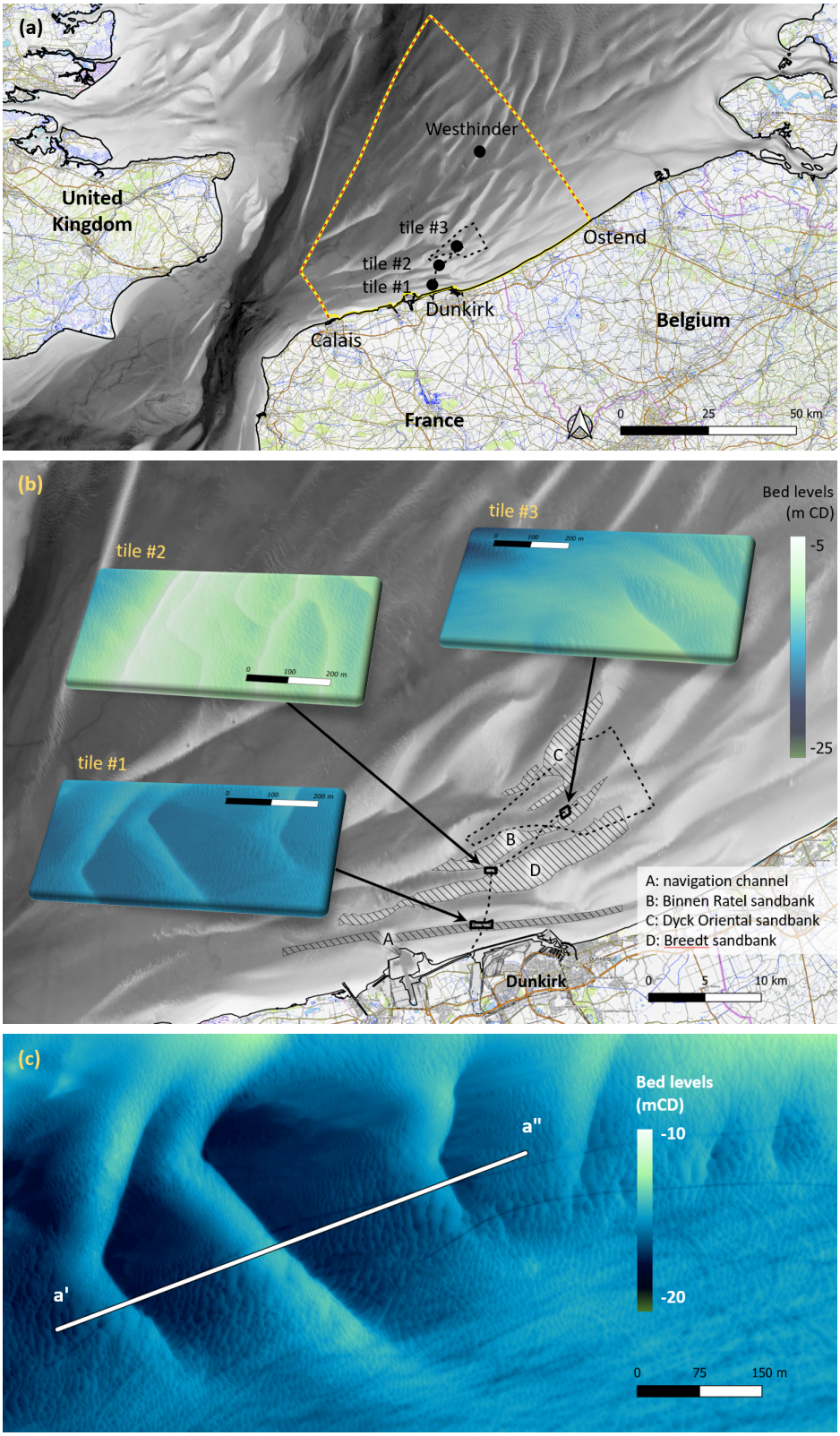

Figure 4.1: (a) General location map. The geographical footprint of the proposed OWF is marked by a dashed black line; the extent of the numerical model is marked by a dashed coloured line. (b) Location of 2019-2021 bathymetric survey tiles in relation to known bathymetric features (Source of the background data: Shom (2015), `https://opentopomap.org/`, and EEA coastline) (c) Close-up view on tile #1 in the navigation channel showing bed levels in November 2019 (Source of the data: (FEM, 2021a)). Dune profiles are extracted along section a'-a"

In the next section, we present the study area in the southern North Sea and the in situ data relevant to this work. A description of the 3D morphodynamic numerical model follows. Simulations are carried out with tidal forcing only, then adding wind and atmospheric pressure contributions. The results of these simulations are presented in Section 4.3 and the implications discussed in Section 4.4. Section 4.5 concludes.

4.2 Study area and methods

4.2.1 Study area and in situ data

Dunkirk is located on the northern coast of France, open to the Southern Bight of the North Sea (Figure 4.1(a)). The region is home to a complex network of large bedforms, ranging from flow-transverse marine dunes to flow-parallel sandbanks. The seabed there is relatively shallow: bed levels shallower than 30 m below Mean Sea Level (MSL) extend as far as ca. 20 km from the coastline. The region is characterised by a semi-diurnal, macro-tidal regime, with a spring tidal range of the order of 5.5 m (Shom, 2020), and flood currents generally stronger than ebb currents.

Metocean surveys

Site-specific meteorological and hydrodynamic campaigns have been conducted in recent years (2016-2022) for the Dunkirk offshore wind farm project and for research purposes. These records complement the information presented by others (for example Latapy, 2020; Tresca, 2013) to qualify the environmental conditions offshore Dunkirk.

Current velocities were measured in September 2016 (Nortek AWAC and AQUADOPP) (Shom, 2017c) and in May-June 2021 (Nortek Signature500, Signature1000 and Vector) (FEM, 2021b). The instruments were mounted on rigid frames and lowered on the seabed, just outside the navigation channel to the port of Dunkirk, and within the footprint of the proposed OWF (Durand et al., 2022b). The Acoustic Doppler Current Profilers (ADCP) were set up to measure the current characteristics throughout the water column, every 50 cm, 1 m or 2 m depending on depth and instrument. Near-surface currents are typically not measured, nor are near-bed currents, due to the configuration of the deployment and the blanking zone of the instrument. This was remedied by using Acoustic Doppler Velocimeters (ADV) positioned close to the seabed. Acoustic Surface Tracking data were collected during the 2021 campaign, concurrently with velocity and pressure data, to derive sea levels.

The flow is aligned with geographical features and topography, trending approximately east-northeast during the flood cycle and west-southwest during the ebb cycle. Current reversal does not occur at high or low tide but 3 to 3.5 hours later, around mean sea level. Peak flood currents are stronger than peak ebb currents in the approach channel to Dunkirk (depth-averaged speed of up to 1.2 m/s vs. 0.8 m/s), resulting in a net current towards the east there. This is in line with current knowledge, on a regional scale, in the southern North Sea. However, the predominance can be reversed locally in favour of ebb currents (Héquette et al., 2008; Vicaire, 1991). This is the case, for example, within the OWF footprint and the sandbank system. Tidal currents are modified by meteorological effects that enhance or abate (even suppress) them depending on the wind direction with respect to the current direction.

The winds offshore Dunkirk have a very distinct seasonality (Guerber et al., 2008). Long-term wind data (1997-2021) measured 10 m above the water surface with a Vaisala anemometer WAA151 and a Vaisala wind vane WAV151 were obtained from the Westhinder platform, located approximately 30 km from the coast (VLIZ, 2022a). The prevailing wind direction is southwesterly, in line with the general atmospheric circulation and the Atlantic pressure fronts moving east. These winds blow parallel to the general orientation of the coastline at Dunkirk, with the flood and against the ebb. However, in spring, there is a high proportion of cold northeasterly winds, fed by high pressure over Scandinavia. These winds blow with the ebb and against the flood. Further analysis of the data shows that gales account for 9.2% of the records. These high wind events (wind speed > 14 m/s, corresponding to Beaufort Scale 7 and above) come mainly from the southwest (50.8%, maximum of 30 m/s), and only marginally from the northeast (4.5%, maximum of 22 m/s).

Bathymetric surveys

Eight bathymetric surveys (S1 to S8) have been carried out between 2019 and 2021 using an R2 Sonic 2024 broadband multibeam echo sounder supplemented by a Trimble BD982/960 GNSS receiver module (positioning system) (FEM, 2021a). The surveys covered three predefined areas selected for the diversity of bedforms encountered: 1) in the approach channel (1000×500 m^2, extended to 1900×500 m^2 for S7 and S8), 2) immediately north of the Breedt sandbank (1000×500 m^2), and 3) on the slopes of the Binnen Ratel sandbank (850×750 m^2). The general location of the bathymetric tiles is shown in Figures 4.1(a) and 4.1(b).

Digital Terrain Models (DTMs) were constructed by the surveyor for each data set at a resolution of 0.5 m (margin of error for position and depth ≈ 0.05 m estimated using the A-priori Multibeam Uncertainty Simulation Tool). The DTMs document the evolution of the dune fields off Dunkirk over successive periods ranging from 1 month to 4.5 months. At times, the morphology of the dunes changes, resulting in an apparent migration of the crest, while at other times the body of the dunes moves as a whole. This is illustrated for tile #1 along section a'-a" in Figure 4.2. There, the dunes are highly mobile during the S1-S2 period (compared with S3-S4 and S6-S7 of similar duration). During this period, the dunes travel about 15 m to the east while retaining their morphology. On the contrary, the steep slopes of the dunes become gentler during periods S2-S3 and S7-S8. Overall, the dunes in tile #1 have been observed to migrate at a net speed reaching 30 m/year (Le Bot et al., 2023). By and large the patterns and rhythms of dune evolution are similar in tile #3, but the dunes are noticeably less mobile.

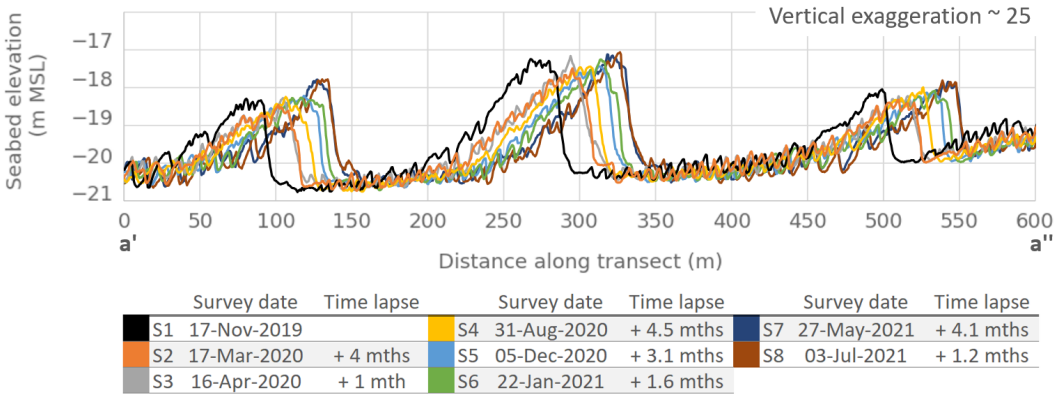

Figure 4.2: Dune profiles along section a'-a" in tile #1 (see Figure 4.1(c) for location), showing the evolution observed in situ between November 2019 and July 2021. Flood currents flow from left to right

A total of 19 bed samples were collected in bathymetric tiles #1 and #2, and in the OWF area, with a Shipek sediment grab sampler on 23 October 2019 and again on 17 May 2020 (FEM, 2020). The samples were analysed by sieving using opening diameters between 63 μm and 12.5 mm. This provides information on the surficial grain size distribution. There is little evidence of spatial or seasonal trends from these limited data. The majority of samples (89%) have a unimodal distribution. The sediments are reasonably well-sorted slightly gravelly and gravelly sands (USCS) with median grain sizes d_{50} between 240 μm and 450 μm. These grain size parameters are in general agreement with the data compiled by the Shom in recent years (Shom, 2017a).

4.2.2 Model set-up and validation

The open**TELEMAC** system (`www.opentelemac.org`) is applied to Dunkirk and its approaches to study the propagation of the marine dune field in response to environmental parameters. To this end, hydrodynamic and morphodynamic models of the area have been developed, independently calibrated and validated, then internally coupled.

The same computational domain and spatial discretisation are used throughout. The domain covers ca. 80 km of coastline, from Calais in the west to Ostend in the east. Its offshore extent varies between ca. 15 km in the west and 75 km in the east (dashed coloured line in Figure 4.1(a)). One of the strengths of the open**TELEMAC** system lies in its use of an unstructured finite element mesh. This allows a spatially variable resolution to be defined, focusing on areas of interest and relaxing the resolution away from these areas. A horizontal mesh size of ca. 10 m is used to represent the bathymetric survey tiles where our aim is to reproduce the evolution of the dune field over time. This spatial resolution was shown to adequately capture variations in the seabed at the scale of marine dunes, while limiting computational cost. Five planes were used in the vertical. Vertical resolution is described in Section 4.2.2 in relation to the choice of the sediment transport predictor. Several seabed maps have been constructed for different modelling purposes, based on the most relevant data available for each time period.

Hydrodynamics

TELEMAC-3D, the 3-dimensional (3D) hydrodynamic module of the open**TELEMAC** system, solves the Navier-Stokes equations without the hydrostatic pressure assumption (Hervouet, 2007) (short module description and governing equations in Section 3.3.1). Bed friction is parameterised with a Nikuradse roughness. Typically, bedform roughness is added to grain roughness to implicitly account for secondary bedforms that large-scale models cannot resolve. However, in this application, secondary bedforms are not present throughout the entire computational domain. Therefore, we only considered skin roughness and adopted a value of $k_s = 2.5 \times d_{50} = 862.5$ μm (Soulsby, 1997), based on a grain size representative of the region. Horizontal and vertical turbulence scales are differentiated in TELEMAC-3D. We adopted a constant kinematic viscosity (10^{-6} m^2/s) in the horizontal direction, and the Tsanis mixing length model in the vertical direction (Tsanis, 1989).

Time-varying tidal sea levels are applied along the open water boundaries of the model from the FES2014 global atlas of ocean tides (Lyard et al., 2021). These astronomical levels are devoid of other influences (e.g., meteorological) and are therefore corrected for the 'inverted barometer' effect caused by variations in atmospheric pressure relative to 1 atm. In addition, spatially and temporally varying wind and atmospheric pressure fields (Bouttier, 2007) are applied over the computational domain to account for this effect as well as set-up and surface currents caused by wind blowing over the water surface.

The calibration and validation of the hydrodynamics is performed in two steps. The first step demonstrates the ability of the model to simulate the astronomical tide. The second step demonstrates the ability of the model to reproduce the non-tidal effects by adding wind and atmospheric pressure contributions (Durand et al., 2022a). For each step, the model predictions are compared over a complete spring-neap tidal cycle with sea levels (calibration) and with depth-averaged currents (validation). In step 1, the model predictions are compared with synthesised data obtained by tidal harmonic analysis (Codiga, 2011) to remove the non-tidal components from the observed records. In step 2, the predictions are directly compared with the measurements. An 'excellent' performance of the model as a whole was obtained according to the classification scheme proposed by Sutherland et al. (2004) (RMAE < 20%) (Durand et al., 2023a).

Prevailing sediment transport mechanisms

Validated numerical models are useful to overcome the spatial and temporal limitations of field observations. Durand et al. (2023a) have produced sediment mobility maps from oceanographic considerations, on the basis of a two-year simulation with this validated hydrodynamic model and a validated wave model of the same area (Durand et al., 2022b). These maps refine our understanding of the dominant sediment transport processes in the region and justify modelling assumptions.

Bedload is identified as the prevailing mechanism of sediment transport based on an analytical indicator, the Rouse number $P = w_s/\kappa u_* > 2.5$ throughout the computational domain (w_s the sediment fall velocity, κ the von Kármán constant, u_* the friction velocity) (Fredsøe & Deigaard, 1992). This is

consistent with the findings of Borsje et al. (2014) and Damen et al. (2018) on the Dutch continental shelf.

Tides are identified as the main driving force overall, and in particular for water depths > 15 mMSL. This analysis uses a classification scheme (Porter-Smith et al., 2004) based on the relative ability of currents and waves, separately, to mobilise sediment from the seabed. The role of waves is however highlighted at the top of the sandbanks, where wave orbital velocities are higher due to shallower water depths.

Sediment transport and bed evolution

GAIA is the morphodynamic module of the open**TELEMAC** system (Tassi et al., 2023) (short module description and governing equations in Section 3.7.1). A unimodal distribution with a median grain diameter of d_{50} = 345 μm, and d_{90} = 1 mm is adopted, in accordance with the uniform bed samples collected in situ in recent years. In the absence of site-specific values, we assume a sediment density of 2650 kg/m^3, an angle of repose of 32°, and a porosity of 40%.

Following the results of the site analysis by Durand et al. (2023a), which indicate that sediments are predominantly mobilised by the strong tidal currents in our areas of interest (depths > 15 mMSL), we omit the contribution of the waves and GAIA is internally coupled with TELEMAC-3D alone to provide the hydrodynamic conditions that drive the sediment transport processes. The suspended load is not treated explicitly by an advection/diffusion equation for sediment concentration in the water column. Bedload fluxes are computed, which participate in the sediment continuity equation (Exner equation) to determine the evolution of seabed levels at each point in the computational domain. We do not apply a morphological acceleration factor in the simulations.

Various formulations of the sediment transport rate have been proposed for sands and the coastal environment (Bailard, 1981; E. W. Bijker, 1968; Dibajnia & Watanabe, 1996; Soulsby, 1997; Soulsby & Damgaard, 2005; van der A et al., 2013; van Rijn, 2007). Several of these predictors have been investigated in a preliminary phase, in a small flume-like representation of tile #1. These tests have shown that the Soulsby-van Rijn total load predictor (hereafter SvR97, Eq. 3.14, based on depth-averaged velocities) is as capable of reproducing the dune migration as a formalism based on shear-stresses. This may be explained by energy arguments. Dune migration is predicted very satisfactorily in tile #1 (Anomaly Correlation Coefficient (ACC) of 95%) when a scaling factor is applied. As the predictor is based on depth-averaged velocities, the number of vertical levels can be relatively small in the model to limit the computational cost. We used five irregularly spaced sigma planes, one for the seabed, one for the water surface, with intermediate planes defined at approximately 1/6th, 1/3rd and 2/3rd of the water column.

The local slope of the seabed can influence both the magnitude and the direction of bedload transport. The transport rate can be corrected accordingly. The correction proposed by Koch and Flokstra (1980) is the only parameterisation in the morphodynamic module GAIA that is consistent with the use of the SvR97 predictor. It modifies directly the bedload transport rate and acts as a diffusion term in the bed evolution equation. Durand et al. (2023b, for a small flume configuration) conclude that taking into account the slope effect is detrimental to the good performance of the model: the dunes subside and decay rapidly over time. We have had the same experience in our coastal area model, and the correction for the local seabed slope is left out in our simulations.

The morphodynamic model is calibrated by comparing its predictions after 4 months with bed levels extracted from the 2nd bathymetric survey S2 along section a'-a" (see Figure 4.1(c) for location). Section 3.7 presents the results of the calibration. The model is validated by comparing its predictions to a greater spatial extent than that of the transect: in bathymetric survey tile #1 and tile #3. Its performance is also assessed for longer time scales of the order of one year (up to S5). While the shape of the dunes tends to become more symmetrical over time in the model, their height and migration speed are reproduced satisfactorily. So are the patterns of evolution, including the slower dynamics observed in tile #3 compared with tile #1.

4.2.3 Simulated scenarios and analysis of results

To determine the role of weather (wind and atmospheric pressure) in the evolution of large marine dunes, we have simulated a one-year period between the first bathymetric survey (S1, 17-Nov-2019) and the fifth survey (S5, 5-Dec-2020). Case I only considers tidal forcing. Weather contributions are added in the form of time- and space-varying wind and atmospheric pressure fields in Case II (validated model configuration). All other model settings are identical between Case I and Case II simulations. The analysis of the results focuses on the four-month period between S1 and S2 (17-Mar-2020), as this is one of the most active periods. We will refer to this period as 'Winter 2020' in the remainder.

To explore specifically how meteorological events from a direction opposite to that of the dominant sediment transport affect dune dynamics, a sustained storm from the northwest was considered. For this, we have simulated the period between bathymetric surveys S4 (31-Aug-2020) and S5 (5-Dec-2020), without (Case III) and with (Case IV) wind and atmospheric pressure contributions. The analysis focuses on the period around the storm: from 25-Sep-2020 6am to 28-Sep-20 9pm (referred to as the 'September 2020 storm' in the following). The storm coincides with a neap tide. A hypothetical case (Case V) was developed, in which the storm coincides with the previous spring tide, by shifting the wind and atmospheric pressure fields 7 days forward compared to Case IV. This simulation was run for a shorter duration, until the end of September 2020.

An overview of the model simulations is presented in Table 4.1.

	Analysis period	**Weather contributions**
Case I	17-Nov-2019 to 17-Mar-2020	No
Case II	17-Nov-2019 to 17-Mar-2020	Wind and atm. pressure
Case III	25-Sep-2020 6am to 28-Sep-2020 9pm	No
Case IV	25-Sep-2020 6am to 28-Sep-2020 9pm	Wind and atm. pressure
Case V	18-Sep-2020 6am to 21-Sep-2020 9pm	Wind and atm. pressure 7 days ahead

Table 4.1: Overview of model simulations

Assessment of residual flow

Bedload transport is approximately proportional to the Shields parameter raised to the power of 3/2 (or the current speed cubed). Therefore, any inequality in the currents results in inequalities in bedload transport. This leads to net sediment transport in the dominant direction, provided the threshold of motion is exceeded. In shallow shelf seas, the tidal wave is distorted due to topographic effects. This process and the interaction between tidal constituents cause an asymmetry of the tidal wave. The flood tends to dominate (faster currents) and the ebb to subordinate (slower currents) (Reynaud & Dalrymple, 2012). This inequality in the ebb and flood currents can be further influenced by other currents such as wind-induced or geostrophic currents.

The peak velocity asymmetry, V_a, is sometimes used as a marker for tidal asymmetry (e.g., Pessanha et al., 2023). Le Bot and Trentesaux (2004) define V_a as the difference between the flood velocity peaks and the ebb velocity peaks and use it, in combination with the strength of wind-driven currents, to explain the types of dune morphology in the Dover Strait. We find this parameter incomplete because it does not take into account the duration of the flood and ebb phases. Albeit faster, the flood is also shorter in duration than the ebb off Dunkirk, and this has an impact on sediment transport rates.

Instead, we use the total residual flow as a marker with which to assess the effect of meteorological conditions on dune migration and we calculate a rolling average of the current velocities over the period of the main tidal cycle (the M2 component in this application) (A. G. Davies & Robins, 2017). Three iterations of a 12-hour boxcar filter are needed since the hourly resolution of the model output does not allow the average to be calculated over an exact tidal cycle (= 12h 25min). Diurnal oscillations are still apparent in the analysis. Although this marker has limitations (such as not accounting for the

non-linearities introduced by a threshold of motion and the power of 3), it serves as a simple indicator based solely on hydrodynamics, without any prior assumptions about the sediment transport predictor.

Assessment of dune migration

The evolution of the seabed over a given period is obtained from in situ observations and model predictions by subtracting the initial DTM from the final DTM, and is represented in the form of a difference map. This map identifies areas of erosion and accretion resulting from the migration of the bedforms. The larger the erosion/accretion footprint, the further a bedform has moved from its initial position.

Although this type of analysis provides information on the direction of migration of the marine dunes, it does not quantify the distance they travel (or their migration speed). Therefore, seabed profiles are extracted along sections a'-a" in tile #1, and along sections b'-b" and c'-c" in tile #3 (see Figure 4.5 for location). These latter transects are selected because they illustrate the variability of dune morphologies and sediment transport patterns on the slopes of the sandbank, towards the top (b'-b") and bottom (c'-c"), where water depths are greater. Section b'-b" is drawn more or less perpendicular to the crest of the large dunes. This was not possible for section c'-c" given the constraints (size and shape) of the bathymetric survey tile (Figure 4.5).

Many authors have quantified the speed of dune migration from the ratio of crest displacement to time (including Le Bot et al., 2023, from these bathymetric survey data). However, changes in the position of the crest may result from changes in dune morphology alone, without migration of the dune as a whole. This is illustrated in Figure 4.2 between surveys S3 and S4 for example. In this context, it may be more appropriate to consider the mid-point of the steep face of the dune, rather than the crest, as a marker of dune migration (Dong, 2015). This is the approach we adopt here. A spline is fitted to the seabed levels predicted by the model to add the resolution lacking from the model mesh (from 10 m to 1 cm resolution). The mid-point is taken to be half-way between the highest and the next lowest seabed levels (Figure 4.3). Its horizontal displacement is divided by the model output time step to obtain an hourly migration speed expressed in m/yr. We have restricted this analysis to the second crescent-shaped dune in tile #1, where it crosses section a'-a".

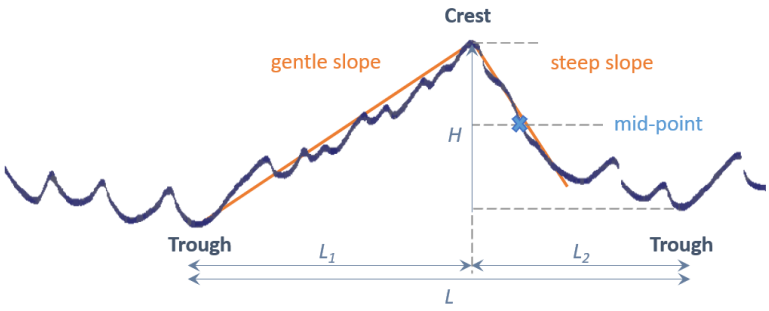

Figure 4.3: Schematic cross-sectional view of a marine dune

4.3 Results

4.3.1 Winter 2020: Cases I and II

Evolution of the seabed

The seabed evolution predicted in tile #1 is depicted in Figure 4.4: in panel (b) for Case I and in panel (c) for Case II. In these maps, shades of blue indicate a lowering of the seabed (erosion), and shades of brown indicate a rising of the seabed (accretion) at the end of the four-month period. The same colour scale is used throughout to enable direct comparisons. A 100 m resolution grid is superimposed on the difference maps to facilitate the georeferencing of seabed features and their evolution. The changes observed in situ during the same period are presented in panel (a) for reference.

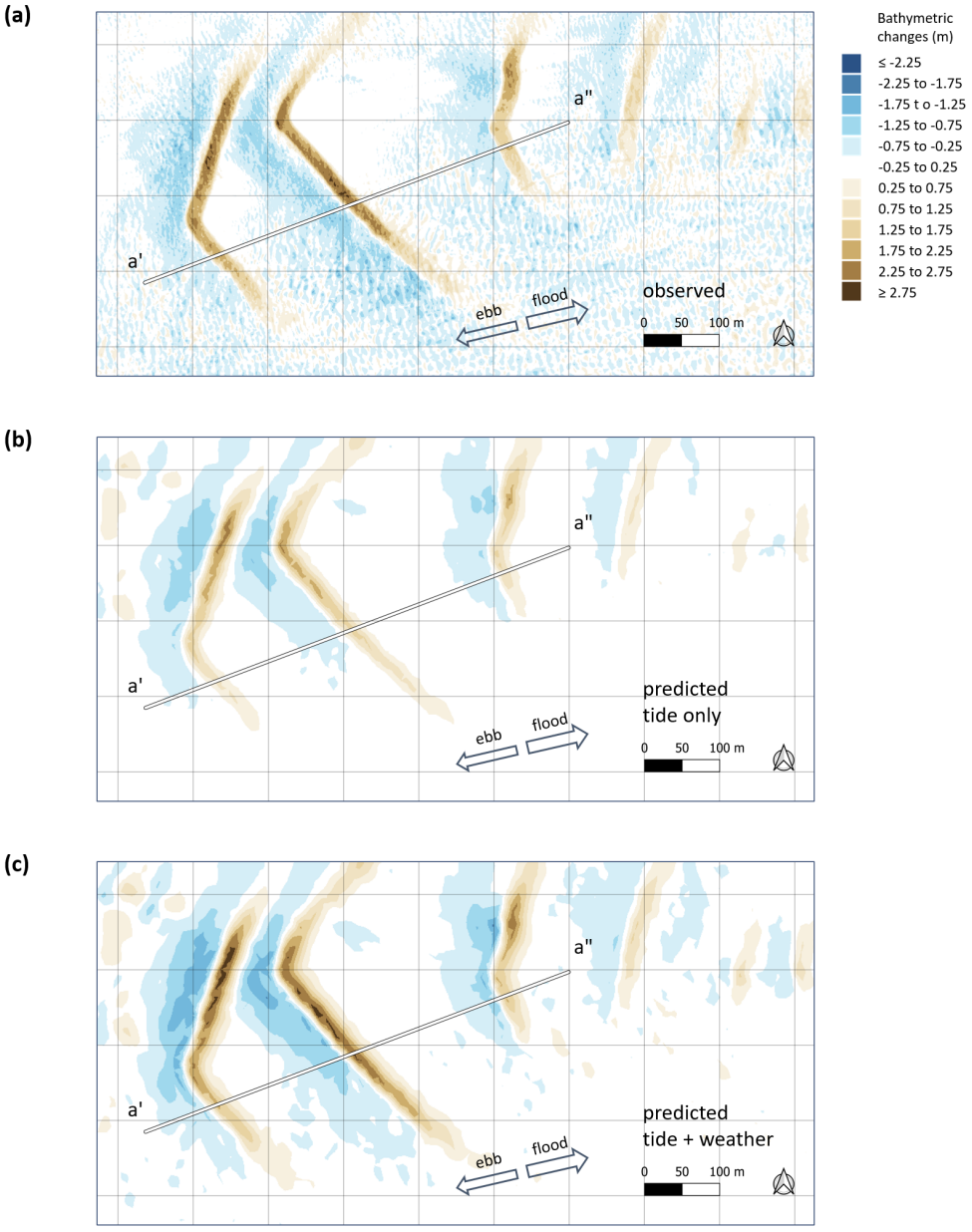

Figure 4.4: (a) Observed bathymetric changes, calculated as the difference between final seabed levels (S2, 17-Mar-2020) and initial seabed levels (S1, 17-Nov-2019) in tile #1. (b) Predicted bathymetric changes for Case I. (c) Predicted bathymetric changes for Case II, for which meteorological contributions are added in the model predictions. Shades of blue indicate lowering of the seabed (erosion) and shades of brown indicate rising (accretion)

The migration of the large dunes is directed to the east, in line with the orientation of the navigation channel. The most significant changes occur to the north of the channel (upper half of the survey tile). A maximum bed level variation of +2.5 m, and a minimum variation of -1.3 m, are predicted for Case I. These variations are associated with the two crescent-shaped dunes and the sinuous dune that follows them, noting that these dunes are also the highest in tile #1 (2 to 3 m in height). The changes are more pronounced for Case II, where a maximum bed level variation of +3.4 m is predicted for the westernmost crescent-shaped dune, and a minimum of -1.9 m for the sinuous dune. Modest changes are predicted in both cases for the smaller dunes further east, which are around 1 m high.

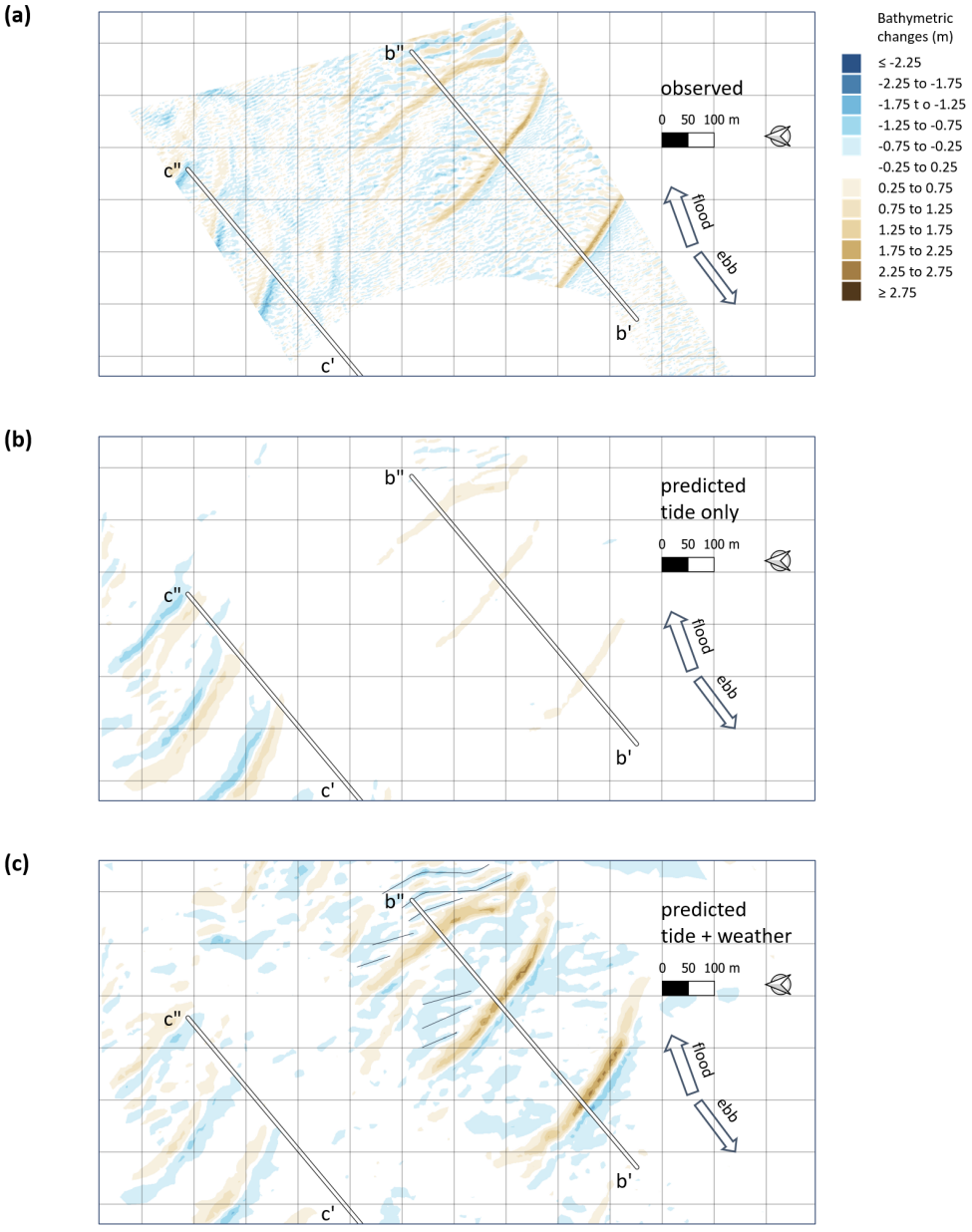

Figure 4.5: (a) Observed bathymetric changes, calculated as the difference between final seabed levels (S2, 17-Mar-2020) and initial seabed levels (S1, 17-Nov-2019) in tile #3. (b) Predicted bathymetric changes for Case I. (c) Predicted bathymetric changes for Case II, for which meteorological contributions are added to the model predictions. The secondary bedforms are identified by dark blue lines around section b'-b". In all figures, blue indicates lowering of the seabed (erosion) and brown indicates rising (accretion). North points to the left

The seabed evolution predicted in tile #3 is depicted in panels (b) and (c) of Figure 4.5 for Cases I and II respectively. The seabed is markedly less mobile than in tile #1. For Case I, most of the changes are predicted to occur at the northern end of the tile, past section c'-c", where the water is deepest. The maximum bed level variation over the four-month period is ± 1.1 m. Remarkably, these dunes migrate to the southwest, as indicated by the brown shades below the blue shades in Figure 4.5(b). This is in agreement with the direction of the local residual flow, which in this simulation is directed to the southwest at the bottom of the Binnen Ratel sandbank, turns about the -21 m MSL isocontour and is directed to the east on the slopes of the sandbank (not shown). This is not in agreement with

the observations (panel (a)). In the remainder of the area, at water depths of less than 21 m, changes in seabed elevation of the order of -0.2/+0.6 m are predicted at most. For Case II, the seabed is more mobile on the slopes of the Binnen Ratel sandbank (water depths shallower than ca. 16 m, top right of the figure) than further down towards the natural channel between the Binnen Ratel sandbank and the Dyck Oriental sandbank (bottom left of the figure). On the slopes, the largest predicted bed level variations after 4 months are -1.9/+2.7 m. They are of the order of -0.5/+0.7 m to the north of the bathymetric survey tile, in the channel. It is interesting to note the moderate changes in seabed elevation predicted by the model between the large dunes. These fluctuations are also observed in the bathymetric survey data (panel (a)) and are attributed to the migration of secondary bedforms at a 20-40° angle to the orientation of the large dunes, identified by dark blue lines in Figure 4.5(c).

The propagation of secondary bedforms (0.2-0.6 m high and 5-10 m long) is apparent in the in situ observations both in tile #1 (lower diagonal in Figure 4.4(a)) and in tile #3 (between dunes in Figure 4.5(a)) whereas model predictions indicate no movement in these regions. This is because these small bedforms are not resolved in the model due to its 10 m horizontal resolution.

As regards the evolution of large marine dunes, Case II predictions agree closely with in situ observations in tile #1 as in tile #3. Although there is a tendency to exaggerate the amount of erosion on the gentle side of the dunes, the order of magnitude of changes in seabed elevation is correctly predicted overall. The footprint of the changes is larger to some extent in the model than in the observations. This is attributed in part to the resolution of the model, but also to the modification of the morphology of the dunes over time, in particular the softening of the steep slopes already noted during the calibration phase (Section 3.7) and illustrated in Figure 4.6.

Dune profiles along predefined sections

If we first examine the dune profile along section a'-a" (tile #1) in Figure 4.6, the height of the dunes remains mostly unchanged after 4 months in the predictions (from black dashed lines to solid orange lines, in panel (a) for Case I as well as in panel (b) for Case II). The model results show that gentle slopes are conserved and steep slopes are softened. The crests stay back instead of dipping forward, resulting in a more symmetrical profile than initially. This effect on the morphology of the dunes is attributed to the predictor chosen for the sediment transport rate (Durand et al., 2023b, in a smaller configuration) and is apparent in both Case I and Case II model predictions. This is not the case in the profiles surveyed (orange dashed line in Figure 4.6) where the leading face retains its steep angle of inclination at the end of the four-month period. The crests predicted for case I have become narrow and sharp (panel (a)), but not for Case II (panel (b)) or the observations (consider, in particular, the last dune of the transect, which is flat-crested).

The dunes travel variable distances for Case I, defined halfway up the steep face: approximately 6.5 m, 10.0 m and 9.0 m starting from the westernmost dune (left). More consistent and longer migration distances are predicted for Case II, with the addition of the meteorological forcing (18.0 m, 20.5 m and 20.0 m starting from the westernmost dune). These values are close to those derived from the survey profiles: approximately 20.0 m for the 3 dunes. This close agreement is further illustrated in Figure 4.6(c) in terms of the anomaly, or the difference between final and initial seabed elevations. It is clear from this figure that the erosion and accretion patterns are correctly predicted along section a'-a" when the meteorological forcing is included in the simulation.

The counterpart of Figure 4.6 for tile #1 is given in Figure 4.7 for tile #3, section b'-b" (panels (a) to (c)) and section c'-c" (panels (d) to (f)). The height of the dunes can be reduced in section b'-b" after 4 months, by approximately 0.25 m for the 2 westernmost dunes and Case I, 0.5 m for the westernmost dune and Case II. Sharp crests and steep slopes are retained for the most part in the model predictions, noting that, in contrast, the leading faces have become steeper in the observations.

Migration distances under 5.0 m are predicted towards the top of the Binnen Ratel sandbank for Case I over the four-month period. Noticeably longer distances are predicted for Case II: 19.0 m, 18.5 m and 22.0 m respectively along section b'-b", exceeding those observed (12.0 m, 13.5 m and 14.0 m) by 5 to 8 metres. Section c'-c" is located on the edge of the mobile bedforms and little movement is shown

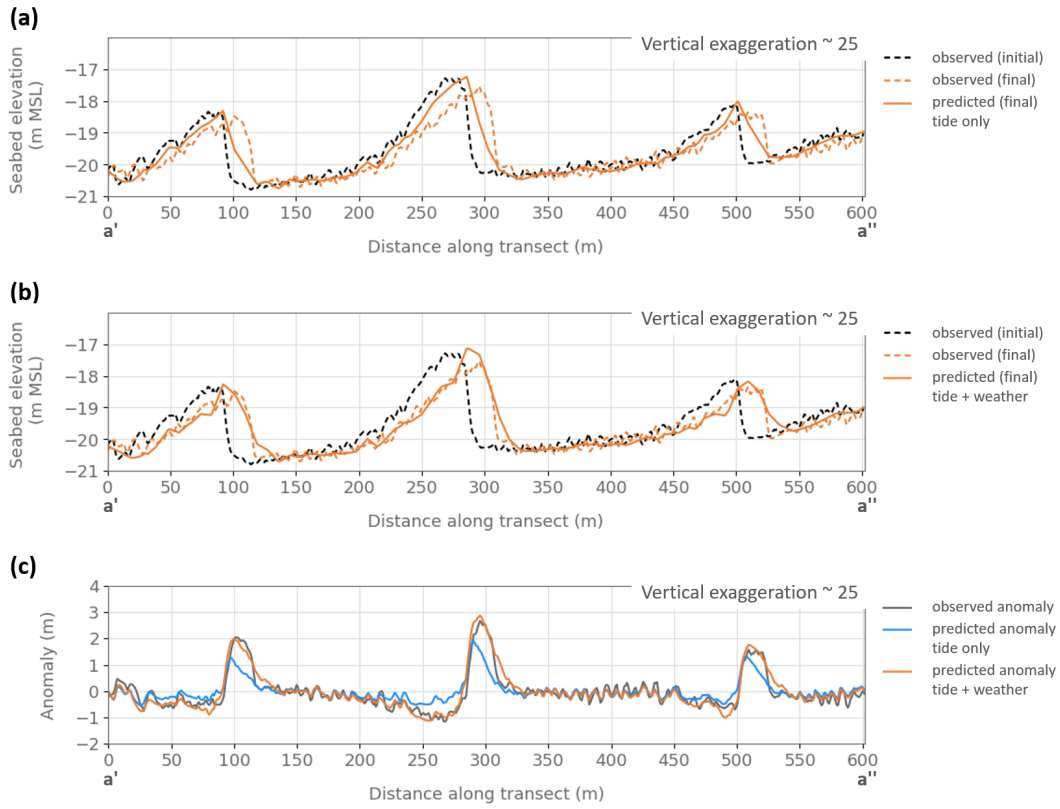

Figure 4.6: Evolution of the dune profile between S1, 17-Nov-2019 (initial) and S2, 17-Mar-2020 (final), extracted in tile #1 along section a'-a" (a) from the survey data and Case I model predictions; (b) from the survey data and Case II model predictions; (c) observed and predicted anomaly, calculated as the difference between the final and initial dune profiles

in the observations as well as in the model predictions. Note that the dunes travel by an estimated distance of -9.0 m, for Case I, with tidal forcing only, in the opposite direction to that observed. This is also shown in panel (f) where the patterns of erosion and accretion are out of sync with observations. The dunes travel in the correct direction for Case II, at the rate of 2.0 m in 4 months. This value is close to that derived from the survey profiles = 2.5 m. The water depth at the base of the dunes is of the order of 20 m below MSL there (as was the case for section a'-a" where equally satisfactory agreement was obtained).

The agreement between predictions and observations is quantified with statistical metrics: bias, Root Mean Square Error (RMSE), Anomaly Correlation Coefficient (ACC) and Brier Skill Score (BSS). The result of this analysis is summarised in Table 4.2 for sections a'-a" and b'-b" (section c'-c" is incomplete and therefore statistics were not computed for it) and confirms that including meteorological (wind) forcing (Case II) improves the skill of the morphodynamic model.

	bias (m)	**RMSE (m)**	**ACC (-)**	**BSS (-)**
section a'-a"				
Case I	0.02	0.37	0.89	0.71
Case II	0.01	0.23	0.95	0.89
section b'-b"				
Case I	-0.04	0.33	0.74	0.46
Case II	-0.01	0.34	0.84	0.41

Table 4.2: Performance of the model predictions against observed data (S1 to S2)

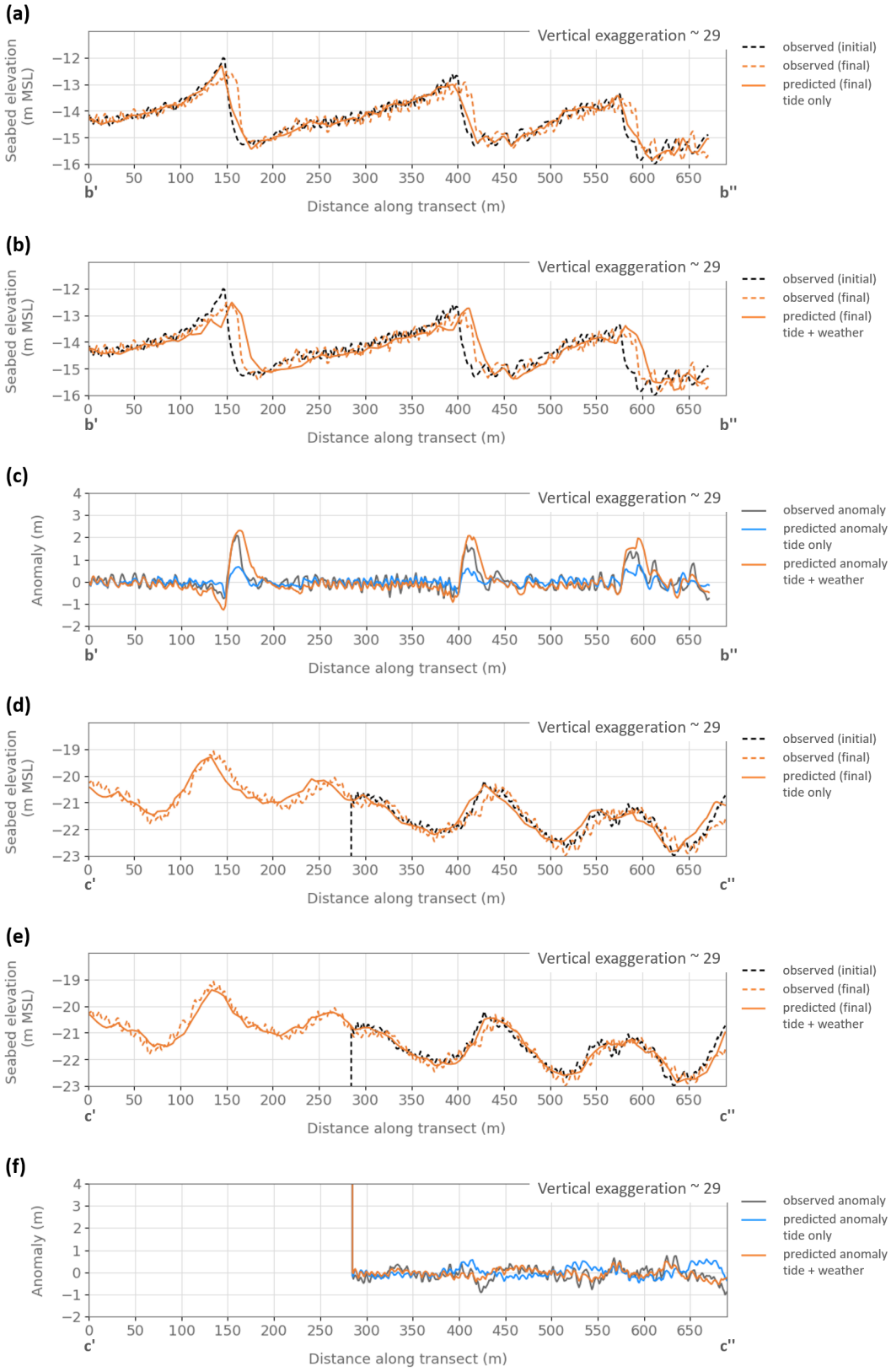

Figure 4.7: Evolution of the dune profile between S1, 17-Nov-2019 (initial) and S2, 17-Mar-2020 (final), extracted in tile #3 along section b'-b" (a) from the survey data and Case I model predictions; (b) from the survey data and Case II model predictions; (c) observed and predicted anomaly, calculated as the difference between the final and initial dune profiles. (d), (e), (f) for section c'-c"

4.3.2 September 2020 storm: Cases III, IV and V

Maps of seabed evolution were not produced, nor were dune profiles extracted along the predefined transects for these simulations (too short a period to show significant change). Instead, we examine residual bedload transport rates to determine the effect of the storm on dune dynamics, focusing on the navigation channel. These are calculated from the instantaneous bedload transport extracted from the model, taking vector averages over the duration of the storm. They are presented in Figure 4.8 for Case III (tide only, panel (a)), Case IV (tide, wind and atmospheric pressure, panel (b)) and Case V (tide, wind and atmospheric pressure brought forward 7 days, panel (c)).

A comparison of the results reveals contrasting characteristics. With tidal forcing alone, residual transport vectors are generally directed eastwards (75°N). They are relatively weak (the storm coincides with a neap cycle), with mean and maximum values of 0.0007 kg/m/s and 0.0026 kg/m/s respectively over the extent of tile #1 (minimum value close to zero). Higher values are predicted to the north of the navigation channel, where the flow is more strongly flood-dominated, than to the south where little sediment transport is expected. Residual transport vectors are an order of magnitude higher when meteorological forcing is added (Case IV), with mean, maximum, and minimum values of 0.008 kg/m/s, 0.017 kg/m/s and 0.002 kg/m/s respectively. In this case, higher values are predicted to the south of the navigation channel, increasing over the dunes and directing sediment transport westwards (260°N).

Tidal currents being stronger for a spring tide than for a neap tide, a significant residual sediment transport is generated for Case V. Mean, maximum, and minimum values of 0.045 kg/m/s, 0.097 kg/m/s and 0.005 kg/m/s are predicted respectively. The residual is again directed westwards to the south of the navigation channel. However, its direction reverses to the north of the channel, where the ebb currents are weaker and insufficient to sustain westward transport.

Not presented here, similar findings extend to tile #3. Residual transport vectors are strong and directed southwestwards at the bottom of the Binnen Ratel sandbank slope, but are weak and generally directed eastwards (70°N) in tile #3 (Case III). Residual transport vectors are stronger, particularly atop the dunes, and consistently directly southwestwards (235°N) for Case IV. They are even stronger for Case V, but turn around on the slopes of the sandbank, in shallower depths, to be directed eastwards, noting that this corresponds to the direction of the smaller secondary bedforms.

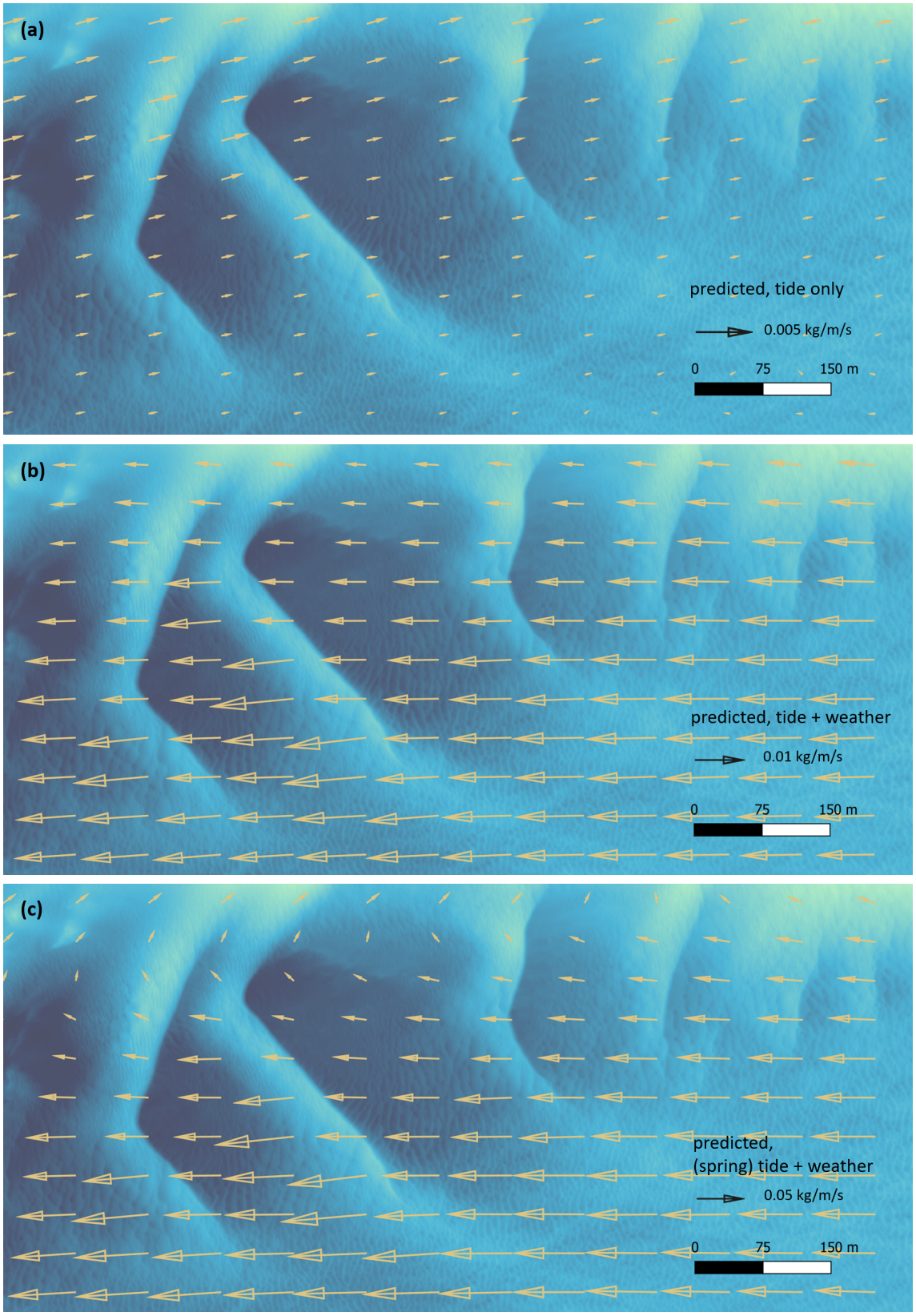

Figure 4.8: Residual sediment transport predicted by the model over the NW storm (25-Sep-20 6am and 28-Sep-20 9pm). (a) Case III: tidal contributions only in the 3D model. (b) Case IV: with actual wind and atmospheric pressure fields (this means that the event coincides with a neap tide). (c) Case V: for a hypothetical scenario in which the wind and atmospheric pressure fields are brought forward to coincide with a spring tide. Vectors are shown on a regular 80 m × 45 m grid for clarity; the scale is different for each panel

4.4 Discussion

In this work, the effect of including weather contributions (actual wind and atmospheric pressure) in morphodynamic simulations was quantified. Total sediment transport was modelled as bedload, and wave processes were not included. These simplifications are justified by a site analysis of environmental conditions in Durand et al. (2023a). The results of the simulations show that, although the tide is an important (and predictable) factor in the sediment dynamics of the region, meteorological events significantly influence these dynamics. A better prediction of marine dune migration is obtained when simulations take into account both tidal and meteorological forcings. Winds blowing in the opposite direction to the predominant sediment transport pathways are capable of reversing them. These results and their implications on large-scale marine dune dynamics are discussed in the following sections. When time histories are presented or figures quoted, they are used to illustrate the argument, and are relevant to the navigation channel to Dunkirk, and a point located near the second crescent-shaped dune in tile #1.

4.4.1 Influence of wind conditions on residual flow

Dune migration is the result of an asymmetry in the flow (Fredsøe & Deigaard, 1992; Németh et al., 2002; van Gerwen et al., 2018). Without it, whatever its origin, marine dunes grow towards their equilibrium height (Hulscher, 1996). There can only be oscillations about a fixed position, but no (net) migration. This is the result obtained, for example, by Campmans et al. (2018a) with simplified representations of tides and waves, based on the M2 constituent and linear wave theory. No movement was predicted as a result of the symmetrical excursions of the tides and waves.

The tide is described by 34 constituents in our model (Section 3.3). This gives a realistic representation of site conditions and, in particular, of the (spatially varying) asymmetry between the flood and the ebb phases. Focusing on the navigation channel to Dunkirk, the flood is predominant there. An eastbound net velocity of the order of 0.04 m/s is calculated when only tidal currents are considered (Cases I and III). This value is slightly low compared with the values van Gerwen et al. (2018) quote from the literature for the southern North Sea but is consistent with those used in idealised models (Besio et al., 2004; Németh et al., 2002; van Gerwen et al., 2018). However, tidal currents alone are insufficient to fully describe the migration of the marine dunes (compare panels (b) with panels (a) in Figures 4.4 and 4.5). It is therefore expected that wind events influence noticeably the total residual flow (net velocity).

As a general rule, wind-induced currents are of the order of 2% of the wind speed near the water surface (Weber, 1983). Their amplitude decreases with depth. On their own, wind-induced currents are too weak to mobilise the sediment on the seabed (consider that a gale force wind of 20 m/s generates a surface current of the order of 0.4 m/s). But superimposed on tidal currents, they can enhance, hinder (or even suppress) them depending on their direction relative to the tide, and on the state of the tide (Figures 4.9(b), (d) and (e)). This directly affects the balance between ebb and flood currents, and therefore the residual flow responsible for sediment transport (P. T. Harris, 1991). In the following, we consider the depth-averaged velocities predicted by the 3D model since this is the input parameter for the SvR97 sediment transport predictor.

Strong positive net velocities (in excess of 0.15 m/s) in the navigation channel are associated with periods of intense southwesterly wind. For example, values of up to 0.32 m/s are predicted on 9 February 2020 (Case II). On this occasion, the wind speed exceeds 20 m/s for more than 12 hours. Southwesterly winds are prevalent during the Winter 2020 period (S1 to S2) (20%, 35% and 19% of records from the S, SW and W sectors, respectively). Only a small proportion comes from the North Sea (8% from the NW and 5% from the N). This is specific to winter winds. Over a year, the directional distribution is less skewed towards the S to W sectors, with a higher proportion of northerly winds (in particular in spring, 14% from the NE). As a result of the predominant southwesterly wind, an average net velocity of 0.07 m/s is calculated over the four-month period between S1 and S2 (Case II), an increase of a factor 1.5 compared with the 0.04 m/s calculated for Case I and tidal forcing alone.

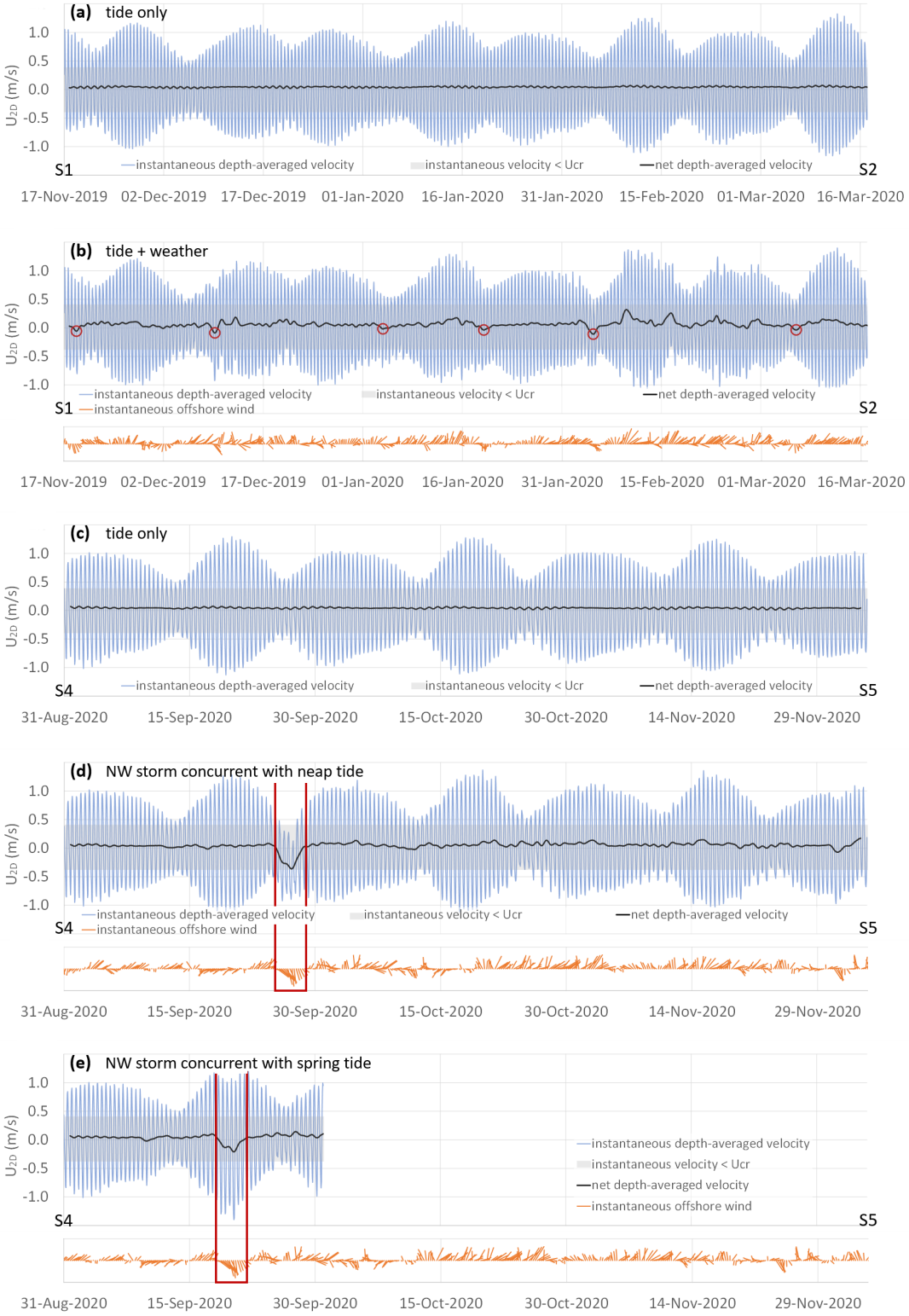

Figure 4.9: Instantaneous depth-averaged velocities predicted by the 3D model in the navigation channel for Case I to V (a) to (e). Positive values are associated with the flood cycle, trending eastwards; negative values with the ebb cycle, trending westwards. The shading encompasses velocities below the threshold of motion: U_{cr} (Equation 3.15). Negative net velocities, marked by dark red circles in panel (b), are directed opposite the prevailing easterly direction. When applicable, the offshore wind is represented by segments whose length and orientation are true to the wind speed and direction at 10 m above sea level

If winds broadly following the flood currents (i.e. propagating from the Channel) enhance the flood-dominated residual flow, winds opposing them (i.e. originating in the North Sea) weaken it. Negative net velocities in the navigation channel occur during periods of northwesterly or northerly winds. They are few during the Winter 2020 period and marked by dark red circles in Figure 4.9(b). But strong winds blew from the northwest (310°N to 360°N) between 25 September 6am and 28 September 9pm (September 2020 storm). Most of the time above 10 m/s, they reached 23 m/s (9 on the Beaufort scale) on 25 September at 6pm. This event was the strongest of the year from this direction. It was associated with an episode of low pressure in the southern North Sea and coincided with a neap tidal cycle. Flood currents were significantly reduced as a result, with peak velocities of 0.13 m/s in the morning of 27 September 2020 (compared with 0.64 m/s for Case III). The residual flow, generally oriented towards the east in the navigation channel, is reversed during this period. This is illustrated in Figures 4.9 (d) and (e), where the September 2020 storm is identified by a dark red rectangle.

4.4.2 Influence of wind conditions on dune migration

The results presented in Section 4.3 demonstrate that wind and atmospheric pressure conditions are crucial to correctly reproduce dune migration in the model. The dynamics of the marine dunes is slower compared to observations with tidal forcing only: in tile #1 by a factor of 2 to 3, and in tile #3 by up to a factor of 4. Importantly, the direction of migration of the dunes can be misrepresented. This is the case, for example, in tile #3, where the dunes in section c'-c" are predicted to move in the opposite direction to that observed in situ during the Winter 2020 period. The role of meteorological events in the evolution of large marine dunes is further evidenced when we consider the September 2020 storm and the resulting reversal of predicted sediment transport direction.

Focusing on the second crescent-shaped dune in tile #1, the effects of wind and atmospheric pressure conditions are reflected in the dynamics of the dunes. Migration speed varies with time. The cyclical variations in Figure 4.10 (with a period of about 12 hours) correspond to tidal forcing and variations in current velocity with the state of the tide. There are periods when the dunes are immobile (zero migration). These periods are largely associated with neap tides, for which even peak tidal currents barely exceed the threshold velocity U_{cr} in the SvR97 transport rate predictor (= 0.41-0.43 m/s for the in situ sediments and range of water depths, Equation 3.15) if not combined with wind-induced currents. Increased migration towards the east (positive values) is broadly correlated to winds from the southwest (S to W sectors) (for example, from 9 to 16 February 2020); increased migration towards the west (negative values) to winds from the W to NE sectors (for example, the September 2020 storm).

The net migration speed calculated over 4 months is more than doubled (54.1 m/yr vs 23.3 m/yr, Table 4.3) when both tidal and meteorological forcings are taken into account. This observation is consistent with the findings of e.g., van Gerwen et al. (2018) who suggested that the migration speed of marine dunes increased with the strength of the residual flow and Overes et al. (2024) who suggested that it could be twice as fast when non-tidal influences were considered. Overes et al. (2024) also observed the temporal variability of the erosion and accretion patterns, which is introduced when non-tidal influences are considered at the boundaries of their model.

	Case I	**Case II**	**Case III**	**Case IV**
17-Nov-2019 to 17-Mar-2020	23.3 m/yr	54.1 m/yr	–	–
31-Aug-2020 to 5-Dec-2020	–	–	25.8 m/yr	34.5 m/yr
25-Sep-2020 6am to 28-Sep-2020 9pm	–	–	0.8 cm/day	-8.4 cm/day
17-Nov-2019 to 5-Dec-2020	29.5 m/yr	39.9 m/yr	–	–

Table 4.3: Migration speeds calculated for the second crescent-shaped dune in tile #1

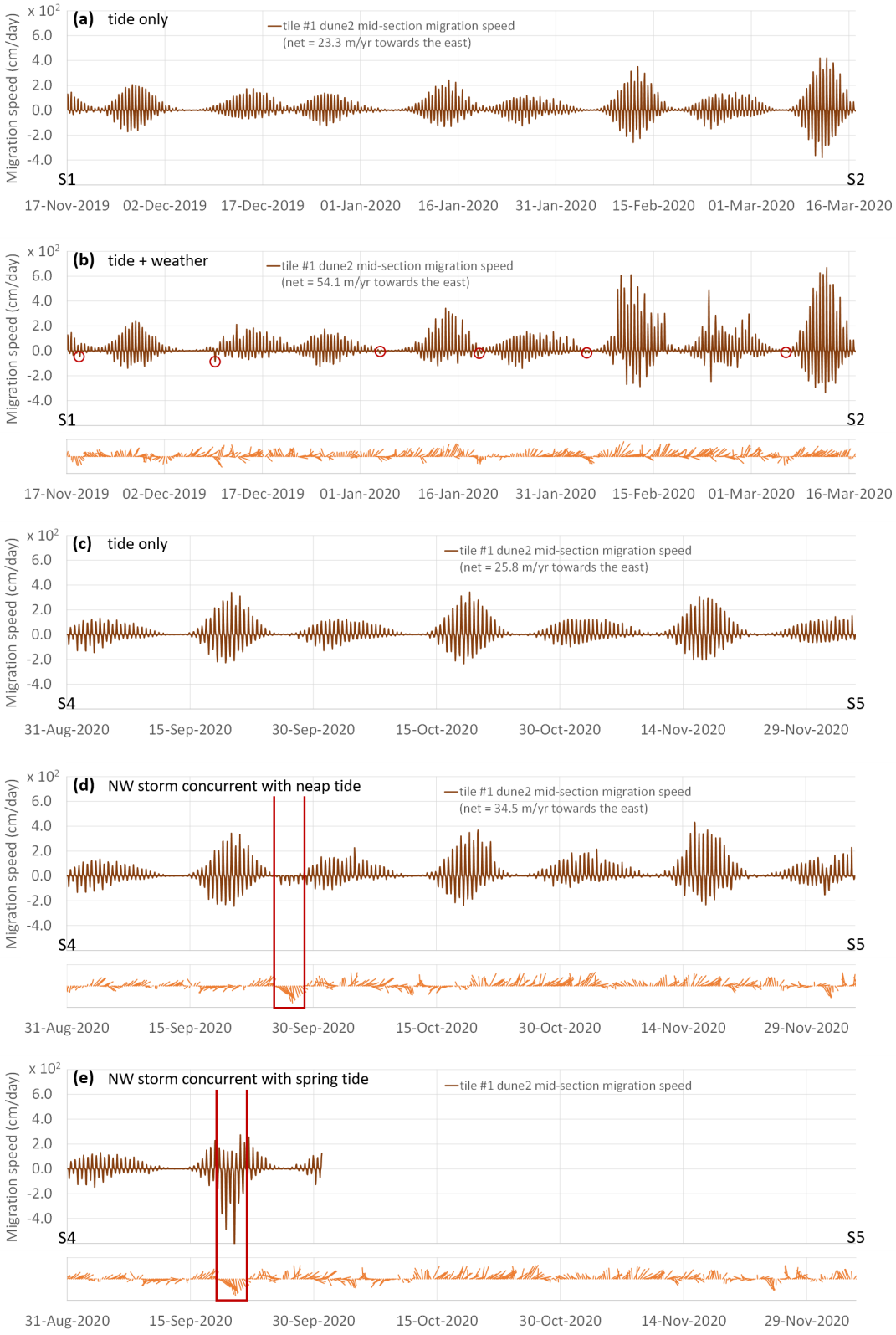

Figure 4.10: Instantaneous migration speed of the mid-point of the dune steep face predicted by the sediment transport and bed evolution model in the navigation channel for Case I to V (a) to (e). Positive values are associated with the flood cycle, trending eastwards; negative values with the ebb cycle, trending westwards. When applicable, the offshore wind is represented by segments whose length and orientation are true to the wind speed and direction at 10 m above sea level

These results agree qualitatively with observational evidence that meteorological events play a part in the evolution of marine dunes. P. T. Harris (1989, 1991), for example, attributed the seasonal inversion of large dune asymmetry in Australia to seasonal changes in wind-induced currents during the monsoon season (bearing in mind that asymmetry is generally accepted as an indicator of the sediment transport in the direction of the steep dune side). Le Bot and Trentesaux (2004) correlated the types of dune morphology to the asymmetry of tidal currents (the imbalance between the ebb and flood cycles) and to the relative strength and orientation of wind-induced currents (their Figure 10). They remarked that dune migration is accelerated if wind-induced currents follow the tidal residual and that it is reduced, or even reversed, in the opposite direction. In the southern North Sea, off Great Yarmouth, Krewinkel (2017) identified annual variability in the speed and direction of observed dune migration, which he ascribed to the wind conditions. The rate of migration was higher and the direction deviated when the climate was more extreme and with a higher proportion of southerly winds.

A few authors have studied the role of wind forcing on dune migration numerically. Campmans et al. (2018a) offered that the speed of migration decreases with increasing obliquity of the winds in relation to the tidal axis (0°, 30°, 60° and 90° tested). In their (idealised) model, winds at 90° to the main current do not result in migration. These conclusions are not in line with our findings. We have not simulated a case where net movement does not occur as a result of tide alone, as in Campmans et al. (2018a). But the northwesterly winds considered in the September 2020 storm and present in the Winter 2020 period broadly correspond to their 90° case. These winds are not only responsible for migration, they are also responsible for reversing the direction of sediment transport. These results may not apply to all configurations. In our 3D model, the regional flow patterns are modified horizontally and vertically when a wind field is applied, over the shallow areas atop the sandbanks, which in turn alters the general circulation. The currents being constrained by the channels between the sandbanks and the proximity of the coast, their direction in deeper areas (for example in the navigation channel and tile #1) does not substantially change when a wind blows, but their magnitude does, with the results we have shown. In any case, we interpret that results presented by Campmans et al. (2018a) are a direct consequence of their modelling assumptions. By design, only the projection of the wind stress on the tidal axis is considered (source term reduced to its x-component $\vec{S} = (S_x, 0)$ in the momentum equation). This component decreases the further the wind direction is from that of the tidal currents, to become exactly 0 for winds at 90°. What it does highlight, however, in agreement with other authors (e.g., van Gerwen et al., 2018), is that the speed of dune migration is linked to the strength of the residual flow, with stronger flow (0° case) leading to higher rates than weaker flow (60° case).

Pessanha et al. (2023) have also investigated wind contributions to marine dune dynamics, in a local 3D model this time. They indicated that the migration speed of the dunes was underestimated by more than 50% compared with bathymetric survey data collected on Wasque Shoals, in the southeastern corner of Martha's Vineyard, when tidal and wind-induced currents only were considered in their modelling. The model is based on a realistic representation of hydro-meteorological forcings. Winds were blowing from the northwest during the measurement period. The fetch is quite limited from this direction due to the presence of the island, and it could well be that the wind-induced currents are not completely developed when they reach Wasque Shoals. Furthermore, unlike our study area, Wasque Shoals is a very shallow environment (less than 7 m water depth), open to the Atlantic Ocean, where wave action can be expected to play a significant role, particularly in winter. Therefore, it is not surprising that the tidal and meteorological forcings were unable to describe the migration of the Wasque Shoals dunes with sufficient accuracy, and that wave forcing was also necessary.

Albeit included in the simulations, the effects of atmospheric pressure gradients have not been discussed in this work. Németh et al. (2002) indicated that the speed of dune migration is higher when the residual flow is generated by a pressure gradient rather than a wind stress. They concluded that shear-stress drives sediment transport in linear dune dynamics and that the velocity profile across the water column is of lesser importance. This view was tested with our model in a simulation in which the input wind field was left out. Only the atmospheric pressure field was applied to simulate the September 2020 storm. The results are not presented here but do indicate little effect on the residual sediment transport. Therefore, we conclude that atmospheric pressure gradients are not a significant factor in the migration of large marine dunes under real conditions.

4.4.3 Implications for dune dynamics (migration and shape)

Campmans et al. (2018b) have attempted to formulate the dynamics of dunes in terms of the relative influence of moderate and frequent events versus more energetic and infrequent events. The question is perhaps best put in terms of the proportion (frequency and duration) of favourable events that amplify the dynamics induced by the tide alone, versus adverse events that counteract these dynamics. On the one hand, adverse wind events that differ from the prevailing conditions temporarily affect and may reverse the general migration trend. On the other hand, events such as the September 2020 storm are, for the most part, short-lived and sporadic. They result in transient dune evolution, which may be substantial but dissipate once the driving winds die down or change direction. Predicted residual sediment transport vectors calculated over a full spring/neap tidal cycle around the September 2020 storm are directed eastwards (75°N, not presented), despite the short incursion to the west shown in Figure 4.8, with a maximum value of 0.027 kg/m/s over the northernmost part of the first crescent-shaped dune in tile #1, and a spatial mean value of 0.013 kg/m/s. This supports the view that if adverse wind events influence short-term sediment transport patterns, as also noted by Le Bot et al. (2000), the long-term dynamics of large marine dunes is likely governed by the consistent, prevailing conditions (e.g., Campmans et al., 2018b; Idier et al., 2002). This view is further corroborated by the in situ data: the in situ bathymetric data collected between 31-Aug-20 (S4) and 5-Dec-20 (S5) also show a net eastward migration over the 3-month period including the September 2020 storm.

In proportion to the time elapsed between bathymetric surveys, the net dune migration is less significant between surveys S4 and S5 (34.5 m/yr for 96 days = 43.5 m/yr for 121 days) than that observed between surveys S1 and S2 (54.1 m/yr for 121 days) (Table 4.3). This reduction can be attributed in part to events such as the September 2020 storm, which, by reversing the dynamics of the dune, cause their position to fluctuate, and therefore slow the net migration over the period. It is perhaps above all a reflection of the seasonality of wind conditions (Campmans et al., 2018b). Indeed, the net migration of the second crescent-shaped dune in tile #1 is also predicted to be a factor of 1.4 faster during the winter than it is over a full year, with respective speeds of 54.1 m/yr (S1-S2) and 39.9 m/yr (S1-S5).

The asymmetry of the dune profile is generally accepted to be an indicator of the direction of its migration, from soft to steep dune sides (Knaapen, 2005, although its use as a predictor is disputed, van Landeghem et al., 2012). We consider that dune asymmetry reflects the prevailing direction of migration, not the instantaneous direction. There will be times, as this work shows, when dune migration will occur in the opposite direction to that indicated by their shape due to adverse winds. However, the volume of sediment in large marine dunes is such that complete reversal of their asymmetry is not conceivable on short time scales (Ernstsen et al., 2006) and would require sustained adverse conditions.

Complete reversal has been observed, for example in the Torres Strait, Australia, where it is attributed to seasonal changes in the wind regime (mainly southeasterly trade winds versus mainly northwesterly monsoon winds) (P. T. Harris, 1989, 1991). But this is unlikely to occur following short-lived wind events. The model results show a discreet westward migration of the dunes during the September 2020 storm, most apparent in its upper section. They do not indicate any significant change in morphology, noting that net migration was estimated at -8 cm/day for the second crescent-shaped dune in tile #1 (Table 4.3), which would be barely noticeable on the scale of a dune 3 m high and 175 m long after 3.5 days.

Winds blew from the northeast for extended periods between surveys S2, 17-Mar-20 and S3, 16-Apr-20 (40% of the records from the sector centred on 45°N, typical duration greater than 5 days). The reversal of the upper section of the dune, which responds more closely to the local flow direction, is apparent in both the observations (Figure 4.11) and in the model results along section a'-a". This translates into softer leading faces, if not a complete reversal of the asymmetry of the dunes.

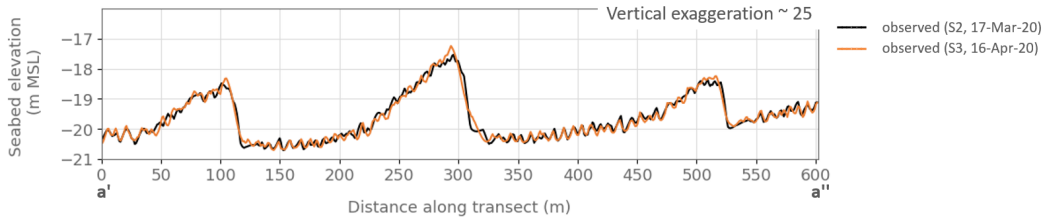

Figure 4.11: Evolution of the observed dune profile extracted in tile #1 along section a'-a", between S2, 17-Mar-2020 and S3, 16-Apr-2020

4.4.4 Predictive model capabilities

What does this mean for the prediction of the large-scale evolution and migration of marine dunes? First and foremost, if morphodynamic models are useful to overcome spatial and temporal limitations, there is no doubt that they must first be calibrated against site-specific data. There exists no universal predictor or set of parameters that can describe the complex processes and interactions between tides, winds, (waves,) sediment transport and bed evolution in a coastal environment. Blind tests conducted by six research laboratories as part of the SEDMOC project (van Rijn et al., 2001) revealed a significant spread (typically of the order of 100) in predicted sediment transport rates. Krabbendam et al. (2021) reached similar conclusions, who were able to obtain good agreement on dune migration after calibration of the sediment transport predictor to site-specific data but warned against the generalisation of these parameters (scale factor and slope parameter) to other areas or periods. Therefore, it seems essential to calibrate the model to improve its predictive ability when in situ data are available (Soulsby, 1997). Failing that, predictions are speculative at best (Anthony & Aagaard, 2020).

Separately, we have shown that tidal currents, which effect is predictable, are important but not sufficient to completely describe dune dynamics in our study area. The migration of the dunes responds closely to wind conditions and, as such, is subject to seasonal to decennial variability. In this context, it is clear that time scale is an essential factor. We only need to cite Lanckneus and de Moor (1991), who observed a net yearly migration near zero in the northern Kwintebank, on the Belgian continental shelf, but reported that the dunes had in fact moved 28 m back and forth in that time. Extrapolating the speed of migration from short to long periods is a hazardous exercise. Langhorne (1982) reached the same conclusion from observational evidence, who indicated that the alteration of sediment transport trends as a result of meteorological influences did not allow the extrapolation of the migration speed.

Figure 4.12 shows the evolution of statistical metrics: bias, Root Mean Square Error (RMSE), Anomaly Correlation Coefficient (ACC) and Brier Skill Score (BSS) calculated in relation to bathymetric surveys S2 to S8 (section a'-a"). The metrics remain stable for approximately one year, but after that period, they start to deteriorate. While the RMSE consistently increases over time (which we attribute partly

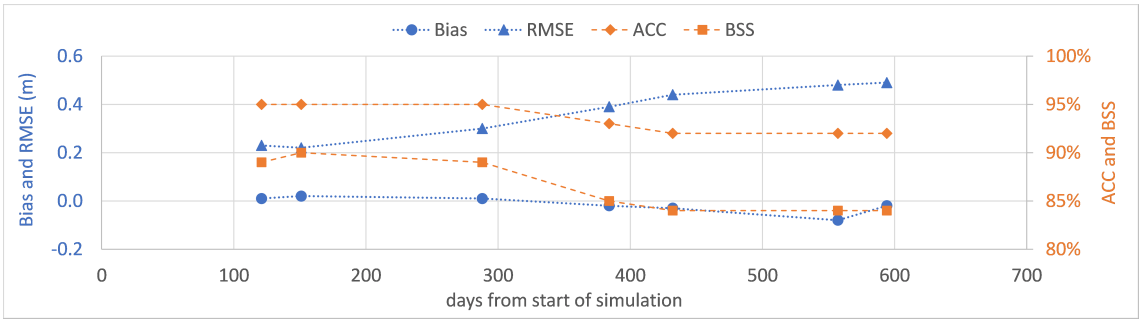

Figure 4.12: Evolution of model performance metrics along section a'-a", in tile #1, in relation to observations from S2 (17-Mar-2020) to S8 (21-Jul-2021)

to the predicted dune profile, and partly to diffusion), the ACC reaches a new plateau and remains relatively constant between the first and second year. This analysis supports using the model as a predictive tool for time frames of 1 to 2 years. Caution should be exercised beyond that.

The lifespan of an OWF is now typically 30 years, with leases that can last up to 60 years (two full project life cycles). Simulations of this length are difficult to envisage at the present time with complex process-based 3D models and realistic input, which is why idealised configurations (models, geometries, or forcings) are still widely used. However, these models lack a complete representation of the physical processes, which in our opinion precludes their use. Another common approach consists in the use of a morphological acceleration factor (Lesser et al., 2004; Ranasinghe et al., 2011) for simulations spanning several decades. However, this approach is limited by the non-linearity introduced when considering meteorological events (and other non-tidal processes). A compromise seems necessary. A sensible approach would perhaps be to determine the response of the system for one representative year (including wind and atmospheric pressure contributions) and to refine this analysis with the predicted response to a matrix of specific adverse or extreme events carefully selected from the long-term site-specific metocean data. In our opinion, simulation of real-life conditions should still be favoured for periods of the order of a few years.

4.5 Closing remarks

The 3D numerical model developed in Chapter 3, based on the process-based open**TELEMAC** system, is used to study the migration of large marine dunes in the Southern Bight of the North Sea in response to tidal and meteorological influences. This area features a range of bedforms, including marine dunes 1 to 5 metre high and hundreds of metre long.

The model has been successfully calibrated and validated against in situ metocean and bathymetric data for a dynamic period during the winter of 2019-20. It accurately simulates the evolution of the seabed off Dunkirk for time scales of the order of months (up to 1-2 years).

We hypothesised that marine dune migration is intimately linked to the amplitude and direction of the residual flow, which are tidally induced and influenced by weather conditions (particularly wind). The results of our model demonstrate the need to include meteorological forcing in the modelling to obtain an accurate representation of changes in the seabed over time. Failing that, dune migration speeds could be underestimated by as much as a factor of 2.

North Sea winds, which differ from prevailing conditions, influence the short-term evolution of the dune field. In this application, we show that sustained northwesterly winds can counteract the weak tidal residual trending east and cause migration towards the west, contrary to the general trend, and the shape of the dunes. These events are too sporadic to fundamentally alter the sediment dynamics of the area, but are expected to slow down net migration over long periods of time.

These results provide a better understanding of the role of weather contributions in an open marine environment. They can be transferred to similar environments: shallow shelf seas dominated by tides, relatively strong currents of the order of 0.5 to 1.0 m/s, moderate winds with a marked directionality, and sandy seabed with median grain size of the order of 200 to 500 μm. By using complex process-based 3D modelling on a large scale and with realistic forcing, this work extends previous research that relied on the analysis of observational data or idealised modelling.

The migration of marine dunes is subject to seasonal and multi-year variability in the wind regime, which raises questions about suitable time scales to monitor dune movement, and strategies for long-term forecasting. This becomes especially relevant over the lifetime of an OWF project, considering the potential impacts of climate change.

Chapter 5

Modelling marine dune dynamics in an OWF context: interactions with foundations

5.1 Introduction

The hydrodynamics of the coastal zone is driven by tides, winds, and waves. Under their action, the seabed can be mobilised to form what is collectively known as 'bedforms'. A variety of bedforms have been observed in nature. In sandy marine environments, these include sand ripples, marine dunes, and sandbanks (see Table 1 in Knaapen, 2005, for a classification overview). Consistent with the terminology established by the Society for Sedimentary Geology (Ashley, 1990), we call marine dunes large, flow-transverse bedforms with a height of 1-5 m and a wavelength of the order of hundreds of metres. In the literature, they are sometimes referred to as sand waves.

Marine dunes are highly mobile sedimentary structures, with documented migration rates of up to tens of metres per year (e.g., Bartholdy et al., 2002; Katoh et al., 1998; Le Bot et al., 2023). This constant remodelling of the seabed is a defining characteristic of marine dunes. They are frequently observed on the bed of shallow shelf seas where offshore wind farms (OWFs) are - or will be - situated. By the end of 2020, approximately 5,400 offshore wind turbines had been installed or were under construction in European waters alone (The Crown Estate, 2020). This figure is expected to increase over the coming decades to help achieve ambitious climate neutrality targets.

Therefore, more research is needed to understand how wind turbine foundations interact with their surroundings, as this topic has not been extensively explored yet. The industry has a legitimate interest in studying scour processes (van der Tempel et al., 2004; S.-Y. Wang et al., 2024; Whitehouse et al., 2011), which have the potential to weaken the structural integrity of the foundations. Little is known about the effects beyond the immediate vicinity (e.g., on sediment dynamics and seabed mobility), which are often dismissed as localised (e.g., Cooper & Beiboer, 2002; Clark et al., 2014). The Oil and Gas industry has dealt with seabed scouring around platforms or free spanning of pipelines, for example, in recent decades. However, the Offshore Wind industry faces two unique challenges: first, the large number of man-made structures in an OWF makes it more difficult to avoid problematic areas altogether, in contrast to a single oil platform; second, electric cables are less robust than pipelines, rendering them more vulnerable to overburden and damage (Games & Gordon, 2014).

This chapter is based on the following journal article:

Durand, N., Tassi, P., Blanpain, O., & Lefebvre, A. On the Attraction of Marine Dunes to OWF Fixed Foundations. *Submitted for publication in Geomorphica*

To our knowledge, no previous studies in the literature have thoroughly examined the interaction between immobile structures, such as OWF monopiles, and a dune field in a marine setting at space and time scales of the order of kilometres and months, respectively. One notable exception is the study by Couldrey et al. (2020), which used recurrent multi-beam bathymetric surveys to document the progression of an isolated crescent-shaped dune as it migrated past an offshore wind turbine foundation. These surveys spanned six years, with one survey conducted before the installation of the monopile. Post-installation surveys focused on the cable route and wind turbine foundation, thus not covering the full extent of the dune. However, the authors noted that the dune was temporarily elongated as it passed the monopile. This stretching was partly due to natural causes, likely changes in hydrodynamics, which also affected other nearby bedforms. It was also associated with increased sediment transport rates as the dune interacted with the scour hole at the base of the structure, so sediment was taken from the toe of the dune and deposited a short distance downstream of the monopile in its wake. This process is in accordance with the findings of Chiew (1984) and Hong et al. (2017). The authors concluded that there was no lasting impact on the dune morphology, based on the observation that transects taken 25 m on either side of the centre line are comparable pre-installation and 3 years post-installation.

In his numerical models, Margalit (2017) examined the formation of natural bedforms and the impact of offshore wind farms. Although most of his research focused on sandbanks, one simulation considered a monopile installed within a linear marine dune field (comprising dunes measuring 3 m in height and 300 m in length). The migration rate of the dunes was said to slow as a result of the presence of the monopile. The author himself acknowledged that this simulation was exploratory. It raises questions about the model setup, particularly regarding the boundary conditions, as bed levels appear to be invariant at the upstream boundary, and sediment accumulates from there to the monopile without passing beyond it. This work has the merit of initiating a discussion about the influence of monopiles on their environment.

In Chapter 3, we have described the development of a complex process-based 3D model, with realistic input, for an area offshore Dunkirk in the Southern Bight of the North Sea (Figure 5.1), where large marine dunes are present. The model has been shown to be capable of simulating the dynamics, particularly the migration rate, of these dunes (Durand et al., 2024). The aim of the current work is to explore the impact of the foundations of offshore wind turbines on these dynamics. In the next section, we present the study area, the model setup, and validation. Initial simulations are carried out with a single monopile and then extended to a realistic OWF layout, consisting of an array of 46 wind turbines. The results of these simulations are presented in Section 5.3, with implications discussed in Section 5.4. Section 5.5 concludes this work.

5.2 Material and methods

5.2.1 Study area

Dunkirk, situated in the Southern Bight of the North Sea near the French-Belgian border (Figure 5.1), was selected as a suitable site for an offshore wind project during the third French call for tenders in 2016. The location benefits from excellent resources, with average wind speeds between 9 and 9.5 m/s at elevations of 100 to 140 m above sea level, favourable water depths shallower than 30 m up to 20 km from the coast, and access to a robust electricity grid that is capable of handling the OWF output (Parc éolien en mer de Dunkerque website). Furthermore, Dunkirk is home to a prominent industrial port complex: the Grand Port Maritime de Dunkerque.

A comprehensive metocean data set has been collected to support the Dunkirk OWF project and for research purposes. Site-specific meteorological and hydrodynamic campaigns have been conducted for up to six months. In addition, long-term metocean observations are available from the Flanders Marine Institute (VLIZ) at the Westhinder measurement station. These records provide information on wind velocity, atmospheric pressure, water level, current and wave conditions.

The region is characterised by a macro-tidal regime, with a spring tidal range = 5.5 m. The tide rises faster than it falls, an asymmetry that is also reflected in the tidal currents. The flood current is

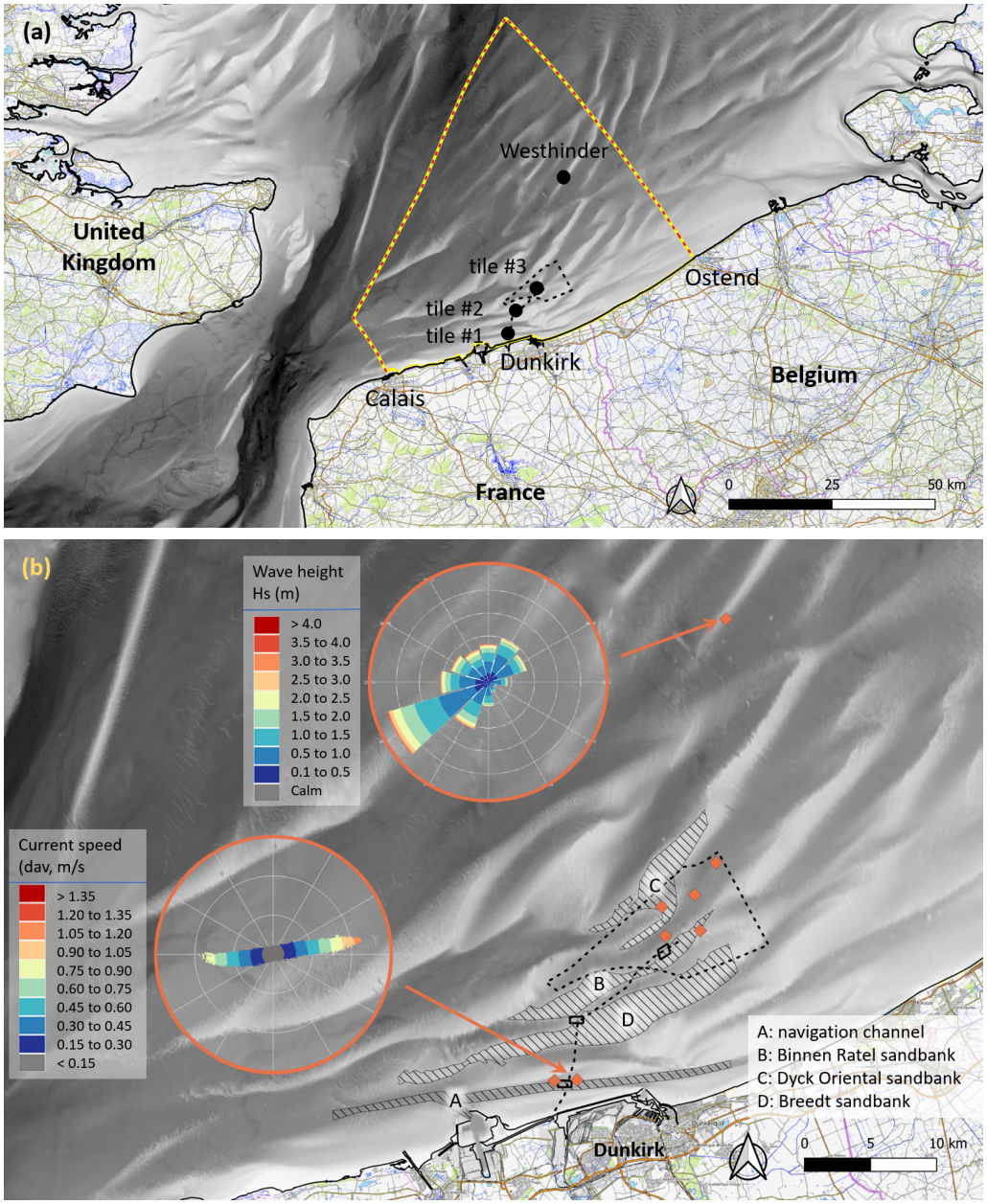

Figure 5.1: (a) General location map. The geographical footprint of the proposed offshore wind farm is marked by a dashed black line; the extent of the numerical model by a dashed coloured line. (b) Location of metocean (filled diamonds) and bathymetric (polygons) survey data in relation to known bathymetric features (Source of the background data: Shom (2015), OpenTopoMap, and EEA coastline)

generally stronger than the ebb, resulting in a net current trending east-northeast. In the navigation channel (FEM, 2021b, Figure 5.1(b)), for example, peak depth-averaged speeds reach 1.22 m/s during the flood compared to 0.85 m/s during the ebb. This predominance is reversed in the gullies between the offshore sandbanks (FEM, 2021b). The near-bed currents (approximately 1 m above the bed) can reach 0.70 m/s at the peak. The offshore wind and wave climate is characterised by the prevalence of south-westerly events from the English Channel. However, significant events also occur from the northwest to the northeast, originating from the North Sea (Figure 5.1(b)). The wave condition with a return period of 1 year is estimated to have a significant wave height (H_s) of 4.4 m and a mean period (T_z) of approximately 7 s, as determined by an extreme value analysis of data from VLIZ (2022b). It

is noteworthy that 56% of the waves are less than 1 m high.

The seabed is mainly composed of sand with median grain sizes (d_{50}) ranging from 240 μm to 450 μm (FEM, 2020). The diameter d_{10} is estimated to be 210 μm on average. Consequently, it is unlikely that the sediment will exhibit cohesive properties. This provides an optimal environment for the development of marine dunes. Detailed bathymetric surveys have been carried out to provide an accurate representation of the seabed at different times. Two large-area surveys were carried out over a period of two years, from 2016 to 2017 (Shom), and again in June 2021 (EMD), to cover the entire footprint of the wind farm (black dashed outline in Figure 5.1(a)). Separately, eight surveys were performed between 2019 and 2021 in three pre-defined tiles, selected to encompass a range of bedforms (FEM, 2021a, black filled circles in Figure 5.1(a) and black polygons in Figure 5.1(b)). These surveys have corroborated the existence of marine dunes with a height of between 2 and 3 m, offshore Dunkirk, and allowed their migration rate to be quantified (Le Bot et al., 2023). Overall, the dunes have been observed to travel at a net rate of approximately 30 m/yr towards the northeast.

5.2.2 Model set-up and validation

A three-dimensional (3D) coastal area model was developed based on the open**TELEMAC** system to improve our understanding of the processes involved in a marine dune field (Durand et al., 2024). The hydrodynamic module, TELEMAC-3D, is coupled with the sediment transport and bed evolution module, GAIA, to consider the interactions between tidal flows, weather and sediment transport processes. The influence of waves has been omitted in this model since Durand et al. (2023a) suggested that waves are of secondary importance in waters deeper than approximately 15 mMSL, which is mostly the case in our areas of interest. TELEMAC-3D solves the 3D Reynolds-Averaged Navier-Stokes equations without hydrostatic pressure assumption (Hervouet, 2007) (short module description and governing equations in Section 3.3.1). GAIA solves the sediment continuity equation, also known as the Exner equation, to compute the seabed evolution from empirical sediment transport rate predictors (Tassi et al., 2023) (short module description and governing equations in Section 3.7.1). The suspended load has been excluded from the model since bedload transport was identified as the dominant mode of transport (Durand et al., 2023a), consistent with the presence of marine dunes in the area.

The computational domain extends from Calais to Ostend in Belgium, covering approximately 80 km of coastline. Its offshore extent varies between 15 km in the Dover Strait and 75 km in the east (dashed coloured line in Figure 5.1(a)). An unstructured finite element mesh with spatially varying resolution is used. The size of the triangular elements varies gradually from 10 m in the areas of interest to a maximum of 3000 m away from them. Digital terrain models of the seabed throughout the computational domain have been constructed from a range of data sources, with the most recent and detailed data given precedence over data of lesser quality.

The open-sea boundaries of the model are driven by tidal harmonic constituents from the FES2014 database (Lyard et al., 2021; Noveltis, Legos and CLS, 2019). To account for meteorological influences on hydrodynamics, spatially varying wind and atmospheric (sea level) pressure fields from the AROME operational forecast (Bouttier, 2007) are applied. The hydrodynamics were calibrated and validated by comparing the model predictions over complete spring-neap cycles with site-specific level and current data at 7 locations across the computational domain (EMD, 2022; FEM, 2021b; Shom, 2017c; VLIZ, 2022a) (Chapter 3). The formulations and parameters that achieved 'excellent' performance according to the classification scheme proposed by Sutherland et al. (2004) are summarised in Table 5.1. The morphodynamics were subsequently calibrated and validated by comparing the model predictions with surveyed seabed levels (FEM, 2021a) (Chapter 3, Durand et al., 2024). The formulations and parameters that resulted in a good replication of the migration patterns of the marine dunes are also summarised in Table 5.1.

Vertical discretisation	3D with 5 irregularly spaced sigma planes
Bathymetry	EMD (2021); FEM (2021a); Shom (2015, 2016, 2017b); Shom - ROLNHDF (2022); Flemish Hydrography (2022)
Tidal constituents	34 harmonic constituents (FES2014 global model tide database; Lyard et al., 2021)
Wind & sea level pressure	Hourly data at 1/40° resolution (AROME 30-hour forecast; Bouttier, 2007)
Friction	Nikuradse roughness k_s = 2.5×d_{50} (Soulsby, 1997)
Horizontal turbulent diffusion	Constant kinematic viscosity = 10^{-6} m^2/s
Vertical turbulent diffusion	Tsanis mixing length model (Tsanis, 1989)
Dynamic pressure	Yes
Sediment type	One class of non-cohesive sediment; d_{50} = 345 μm
Transport mechanism	Bedload; suspended load discarded
Sediment transport predictor	SvR97 total load predictor (Soulsby, 1997)
Slope effect	No
Morphological factor	No

Table 5.1: TELEMAC-3D+GAIA modelling parameters and processes

5.2.3 Simulated scenarios and analysis of results

To assess the impact of turbine foundations on the evolution of large marine dunes, we have simulated a two-year period. A baseline simulation was initially performed to model the hydrodynamic and sediment transport processes naturally occurring offshore Dunkirk, without any monopile(s) influencing them. Exploratory scenarios were then devised, which considered a single monopile. A realistic scenario was later implemented that included an array of monopiles within the projected footprint of the Dunkirk OWF.

In each case, we define the monopiles as obstacles in the computational domain, meaning the triangular elements at the location of the monopiles are removed from the mesh. This method is more practical and efficient to implement than the alternative of defining the monopiles as additional drag, which requires estimating the undisturbed upstream flow. It has the added benefit of recognising a physical reality: monopiles act as obstructions to both water flow and seabed sediment. Rivier et al. (2015, 2016) used a 3D hydrodynamic and sediment transport model to explore potential differences arising from the parameterisation of the monopile (be it implicit, through the use of a resistance term in the momentum equation and a source term in the turbulence equation, or explicit, in the model mesh with refinement to resolve the flow structure). The authors observed minimal impact in the near-field. In our case, one triangular element is removed from the mesh for each monopile. Its effective diameter is therefore determined by the horizontal resolution of the mesh.

Exploratory scenarios

To understand the dynamics between marine dune movement and a fixed foundation, we developed hypothetical scenarios with only one monopile as a first step - a later step will consider the impact of an OWF array as a whole. We selected tile #1, in the navigation channel leading to the port of Dunkirk, and tile #3 close to the proposed location of the offshore transformer station, for this (see Figure 5.1 for location). This is justified since the bed evolution in these areas has been extensively studied and validated in a previous work to examine the influence of hydro-meteorological events on the natural evolution of marine dunes (Chapter 4, Durand et al., 2024). This is also where the model is most resolved (ca. 10 m horizontal resolution).

In Case IA, we placed a monopile approximately 90 m ahead of the second large crescent-shaped dune (3 m high) in tile #1, ensuring a sufficient distance to avoid initial disturbance to the dune, and before the following sinuous dune. In Case IB, we placed a monopile on the slope on the Binnen Ratel sandbank in tile #3, ca. 50 m ahead of an approaching 2 m high sinuous dune. There, the

seabed topography does not constrain the flow as is the case for Case IA, leading to a broader range of directions.

These two cases are complementary and illustrate the range of possibilities. The first location (Case IA) is representative of a monopile sited in a gully between sandbanks, subjected to bidirectional flows that switch direction with the tidal phase, hence bidirectional sediment transport pathways. The second location (Case IB) is representative of a monopile installed on the slopes of a sandbank, in open conditions with a wider spread of directions. Table 5.2 and Figure 5.2 summarise the monopile positions and characteristics for both cases.

	Latitude	Longitude	Water depth	Average edge length	Effective pile diameter
Case IA	51°03.830' N	2°15.801' E	-20.1 mMSL	10.7 m	7.9 m
Case IB	51°09.239' N	2°22.644' E	-15.6 mMSL	10.3 m	7.6 m

Monopile diameters ranging from 7.0 m to 11.5 m are planned for the Dunkirk OWF

Table 5.2: Characteristics of the monopiles in the exploratory scenarios

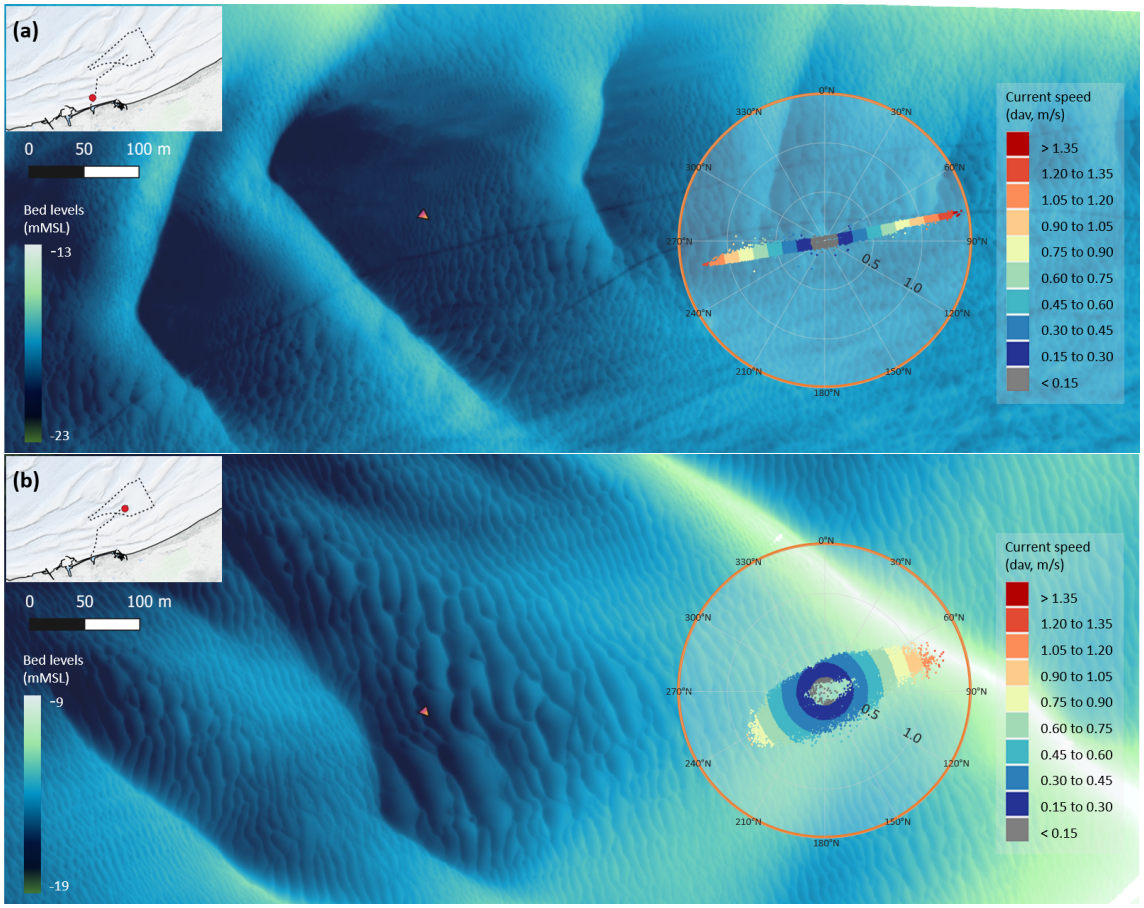

Figure 5.2: Location of the monopile, indicated by a coloured triangle to scale for both Case IA (a) and Case IB (b). The current ellipses characterise the local hydrodynamic conditions

OWF scenario

Following these initial scenarios, the entire array of monopiles projected for Dunkirk OWF first scenario was modelled. This includes 46 monopiles that support wind turbines, each with a diameter of 220 m,

spaced a minimum of 1 km apart and at least 10 km from the coastline, covering an area close to 50 km^2 (Parc éolien en mer de Dunkerque website). The precise location of the monopiles was not available at the time of our work and we georeferenced the map for the 'OWF project off Dunkirk and its electrical connection' published on `http://parc-eolien-en-mer-dunkerque.geophom.info/` (last updated on March 17, 2022) to extract approximate locations. Figure 5.3 shows this layout, including the marine dunes identified in preliminary site studies (Shom, 2017e) to provide some context. It is clear that dunes are not uniformly distributed throughout the OWF footprint. They are predominantly associated with the sandbanks, with relatively fewer dunes in the gullies between them.

We applied the same approach to represent monopiles as in exploratory scenarios, where certain elements were removed from the computational domain to define obstructions. For this simulation, the mesh was uniformly refined to a horizontal resolution of 10 m in the OWF area (the baseline was rerun with this updated mesh discretisation for consistency). The exact size of the triangular elements varies, which in turn affects the size of the monopiles between different locations, as detailed in Table 5.3. Of the 46 monopiles, 42 have an effective diameter between 7.0 and 11.5 m (the projected diameter). To specifically investigate the implications of wind turbine placement, we have also simulated an array comprising only half the number of wind turbines (Cases IIA and IIB). In these simulations, the turbines have been selected in a way that ensures that their effect does not overlap a priori.

	Water depths	**Average edge lengths**	**Effective pile diameters**
Case II	-10.6 to -28.8 mMSL	9.0 to 32.2 m (11.5 m)	6.5 to 23.6 m (9.0 m)
Case II*	-10.6 to -28.8 mMSL	9.0 to 14.7 m (10.6 m)	6.5 to 10.9 m (7.9 m)

* excluding 2 monopiles placed on the edge of the finely resolved area

Table 5.3: Characteristics of the monopiles in the OWF scenario

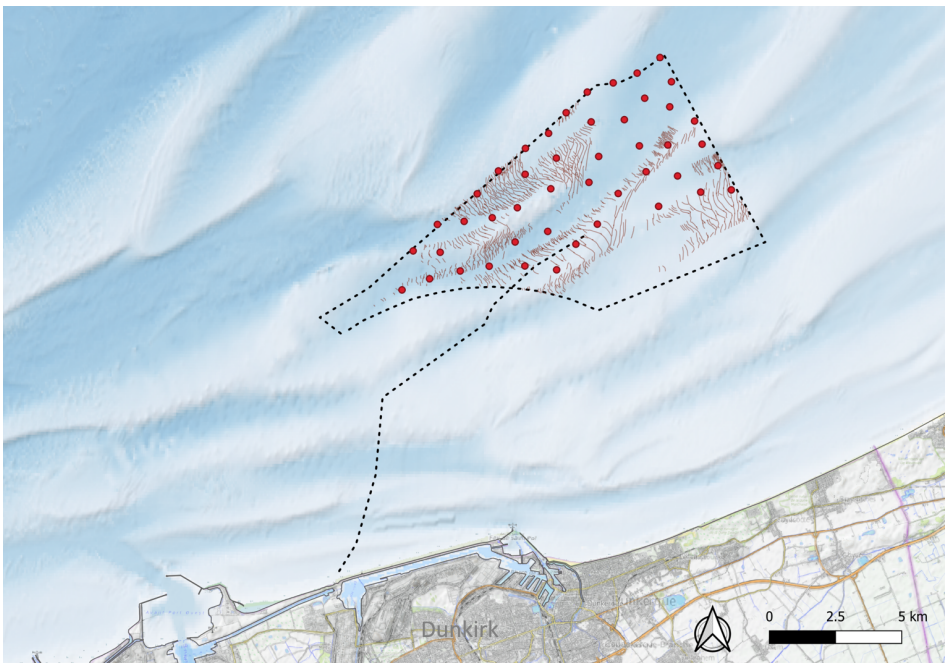

Figure 5.3: One of the proposed layouts for the Dunkirk OWF; the geographical footprint and cable corridor are indicated by dashed black lines; marine dunes inventoried in Shom (2017e) are represented by sinuous brown lines (Source of the background data: Shom (2015), OpenTopoMap, and EEA coastline)

The wind farm is located within a sandbank system where the prevalence of flood and ebb flows varies spatially, also influenced by meteorological conditions. As a result, sediment transport patterns and dune mobility vary spatially, as illustrated in Figure 5.4. We focus our analysis on 3 morphological behaviour zones: 1) in the gully between the Binnen Ratel and the Dyck Oriental sandbanks, where the marine dunes travel towards the southwest, contrary to the general trend, 2) on the slopes of the Dyck Oriental sandbank, and 3) in a relatively flat and featureless area situated in the northern corner. These zones are marked in Figure 5.4.

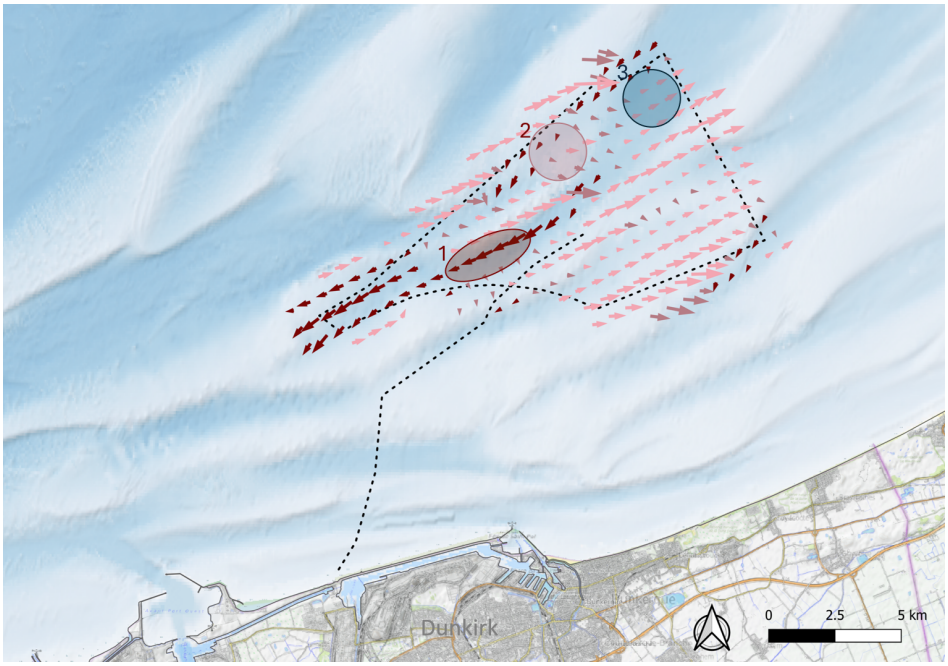

Figure 5.4: Predicted sediment transport pathways for the baseline simulation, coloured by directional quadrant, also highlighting 3 zones of interest (Source of the background data: Shom (2015), OpenTopoMap, and EEA coastline)

Assessment of monopile influence: first-order moment of sediment transport rate

The presence of a wind turbine impacts the surrounding environment in various ways. Above sea level, it creates an atmospheric wake, which refers to a reduction in wind speed downstream of the blades. Although this can influence hydrodynamic conditions, it is usually not considered in morphodynamic modelling. Below sea level, the turbine foundation obstructs the flow, causing a downstream reduction in current speeds, known as the hydrodynamic wake. Additionally, turbulent wakes, such as horseshoe vortices near the seabed immediately upstream of the monopile and downstream vortex shedding, are generated. At the seabed level, the presence of the foundation alters the seabed morphology, with areas of erosion and accretion. This morphodynamic wake is linked to the hydrodynamic and turbulent wakes, as sediment transport processes respond to the changes in hydrodynamics caused by the monopile. In the remainder, the term ‘wake’ without a qualifier refers to the ‘hydrodynamic wake’.

To visualise the area of influence of the monopile(s) on the sediment dynamics and morphological processes specifically, we use the first-order moment of the transport rate (essentially the average value) over a 360-day period. The sediment transport rate (a vector) is obtained at an hourly resolution from simulations conducted both with and without monopile(s). The vector difference is calculated at each point and time within the computation domain. The norm of this difference is signed such that an increase in magnitude due to the presence of a monopile is considered positive, while a decrease is considered negative, irrespective of the direction of the sediment transport rate. Higher-order moments (variance, skewness, and kurtosis) were also calculated, but are not discussed here.

Assessment of dune migration

The impact of monopile(s) on seabed evolution, particularly on the propagation of marine dunes, is assessed by comparing the (predicted) baseline Digital Terrain Model (DTM) for the natural state with the (predicted) DTM including monopile(s). This analysis focuses on the first year of simulation. The difference map highlights areas of erosion and accretion resulting from changes in bedform migration patterns. In this representation, the white areas indicate regions where the presence of the monopile(s) does not alter natural sand transport pathways. To complement this analysis, the temporal evolution of specific transverse profiles is plotted through the monopile(s) for the entire simulation period. This representation allows for a synthetic visualisation of dune propagation as a function of time. A comparison of the predicted time evolution without and with monopiles gives insight into their effect.

In parallel, the dune crest lines are extracted to assess more precisely the impact on dune plan shape (for example, distortion, direction changes). For this, a spline is fitted to the seabed levels predicted by the model to add the resolution lacking from the model mesh (from 10 m to 1 m resolution). The resulting DTM is smoothed (SAGA 7.8.2 square 'simple filter') and is then used to extract local maximum values of seabed levels along horizontal lines with 0.5 m spacing, applying a threshold to exclude secondary bedforms. This analysis is restricted to a few subset areas and times due to its high demands on computer time and disk space.

5.3 Results

5.3.1 Exploratory scenarios: Cases IA and IB

The predicted changes to the seabed one year after the installation of a single monopile within the dune field are depicted in Figure 5.5 for Case IA and Figure 5.6 for Case IB. These changes are calculated as the difference between the seabed levels without the monopile and with the monopile. Shades of blue indicate a lowering of the seabed (erosion) and shades of brown indicate a rising of the seabed (accretion) after one year. The colour scale is designed to highlight changes in the propagation of marine dunes, with the caveat that local variations may exceed these limits (e.g., in the immediate vicinity of the foundation).

Wind turbine monopiles, like bridge piers, locally alter hydrodynamics, creating a complex 3D flow structure (e.g., Melville, 1988; Sumer & Fredsøe, 2002; Whitehouse, 1998). The increased turbulence can lead to the formation of a scour hole around the structure. It is important to note that these physical processes require much finer (horizontal and vertical) resolution than what is used here to model the large-scale dynamics of marine dunes. Therefore, it cannot be expected that local scour processes are adequately represented in our model.

As expected, the most significant morphological changes occur along the tidal axis and immediately around the monopile. Their spatial extent stabilises after an initial period of 90 to 180 days (not shown), but their magnitude increases with time. After one year, bed level variations greater than 0.25 m extend to 830 m west of the monopile and 900 m east of the monopile for Case IA. The largest predicted bed level variations (on the tidal axis, beyond 4 pile diameters) are -1.5/+5.0 m west of the monopile and -1.5/+2.2 m east of the monopile. These variations, which are comparable to the heights of the marine dunes, indicate significant movement of the dunes.

There is a gradual accumulation of sediment in the streamwise direction in front of the monopile, particularly on the west side (+5.0 m in height after one year). This accumulation is consistent with the natural direction of sediment transport from west to east in Figure 5.5, due to the dominance of the flood currents. However, it appears to be exaggerated and is likely a result of the mesh size of the model. After approximately one year, this results in oscillations in the seabed, as shown in Figure 5.7(b) for example. In nature, these accumulated sediments might be expected to be drawn towards the scour hole and passed around the structure (Hong et al., 2017).

One year after the installation of the monopile, the seabed changes are less pronounced for Case IB than for Case IA when compared to the baseline simulation without the monopile. Consistent with the lower dynamics observed in this area (Section 4.3), the spatial extent of the seabed changes is also

reduced compared to Case IA (approximately 500 m in each direction). The largest predicted changes in bed level (on the tidal axis, beyond 4 pile diameters) are -0.3/+1.2 m southwest of the monopile and -0.6/+1.4 m northeast of the monopile.

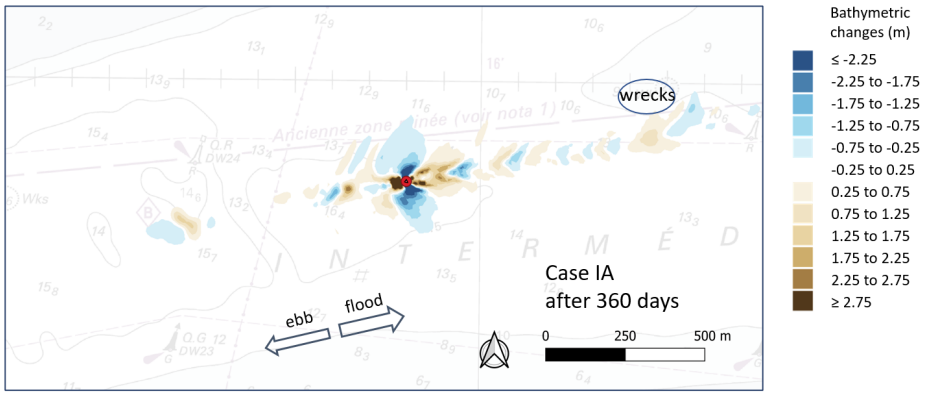

Figure 5.5: Bathymetric changes one year after the implementation of Case IA, calculated as the difference between predicted seabed levels (including the monopile, shown as a filled red circle) and baseline levels (without monopile), both after one year. Shades of blue indicate lowering of the seabed (erosion) and shades of brown indicate rising (accretion) (Source of the background data: Shom nautical chart 7057)

Figure 5.6: Bathymetric changes one year after the implementation of Case IB, calculated as the difference between predicted seabed levels (including the monopile, shown as a filled red circle) and baseline levels (without monopile), both after one year. Shades of blue indicate lowering of the seabed (erosion) and shades of brown indicate rising (accretion) on the tidal axis (Source of the background data: Shom nautical chart 7214)

The temporal evolution of the seabed, extracted along the tidal axis through the monopile, is illustrated in Figures 5.7 and 5.8 for Cases IA and IB, respectively, where the dune crests naturally appear as lighter-coloured features. These figures corroborate our earlier observations that the navigation channel area is very dynamic (migration speed of 40-59 m/yr in the natural state), while the slopes of the Binnen Ratel sandbank are relatively less active (comparatively slower migration speed of 20–40 m/yr). The propagation is directed eastward, which is explained by stronger flood than ebb currents in these regions. Furthermore, Figures 5.7 and 5.8 demonstrate that, in the long term (order of years), the progression of the dunes is steady, as indicated by an overall linear evolution.

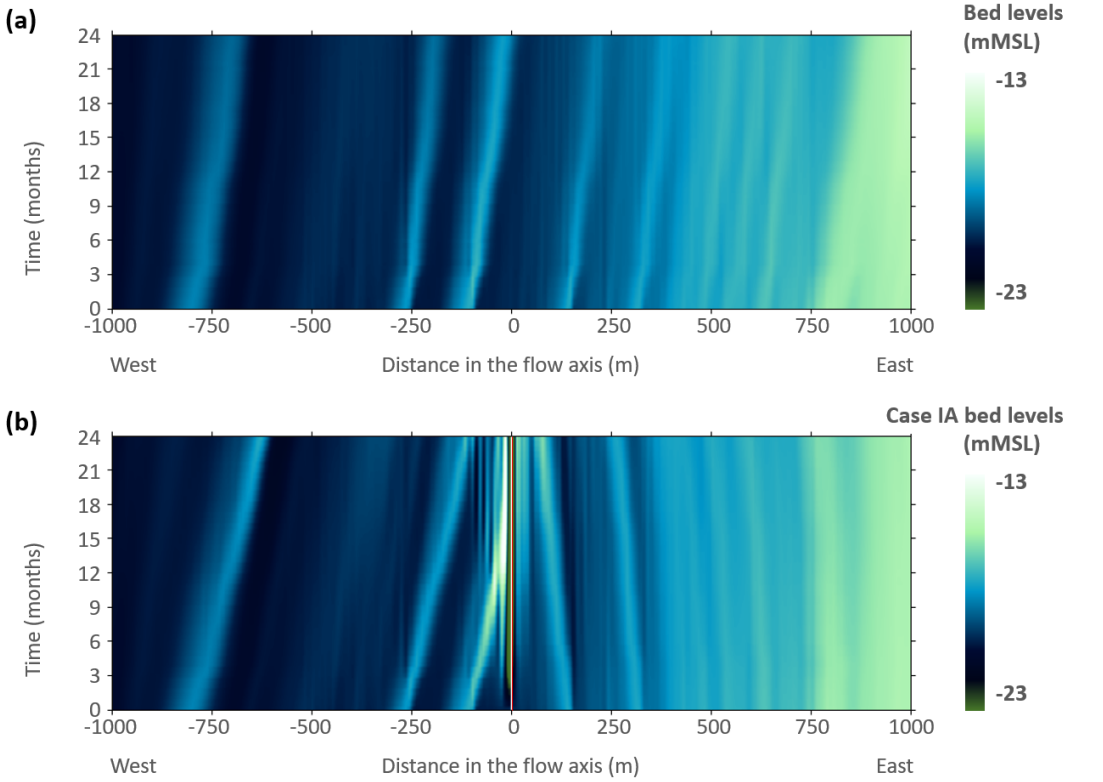

Figure 5.7: Temporal evolution of bed levels extracted along the tidal axis through the monopile (a) from the baseline simulation and (b) from the Case IA simulation, where the monopile is marked by a red line

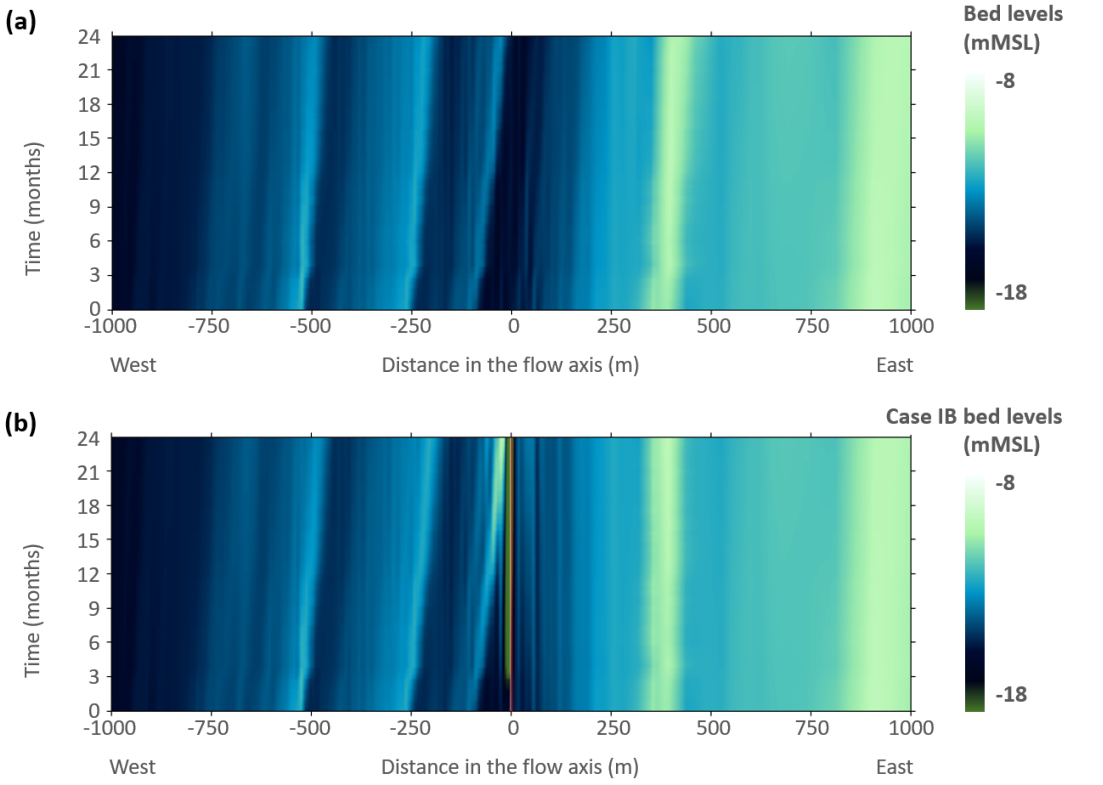

Figure 5.8: Temporal evolution of bed levels extracted along the tidal axis through the monopile (a) from the baseline simulation and (b) from the Case IB simulation, where the monopile is marked by a red line

It is clear from these figures that the changes in the seabed documented in Figures 5.5 and 5.6 correspond to the convergence of the dunes towards the monopile. The propagation is accelerated in areas where the general sediment transport was already directed towards the structure in the natural state (namely west of the monopile). Conversely, a reduction (Case IB) or even a reversal (Case IA) of the propagation is predicted in areas where the general direction of sediment transport was away from the structure (east of the monopile).

This convergence is quantified in Table 5.4, which presents the displacement of the crests of the large marine dunes after a one-year period. The transect used for this analysis is 2000 metres long, as per Figures 5.7 and 5.8, so the table includes data on more dunes than those depicted in Figure 5.2. The acceleration rate, defined as the ratio of the difference in migration speed with the monopile to the baseline speed, varies between dunes. For Case IA, the average acceleration rate is 73% to the west and -164% to the east of the monopile. In comparison, Case IB shows a less pronounced effect, with acceleration rates of 17% to the west and -73% to the east of the monopile. Negative values indicate deceleration, and values below -100% indicate a reversal of dune migration.

Initial crest location along transect	**Displacement in the natural state (baseline scenario)**	**Displacement in a scenario with a monopile**
		Case IA
-801.7 m	59.1 m	92.1 m
-262.7 m	41.3 m	75.9 m
-104.5 m	45.9 m	82.0 m
142.0 m	41.3 m	-30.0 m
312.2 m	40.2 m	-22.4 m
		Case IB
-523.5 m	27.5 m	31.5 m
-261.3 m	28.9 m	35.8 m
-104.1 m	41.8 m	47.4 m
388.0 m	19.8 m	5.4 m

Table 5.4: Displacement of the marine dune crests predicted after one year for Cases IA and IB along the transverse profiles used in Figures 5.7 and 5.8, respectively. The transects are oriented from west to east, with 0 corresponding to the monopile location. Positive displacement values indicate eastward propagation

5.3.2 OWF scenario: Case II

The changes to the seabed resulting from the implementation of the OWF offshore Dunkirk are illustrated in Figure 5.9 for Case II. The same colour scale as that used for Cases IA and IB is used to facilitate comparisons. In this representation, shades of blue indicate a decrease in seabed levels (erosion) from the baseline levels without monopiles, and shades of brown indicate an increase in seabed levels (accretion) at the end of one year.

Numerical instabilities are apparent on the steep slope of the Dyck Oriental sandbank (centre of Figure 5.9(a)). They manifest early on, as observed in the simulation after only 3 months. Although the magnitude of the oscillations increases with time, these instabilities do not propagate or affect other areas of the computational domain. Apart from this area, the most notable changes in seabed levels occur in the western part of the OWF, particularly between sandbanks (e.g., in Zone 1) and on the Dyck Oriental sandbank (e.g., in Zone 2).

In Zone 1, the wind turbines are placed in the gully between the Binnen Ratel and the Dyck Oriental sandbanks. The currents are channelled and very much bidirectional. Large marine dunes migrate in a southwesterly direction, contrary to the prevailing northeasterly trend (Figure 5.4). The area is dynamic, and the monopiles exert a significant influence on the surrounding environment (over more than 1 km), with the morphodynamic wake extending to adjacent wind turbines (Figure 5.9(b)).

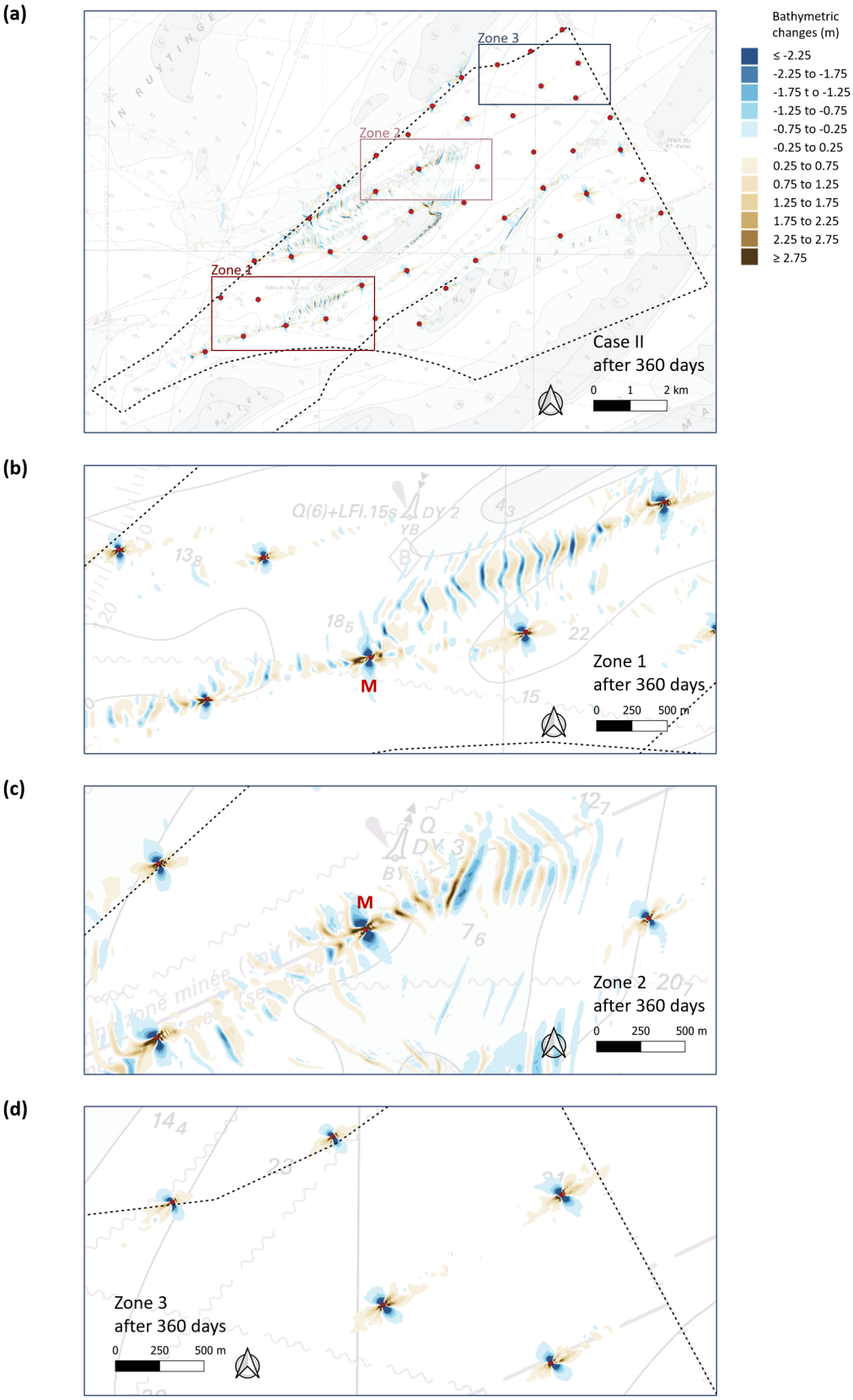

Figure 5.9: (a) Bathymetric changes one year after the implementation of Case II, calculated as the difference between predicted seabed levels (including 46 monopiles, shown as filled red circles) and baseline levels (without monopiles), both after one year. The 3 morphological behaviour zones defined in Figure 5.4 are identified by rectangles. Close-up views are presented in (b) for Zone 1, (c) for Zone 2 and (d) for Zone 3 (Source of the background data: Shom nautical chart 7214)

The rhythmic succession of erosion and accretion patterns is testament to the impact on the marine dunes. The largest predicted variations in bed level (on the tidal axis of the monopiles, beyond 4 pile diameters) are -2.5/+3.7 m west of the monopiles and -0.9/+3.3 m east of the monopiles. Variations of this magnitude indicate a significant difference in the position of the dunes without and with the monopiles, given that dunes in Zone 1 reach heights of 3 to 4 metres.

In Zone 2, the wind turbines are placed on the slopes of the Dyck Oriental sandbank. There, the prevailing currents align with the coastline but exhibit a wide range of directions corresponding to the turning of the tide. The morphodynamics of the area are complex, characterised by sediment transport directions that change by more than 90° within a short distance around buoy DY3 (Figure 5.4), and dune morphology that transitions from 3D and northwest to southeast orientation to 2D and north-south orientation down the sandbank slope towards the gully. The bed changes shown in Figure 5.9(c) reflect these patterns. In this active area, the impact of the monopiles is again far reaching (more than 1 km). The largest variations are -1.5/+2.4 m either side of the monopile.

In Zone 3, in the northern corner of the OWF, the wind turbines are placed in a relatively flat and featureless area. The structures only affect their immediate surroundings, resulting in erosion on the sides of the monopiles due to vortex shedding and deposition along the flow axis (Figure 5.9(d)). These patterns typically develop in flat-bed tidal settings, as observed experimentally by Whitehouse and Stroescu (2023) and S.-Y. Wang et al. (2024). During one phase of the tidal cycle, the sediment that has been mobilised at the front of the monopile by the downflow and added turbulence is transported and deposited to the rear. With the reversal of the current in the subsequent tidal phase, the pattern is mirrored, with sediment from the new front side transported to the new rear side, resulting in sediment accretion on either side of the monopile. These depositional areas (indicated by brown shades in Figure 5.9(d)) grow steadily over time, reaching distances of between 15 and 33 pile diameters after one year.

Zone 3 will not be considered further due to the absence of large bedforms, which are the focus of this study. Instead, our attention will turn to Zones 1 and 2. The temporal evolution of the seabed is depicted in Figures 5.10 and 5.11, respectively, along transects passing through the monopile marked 'M' in Figure 5.9. In these figures, the colour scale has been adjusted in order to best reflect the dynamics of the dunes. While the dunes are predicted to naturally travel towards the west-southwest (left) for the first profile, in Zone 1, their direction of propagation is found to vary spatially for the profile in Zone 2, in accordance with the sediment transport pathway map presented earlier in the natural state. The presence of monopiles alters the natural propagation of the dunes, causing them to converge on the structures.

This phenomenon has been previously documented in Cases IA and IB, and is quantified in Table 5.5 for Case II. It is clear that the impact of the monopile diminishes as the distance from it increases. In Zone 1, for example, dune migration is directed towards the monopile, contrary to the usual trend, only for the first 2 dunes west of the structure (ca. 20 pile diameters away, with acceleration rates as low as -171%). Further away, the migration merely slows down, with values ranging from -55% to -89% the west of the monopile. Note that negative values indicate deceleration, and values below -100% a reversal of dune migration. In comparison, in Zone 2, the structure is predicted to have no impact on the furthest dune in the profile, west of the monopile (distance of ca. 80 pile diameters).

5.4 Discussion

5.4.1 Influence of OWF monopiles on dune dynamics

The impact of monopiles on hydrodynamics has been the subject of extensive investigation. The existence of distinct wake patterns in the lee of monopiles that disturb currents (X. Li et al., 2014; Miles et al., 2017; Rivier et al., 2016) and stratification (Cazenave et al., 2016; Schultze et al., 2020) has been demonstrated by field data, experimental data and numerical simulations. The streamwise extent of these patterns is dependent on the strength of the current and the size of the obstructing structure. Although some studies have indicated a return to background levels by 8 pile diameters

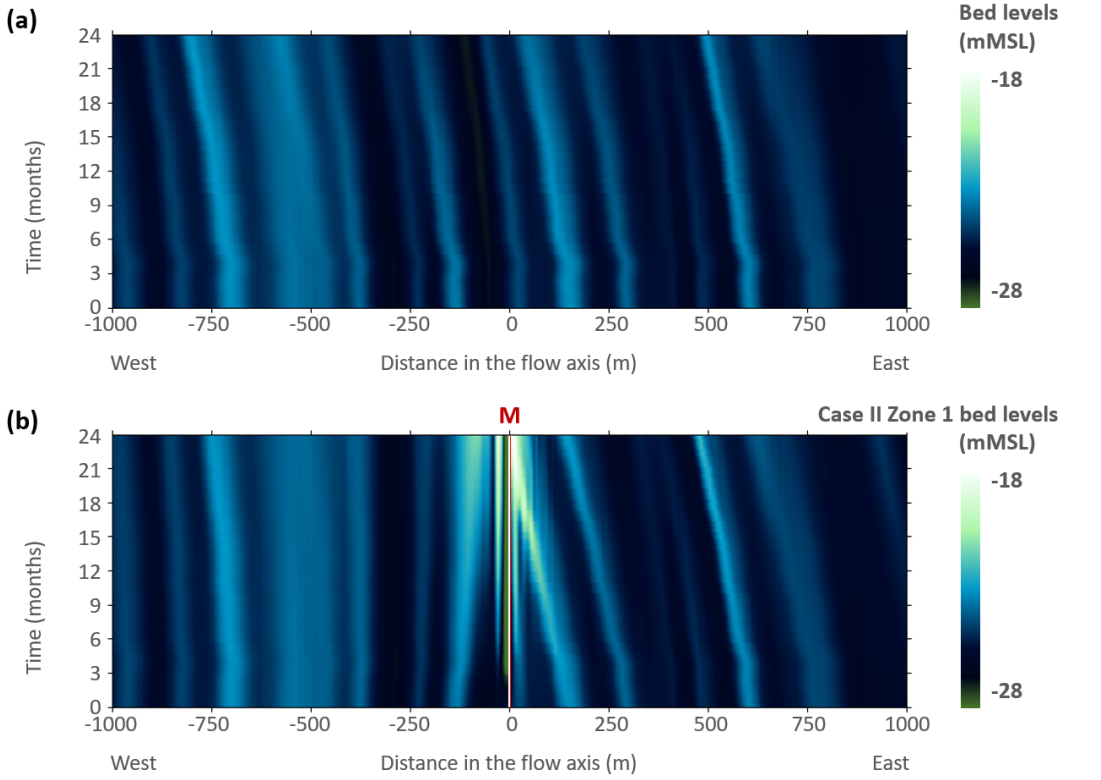

Figure 5.10: Temporal evolution of bed levels extracted in Zone 1: (a) for the baseline simulation and (b) for the Case II simulation, along the tidal axis through the monopile marked 'M' in Figure 5.9(b) and identified by a red line

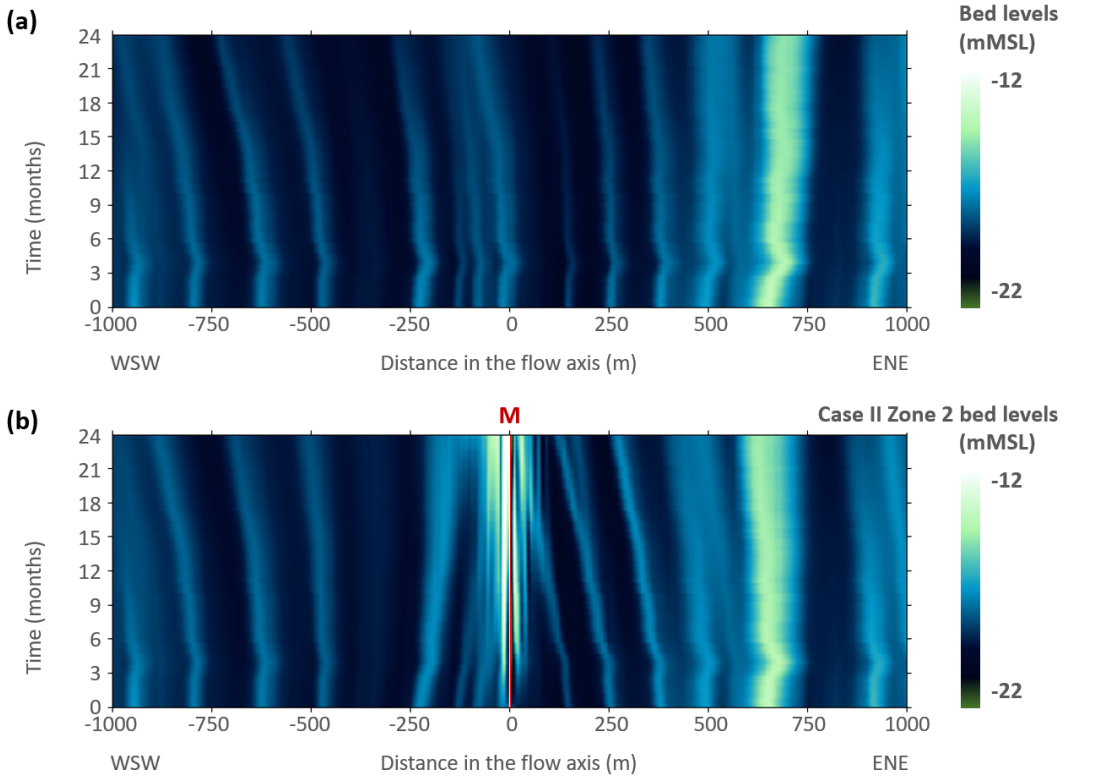

Figure 5.11: Temporal evolution of bed levels extracted in Zone 2: (a) for the baseline simulation and (b) for the Case II simulation, along the tidal axis through the monopile marked 'M' in Figure 5.9(c) and identified by a red line

Initial crest location along transect	Displacement in the natural state (baseline scenario)	Displacement in Case II with an array of monopiles
		Zone 1
-938.8 m	-38.7 m	-4.1 m
-802.3 m	-34.7 m	-8.2 m
-679.9 m	-34.7 m	-6.1 m
-514.8 m	-18.3 m	-8.2 m
-353.8 m	-30.6 m	0.0 m
-209.0 m	-24.5 m	12.2 m
-113.2 m	-42.8 m	30.6 m
176.3 m	-48.9 m	-77.5 m
321.0 m	-44.8 m	-71.4 m
506.5 m	-24.5 m	-34.7 m
628.9 m	-48.9 m	-59.1 m
814.4 m	-67.3 m	-83.6 m
		Zone 2
-773.7 m	-24.5 m	-24.5 m
-604.5 m	-26.5 m	-18.3 m
-455.7 m	-22.4 m	-2.0 m
-209.0 m	-2.0 m	42.8 m
-111.2 m	–	55.0 m
-58.2 m	-18.3 m	–
164.1 m	-2.0 m	-51.0 m
276.2 m	-8.2 m	-57.1 m
396.5 m	0.0 m	-42.8 m
512.7 m	16.3 m	-12.2 m
671.7 m	30.6 m	0.0 m
934.7 m	20.4 m	-6.1 m

Table 5.5: Displacement of the marine dune crests predicted after one year for Case II along transverse profiles through the monopiles marked 'M' in Figure 5.9. The transects are oriented from west to east, with 0 corresponding to the monopile location. Positive displacement values indicate eastward propagation

(Miles et al., 2017), satellite radar (SAR) imagery has revealed kilometre-scale hydrodynamic wakes trailing monopiles down-current (X. Li et al., 2014; Vanhellemont & Ruddick, 2014).

Questions remain about the impact of monopiles on sediment transport processes, in particular in live-bed regime (characterised by sufficient flow velocities to continuously mobilise the seabed sediment). In the previous section, we demonstrated that the presence of monopiles creates a morphodynamic wake along the tidal axis, causing the dune plan shape to distort and converge towards the structure. We will now explore the underlying mechanisms responsible for this effect.

Consider a monopile placed in an environment with a steady current fast enough to support dune movement. In the downstream wake of the structure, the flow velocity is lower compared to the surrounding areas (e.g., X. Li et al., 2014; Rivier et al., 2016). Since sediment transport depends on flow velocity, the dune moves forward more slowly in the hydrodynamic wake than in other regions.

Now, consider that the current changes direction with the following phase of the tide. The downstream becomes the new upstream and vice versa; the sedimentary process is mirrored. If the currents are stronger during one phase of the tidal cycle than during the other, the dune naturally travels in the direction of the net flow (Fredsøe & Deigaard, 1992; van Gerwen et al., 2018). The downstream wake created in turn by each tidal phase causes the section of the dune on the flow axis to converge towards the structure, while the rest of the dune moves at its natural speed in other areas.

This mechanism, which we introduce as the 'wake effect', is illustrated schematically in Figure 5.12.

The predominance of the flood (directed to the right in this sketch) is materialised by a brown net sediment transport vector outside the monopile wake. As a result, the dunes travel to the right, and the position of the dune crest after some time is indicated by a dashed brown line. In the hydrodynamic wake, however, shown as a shaded area, the net sediment transport vector is modified (orange). It becomes stronger to the left of the obstacle due to the reduction of the opposing ebb sediment transport vector, and weaker to the right of the obstacle due to the reduction of the dominant flood sediment transport vector. These changes cause the dune migration to accelerate upstream of the monopile (where 'upstream' is defined in relation to the predominant direction of transport) and to slow or reverse downstream of the monopile. The resulting position of the dune crest in the monopile wake is indicated by a solid orange line.

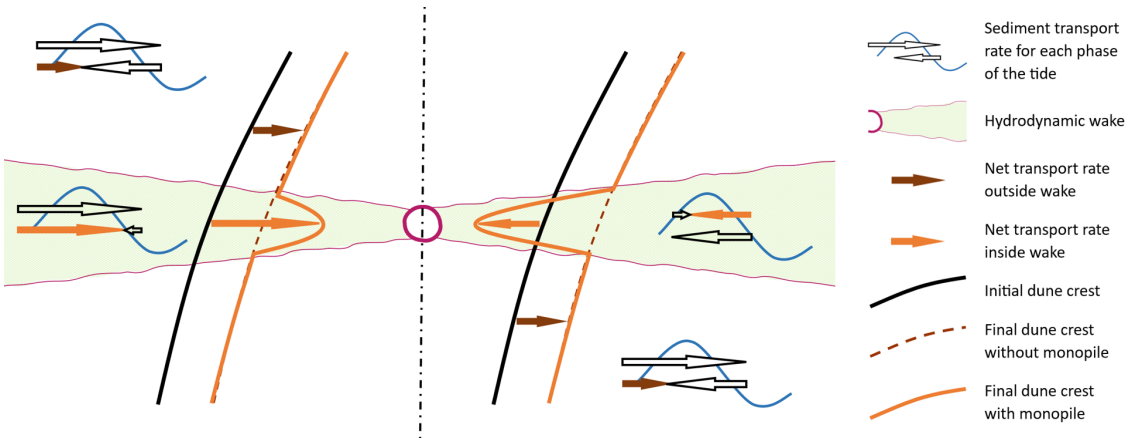

Figure 5.12: Schematic diagram of the influence of a monopile on net sediment transport rates (filled arrows) and marine dune migration (lines). Brown shows the natural state without a monopile; orange the modified state due to the inclusion of a monopile (area of influence indicated by shading). The predominant flow direction is from left to right

The wider the tidal ellipse at the site, the less focused the impact of the monopile. The further the dune from the monopile, the less pronounced its impact. Similarly, a streamlined structure is expected to reduce the hydrodynamic wake (Aly & Dougherty, 2021), thereby minimising the 'wake effect' on dune propagation.

This 'wake effect' differs from the mechanism described by Hong et al. (2017) for linear dunes approaching a monopile with an already formed scour hole under steady currents. Based on experimental observations, such as those by Chiew (1984), the authors indicate that the dune section upstream of the monopile is drawn into the scour hole. The increased turbulence at the base of the structure then picks up and transports the sediment, resulting in a higher transport rate compared to the areas around the monopile. This leads to a stretched, elongated plan shape in the streamwise direction.

It is conceivable that both mechanisms coexist in reality. However, scour processes alone cannot explain the impact on the seabed documented in Section 5.3. This is consistent with the observations made by Couldrey et al. (2020) that factors beyond scour, including natural variations in the hydrodynamics, contributed to the stretching of an isolated crescent-shaped dune they studied off the east coast of the UK.

Not shown in Figure 5.12 for clarity, the presence of the monopile not only creates a hydrodynamic wake but also causes the flow to deviate and increase around the sides of the structure (e.g., Rivier et al., 2016). This deviation will result in a local acceleration of dune propagation.

The 'wake effect' on dune propagation is depicted in Figure 5.13 for Case IA and for Case II in Zone 1. In Case IA, a monopile was placed in the navigation channel to Dunkirk. During the flood phase, currents trend east-northeast, while during the ebb phase, they trend west-southwest. The natural sediment transport pathway and the progression of the dune, driven by the stronger flood, are directed

east-northeast (Durand et al., 2024; Le Bot et al., 2023). The presence of the monopile modifies the velocity and consequently the distribution of sediment transport along the tidal axis. Green shades indicate a decrease in the first-order moment of sediment transport (see Section 5.2.3 for calculation), attributed to a reduction during one of the tidal phases. This distorts and pulls the plan shape of the dunes towards the monopile, as previously explained. At the same time, while the heights remain mostly unchanged, the dune cross-sectional profile is modified with steep slopes facing the monopile on either side (not shown). Green shades are associated with convergence. In contrast, pink lobes indicate an increase due to flow acceleration around the sides, resulting in an accelerated migration of the dune. Pink shades are associated with divergence.

In Case IB (not shown), a monopile was placed on the slope of the Binnen Ratel sandbank. The natural sediment transport pathway and dune progression are also directed east-northeast, but the seabed there is less mobile (Section 4.3). Consequently, the 'wake effect', while still apparent, is less pronounced.

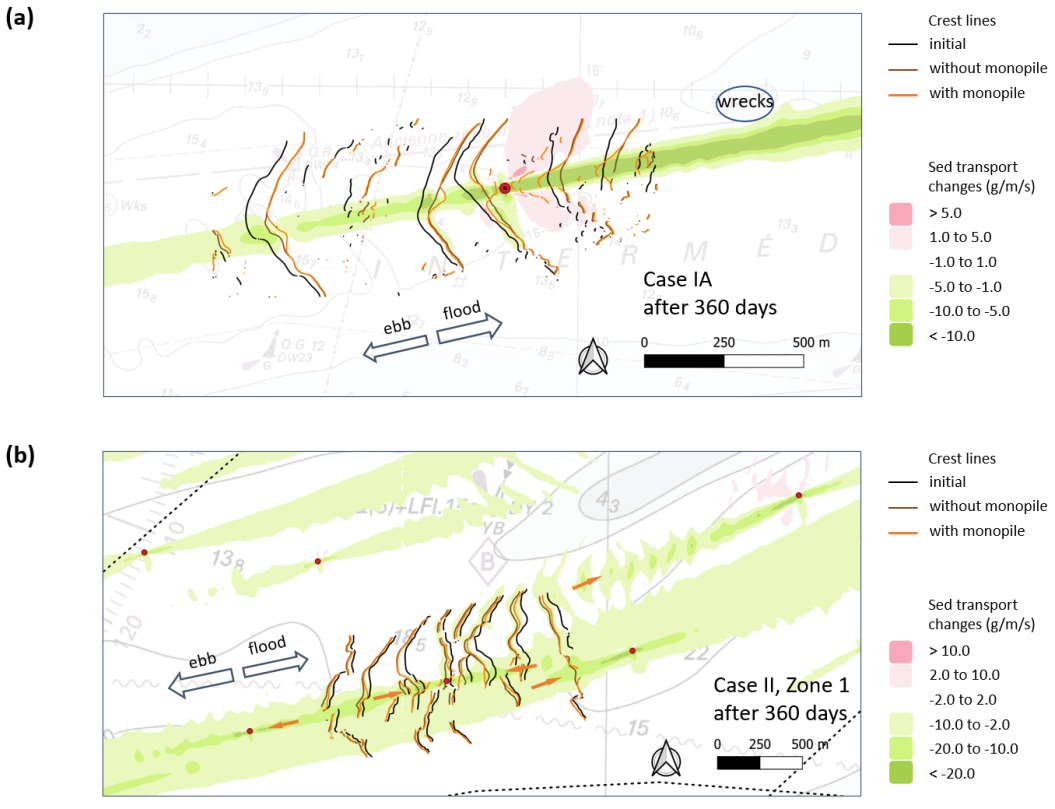

Figure 5.13: Distortion of the dune plan shape on the tidal axis of the monopiles (filled red circles) after one year: (a) for Case IA and (b) for Case II, Zone 1 (Source of the background data: Shom nautical charts 7057 and 7214 respectively)

Interpreting dune behaviour in Case II is considerably more difficult due to the number of monopiles in the array and the competing 'wake effect' each monopile exerts on different sections of the dunes. This complexity is illustrated in Figure 5.13(b) (note the different colour scale) for monopiles located in the gully between the Binnen Ratel and Dyck Oriental sandbanks, in the area we refer to as Zone 1. For clarity, not all dune crests are shown in this figure. Orange arrows identify sections that are pulled east-northeast (because the dominant flow is reduced in the monopile wake) and others that are pulled to the west-southwest (because the opposing flow is reduced) in comparison to the natural progression of the dunes.

It is important to recognise that the first-order moment of sediment transport alone may not fully capture the impact of hard, immobile structures like monopiles on dune dynamics. Changes in the kinetics of dune propagation are observed beyond the coloured areas of influence. For instance, in Case IA, the second and third crescent-shaped dunes north of the wakes (Figure 5.13(a)) migrate at a slightly slower speed when the monopile is in place compared to the baseline. This would be consistent with increased sediment transport around the monopile during ebb flows (we might expect two lobes either side of the tidal axis similar to the flood), but this is not reflected in the first-order moment, even with a finer colour scale.

5.4.2 Impact in relation to the natural variability of sedimentary processes

It is interesting to consider the impact of monopiles in the context of the natural variability of sedimentary processes. Sedimentary processes, particularly dune migration, are influenced by meteorological conditions (Campmans et al., 2018b; P. T. Harris, 1991; Le Bot & Trentesaux, 2004). Offshore Dunkirk, Durand et al. (2024) have suggested a 36% increase in dune migration rate in winter compared to the entire year. These findings are corroborated by the temporal evolution plots presented in Section 5.2, which show periods of accelerated and decelerated migration, as well as periods of reversed migration.

For example, markedly different behaviour is noted between month 4 (17-Mar-2020) and month 7 (17-Jun-2020), usually manifesting as a stabilisation of the dune position. This change is particularly evident in Zone 2 of the OWF, where a sharp acceleration of dune migration towards the west-southwest (left) is observed during this period (Figure 5.11). This corresponds to an unusual spring in 2020. Winds from the southwest prevail annually. The proportion of northeasterly winds typically increases in spring due to cold fronts from Scandinavia, reaching approximately 20%. In spring 2020, however, this proportion rose to nearly 50%, which explains the reversal observed between mid-March and mid-June.

In Section 4.4, we calculated the natural migration speed of the crescent-shaped dune nearest to the Case IA monopile, for each time step in a one-year simulation of the baseline. We conducted a similar analysis for the same period, from December 2019 to November 2020, in the OWF area for dune (sections) just west of the Case II monopiles labelled 'M' in Zones 1 and 2. The monthly variability in migration speed can be evaluated from these hourly data. The results are shown in Figure 5.14. Since we use calendar months, the careful reader will note a slight discrepancy with the data presented in the temporal evolution plots, where the zero time is the start of the simulation, i.e., 17-Nov-2019.

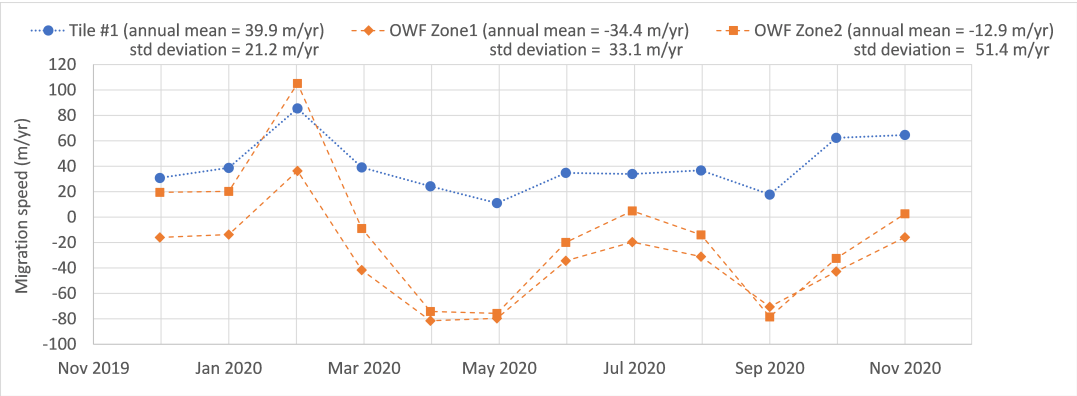

Figure 5.14: Natural variability in the migration speed of dunes in the navigation channel (tile #1, Figure 5.1) and in the OWF area Zones 1 and 2 (Figure 5.4). The dune migration speed is derived from the predicted position of the mid-point of the steep side, as per Durand et al. (2024)

These results indicate significant variability in the migration speed of the dunes, with a standard deviation ranging from 21 m/yr to 51 m/yr. Although it is important to note that the OWF data

(orange) have greater uncertainty due to the coarser resolution used in the analysis, this variability is not unusual. For instance, in the northern Kwintebank on the Belgian continental shelf, Lanckneus and de Moor (1991) observed dune movement of 28 m in one direction over 4 months, followed by 29 m in the opposite direction over the next 5 months (and a net yearly migration close to zero).

Some variability is also observed in the direction of migration, particularly in Zone 2, identified earlier as an area where the sediment transport vectors were turning. The dune selected for the analysis there travels towards the east-northeast during winter (positive speed according to our convention) but towards the west-southwest for the remainder of the year.

In comparison, we calculated the migration speed of the same dune sections for the Case II simulation with monopiles. The results, presented in Table 5.6, demonstrate a significant impact of monopiles, with modified speeds clearly outside natural variability, at least in proximity to the structures. This impact decreases with increasing distance from the monopile, extending several hundred meters within the OWF area.

Zone 1:	natural:	-34.4 m/yr ± 33.1 m/yr
	west of monopile:	+20.9 m/yr ± 14.2 m/yr
	east of monopile:	-69.5 m/yr ± 29.5 m/yr
Zone 2:	natural:	-12.9 m/yr ± 51.4 m/yr
	west of monopile:	+46.4 m/yr ± 25.7 m/yr
	east of monopile:	-57.2 m/yr ± 34.3 m/yr

Table 5.6: Migration speeds calculated for selected dunes in Zones 1 and 2 (Case II), including natural variability

5.4.3 Implications of turbine placement (cumulative effect)

Strategic placement of wind turbines within an array is crucial for several reasons. Firstly, it ensures that the turbines are not positioned in the atmospheric wake of the upstream units (Frandsen et al., 2006; Stevens & Meneveau, 2017), thus maximising the efficiency of the wind resource. Typically, turbines are spaced 8-10 times the rotor diameter in the prevailing wind direction and 3-5 times in the perpendicular direction (Bhattacharya, 2019). Furthermore, careful placement aims to reduce construction and installation costs, particularly by optimising the electrical system and minimising the length of intra-array and export cables (Hou et al., 2019). Separately, micro-siting of wind turbines plays an important role in minimising the environmental impact on marine life and seabed ecosystems. By carefully selecting turbine locations, the overall region of hydro- and/or morphodynamic influence of the OWF can be reduced, and sensitive areas avoided.

Elongated monopile wakes are predicted in Case IA (Figure 5.13(a), single monopile), whose length is consistent with recent observations of kilometre-scale sediment plumes by X. Li et al. (2014) at the East China Sea offshore wind farm, or Vanhellemont and Ruddick (2014) and Forster (2018) at offshore wind farms in the southern North Sea (UK). In Case II, the impact of a 46-turbine wind array is modelled. Given the relatively dense configuration, with a spacing of approximately 1000 m (just under 5 rotor diameters), we anticipate wake interference. Indeed, the wakes associated with the first-order moment of sediment transport are predicted to exceed the spacing distance between neighbouring wind turbines, affecting upstream units. This cumulative effect is apparent when comparing the overlain impact of Cases IIA and IIB (each with only half the number of wind turbines, Figure 5.15(a)) with the impact predicted for the entire array (Figure 5.15(b)).

The areas where combined influences are observed correlate with significant modifications in the kinetics of dune propagation. For example, in the gully between the Binnen Ratel and Dyck Oriental sandbanks, the area of influence of the monopiles is more extensive when all structures are considered collectively rather than individually, due to their alignment with the dominant flow direction. Another area where significant changes are predicted is the region north of Zone 1 and southwest of Zone 2

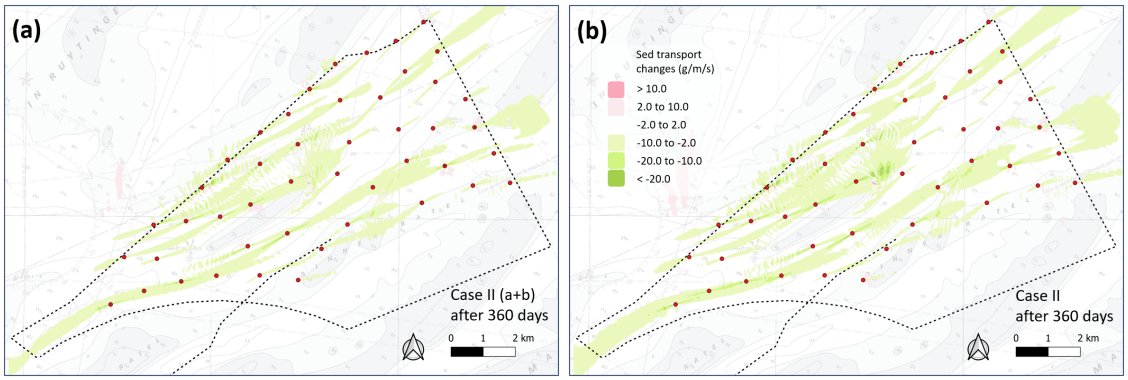

Figure 5.15: Area of influence of monopiles considered (a) individually or (b) collectively in a realistic offshore wind farm, illustrating the cumulative effect of the turbine placement. The first-order moment of sediment transport rate is used as an indicator of the 'wake effect'

(see Figure 5.4 for location). This suggests that the placement of wind turbines must be meticulously considered to minimise impacts on sediment dynamics, dune propagation and, more generally, on marine life and seabed ecosystems (Isaksson et al., 2023).

5.5 Closing remarks

A large-scale 3D numerical model, based on the process-based open**TELEMAC** system, is used to investigate the influence of offshore wind foundations on marine dune fields. This model is applied to a large coastal area in the Southern Bight of the North Sea, where a 600 MW offshore wind project is planned. The area is subject to strong tidal flows and winds originating from the Atlantic Ocean and the North Sea. Marine dunes and sandbanks are present within the wind farm area, with dune migration rates of up to 30 m/year.

Our findings indicate that monopiles significantly affect their environment, causing dunes to converge towards the monopile along the tidal flow axis, while the rest of the dune moves at its natural speed in other areas. In a realistic scenario with 46 wind turbines, each monopile in the array exerts a competing impact on sections of the dune.

We have termed this convergence towards the monopile 'wake effect', which refers to the down-current velocity deficit and subsequent reduction in sediment transport during a tidal phase. This results in an increase in the speed of dune migration in the dominant direction and a reduction (or even reversal) in the subordinate direction.

Although there is considerable natural variability in seasonal dune dynamics due to meteorological influences, the impact of the monopiles is predicted to be greater than this natural variability. Dune propagation is accelerated (in the same or opposite direction) by a factor of 2 to 4.

The cumulative impact of the monopiles on the first-order moment of sediment transport, which we use as an indicator of the 'wake effect', underscores the need for careful placement of the wind turbines in the array to avoid or, at the very least, mitigate the effects on the dune field.

These results contribute to our understanding of the interaction between fixed offshore wind foundations and marine dunes at an intermediate scale that fits between the broader wind farm level and the more localised monopile level. They help to bridge the gap between these two commonly considered approaches.

Chapter 6

Conclusions and recommendations for future work

6.1 Conclusions

This research aims to extend our knowledge of marine dune dynamics and modelling over time and space scales ranging from days to years and metres to kilometres. It also seeks to advance our understanding of the interactions between marine dunes and Offshore Wind Farm (OWF) foundations (Section 1.5.2). To achieve this, we have developed and calibrated a three-dimensional (3D) coastal area model using the open**TELEMAC** system for an application offshore Dunkirk, France, where extensive site-specific data are available. This area is characterised by strong tidal flows and winds originating from the Atlantic Ocean and the North Sea. It features a range of bedforms, including large marine dunes 1 m to 5 m high and hundreds of metres long, with dune migration rates of up to 30 m/yr. Dunkirk is the proposed site for a 600 MW offshore wind project.

In this section, we answer the research questions formulated in Section 1.5.3 of this dissertation.

RQ1. What are the environmental parameters controlling marine dune migration in shallow shelf seas?

Calibrated numerical models can effectively overcome the spatial and temporal constraints inherent to field observations. In Chapter 3, Section 3.5, we presented the findings of a two-year coupled simulation using hydrodynamic and wave models, validated with a comprehensive data set (Chapter 2). A comparison of sediment mobility (excess bed shear-stress) due to tides alone versus waves alone allows the determination of the hydrodynamic processes that control sediment transport.

Our analysis indicates that tidal currents are the primary mechanism responsible for mobilising seabed sediments in areas deeper than 15 mMSL (Figure 3.14). As water depths decrease, the influence of wave processes is expected to increase, particularly in the upper reaches of sandbanks.

Since tidal currents are influenced by wind conditions, the next step of our investigations (Chapter 4) consisted in running numerical simulations using our calibrated 3D morphodynamic model with and without meteorological effects to determine their influence on the dynamics of large marine dunes. This model was shown to accurately reproduce the evolution of the seabed off Dunkirk over periods of months to 1-2 years, including a dynamic winter period in 2019-20.

Our results confirm that marine dune migration is strongly correlated with the amplitude and direction of residual tidal flow and demonstrate that wind conditions play a significant role in this process. When meteorological forcing is excluded from the model, the migration speeds are underestimated by up to a factor of 2.

These insights enhance our understanding of the environmental parameters that control marine dune movements in shallow shelf seas. By recognising the role of meteorological conditions (in particular, winds) in predictive morphodynamic models, it is possible to make more accurate predictions of

sediment transport and seabed evolution, which contributes to the development of more sustainable coastal management practices.

RQ2. How does a marine dune field evolve in space and time in shallow shelf seas?

In Chapter 4, we also examined the impact on dune dynamics of meteorological events from directions opposite to the dominant sediment transport. For this, a period covering a sustained storm from the northwest was simulated.

Our research demonstrates that anomalous winds can counteract the tidal residual (Figure 4.8), causing dune migration that is contrary to the general trend - and to the cross-sectional shape of the dunes. However, these anomalous wind events are typically short-lived and sporadic, and their effect on dune evolution dissipates once the winds subside or change direction.

If adverse wind events influence short-term sediment patterns, it can be argued that the long-term dynamics of large marine dunes is primarily governed by consistent and prevailing wind conditions. We suggest that the proportion of the following versus adverse winds should be considered (in terms of frequency and duration) when assessing dune dynamics, as the following winds amplify tidal effects, whereas adverse winds counteract them.

The seasonal and multi-year variability in the wind regime also raises important questions regarding the most appropriate time scales for monitoring dune movement and developing long-term forecasting strategies. This is particularly relevant when considering the potential implications of climate change over the lifespan of an OWF project.

Our findings provide a better understanding of how dune fields respond to weather in open marine environments. By using a complex process-based 3D modelling approach on a large scale and with realistic forcing, this research extends previous studies that relied mainly on the analysis of observational data or idealised modelling.

RQ3. To which extent does the presence of an offshore wind farm impact the marine dune field it was developed in?

In Chapter 5, we presented the results of numerical simulations using our 3D morphodynamic model, where a triangular element was removed from the mesh for each monopile foundation. Initial exploratory scenarios were run for a single wind turbine, and subsequently extended to a realistic scenario comprising 46 turbines in the proposed Dunkirk OWF footprint. The results of these two-year simulations were compared with a baseline simulation, representing the natural state without wind turbines, to understand the dynamics between marine dunes and fixed monopile foundations.

Our analysis indicates that the effect of the monopile, which we term the monopile ‘wake effect’, manifests as the convergence of part of the dune (along the flow axis) towards the structure, while the rest of the dune continues to move at its natural speed in other areas. This results in a distortion of the plan shape of the dune (Figure 5.12). In a realistic scenario with an array of wind turbines, each monopile exerts a competing ‘wake effect’ on sections of the dune.

This phenomenon is attributed to the velocity deficit in the wake of monopiles, which reduces the sediment transport rate during a tidal phase. In the dominant transport direction, this results in a higher migration speed of the dune section on the flow axis compared to areas outside it. Conversely, in the subordinate transport direction, the migration speed along the flow axis is reduced, to the extent that the balance between dominant and subordinate directions can be reversed, changing the direction of migration.

Our research shows that these changes in migration speed are significant, defined here as exceeding the natural levels of inter-seasonal variability in dune dynamics - which we have previously linked to meteorological influences. Dune propagation is accelerated by a factor of 2 to 4. Separately, we have demonstrated the cumulative impact of monopiles in an array on the first-order moment of sediment

transport, which we use as an indicator of the 'wake effect'. These findings highlight the need for strategic siting of wind turbines to minimise the impact on dune fields.

These results improve our understanding of how fixed offshore wind foundations interact with marine dunes at an intermediate scale. This bridges the knowledge gap between the broader wind farm scale and the more localised monopile scale. The knowledge gained can guide the design and placement of offshore wind farms to minimise environmental disturbances.

6.2 Perspectives

We conclude this chapter with the most relevant recommendations for future research on large marine dunes.

Developing strategies for long-term morphodynamic predictions

Although it is preferable to run simulations for periods spanning several years in real time, it is currently challenging to envisage simulations that extend over several decades using complex process-based 3D models with realistic inputs.

Running a one-year simulation with our 3D morphodynamic model (TELEMAC-3D+GAIA modules) requires a minimum of 3 days, depending on the allocation of the HPC queue, using 20 Intel® Xeon® Platinum processors (960 cores). Unlike hydrodynamic simulations, which can be split and run in parallel after an adequate spin-up period, yearly morphodynamic simulations must be run sequentially. This sequential approach is necessary to accurately account for bed levels in the morphodynamic feedback loop (Figure 1.4). The typical lifespan of an Offshore Wind Farm (OWF) is 30 years, with leases potentially lasting two full project life cycles. A simulation of that length (60 years) would require at least half a year of computer time. Therefore, it is essential to develop long-term forecast strategies.

Idealised configurations (such as 2DV models, simplified geometries, or forcings) lack a complete representation of physical processes, which, in our opinion, precludes their use in comprehensive studies. Unlike the astronomical tide, which is purely deterministic and allows simplifying assumptions in long-term morphological simulations (e.g., Latteux, 1995; Schrijvershof et al., 2023), other influential hydrodynamic forcings (such as winds and waves) are inherently variable. In this context, using a morphological acceleration factor that distorts the hydrodynamic and morphodynamic timelines (Lesser et al., 2004; Ranasinghe et al., 2011) is also undesirable due to the non-linearity introduced when considering meteorological events (and other non-tidal processes).

A sensible approach might be to determine the response of the system for one representative year (defined by the wind regime in tidally dominated regions) as a first approximation. This analysis could subsequently be refined with the predicted response to a matrix of specific adverse or extreme events carefully selected from long-term site-specific metocean data.

Ideally, this approach would be supported by repeated bathymetric surveys to ensure the continued relevance of the model predictions. This would also allow for corrections as needed, similar to data assimilation processes. Furthermore, conducting surveys immediately after severe weather would enhance the prediction of extreme events.

Exploring the contribution of wave processes

In this research, we have quantified the influence of wind and pressure on dune dynamics. Future work could consider the influence of (non-linear) waves.

Although tidal currents often have a more persistent and predictable influence on sediment transport processes and seabed evolution, surface water waves can also play a role in shallow shelf seas. This is particularly true at shallow water depths (depth/wavelength ratio less than 1/20, region to the left of Figure 6.1) and during stormy conditions. Under these conditions, wave-induced motions

can extend to the seabed. Durand et al. (2022b), for example, provided estimates of wave-induced shear-stresses compared to current-induced shear-stresses in winter versus summer, highlighting the relative importance of wave processes in severe weather.

Typically, waves are divided into frequently occurring conditions (the general wave climate) and less frequent but much more energetic events (extreme wave conditions). For coastal engineers, extreme events are most relevant for the design of offshore structures, the assessment of coastal defences, or the protection of harbours. For geomorphologists, however, the distinction is less clear. It would be interesting to build on the work of Campmans et al. (2018b, with an idealised modelling approach) to investigate which influence is more important for dune dynamics, as we have done for winds, bearing in mind that the timing of events may also play a role.

As waves travel into shallower water, they begin to interact with the seabed, resulting in an asymmetric wave profile. This asymmetry not only participates in stirring up the seabed sediment, but also generates net sediment transport since the velocities below the wave crest (in the direction of wave travel) are higher than the velocities below the trough (directed offshore). This process is not captured by the SvR97 sediment transport predictor, which was developed by applying the turbulent kinetic energy principles of Grass (1981) to the current alone predictor of van Rijn (1984b): waves only help to mobilise sediment, which is then transported by currents.

This is where the SD05 predictor has an advantage as it accounts for the contribution of asymmetric waves (2nd harmonic). Soulsby and Damgaard recommend using Stokes 2nd order wave theory to obtain the 2nd harmonic for wave orbital velocities. We suggest using the method of Isobe and Horikawa (1982), which is consistent with the observation in Soulsby (1997) that linear wave theory predicts orbital velocities below the crest reasonably well, while exaggerating the velocities below the trough. From these velocities, the bed shear-stresses needed for the SD05 predictor can be calculated using a quadratic friction law. Strategies then need to be devised to stabilise the SD05 predictor over the long term, as our research has shown it is prone to instabilities, making it less reliable over periods longer than a few months.

For illustrative purposes, data points extracted from our coupled hydrodynamic and wave model (Section 3.5) for a location on the upper reaches of the Binnen Ratel sandbank are overlaid as dark pink points on the Le Méhauté diagram (Figure 6.1). This diagram is a tool used in coastal engineering

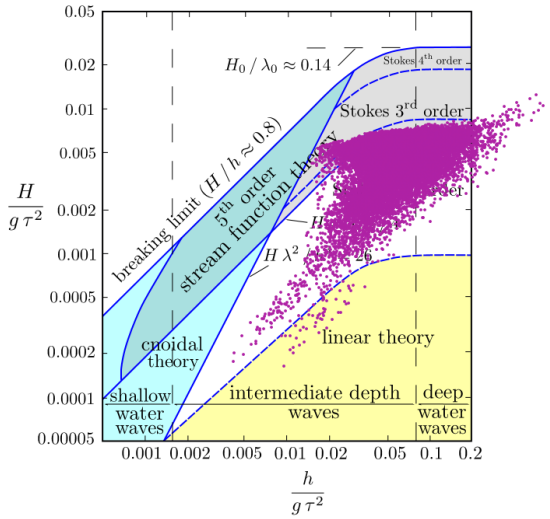

Figure 6.1: Model data for a location atop the Binnen Ratel sandbank, overlaid as dark pink data points on the Le Mehauté Diagram to illustrate wave non-linearity (Data source: Section 3.5, period: 2019-21)

to determine the appropriate wave theory for a given set of wave height (H), wave period (T), and water depth (h). The yellow area in Figure 6.1 corresponds to linear wave theory, i.e., sinusoidal waves. It is clear that, while the waves are considered intermediate to deep water waves, they are non-linear on top of the Binnen Ratel sandbank.

Integrating fine-scale processes into medium-scale modelling

We have alluded to the question of scale in this dissertation. The aim of our research was to gain insight into the hydrodynamics, the sediment transport and morphological processes in a marine dune environment, at a coastal scale. Much work, in particular relating to scour processes, is conducted at the scale of a single monopile. Integrating the knowledge gained at this fine scale into larger area models would be extremely relevant, for example to capture the trubulent wake.

Our research was part of the MODULLES project (`https://www.france-energies-marines.org/en/projects/modulles/`), a three-year initiative led by France Energies Marines, aimed at improving our understanding of marine dunes and their interactions with offshore wind farms. Several work packages were included under the MODULLES umbrella, particularly:

- WP2 - Numerical modelling of scouring and sediment transport close to OWF components;
- WP3 - Numerical modelling of marine dune fields in an offshore wind farm context, of which our research is a part; and
- WP4 - Physical modelling of marine dunes in offshore wind farms context.

The MODULLES project is approaching its end. As the outcomes of the WP2 and WP4 work packages become available, consolidating our knowledge of fine-scale processes both from a numerical viewpoint (WP2, with a CFD model, see also Nagel et al. (2018)) and through physical experiments (WP4, see also S.-Y. Wang et al. (2024); Whitehouse and Stroescu (2023)), they should be used to develop proxies that allow better integration of OWF elements in morphodynamic modelling.

This may address, for example, the physical processes absent from our current modelling approach that will prevent sediment from accumulating on either side of the monopile when the dunes converge on it, trapped by the attractive 'wake effect' at present. It is possible that suspension processes may play a crucial role in this context, effectively transporting sediment suspended in the water column by turbulence near the monopile away from the area of influence (Bailey et al., 2024, Figure 6.2).

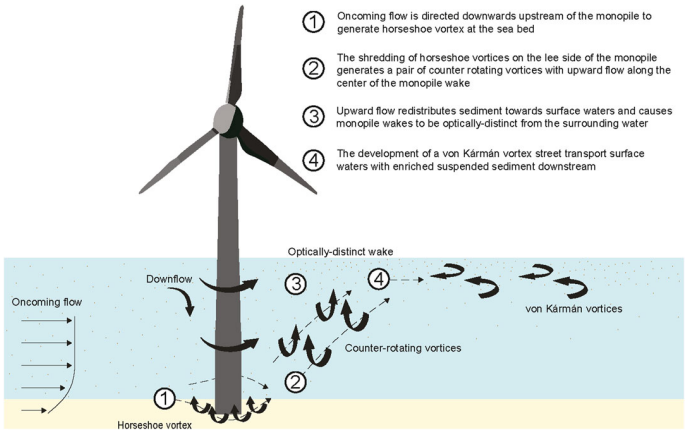

Figure 6.2: Schematic diagram of the influence of a bottom-mounted vertical structure on surrounding flow and mechanisms to redistribute suspended sediment to the surface (Bailey et al., 2024)

In conjunction with our research findings, medium-scale modelling could address several technical challenges in the Offshore Wind industry. For example, it could help refine the reference seabed level used in designing structures like monopile and jacket foundations. It could also aid in developing effective scour protection measures to ensure the structural integrity of these foundations. Additionally,

for cable laying, it could assist in evaluating the sediment layer thickness above the reference seabed level and the dune residence time. This information is crucial for designing the cable as well as for determining trench depth, balancing the maximum burial depth desirable for heat transfer and the minimum burial depth necessary for protection.

Investigating implications on ecosystem functioning

In recent years, there has been considerable interest in the effects of human activities on ecosystems, particularly offshore wind (e.g., Isaksson et al., 2023; Lefaible et al., 2018, 2019; Trifonova & Scott, 2023). The Ecological Consequences of Offshore Wind (ECOWind) research initiative (2022-2026, ECOWind research programme website) has caught our attention. This programme aims to understand the ecological implications of Offshore Wind Farms, with the goal of minimising negative effects on marine life while supporting the shift to renewable energy.

Marine dunes are ecologically significant areas. Although they host a limited number of species, these species are unique and specifically adapted to these dynamic ecosystems, which Robert et al. (2024) suggest may also extend to anthropogenic disturbances. The MODULLES project included a work package (WP6) aimed at identifying the environmental parameters essential for studying the ecological resilience of marine dune ecosystems (Figure 6.3). As a pre-study, its purpose was to lay the groundwork for a new project focusing on the ecological responses of marine dunes to OWFs, covering different spatial and temporal scales of environmental impact. To our knowledge, the ECOWind programme does not specifically address the impact of the remodelling of marine dunes within OWFs. Potential synergies could be explored, in particular with the ECOWind-ACCELERATE work package, which focuses on the ecological implications of increased seabed mobility around wind farms. Finer scale modelling may be required for this, as different species may be sensitive not only to changes in the seabed morphology but also the sediment composition (e.g., fining and organic matter enrichment).

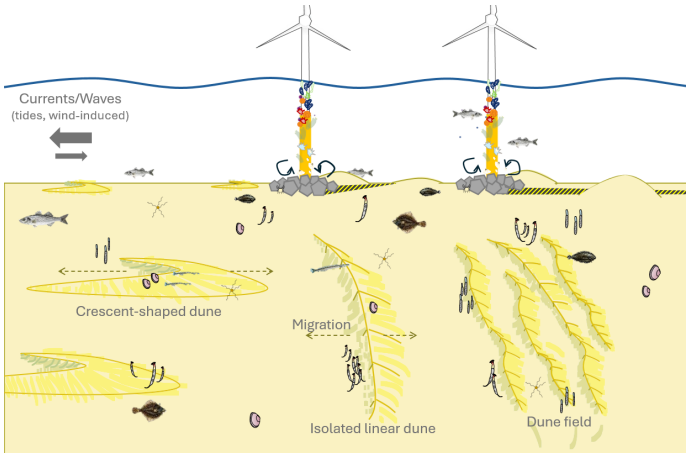

Figure 6.3: Marine dunes are not barren! Their ecological responses to OWFs (Credit: Nolwenn Quillien, FEM)

Bibliography

Aliotta, S., & Perillo, G. M. E. (1987). A sand wave field in the entrance to Bahía Blanca Estuary, Argentina. *Marine Geology*, *76*, 1-14. https://doi.org/10.1016/0025-3227(87)90013-2

Allen, J. R. L. (1968). The nature and origin of bed-form hierarchies. *Sedimentology*, *10*(3), 161-182. https://doi.org/10.1111/j.1365-3091.1968.tb01110.x

Aly, A. M., & Dougherty, E. (2021). Bridge pier geometry effects on local scour potential: A comparative study. *Ocean Engineering*, *234*, 109326. https://doi.org/10.1016/j.oceaneng.2021.109326

Anthony, E. J., & Aagaard, T. (2020). The lower shoreface: Morphodynamics and sediment connectivity with the upper shoreface and beach. *Earth-Science Reviews*, *210*, 1-32. https://doi.org/10.1016/j.earscirev.2020.103334

Apsley, D. D., & Stansby, P. K. (2008). Bed-load sediment transport on large slopes: Model formulation and implementation within a RANS solver. *Journal of Hydraulic Engineering*, *134*(10). https://doi.org/10.1061/(ASCE)0733-9429(2008)134:10(1440)

Ardhuin, F., Rogers, E., Babanin, A. V., Filipot, J.-F., Magne, R., Roland, A., ... Collard, F. (2010). Semiempirical dissipation source functions for ocean waves. part i: Definition, calibration, and validation. *Journal of Physical Oceanography*, *40*(9), 1917 - 1941. https://doi.org/10.1175/2010JPO4324.1

Ashley, G. M. (1990). Classification of large-scale subaqueous bedforms: A new look at an old problem - SEPM bedforms and bedding structures. *Journal of Sedimentary Petrology*, *60*(1), 160-172. https://doi.org/10.2110/jsr.60.160

Augris, C., Clabaut, P., & Vicaire, O. (1990). *Le domaine marin du Nord-Pas de Calais : nature, morphologie et mobilité des fonds*. Institut Français de Recherche pour l'Exploitation de la Mer.

Auguste, C., Marsh, P., Nader, J.-R., Penesis, I., & Cossu, R. (2021). Modelling morphological changes and migration of large sand waves in a very energetic tidal environment: Banks Strait, Australia. *Energies*, *14*(13). https://doi.org/10.3390/en14133943

Auguste, C., Nader, J.-R., Marsh, P., Penesis, I., & Cossu, R. (2022). Modelling the influence of tidal energy converters on sediment dynamics in Banks Strait, Tasmania. *Renewable Energy*, *188*, 1105-1119. https://doi.org/10.1016/j.renene.2022.02.077

Bagnold, R. A. (1966). An approach to the sediment transport problem from general physics. *Geological Survey Professional Paper*, *422*(I). https://doi.org/10.3133/pp422I

Bailard, J. A. (1981). An energetics total load sediment transport model for a plane sloping beach. *Journal of Geophysical Research: Oceans*, *86*(C11), 10938-10954. https://doi.org/10.1029/JC086iC11p10938

Bailey, L. P., Dorrell, R. M., Kostakis, I., McKee, D., Parsons, D., Rees, J., ... Forster, R. (2024). Monopile-induced turbulence and sediment redistribution form visible wakes in offshore wind farms. *Frontiers in Earth Science*, *12*. https://doi.org/10.3389/feart.2024.1383726

Bao, J., Cai, F., Shi, F., Wu, C., Zheng, Y., Lu, H., & Sun, L. (2020). Morphodynamic response of sand waves in the Taiwan Shoal to a passing tropical storm. *Marine Geology*, *426*, 106196. https://doi.org/10.1016/j.margeo.2020.106196

Barnard, P. L., Erikson, L. H., & Kvitek, R. G. (2011). Small-scale sediment transport patterns and bedform morphodynamics: new insights from high-resolution multibeam bathymetry. *Geo-Marine Letters*, *31*, 227-236. https://doi.org/10.1007/s00367-011-0227-1

Barnard, P. L., Hanes, D. M., Rubin, D. M., & Kvitek, R. G. (2006). Giant sand waves at the mouth of San Francisco Bay. *Eos, Transactions American Geophysical Union*, *87*(29), 285-289. https://doi.org/10.1029/2006EO290003

Barrie, J. V., & Conway, K. W. (2014). Seabed characterization for the development of marine renewable energy on the Pacific margin of Canada. *Continental Shelf Research*, *83*, 45-52. Geoscience and Habitat Mapping for Marine Renewable Energy https://doi.org/10.1016/j.csr.2013.10.016

Bartholdy, J., Bartholomä, A., & Flemming, B. W. (2002). Grain-size control of large compound flow-transverse bedforms in a tidal inlet of the Danish Wadden Sea. *Marine Geology*, *188*(3), 391-413. https://doi.org/10.1016/S0025-3227(02)00419-X

Belderson, R. H., Johnson, M. A., & Kenyon, N. H. (1982). Bedforms. In A. H. Stride (Ed.), *Offshore tidal sands, processes and deposits* (p. 27 - 57). Springer.

Bellec, V. K., Bøe, R., Bjarnadóttir, L. R., Albretsen, J., Dolan, M. F. J., Chand, S., ... Elvenes, S. (2019). Sandbanks, sandwaves and megaripples on Spitsbergenbanken, Barents Sea. *Marine Geology*, *416*. https://doi.org/10.1016/j.margeo.2019.105998

Benoit, M., Marcos, F., & Becq, F. (1996). Development of a third generation shallow-water wave model with unstructured spatial meshing. In *Coastal engineering 1996* (p. 465-478). ASCE. September 2-6, 1996. Orlando, Florida

Berné, S., Allen, G., Auffret, J. P., Chamley, H., Durand, J., & Weber, O. (1989, 11). Essai de synthèse sur les dunes hydrauliques géantes tidales actuelles. *Bulletin de la Société Géologique de France*, *V*(6), 1145-1160. https://doi.org/10.2113/gssgfbull.V.6.1145

Bertier, J. (2009). *Analyse multi-échelle de la morphodynamique d'une plage artificielle, Avant-port Ouest de Dunkerque (Nord de la France).* (PhD thesis, in French). Université du Littoral Côte d'Opale. Retrieved from https://hal.archives-ouvertes.fr/tel-00463152v1

Besio, G., Blondeaux, P., Brocchini, M., Hulscher, S. J. M. H., Idier, D., Knaapen, M. A. F., ... Vittori, G. (2008). The morphodynamics of tidal sand waves: A model overview. *Coastal Engineering*, *55*(7), 657-670. https://doi.org/10.1016/j.coastaleng.2007.11.004

Besio, G., Blondeaux, P., Brocchini, M., & Vittori, G. (2004). On the modeling of sand wave migration. *Journal of Geophysical Research: Oceans*, *109*(C4). https://doi.org/10.1029/2002JC001622

Besio, G., Blondeaux, P., & Frisina, P. (2003). A note on tidally generated sand waves. *Journal of Fluid Mechanics*, *485*, 171-190. https://doi.org/10.1017/S0022112003004415

Besio, G., Blondeaux, P., & Vittori, G. (2006). On the formation of sand waves and sand banks. *Journal of Fluid Mechanics*, *557*, 1-27. https://doi.org/10.1017/S0022112006009256

Best, J. (2005). The fluid dynamics of river dunes: A review and some future research directions. *Journal of Geophysical Research: Earth Surface*, *110*(F4). https://doi.org/10.1029/2004JF000218

Bhattacharya, S. (2019). *Design of foundations for offshore wind turbines*. John Wiley & Sons. https://doi.org/10.1002/9781119128137

Bijker, E. W. (1968). Littoral drift as function of waves and current. In *Coastal engineering 1968.* ASCE. London, UK

Bijker, R., Wilkens, J., & Hulscher, S. J. M. H. (1998). Sandwaves: Where and why. In *Proceedings of the 8th international offshore and polar engineering conference* (p. 153-158). May 24-29, 1998. Montreal, Canada

Blunden, L., Haynes, S. G., & Bahaj, A. (2020). Tidal current power effects on nearby sandbanks: a case study in the Race of Alderney. *Philosophical Transactions of The Royal Society A*, *378*(2178). https://doi.org/10.1098/rsta.2019.0503

Bonnefille, R., Lepetit, J. P., Graf, M., & Leroy, J. (1971). *Nouvel avant-port de Dunkerque. Mesures en nature* (Tech. Rep. No. report HC042/05). E.D.F., Laboratoire National d'Hydraulique.

Boothroyd, J. C. (1978). Mesotidal inlets and estuaries. In R. A. Davis (Ed.), *Coastal sedimentary environments* (p. 287-360). Springer US.

Borsje, B. W., Kranenburg, W. M., Roos, P. C., Matthieu, J., & Hulscher, S. J. M. H. (2014). The role of suspended load transport in the occurrence of tidal sand waves. *Journal of Geophysical Research: Earth surface*, *119*(4), 701–716. https://doi.org/10.1002/2013JF002828

Borsje, B. W., Roos, P. C., Kranenburg, W., & Hulscher, S. J. M. H. (2013). Modeling tidal sand wave formation in a numerical shallow water model: The role of turbulence formulation. *Continental shelf research*, *60*, 17–27. https://doi.org/10.1016/j.csr.2013.04.023

Bouma, A. H., Rappeport, M. L., Orlando, R. C., & Hampton, M. A. (1980). Identification of bedforms in Lower Cook Inlet, Alaska. *Sedimentary Geology*, *26*(1), 157-177. https://doi.org/10.1016/0037-0738(80)90010-x

Bousquet, N., & Bernardara, P. (2018). Outils informatiques. In *Événements naturels extrêmes: théorie statistique et mitigation du risque* (pp. 489–490). Lavoisier.

Bouttier, F. (2007). Arome, avenir de la prévision régionale. *La Météorologie*(58), 12-20. https://doi.org/10.4267/2042/18203

Calafat, F. M., Wahl, T., Tadesse, M. G., & Sparrow, S. N. (2022). Trends in Europe storm surge extremes match the rate of sea-level rise. *Nature*, *603*(7903), 841-845. https://doi.org/10.1038/s41586-022-04426-5

Campmans, G. H. P., Roos, P. C., de Vriend, H. J., & Hulscher, S. J. M. H. (2017). Modeling the influence of storms on sand wave formation: A linear stability approach. *Continental Shelf Research*, *137*, 103-116. https://doi.org/10.1016/j.csr.2017.02.002

Campmans, G. H. P., Roos, P. C., de Vriend, H. J., & Hulscher, S. J. M. H. (2018a). The influence of storms on sand wave evolution: A nonlinear idealized modeling approach. *Journal of Geophysical Research: Earth Surface*, *123*(9), 2070-2086. https://doi.org/10.1029/2018JF004616

Campmans, G. H. P., Roos, P. C., & Hulscher, S. J. M. H. (2019). Storm influences on sand wave dynamics: an idealized modelling approach. In *Marine and river dune dynamics vi book of proceedings* (p. 33-39). April 1-3, 2019. Bremen, Germany

Campmans, G. H. P., Roos, P. C., Schrijen, E. P. W. J., & Hulscher, S. J. M. H. (2018b). Modeling wave and wind climate effects on tidal sand wave dynamics: A North Sea case study. *Estuarine, coastal and shelf science*, *213*, 137–147. https://doi.org/10.1016/j.ecss.2018.08.015

Campmans, G. H. P., Roos, P. C., Van der Sleen, N. R., & Hulscher, S. J. M. H. (2021). Modeling tidal sand wave recovery after dredging: effect of different types of dredging strategies. *Coastal Engineering*, *165*, 103862. https://doi.org/10.1016/j.coastaleng.2021.103862

CANDHIS. (2022). *Integrated wave parameters obtained from the gravelines buoy.* `https://candhis.cerema.fr/`.

Cavaleri, L., & Rizzoli, P. M. (1981). Wind wave prediction in shallow water: Theory and applications. *Journal of Geophysical Research: Oceans*, *86*(C11), 10961-10973. https://doi.org/10.1029/JC086iC11p10961

Cazenave, P. W., Torres, R., & Allen, J. I. (2016). Unstructured grid modelling of offshore wind farm impacts on seasonally stratified shelf seas. *Progress in Oceanography*, *145*, 25-41. https://doi.org/10.1016/j.pocean.2016.04.004

Cerema. (2021). *Fiches synthétiques de mesure des états de mer - Tome 1 - Mer du Nord, Manche et Atlantique* (Tech. Rep. No. ISBN : 978-2-37180-497-5). Cerema.

Chiew, Y. M. (1984). *Local scour at bridge piers* (PhD thesis). University of Auckland.

Christiansen, M. B., & Hasager, C. B. (2005). Wake effects of large offshore wind farms identified from satellite SAR. *Remote Sensing of Environment*, *98*(2), 251–268. https://doi.org/10.1016/j.rse.2005.07.009

Christiansen, N., Daewel, U., Djath, B., & Schrum, C. (2022). Emergence of large-scale hydrodynamic structures due to atmospheric offshore wind farm wakes. *Frontiers in Marine Science*, *9*. https://doi.org/10.3389/fmars.2022.818501

Christie, E., Li, M., & Moulinec, C. (2012). Comparison of 2D and 3D large scale morphological modeling of offshore wind farms using HPC. In *Coastal engineering 2012.* ASCE. Santander, Spain

Clark, S., Schroeder, F., & Baschek, B. (2014). *The influence of large offshore wind farms on the North Sea and Baltic Sea - a comprehensive literature review* (Tech. Rep. No. HZG Report 2014-6). Helmholtz-Zentrum Geesthacht.

Codiga, D. L. (2011). *Unified tidal analysis and prediction using the UTide Matlab functions* (Tech. Rep. No. 2011-01). Graduate School of Oceanography, University of Rhode Island.

Cooper, B., & Beiboer, F. (2002). *Potential effects of offshore wind developments on coastal processes* (Tech. Rep. No. URN 02/1336). ABP Marine Environmental Research Ltd.

Coughlan, M., Guerrini, M., Creane, S., O'Shea, M., Ward, S. L., Van Landeghem, K. J. J., ... Doherty, P. (2021). A new seabed mobility index for the Irish Sea: Modelling seabed shear stress and classifying sediment mobilisation to help predict erosion, deposition, and sediment distribution. *Continental Shelf Research*, *229*, 104574. https://doi.org/10.1016/j.csr.2021.104574

Couldrey, A. J., Benson, T., Knaapen, M. A. F., Marten, K., & Whitehouse, R. J. S. (2020). Morphological evolution of a barchan dune migrating past an offshore wind farm foundation. *Earth Surface Processes and Landforms*, *45*, 2884-2896. https://doi.org/10.1002/esp.4937

Courrech du Pont, S., Rubin, D. M., Narteau, C., Lapôtre, M. G. A., Day, M., Claudin, P., ... Wiggs, G. F. S. (2024). Complementary classifications of aeolian dunes based on morphology, dynamics, and fluid mechanics. *Earth-Science Reviews*, *255*, 104772. https://doi.org/10.1016/j.earscirev.2024.104772

Creane, S., Coughlan, M., O'Shea, M., & Murphy, J. (2022). Development and dynamics of sediment waves in a complex morphological and tidal dominant system: Southern Irish Sea. *Geosciences*, *12*(12). https://doi.org/10.3390/geosciences12120431

Creane, S., O'Shea, M., Coughlan, M., & Murphy, J. (2023). Morphological modelling to investigate the role of external sediment sources and wind and wave-induced flow on sand bank sustainability: An Arklow Bank case study. *Journal of Marine Science and Engineering*, *11*(10). https://doi.org/10.3390/jmse11102027

da Silva, P. A., Temperville, A., & Seabra Santos, F. (2001). Parameterized sand transport model for combined currents and waves in rippled and flat bed regimes. In L. C. van Rijn, A. G. Davies, J. van de Graaff, & J. S. Ribberink (Eds.), *SEDMOC Sediment transport modelling in marine coastal environments* (p. CE1-CE10). Aqua Publications.

Dalrymple, R. W., Knight, R. J., & Lambiase, J. J. (1978). Bedforms and their hydraulic stability relationships in a tidal environment, Bay of Fundy, Canada. *Nature*, *275*, 100-104. https://doi.org/10.1038/275100a0

Damen, J. M., van Dijk, T. A. G. P., & Hulscher, S. J. M. H. (2018). Spatially varying environmental properties controlling observed sand wave morphology. *Journal of Geophysical Research: Earth Surface*, *123*(2), 262-280. https://doi.org/10.1002/2017JF004322

Damveld, J. H., Borsje, B. W., Roos, P. C., & Hulscher, S. J. M. H. (2020). Horizontal and vertical sediment sorting in tidal sand waves: Modeling the finite-amplitude stage. *Journal of Geophysical Research: Earth Surface*, *125*(10), e2019JF005430. https://doi.org/10.1029/2019JF005430

Damveld, J. H., Roos, P. C., Borsje, B. W., & Hulscher, S. J. M. H. (2019). Modelling the two-way coupling of tidal sand waves and benthic organisms: a linear stability approach. *Environmental Fluid Mechanics*, *19*(5), 1073-1103. https://doi.org/10.1007/s10652-019-09673-1

Daniell, J. J., Harris, P. T., Hughes, M. G., Hemer, M., & Heap, A. (2008). The potential impact of bedform migration on seagrass communities in Torres Strait, northern Australia. *Continental Shelf Research*, *28*(16), 2188-2202. https://doi.org/10.1016/j.csr.2008.03.036

Daubert, O., Hervouet, J.-M., & Jami, A. (1989). Description of some numerical tools for solving incompressible turbulent and free surface flows. *International Journal for Numerical Methods in Engineering*, *27*(1), 3-20. https://doi.org/10.1002/nme.1620270103

Davies, A. G., & Robins, P. E. (2017). Residual flow, bedforms and sediment transport in a tidal channel modelled with variable bed roughness. *Geomorphology*, *295*, 855-872. https://doi.org/10.1016/j.geomorph.2017.08.029

Davies, J. L. (1964). A morphogenic approach to world shorelines. *Zeitschrift für Geomorphologie*, *8*(5), 127-142. https://doi.org/10.1127/zfg/mortensen/8/1964/127

Dibajnia, M., & Watanabe, A. (1992). Sheet flow under non-linear waves and currents. In *Coastal engineering 1992* (p. 2015-2029). ASCE. 1992. Venice, Italy

Dibajnia, M., & Watanabe, A. (1996). A transport rate formula for mixed-size sands. In *Coastal engineering 1996* (p. 3791-3804). ASCE. September 2-6, 1996. Orlando, Florida

DNV GL AS. (2021). *Environmental conditions and environmental loads* (Tech. Rep. No. DNV-RP-C205). DNV GL AS.

Dong, P. (2015). Automated measurement of sand dune migration using multi-temporal lidar data and GIS. *International Journal of Remote Sensing*, *36*(21), 5426-5447. https://doi.org/10.1080/01431161.2015.1093192

Droghei, R., Falcini, F., Casalbore, D., Martorelli, E., Mosetti, R., Sannino, G., ... Chiocci, F. L. (2016). The role of internal solitary waves on deep-water sedimentary processes: the case of up-slope migrating sediment waves off the Messina Strait. *Scientific Reports*, *6*. https://doi.org/10.1038/srep36376

Durand, N., Tassi, P., Blanpain, O., & Lefebvre, A. (2022a). Towards numerical modelling of marine dunes in a shallow shelf sea. In *Actes des XVIIèmes Journées Nationales Génie Côtier - Génie Civil* (p. 337-346). October 11-13, 2022. Chatou, France. https://doi.org/10.5150/jngcgc.2022.035

Durand, N., Tassi, P., Blanpain, O., & Lefebvre, A. (2022b). Hydrodynamic modelling as a first step to assess marine dune dynamics: Influence of waves. In *XXVIIIth Telemac-Mascaret user*

conference (p. 79-86). October 18-19, 2022. Paris-Saclay, France. https://hdl.handle.net/20.500.11970/110839

Durand, N., Tassi, P., Blanpain, O., & Lefebvre, A. (2023a). Understanding marine dune dynamics in a shallow shelf sea using sediment mobility indices. In *Marine and River Dune Dynamics VII Book of Proceedings* (p. 109-116). April 1-3, 2023. Rennes, France. https://maridnet.files.wordpress.com/2023/06/maridvii-durand-noemie.pdf

Durand, N., Tassi, P., Blanpain, O., & Lefebvre, A. (2023b). GAIA can model large marine dunes: Results from a sensitivity study in the southern North Sea. In *XXIXth Telemac-Mascaret user conference* (p. 190-197). October 12-13, 2023. Karlsruhe, Germany. https://hdl.handle.net/20.500.11970/112839

Durand, N., Tassi, P., Blanpain, O., & Lefebvre, A. (2024). Meteorological conditions influence the migration of a marine dune field in the southern North Sea. *Journal of Geophysical Research: Earth Surface*. Accepted for publication

ECOWind research programme website. (Last accessed May 29, 2024). `https://ecowind.uk/projects`.

Egbert, G. D., & Erofeeva, S. Y. (2002). Efficient inverse modeling of barotropic ocean tides. *Journal of Atmospheric and Oceanic Technology*, *19*(2), 183 - 204. https://doi.org/10.1175/1520-0426(2002)019<0183:EIMOBO>2.0.CO;2

EMD. (2021). *June 2021 multi-beam bathymetric survey conducted as part of pre-feasibility studies for the Dunkirk offshore wind farm area.* Proprietary data not available to the public at this time.

EMD. (2022). *2021-2022 wind, pressure, level, current and wave measurements collected as part of pre-feasibility studies for the Dunkirk offshore wind farm area.* Proprietary data not available to the public at this time.

Engelund, F., & Hansen, E. (1967). *A monograph on sediment transport in alluvial streams* (Tech. Rep. No. Hydraulic Engineering Report). Technical University of Denmark.

Ernstsen, V. B., Noormets, R., Winter, C., Hebbeln, D., Bartholomä, A., Flemming, B. W., & Bartholdy, J. (2006). Quantification of dune dynamics during a tidal cycle in an inlet channel of the Danish Wadden Sea. *Geo-Marine Letters*, *26*(3), 151-163. https://doi.org/10.1007/s00367-006-0026-2

Everaert, M., & Marquise, F. (Last accessed December 7, 2023). *Epaves au large de Dunkerque.* `http://dkepaves.free.fr/`.

FEM. (2020). *2019-2020 bed samples collected as part of pre-feasibility studies for the Dunkirk offshore wind farm area (DUNES project).* Proprietary data not available to the public at this time.

FEM. (2021a). *2019-2021 multi-beam bathymetric surveys conducted as part of pre-feasibility studies for the Dunkirk offshore wind farm area (DUNES project).* Proprietary data not available to the public at this time.

FEM. (2021b). *2021 level and current measurements collected as part of pre-feasibility studies for the Dunkirk offshore wind farm area (DUNES project).* Proprietary data not available to the public at this time.

Ferret, Y., Le Bot, S., Tessier, B., Garlan, T., & Lafite, R. (2010). Migration and internal architecture of marine dunes in the eastern English Channel over 14 and 56 year intervals: the influence of tides and decennial storms. *Earth Surface Processes and Landforms*, *35*, 1480-1493. https://doi.org/10.1002/esp.2051

Flather, R. A. (1979). Recent results from a storm surge prediction scheme for the North Sea. In J. C. Nihoul (Ed.), *Marine forecasting* (Vol. 25, p. 385-409). Elsevier. https://doi.org/10.1016/S0422-9894(08)71140-1

Flemish Hydrography - Maritime and Coastal Services. (2022). *Depth model belgian continental shelf and nautical data.* `https://www.vliz.be/en/datasets-belgian-coast-and-sea?module=dataset&dasid=5643`.

Flemming, B. (1988). Zur klassifikation subaquatischer, stromungstransversaler transportkorper. *Bochumer geologische und geotechnische Arbeiten*, *29*(93-97), 44-47.

Folk, R. L. (1954). The distinction between grain size and mineral composition in sedimentary-rock nomenclature. *The Journal of Geology*, *62*(4), 344–359. https://doi.org/10.1086/626171

Foreman, M. G. G. (2004a). *Manual for tidal currents analysis and prediction* (Tech. Rep. No. Pacific Marine Science Report 78-6). Institute of Ocean Sciences. 1978 edition reprinted with revisions

Foreman, M. G. G. (2004b). *Manual for tidal heights analysis and prediction* (Tech. Rep. No. Pacific Marine Science Report 77-10). Institute of Ocean Sciences. 1977 edition reprinted with revisions

Forster, R. M. (2018). *The effect of monopile-induced turbulence on local suspended sediment patterns around UK wind farms: field survey report* (Tech. Rep. No. IECS-YBB313-2017). Institute of Estuarine & Coastal Studies (IECS).

Frandsen, S., Barthelmie, R., Pryor, S., Rathmann, O., Larsen, S., Højstrup, J., & Thøgersen, M. (2006). Analytical modelling of wind speed deficit in large offshore wind farms. *Wind Energy*, *9*(1-2), 39-53. https://doi.org/10.1002/we.189

Frederikse, T., Landerer, F., Caron, L., Adhikari, S., Parkes, D., Humphrey, V. W., ... Wu, Y.-H. (2020). The causes of sea-level rise since 1900. *Nature*, *584*, 393-397. https://doi.org/10.1038/s41586-020-2591-3

Fredsøe, J., & Deigaard, R. (1992). *Mechanics of coastal sediment transport*. World Scientific. https://doi.org/10.1142/1546

Games, K. P., & Gordon, D. I. (2014). Study of sand wave migration over five years as observed in two windfarm development areas, and the implications for building on moving substrates in the North Sea. *Earth and Environmental Science Transactions of the Royal Society of Edinburgh*, *105*(4), 241-249. https://doi.org/10.1017/S1755691015000110

Garlan, T. (2007). Study on marine sandwave dynamics. *International Hydrographic Review*, *8*(2), 26-37.

Garlan, T., Le Faou, Y., Guyomard, P., & Gabelotaud, I. (2008). French marine sand dune project. In *Marine and river dune dynamics iii book of proceedings* (p. 133 - 139). April 1-3, 2008. Leeds, United Kingdom

GEBCO. (Last accessed March 31, 2022). *General bathymetric chart of the oceans, 2021 grid*. `https://www.gebco.net/data_and_products/gebco_web_services/web_map_service`. https://doi.org/10.5285/c6612cbe-50b3-0cff-e053-6c86abc09f8f

Goll, A. (2016). *3D numerical modelling of dune formation and dynamics in inland waterways* (PhD thesis). Université Paris-Est. Retrieved from https://pastel.archives-ouvertes.fr/tel-01542852

Goll, A., Kopmann, R., & Brudy-Zippelius, T. (2011). Numerical modelling of bed formes (dunes) with TELEMAC-3D and SISYPHE. In *Xviiith telemac-mascaret user conference* (p. 16-21). October 19-21, 2011. Chatou, France

Grass, A. J. (1981). *Sediment transport by waves and currents* (Tech. Rep. No. FL29). SERC London Cent. Mar. Technol.

Guerber, E., Le Cozannet, G., & Pedreros, R. (2008). Modélisation statistique du vent. Influence du changement climatique sur le transport éolien. In *Actes des Xèmes Journées Nationales Génie Côtier - Génie Civil*. October 14-16, 2008. Sophia Antipolis, France. In French

Hallermeier, R. J. (1981). Terminal settling velocity of commonly occurring sand grains. *Sedimentology*, *28*(6), 859-865. https://doi.org/10.1111/j.1365-3091.1981.tb01948.x

Harris, J., & Whitehouse, R. J. S. (2014). Marine scour: Lessons from nature's laboratory. In *Scour and erosion - proceedings of the 7th international conference on scour and erosion, icse 2014*. December 2-4, 2014. Perth, Australia

Harris, P. T. (1989). Sandwave movement under tidal and wind-driven currents in a shallow marine environment: Adolphus Channel, northeastern Australia. *Continental Shelf Research*, *9*(11), 981-1002. https://doi.org/10.1016/0278-4343(89)90003-4

Harris, P. T. (1991). Reversal of subtidal dune asymmetries caused by seasonally reversing wind-driven currents in Torres Strait, northeastern Australia. *Continental Shelf Research*, *11*(7), 655-662. https://doi.org/10.1016/0278-4343(91)90018-2

Harris, P. T., Macmillan-Lawler, M., Rupp, J., & Baker, E. K. (2014). Geomorphology of the oceans. *Marine Geology*, *Special Issue 352*, 4-24. https://doi.org/10.1016/j.margeo.2014.01.011

Heaps, N. S. (1965). Storm surges on a continental shelf. *Philosophical Transactions of the Royal Society of London. Series A, Mathematical and Physical Sciences*, *257*(1082), 351-383. https://doi.org/10.1098/rsta.1965.0009

Hedges, T. S., Anastasiou, K., & Gabriel, D. (1985). Interaction of random waves and currents. *Journal of Waterway, Port, Coastal, and Ocean Engineering*, *111*(2), 275-288. https://doi.org/10.1061/(ASCE)0733-950X(1985)111:2(275)

Héquette, A., Hemdane, Y., & Anthony, E. J. (2008). Sediment transport under wave and current combined flows on a tide-dominated shoreface, northern coast of France. *Marine Geology*, *249*(3), 226-242. https://doi.org/10.1016/j.margeo.2007.12.003

Hersbach, H., Bell, B., Berrisford, P., Hirahara, S., Horányi, A., Muñoz-Sabater, J., ... Thépaut, J.-N. (2020). The era5 global reanalysis. *Quarterly Journal of the Royal Meteorological Society*, *146*(730), 1999-2049. https://doi.org/10.1002/qj.3803

Hervouet, J.-M. (2007). *Hydrodynamics of free surface flows : Modelling with the finite element method*. John Wiley & Sons. https://doi.org/10.1002/9780470319628

Hervouet, J.-M., & Watrin, A. (1987). *Code TELEMAC (Système Ulysse) Résolution des équations de Saint-Venant bidimensionnelles* (Tech. Rep. No. report HE-43 87.37). E.D.F.

Hong, J.-H., Chiew, Y. M., Yeh, P.-H., & Chan, H.-C. (2017). Evolution of local pier-scour depth with dune migration in subcritical flow conditions. *Journal of Hydraulic Engineering*, *143*(4). https://doi.org/10.1061/(ASCE)HY.1943-7900.0001261

Hou, P., Zhu, J., Ma, K., Yang, G., Hu, W., & Chen, Z. (2019). A review of offshore wind farm layout optimization and electrical system design methods. *Journal of Modern Power Systems and Clean Energy*, *7*(5), 975-986. https://doi.org/10.1007/s40565-019-0550-5

HSE. (2002). *Environmental considerations* (Tech. Rep. No. Offshore Technology Report 2001/010). Norwich, UK: Health and Safety Executive.

Hudson, J., Damgaard, J., Dodd, N., Chesher, T., & Cooper, A. (2005). Numerical approaches for 1D morphodynamic modelling. *Coastal Engineering*, *52*(8), 691-707. https://doi.org/10.1016/j.coastaleng.2005.04.004

Hulscher, S. J. M. H. (1996). Tidal-induced large-scale regular bed form patterns in a three-dimensional shallow water model. *Journal of Geophysical Research: Oceans*, *101*(C9), 20727–20744. https://doi.org/10.1029/96JC01662

Hulscher, S. J. M. H., & van den Brink, G. (2001). Comparison between predicted and observed sand waves and sand banks in the North Sea. *Journal of Geophysical Research: Oceans*, *106*(C5), 9327–9338. https://doi.org/10.1029/2001JC900003

Huthnance, J. M. (1982). On one mechanism forming linear sand banks. *Estuarine, Coastal and Shelf Science*, *14*(1), 79-99. https://doi.org/10.1016/S0302-3524(82)80068-6

Idier, D., Ehrhold, A., & Garlan, T. (2002). Morphodynamique d'une dune sous-marine du détroit du Pas de Calais. *Comptes Rendus Géoscience*, *334*(15), 1079–1085. in French https://doi.org/10.1016/S1631-0713(02)01852-7

Idier, D., Hommes, S., Brière, C., Roos, P. C., Walstra, D.-J. R., Knaapen, M. A. F., & Hulscher, S. J. M. H. (2010). Morphodynamic models used to study the impact of offshore aggregate extraction: a review. *Journal of Coastal Research*, *Special Issue 51*, 39–52.

International Energy Agency. (2019). *Offshore wind outlook 2019* (Tech. Rep. No. World Energy Outlook Special Report). International Energy Agency.

International Hydrographic Organization. (Last accessed March 1, 2022). *S-32 IHO - Hydrographic Dictionary (Hydrographic Dictionary Working Group (HDWG) - 2019)*. `http://iho-ohi.net/S32/engView.php`.

Isaksson, N., Scott, B. E., Hunt, G. L., Benninghaus, E., Declerck, M., Gormley, K., ... Williamson, B. J. (2023). A paradigm for understanding whole ecosystem effects of offshore wind farms in shelf seas. *ICES Journal of Marine Science*. https://doi.org/10.1093/icesjms/fsad194

Isobe, M., & Horikawa, K. (1982). Study on water particle velocities of shoaling and breaking waves. *Coastal Engineering in Japan*, *25*(1), 109-123. https://doi.org/10.1080/05785634.1982.11924340

Janssen, P. A. E. M. (1989). Wave-induced stress and the drag of air flow over sea waves. *Journal of Physical Oceanography*, *19*, 745-754. https://doi.org/10.1175/1520-0485(1989)019<0745:WISATD>2.0.CO;2

Janssen, P. A. E. M. (1991). Quasi-linear theory of wind-wave generation applied to wave forecasting. *Journal of Physical Oceanography*, *21*, 1631-1642. https://doi.org/10.1175/1520-0485(1991)021<1631:QLTOWW>2.0.CO;2

Jiang, W., & Lin, M. (2016). Research on bilateral reverse migration of one-group seabed sand waves in a small shallow shelf sea. *Coastal Engineering*, *111*, 70-82. https://doi.org/10.1016/j.coastaleng.2016.01.013

Katoh, K., Kume, H., Kuroki, K., & Hasegawa, J. (1998). The development of sand waves and the maintenance of navigation channels in the Bisanseto Sea. In *Coastal engineering 1998* (p. 3490-3502). ASCE. June 22-26, 1998. Copenhagen, Denmark

Kenyon, N. H., Akhmetzhanov, A. M., & Twichell, D. C. (2002). Sand wave fields beneath the Loop Current, Gulf of Mexico: reworking of fan sands. *Marine Geology*, *192*(1), 297-307. https://doi.org/10.1016/S0025-3227(02)00560-1

King, E. L., Bøe, R., Bellec, V. K., Rise, L., Skarðhamar, J., Ferré, B., & Dolan, M. F. J. (2014). Contour current driven continental slope-situated sandwaves with effects from secondary current processes on the Barents Sea margin offshore Norway. *Marine Geology*, *353*, 108-127. https://doi.org/10.1016/j.margeo.2014.04.003

Knaapen, M. A. F. (2004). Measuring sand wave migration in the field. comparison of different data sources and an error analysis. In *Marine sandwave and river dune dynamics ii book of proceedings* (p. 152-160). April 1-2, 2004. Enschede, The Netherlands

Knaapen, M. A. F. (2005). Sandwave migration predictor based on shape information. *Journal of Geophysical Research: Earth Surface*, *110*(F4). https://doi.org/10.1029/2004JF000195

Knaapen, M. A. F., & Hulscher, S. J. M. H. (2002). Regeneration of sand waves after dredging. *Coastal engineering*, *46*(4), 277–289. https://doi.org/10.1016/S0378-3839(02)00090-X

Knaapen, M. A. F., Hulscher, S. J. M. H., Tiessen, M. C. H., & van den Berg, J. (2005). Using a sand wave model for optimal monitoring of navigation depth. In *4th iahr symposium on river, coastal and estuarine morphodynamics (rcem)* (pp. 999–1007). Balkema / Taylor & Francis. October 4-7, 2005. Urbana, Illinois, USA

Koch, F. G., & Flokstra, C. (1980). Bed level computations for curved alluvial channels. In *Proceedings of the xixth congress of the int. ass. for hydr. res.* February, 1981. New Delhi, India

Krabbendam, J. M., Nnafie, A., Borsje, B. W., & de Swart, H. E. (2023). Background topography affects the degree of three-dimensionality of tidal sand waves. *Journal of Geophysical Research: Earth Surface*, *128*(11). https://doi.org/10.1029/2023JF007153

Krabbendam, J. M., Nnafie, A., de Swart, H. E., Borsje, B. W., & Perk, L. (2021). Modelling the past and future evolution of tidal sand waves. *Journal of Marine Science and Engineering*, *9*(10). https://doi.org/10.3390/jmse9101071

Krabbendam, J. M., Nnafie, A., Perk, L., Borsje, B. W., & de Swart, H. E. (2019). Modelling the past evolution of observed tidal sand waves: the role of boundary conditions. In *Marine and river dune dynamics vi book of proceedings* (pp. 141–146). April 1-3, 2019. Bremen, Germany

Krabbendam, J. M., Roche, M., Van Lancker, V. R. M., Nnafie, A., Terseleer, N., Degrendele, K., & de Swart, H. E. (2022). Do tidal sand waves always regenerate after dredging? *Marine Geology*, *451*. https://doi.org/10.1016/j.margeo.2022.106866

Krewinkel, B. C. (2017). *Deflected sand wave migration due to severe wind events along the BBL-pipeline : A 3D-numerical modelling study using eight years of bathymetrical data* (Master's thesis). University of Twente. Retrieved from http://essay.utwente.nl/72470/

Lambkin, D., Harris, J., Cooper, B., & Coates, T. (2009). *Coastal process modelling for offshore wind farm environmental impact assessment: Best practice guide* (Tech. Rep. No. COWRIE COAST-07-08). Collaborative Offshore Windfarm Research Into the Environment, COWRIE.

Lanckneus, J., & de Moor, G. (1991). Present-day evolution of sand waves on a sandy shelf bank. *Oceanologica Acta*, *Special Issue 11*, 123-127. Retrieved from `https://archimer.ifremer.fr/doc/00268/37886/`

Langhorne, D. N. (1977). *Sandwave research and its relevance to present day navigation and engineering problems* (Tech. Rep. No. Internal Document n° 19). Institute of Oceanographic Sciences, Wormley Laboratory, UK.

Langhorne, D. N. (1982). A study of the dynamics of a marine sandwave. *Sedimentology*, *29*(4), 571-594. https://doi.org/10.1111/j.1365-3091.1982.tb01734.x

Latapy, A. (2020). *Influence des modifications morphologiques de l'avant-côte sur l'hydrodynamisme et l'évolution du littoral des Hauts-de-France depuis le XIXe siècle* (PhD thesis, in French). Université du Littoral Côte d'Opale. Retrieved from https://tel.archives-ouvertes.fr/tel-02899411v2

Latteux, B. (1995). Techniques for long-term morphological simulation under tidal action. *Marine Geology*, *126*(1), 129-141. https://doi.org/10.1016/0025-3227(95)00069-B

Le Bot, S. (2001). *Morphodynamique de dunes sous-marines sous influence des marées et des tempêtes : processus hydro-sédimentaires et enregistrement : exemple du Pas-de-Calais* (PhD

thesis, in French). Université des Sciences et Technologies de Lille, U.F.R. des Sciences de la Terre. Lille 1. Retrieved from http://www.theses.fr/2001LIL10016

Le Bot, S., Bary, M., Fournier, M., Husté, A., Michelet, N., Blanpain, O., ... Garlan, T. (2023). Marine dune morphodynamics and sediment fluxes (off Dunkirk, France). Spatio-temporal variability and relations with hydrodynamic forcings. In *Marine and river dune dynamics vii book of proceedings* (p. 155-162). April 1-3, 2023. Rennes, France

Le Bot, S., & Trentesaux, A. (2004). Types of internal structure and external morphology of submarine dunes under the influence of tide- and wind-driven processes (Dover Strait, northern France). *Marine Geology*, *211*(1), 143-168. https://doi.org/10.1016/j.margeo.2004.07.002

Le Bot, S., Trentesaux, A., Garlan, T., Berné, S., & Chamley, H. (2000). Influence des tempêtes sur la mobilité des dunes tidales dans le détroit du Pas-de-Calais. *Oceanologica Acta*, *23*(2), 129-141. in French https://doi.org/10.1016/S0399-1784(00)00115-8

Lefaible, N., Braeckman, U., & Moens, T. (2018). Effects of wind turbine foundations on surrounding macrobenthic communities. In S. D. et al. (Ed.), *Environmental Impacts of Offshore Wind Farms in the Belgian Part of the North Sea: Assessing and Managing Effect Spheres of Influence* (p. 57-77). Royal Belgian Institute for Natural Sciences.

Lefaible, N., Colson, L., Braeckman, U., & Moens, T. (2019). Evaluation of turbine related impacts on macrobenthic communities within two offshore wind farms during the operational phase. In S. D. et al. (Ed.), *Environmental Impacts of Offshore Wind Farms in the Belgian Part of the North Sea: Marking a Decade of Monitorig, Research and Innovation* (p. 57-64). Royal Belgian Institute for Natural Sciences.

Lefebvre, A., & Cisneros, J. (2023). The influence of dune lee side shape on time-averaged velocities and turbulence. *Earth Surface Dynamics*, *11*(4), 575–591. https://doi.org/10.5194/esurf-11-575-2023

Lefebvre, A., Paarlberg, A. J., & Winter, C. (2016). Characterising natural bedform morphology and its influence on flow. *Geo-Marine Letters*, *36*(5), 379-393. https://doi.org/10.1007/s00367-016-0455-5

Lesser, G. R., Roelvink, J. A., van Kester, J. A. T. M., & Stelling, G. S. (2004). Development and validation of a three-dimensional morphological model. *Coastal Engineering*, *51*(8), 883-915. https://doi.org/10.1016/j.coastaleng.2004.07.014

Li, M. Z., Hannah, C. G., Perrie, W. A., Tang, C. C. L., Prescott, R. H., & Greenberg, D. A. (2015). Modelling seabed shear stress, sediment mobility, and sediment transport in the Bay of Fundy. *Canadian Journal of Earth Sciences*, *52*(9), 757-775. https://doi.org/10.1139/cjes-2014-0211

Li, M. Z., Zou, Q., Hannah, C. G., Perrie, W. A., Prescott, R. H., & Toulany, B. (2009). *Numerical modelling of seabed disturbance and sediment mobility, with applications to morphodynamics on the storm-dominated Sable Island Bank, Scotian Shelf* (Tech. Rep. No. Open File 6155). Geological Survey of Canada.

Li, X., Chi, L., Chen, X., Ren, Y., & Lehner, S. (2014). SAR observation and numerical modeling of tidal current wakes at the East China Sea offshore wind farm. *Journal of Geophysical Research: Oceans*, *119*(8), 4958-4971. https://doi.org/10.1002/2014JC009822

Liebreich, M. (2017). *London summit 2017, breaking clean* (Tech. Rep.). Bloomberg New Energy Finance.

Lokin, L. R., Warmink, J. J., & Hulscher, S. J. M. H. (2023). The effect of sediment transport models on simulating river dune dynamics. *Water Resources Research*, *59*(12). https://doi.org/10.1029/2023WR034607

Lyard, F. H., Allain, D. J., Cancet, M., Carrère, L., & Picot, N. (2021). FES2014 global ocean tide atlas: design and performance. *Ocean Science*, *17*(3), 615 - 649. https://doi.org/10.5194/os-17-615-2021

Malikides, M., Harris, P. T., Jenkins, C. J., & Keene, J. B. (1988). Carbonate sandwaves in Bass Strait. *Australian Journal of Earth Sciences*, *35*(3), 303-311. https://doi.org/10.1080/08120098808729449

Margalit, J. (2017). *Development of natural seabed forms and their interaction with off shore wind farms* (PhD thesis). DTU - Technical University of Denmark. Retrieved from https://orbit.dtu.dk/en/publications/development-of-natural-seabed-forms-and-their-interaction-with-of

Maspataud, A., Schmitt, T., Biscara, L., & Créach, R. (2016). High resolution coastal DEM of the Dover Strait: managing dynamic bedforms. In *Marine and River Dune Dynamics V Book of Proceedings.* April 4-5, 2016. North Wales, UK

Melville, B. W. (1988). Scour at bridge sites. In P. N. Cheremisinoff & N. P. Cheremisinoff (Eds.), *Civil engineering practice* (p. 327-362). Technomic Publishing Company.

Menninga, P. J. (2012). *Analysis of variations in characteristics of sand waves observed in the Dutch coastal zone: a field and model study* (Master's thesis). Utrecht University. Retrieved from https://studenttheses.uu.nl/handle/20.500.12932/13034

Miles, J., Martin, T., & Goddard, L. (2017). Current and wave effects around windfarm monopile foundations. *Coastal Engineering*, *121*, 167-178. https://doi.org/10.1016/j.coastaleng.2017.01.003

Morvan, A., Rivière, A., & Maison, A. (2023). Potential thermal impact of wind farms within a dynamic seabed. In *Marine and River Dune Dynamics VII Book of Proceedings* (p. 261-262). April 1-3, 2023. Rennes, France

Nagel, T., Chauchat, J., Wirth, A., & Bonamy, C. (2018). On the multi-scale interactions between an offshore-wind-turbine wake and the ocean-sediment dynamics in an idealized framework – a numerical investigation. *Renewable Energy*, *115*, 783-796. https://doi.org/10.1016/j.renene.2017.08.078

Németh, A. A., Hulscher, S. J. M. H., & de Vriend, H. J. (2002). Modelling sand wave migration in shallow shelf seas. *Continental Shelf Research*, *22*(18-19), 2795–2806. https://doi.org/10.1016/S0278-4343(02)00127-9

Németh, A. A., Hulscher, S. J. M. H., & de Vriend, H. J. (2003). Offshore sand wave dynamics, engineering problems and future solutions. *Pipeline and gas journal*, *230*(4), 67–69.

Németh, A. A., Hulscher, S. J. M. H., & van Damme, R. M. J. (2007). Modelling offshore sand wave evolution. *Continental shelf research*, *27*(5), 713–728. https://doi.org/10.1016/j.csr.2006.11.010

Németh, A. A., Hulscher, S. J. M. H., & van Damme, R. M. J. (2001). Numerical simulation of sand wave evolution in shallow shelf seas. In *Coastal dynamics '01* (p. 1048-1057). June 11-15, 2001. Lund, Sweden

Nielsen, P. (1992). *Coastal bottom boundary layers and sediment transport*. World Scientific Publishing. https://doi.org/10.1142/1269

Nnafie, A., Krabbendam, J. M., & de Swart, H. E. (2023). Consequences of limited sediment supply for long-term evolution of offshore tidal sand waves, a 3D model perspective. *Marine Geology*, *464*. https://doi.org/10.1016/j.margeo.2023.107148

Noveltis, Legos and CLS. (2019). *Fes2014 global tide model.* `https://www.aviso.altimetry.fr/en/data/products/auxiliary-products/global-tide-fes/description-fes2014.html`.

Ogor, J. (2018). *Design of algorithms for the automatic characterization of marine dune morphology and dynamics* (PhD thesis). ENSTA Bretagne - École nationale supérieure de techniques avancées Bretagne. Retrieved from https://tel.archives-ouvertes.fr/tel-02354454

openTELEMAC. (December 2022). *GAIA validation manual* (Tech. Rep. No. v8p4). Author.

openTELEMAC gitlab. (Last accessed February 24, 2022). `https://gitlab.pam-retd.fr/otm/telemac-mascaret.git`.

OpenTopoMap. (n.d.). `https://opentopomap.org`.

Overes, P. H. P. (2021). *Modeling sand wave field dynamics in the north sea using Delft3D Flexible Mesh* (Master's thesis). Delft University of Technology. Retrieved from `https://repository.tudelft.nl/islandora/object/uuid%3A492ee814-9821-4943-aa16-6299fcf7533e`

Overes, P. H. P., Borsje, B. W., Luijendijk, A. P., & Hulscher, S. J. M. H. (2024). The importance of time-varying, non-tidal currents in modelling in-situ sand wave dynamics. *Coastal Engineering*, *189*, 104480. https://doi.org/10.1016/j.coastaleng.2024.104480

Parc éolien en mer de Dunkerque website. (Last accessed May 10, 2022). `https://parc-eolien-en-mer-de-dunkerque.fr/presentation-du-projet`.

Pessanha, V. S., Chu, P. C., Gough, M. K., Traykovski, P., & Orescanin, M. M. (2023). Sand wave migration near the southeastern corner of Martha's Vineyard, Massachusetts, USA. *International Journal of Sediment Research*. https://doi.org/10.1016/j.ijsrc.2023.04.006

Pezerat, M., Bertin, X., Martins, K., Mengual, B., & Hamm, L. (2021). Simulating storm waves in the nearshore area using spectral model: Current issues and a pragmatic solution. *Ocean Modelling*, *158*. https://doi.org/10.1016/j.ocemod.2020.101737

Phillips, O. M. (1977). *The dynamics of the upper ocean. 2nd edition*. Cambridge University Press.

Pisanò, F. (2019). Input of advanced geotechnical modelling to the design of offshore wind turbine foundations (apport de la modélisation géotechnique avancée au dimensionnement de fondations d'éoliennes offshore). In *Proceedings of the xvii ecsmge-2019*. September 1-6, 2019. Reykjavik, Iceland

Pope, N. D., Widdows, J., & Brinsley, M. D. (2006). Estimation of bed shear stress using the turbulent kinetic energy approach—a comparison of annular flume and field data. *Continental Shelf Research*, *26*(8), 959-970. https://doi.org/10.1016/j.csr.2006.02.010

Porter-Smith, R., Harris, P. T., Andersen, O. B., Coleman, R., Greenslade, D., & Jenkins, C. J. (2004). Classification of the Australian continental shelf based on predicted sediment threshold exceedance from tidal currents and swell waves. *Marine Geology*, *211*(1), 1-20. https://doi.org/10.1016/j.margeo.2004.05.031

products, E. B. (Last accessed June 7, 2022). `https://emodnet.ec.europa.eu/en/bathymetry#bathymetry-products`.

Proudman Oceanographic Laboratory, UK. (1986). *Lecture notes in measurements of currents in the sea, tidal analysis.*

Pugh, D. T. (1996). *Tides, surges and mean sea-level*. John Wiley & Sons. 1987 edition reprinted with corrections

Ranasinghe, R., Swinkels, C., Luijendijk, A., Roelvink, D., Bosboom, J., Stive, M., & Walstra, D.-J. R. (2011). Morphodynamic upscaling with the morfac approach: Dependencies and sensitivities. *Coastal Engineering*, *58*(8), 806-811. https://doi.org/10.1016/j.coastaleng.2011.03.010

Raoult, C., Joly, A., Andreevsky, M., & Joly-Laugel, A. (2018). ANEMOC-3: Improving the ANEMOC-2 sea state database by adding tide effects. In *Actes des 16èmes journées de l'hydrodynamique*. November 27-29, 2018. Marseille, France

Reeder, D. B., Ma, B. B., & Yang, Y. J. (2011). Very large subaqueous sand dunes on the upper continental slope in the South China Sea generated by episodic, shoaling deep-water internal solitary waves. *Marine Geology*, *279*(1), 12-18. https://doi.org/10.1016/j.margeo.2010.10.009

Rees, J., Larcombe, P., Vivian, C., & Judd, A. (2006). *Scroby Sands offshore wind farm - coastal processes monitoring* (Tech. Rep. No. AE0262). Centre for Environment Fisheries and Aquaculture Science (CEFAS).

Rennau, H., Schimmels, S., & Burchard, H. (2012). On the effect of structure-induced resistance and mixing on inflows into the Baltic Sea: A numerical model study. *Coastal Engineering*, *60*, 53-68. https://doi.org/10.1016/j.coastaleng.2011.08.002

Reynaud, J.-Y., & Dalrymple, R. W. (2012). Shallow-marine tidal deposits. In *Principles of tidal sedimentology* (pp. 335–369). Springer Netherlands. https://doi.org/10.1007/978-94-007-0123-6_13

Ribó, M., Puig, P., noz, A. M., Lo Iacono, C., Masqué, P., Palanques, A., ... Gómez Ballesteros, M. (2016). Morphobathymetric analysis of the large fine-grained sediment waves over the Gulf of Valencia continental slope (NW Mediterranean). *Geomorphology*, *253*, 22-37. https://doi.org/10.1016/j.geomorph.2015.09.027

Rivier, A., Bennis, A.-C., Pinon, G., Gross, M., & Magar, V. (2015). Regional numerical modelling of offshore monopile wind turbine impacts on hydrodynamics and sediment transport. In *Renewable energies offshore* (p. 807-813). CRC Press. November 24-26, 2014. Lisbon, Portugal

Rivier, A., Bennis, A.-C., Pinon, G., Magar, V., & Gross, M. (2016). Parameterization of wind turbine impacts on hydrodynamics and sediment transport. *Ocean Dynamics*, *66*(10), 1285-1299. https://doi.org/10.1007/s10236-016-0983-6

Robert, A. E., Quillien, N., Bacha, M., Caulle, C., Nexer, M., Parent, B., ... Desroy, N. (2024). Seasonal dynamic of the benthic food web in subtidal sandbanks. *Marine Ecology Progress Series*, *735*, 27-41. https://doi.org/10.3354/meps14573

Roetert, T. J., Raaijmakers, T., & Borsje, B. W. (2017). Cable route optimization for offshore wind farms in morphodynamic areas. In *Proceedings of the 27th international ocean and polar engineering conference* (pp. 595–607). June 25-30, 2017. San Francisco, United States

Roos, P. C. (2004). *Seabed pattern dynamics and offshore sand extraction* (PhD thesis). University of Twente. Retrieved from https://research.utwente.nl/en/publications/seabed-pattern-dynamics-and-offshore-sand-extraction

Roos, P. C. (2019). On the crest of sandwave modelling: Achievements from the past, directions for the future. In *Marine and River Dune Dynamics VI Book of Proceedings* (p. 197-201). April 1-3, 2019. Bremen, Germany

Roos, P. C., Hulscher, S. J. M. H., der Meer, F. S.-V., van Dijk, T. A. G. P., Wientjes, I. G. M., & van den Berg, J. (2007). Grain size sorting over offshore sandwaves: observations and modelling. In *5th iahr symposium on river, coastal and estuarine morphodynamics (rcem)*. September 17-21, 2007. Enschede, The Netherlands

Roulund, A., Sumer, B. M., Fredsøe, J., & Michelsen, J. (2005). Numerical and experimental investigation of flow and scour around a circular pile. *Journal of Fluid Mechanics*, *534*, 351-401. https://doi.org/10.1017/S0022112005004507

Santoro, V. C., Amore, E., Cavallaro, L., Cozzo, G., & Foti, E. (2002). Sand waves in the Messina Strait, Italy. *Journal of Coastal Research*, *36*(sp1), 640 – 653. https://doi.org/10.2112/1551-5036-36.sp1.640

Scheiber, L., & Lefebvre, A. (2023). The influence of geometric definitions on dune characteristics. In *Marine and River Dune Dynamics VII Book of Proceedings* (p. 293-297). April 1-3, 2023. Rennes, France

Schrijvershof, R. A., van Maren, D. S., Torfs, P. J. J. F., & Hoitink, A. J. F. (2023). A synthetic spring-neap tidal cycle for long-term morphodynamic models. *Journal of Geophysical Research: Earth Surface*, *128*(3), e2022JF006799. https://doi.org/10.1029/2022JF006799

Schultze, L. K. P., Merckelbach, L. M., Horstmann, J., Raasch, S., & Carpenter, J. R. (2020). Increased mixing and turbulence in the wake of offshore wind farm foundations. *Journal of Geophysical Research: Oceans*, *125*(8), e2019JC015858. https://doi.org/10.1029/2019JC015858

Shankar, C. G., & Behera, M. R. (2021). Improved wind drag formulation for numerical storm wave and surge modeling. *Dynamics of Atmospheres and Oceans*, *93*. https://doi.org/10.1016/j.dynatmoce.2020.101193

Shom. (2015). *MNT bathymétrique de façade Atlantique (Projet HOMONIM).* http://dx.doi.org/10.17183/MNT_ATL100m_HOMONIM_WGS84.

Shom. (2016). *MNT topo-bathymétrique côtier à 20m du détroit du Pas-de-Calais (Projet TANDEM).* http://dx.doi.org/10.17183/MNT_COTIER_DETROIT_PDC_TANDEM_20m_WGS84.

Shom. (2017a). *2016-2017 bed samples collected as part of pre-feasibility studies for the Dunkirk offshore wind farm area.* https://www.mongeosource.fr/geosource/1111/fre/catalog.search#/metadata/2a0ca78b-514d-425b-beb8-328469fef861.

Shom. (2017b). *2016-2017 multi-beam bathymetric surveys conducted as part of pre-feasibility studies for the Dunkirk offshore wind farm area.* https://www.mongeosource.fr/geosource/1111/fre/catalog.search#/metadata/813b4f9f-80dd-4c77-a66d-4e989be87b72.

Shom. (2017c). *2016 current measurements collected as part of pre-feasibility studies for the Dunkirk offshore wind farm area.* https://www.mongeosource.fr/geosource/1111/fre/catalog.search#/metadata/672d497d-65e5-4fba-ac0d-682a85401f19.

Shom. (2017d). *2016 wave measurements collected as part of pre-feasibility studies for the Dunkirk offshore wind farm area.* https://www.mongeosource.fr/geosource/1111/fre/catalog.search#/metadata/b7d1fe0e-1f7a-4236-896b-fdf56f545971.

Shom. (2017e). *Sedimentological data produced as part of pre-feasibility studies for the Dunkirk offshore wind farm area.* https://www.mongeosource.fr/geosource/1111/fre/catalog.search#/metadata/a23c84cf-5761-4939-8f39-c1e1224097bd.

Shom. (2018). *Surface zéro hydrographique bathyelli v2.0.* https://diffusion.shom.fr/donnees/references-verticales/surface-zero-hydrographique-bathyelli-20.html.

Shom. (2020). *Références Altimétriques Maritimes, Ports de France métropolitaine et d'outre-mer* (Tech. Rep. No. RAM_2020). Shom.

Shom. (2022). *Epaves et obstructions.* https://diffusion.shom.fr/donnees/base-de-donnees-maritimes-et-littorales/epaves.html.

Shom - ROLNHDF. (2022). *Partie maritime Litto3D® - Normandie et Hauts-De-France 2016-2018.* http://dx.doi.org/10.17183/L3D_MAR_NHDF_2016_2018.

Snyder., R. L., Dobson, F. W., Elliot, J. A., & Long, R. B. (1981). Array measurements of atmospheric pressure fluctuations above surface gravity waves. *J. Fluid Mech.*, *102*, 1-59.

Soulsby, R. L. (1995). The "bailard" sediment transport formula: comparison with data and models. In M. J. F. Stive et al. (Eds.), *Advances in coastal morphodynamics* (p. 2.48-2.53). Delft Hydraulics.

Soulsby, R. L. (1997). *Dynamics of marine sands*. Thomas Telford Publishing. https://doi.org/10.1680/doms.25844

Soulsby, R. L., & Damgaard, J. S. (2005). Bedload sediment transport in coastal waters. *Coastal Engineering*, *52*(8), 673-689. https://doi.org/10.1016/j.coastaleng.2005.04.003

Stadler, L., & Utz, M. (2023). A local Lax-Friedrichs flux applied to the finite volume method of GAIA. In *XXIXth Telemac-Mascaret user conference* (p. 232-237). October 12-13, 2023. Karlsruhe, Germany

Stevens, R. J. A. M., & Meneveau, C. (2017). Flow structure and turbulence in wind farms. *Annual Review of Fluid Mechanics*, *49*, 311-339. https://doi.org/10.1146/annurev-fluid-010816-060206

Sumer, B. M., & Fredsøe, J. (2002). *The mechanics of scour in the marine environment*. World Scientific. https://doi.org/10.1142/4942

Sutherland, J., Walstra, D.-J. R., Chesher, T. J., van Rijn, L. C., & Southgate, H. N. (2004). Evaluation of coastal area modelling systems at an estuary mouth. *Coastal Engineering*, *51*(2), 119-142. https://doi.org/10.1016/j.coastaleng.2003.12.003

Swart, D. H. (1976). Predictive equations regarding coastal transports. In *Coastal engineering 1976* (p. 1113-1132). ASCE. July 11-17, 1976. Honolulu, Hawaii

Tassi, P., Benson, T., Delinares, M., Fontaine, J., Huybrechts, N., Kopmann, R., ... Walther, R. (2023). GAIA - a unified framework for sediment transport and bed evolution in rivers, coastal seas and transitional waters in the TELEMAC-MASCARET modelling system. *Environmental Modelling & Software*, *159*, 105544. https://doi.org/10.1016/j.envsoft.2022.105544

Teles, M., Weiss, M., & Benoit, M. (2022). Assessment of the ANEMOC-3 sea state hindcast database for modelling a series of energetic winter storms along the french coast. In *Actes des XVIIèmes journées nationales génie côtier - génie civil*. October 11-13, 2022. Chatou, France

Terwindt, J. H. J. (1971). Sand waves in the southern bight of the North Sea. *Marine Geology*, *10*(1), 51-67. https://doi.org/10.1016/0025-3227(71)90076-4

The Crown Estate. (2020). *Offshore wind operational report 2020* (Tech. Rep.). The Crown Estate.

Tonnon, P. K., van Rijn, L. C., & Walstra, D.-J. R. (2007). The morphodynamic modelling of tidal sand waves on the shoreface. *Coastal Engineering*, *54*(4), 279-296. https://doi.org/10.1016/j.coastaleng.2006.08.005

Tresca, A. (2013). *Contrôle souple de la dynamique éolienne le long d'un littoral artificialisé et propositions de gestion : Le cas de la façade maritime du Grand Port Maritime de Dunkerque* (PhD thesis, in French). Université du Littoral Côte d'Opale. Retrieved from https://hal.archives-ouvertes.fr/tel-00825877v2

Trifonova, N. I., & Scott, B. E. (2023). Ecosystem indicators: predicting population responses to combined climate and anthropogenic changes in shallow seas. *Ecography*, *2024*(3), e06925. https://doi.org/10.1111/ecog.06925

Tsanis, I. K. (1989). Simulation of wind-induced water currents. *Journal of Hydraulic Engineering*, *115*(8), 1113-1134. https://doi.org/10.1061/(ASCE)0733-9429(1989)115:8(1113)

Turki, I., Le Bot, S., Lecoq, N., Shafiei, H., Michel, C., Deloffre, J., ... Lafite, R. (2021). Morphodynamics of intertidal dune field in a mixed wave-tide environment: Case of baie de somme in eastern english channel. *Marine Geology*, *431*, 106381. https://doi.org/10.1016/j.margeo.2020.106381

University, T. O. (1999). *Waves, tides and shallow-water processes*. Pergamon Press. https://doi.org/10.1016/B978-0-08-036372-1.X5000-4

University of Colorado sea level trends. (Last accessed January 24, 2022). *Sea level trends from satellite altimeters*. `https://sealevel.colorado.edu/trend-map`.

Vaisala. (Last accessed May 10, 2024). *Wind Set WA15 datasheet*. `https://docs.vaisala.com/v/u/B210382EN-H/en-US`.

Valentine, P. C., Cooper, R. A., & Uzmann, J. R. (1984). Submarine sand dunes and sedimentary environments in Oceanographer Canyon. *Journal of Sedimentary Research*, *54*(3), 704-715. https://doi.org/10.1306/212F84DB-2B24-11D7-8648000102C1865D

van den Berg, J., Sterlini, F., Hulscher, S. J. M. H., & van Damme, R. (2012). Non-linear process based modelling of offshore sand waves. *Continental Shelf Research*, *37*, 26-35. https://doi.org/10.1016/j.csr.2012.01.012

van der A, D. A., Ribberink, J. S., van der Werf, J. J., O'Donoghue, T., Buijsrogge, R., & Kranenburg, W. M. (2013). Practical sand transport formula for non-breaking waves and currents. *Coastal Engineering*, *76*, 26–42. https://doi.org/10.1016/j.coastaleng.2013.01.007

van der Tempel, J., Zaaijer, M. B., & Subroto, H. D. (2004). The effects of scour on the design of offshore wind turbines. In *Proceedings of the 3rd international conference on marine renewable energy (marec 2004)* (pp. 27–35). July 7-9, 2004. Blyth, United Kingdom

van der Veen, H., & Hulscher, S. J. M. H. (2008). Effects of large-scale human activities on the North Sea seabed. In *Marine and river dune dynamics iii book of proceedings* (pp. 307–314). April 1-3, 2008. Leeds, United Kingdom

van der Westhuysen, A. J. (2012). Spectral modeling of wave dissipation on negative current gradients. *Coastal Engineering*, *68*, 17-30. https://doi.org/10.1016/j.coastaleng.2012.05.001

van Gerwen, W., Borsje, B. W., Damveld, J., & Hulscher, S. J. M. H. (2018). Modelling the effect of suspended load transport and tidal asymmetry on the equilibrium tidal sand wave height. *Coastal engineering*, *136*, 56–64. https://doi.org/10.1016/j.coastaleng.2018.01.006

van Landeghem, K. J. J., Baas, J. H., Mitchell, N. C., Wilcockson, D., & Wheeler, A. J. (2012). Reversed sediment wave migration in the Irish Sea, NW Europe: A reappraisal of the validity of geometry-based predictive modelling and assumptions. *Marine Geology*, *295-298*, 95-112. https://doi.org/10.1016/j.margeo.2011.12.004

van Landeghem, K. J. J., Wheeler, A. J., Mitchell, N. C., & Sutton, G. (2009). Variations in sediment wave dimensions across the tidally dominated Irish Sea, NW Europe. *Marine Geology*, *263*(1), 108-119. https://doi.org/10.1016/j.margeo.2009.04.003

van Rijn, L. C. (1984a). Sediment transport, part I: Bed load transport. *Journal of Hydraulic Engineering*, *110*(10), 1431-1456. https://doi.org/10.1061/(ASCE)0733-9429(1984)110:10(1431)

van Rijn, L. C. (1984b). Sediment transport, part III: Bed forms and alluvial roughness. *Journal of Hydraulic Engineering*, *110*(12), 1733-1754. https://doi.org/10.1061/(ASCE)0733-9429(1984)110:12(1733)

van Rijn, L. C. (1984c). Sediment transport, part II: Suspended load transport. *Journal of Hydraulic Engineering*, *110*(11), 1613-1641. https://doi.org/10.1061/(ASCE)0733-9429(1984)110:11(1613)

van Rijn, L. C. (2007). Unified view of sediment transport by currents and waves. I: Initiation of motion, bed roughness, and bed-load transport. *Journal of Hydraulic Engineering*, *133*(6), 649-667. https://doi.org/10.1061/(ASCE)0733-9429(2007)133:6(649)

van Rijn, L. C., Davies, A. G., van de Graaff, J., & Ribberink, J. S. (Eds.). (2001). *SEDMOC Sediment transport modelling in marine coastal environments*. Aqua Publications.

van Dijk, T. A. G. P., van der Tak, C., de Boer, W. P., Kleuskens, M. H. P., Doornenbal, P. J., Noorlandt, R. P., & Marges, V. C. (2011). *The scientific validation of the hydrographic survey policy of the Netherlands Hydrographic Office, Royal Netherlands Navy* (Tech. Rep. No. report 1201907-000). Deltares.

Vanhellemont, Q., & Ruddick, K. (2014). Turbid wakes associated with offshore wind turbines observed with Landsat 8. *Remote Sensing of Environment*, *145*, 105-115. https://doi.org/10.1016/j.rse.2014.01.009

van Oyen, T., & Blondeaux, P. (2009a). Grain sorting effects on the formation of tidal sand waves. *Journal of Fluid Mechanics*, *629*, 311-342. https://doi.org/10.1017/S0022112009006387

van Oyen, T., & Blondeaux, P. (2009b). Tidal sand wave formation: Influence of graded suspended sediment transport. *Journal of Geophysical Research: Oceans*, *114*(C7). https://doi.org/10.1029/2008JC005136

Viana, A. R., Faugères, J.-C., & Stow, D. A. V. (1998). Bottom-current-controlled sand deposits — a review of modern shallow- to deep-water environments. *Sedimentary Geology*, *115*(1), 53-80. Contourites, Turbidites and Process Interaction https://doi.org/10.1016/S0037-0738(97)00087-0

Vicaire, O. (1991). *Dynamique hydro-sédimentaire en Mer du Nord méridionale : du Cap Blanc-Nez à la frontière belge* (PhD thesis, in French). Université des Sciences et Techniques de Lille-Flandres-Artois.

VLIZ. (2022a). *Average wind, air pressure and water level data obtained from the Westhinder measuring platform.* https://meetnetvlaamsebanken.be/map.

VLIZ. (2022b). *Wave data obtained from the Westhinder buoy.* https://meetnetvlaamsebanken.be/map.

Wahl, T., Haigh, I. D., Woodworth, P. L., Albrecht, F., Dillingh, D., Jensen, J., ... Wöppelmann, G. (2013). Observed mean sea level changes around the North Sea coastline from 1800 to present. *Earth-Science Reviews*, *124*, 51-67. https://doi.org/10.1016/j.earscirev.2013.05.003

Wang, S.-Y., Qi, W.-G., Li, B., Wang, C., & Gao, F.-P. (2024). Tidal currents-induced scour development around pile foundations: Effects of flow velocity hydrograph. *Coastal Engineering*, *191*, 104533. https://doi.org/10.1016/j.coastaleng.2024.104533

Wang, Z., Liang, B., Wu, G., & w. Borsje, B. (2019). Modeling the formation and migration of sand waves: The role of tidal forcing, sediment size and bed slope effects. *Continental shelf research*, *190*. https://doi.org/10.1016/j.csr.2019.103986

Weber, J. E. (1983). Steady wind- and wave-induced currents in the open ocean. *Journal of Physical Oceanography*, *13*, 524–530. https://doi.org/10.1175/1520-0485(1983)013<0524:SWAWIC>2.0.CO;2

Wengrove, M. E., Foster, D. L., Lippmann, T. C., de Schipper, M. A., & Calantoni, J. (2019). Observations of bedform migration and bedload sediment transport in combined wave-current flows. *Journal of Geophysical Research: Oceans*, *124*(7), 4572-4590. https://doi.org/10.1029/2018JC014555

Whitehouse, R. J. S. (1998). *Scour at marine structures: A manual for practical applications*. Thomas Telford Publishing. https://doi.org/10.1680/sams.26551

Whitehouse, R. J. S., Damgaard, J. S., & Langhorne, D. N. (2000). Sandwaves and seabed engineering; the application to submarine cables. In *Marine sandwave dynamics* (p. 227-234). March 23-24, 2000. Lille, France

Whitehouse, R. J. S., Harris, J. M., Sutherland, J., & Rees, J. (2011). The nature of scour development and scour protection at offshore windfarm foundations. *Marine Pollution Bulletin*, *62*(1), 73-88. https://doi.org/10.1016/j.marpolbul.2010.09.007

Whitehouse, R. J. S., & Stroescu, E. I. (2023). Scour depth development at piles of different height under the action of cyclic (tidal) flow. *Coastal Engineering*, *179*, 104225. https://doi.org/10.1016/j.coastaleng.2022.104225

Whitham, G. B. (1974). *Linear and nonlinear waves*. John Wiley & Sons. https://doi.org/10.1002/eqe.4290040514

Whitmeyer, S. J., & FitzGerald, D. M. (2006). *Sand waves that impede navigation of coastal inlet navigation channels* (Tech. Rep. No. ERDC/CHL CHETN-IV-68). U.S. Army Engineer Research and Development Center, Coastal and Hydraulics Laboratory.

Wölfl, A.-C., Snaith, H., Amirebrahimi, S., Devey, C. W., Dorschel, B., Ferrini, V., ... Wigley, R. (2019). Seafloor mapping - the challenge of a truly global ocean bathymetry. *Frontiers in Marine Science*, *6*. https://doi.org/10.3389/fmars.2019.00283

Wu, J. (1982). Wind-stress coefficients over sea surface from breeze to hurricane. *Journal of Geophysical Research: Oceans*, *87*(C12), 9704-9706. https://doi.org/10.1029/JC087iC12p09704

Wynn, R. B., & Stow, D. A. V. (2002). Classification and characterisation of deep-water sediment waves. *Marine Geology*, *192*(1), 7-22. https://doi.org/10.1016/S0025-3227(02)00547-9

Yalin, M. S. (1964). Geometrical properties of sand wave. *Journal of the Hydraulics Division*, *90*(5), 105-119. https://doi.org/10.1061/JYCEAJ.0001097

Yan, L. (1987). *An improved wind input source term for third generation ocean wave modelling* (Tech. Rep. No. WR-nr 87-8). Royal Netherlands Meteorological Institute.

Yiannoukos, I., van Landeghem, K. J. J., Roberts, M., Smyth, B., Morgan, J., Couldrey, A., ... Quinn, R. (2020). Modelling scour around submerged objects with TELEMAC3D - GAIA. In *Xxviith telemac-mascaret user conference* (p. 68-73). October 14-15, 2021. Antwerp, Belgium

Zhou, J., Wu, Z., Jin, X., Zhao, D., Cao, Z., & Guan, W. (2018). Observations and analysis of giant sand wave fields on the Taiwan Banks, northern South China Sea. *Marine Geology*, *406*, 132-141. https://doi.org/10.1016/j.margeo.2018.09.015

Zhou, J., Wu, Z., Zhao, D., Guan, W., Cao, Z., & Wang, M. (2022). Effect of topographic background on sand wave migration on the eastern Taiwan Banks. *Geomorphology*, *398*, 108030. https://doi.org/10.1016/j.geomorph.2021.108030

Zhou, J., Wu, Z., Zhao, D., Guan, W., Zhu, C., & Flemming, B. W. (2020). Giant sand waves on the Taiwan Banks, southern Taiwan Strait: Distribution, morphometric relationships, and hydrologic influence factors in a tide-dominated environment. *Marine Geology*, *427*. https://doi.org/10.1016/j.margeo.2020.106238

Zijlema, M., van Vledder, G. P., & Holthuijsen, L. H. (2012). Bottom friction and wind drag for wave models. *Coastal Engineering*, *65*, 19-26. https://doi.org/10.1016/j.coastaleng.2012.03.002

Personal contributions

Durand, N., Tassi, P., Blanpain, O., & Lefebvre, A. (2022a). Towards numerical modelling of marine dunes in a shallow shelf sea. In *Actes des XVIIèmes Journées Nationales Génie Côtier - Génie Civil* (p. 337-346). October 11-13, 2022. Chatou, France. https://doi.org/10.5150/jngcgc.2022.035

Durand, N., Tassi, P., Blanpain, O., & Lefebvre, A. (2022b). Hydrodynamic modelling as a first step to assess marine dune dynamics: Influence of waves. In *XXVIIIth Telemac-Mascaret user conference* (p. 79-86). October 18-19, 2022. Paris-Saclay, France. https://hdl.handle.net/20.500.11970/110839

Durand, N., Tassi, P., Blanpain, O., & Lefebvre, A. (2023a). Understanding marine dune dynamics in a shallow shelf sea using sediment mobility indices. In *Marine and River Dune Dynamics VII Book of Proceedings* (p. 109-116). April 1-3, 2023. Rennes, France. https://maridnet.files.wordpress.com/2023/06/maridvii-durand-noemie.pdf

Durand, N., Tassi, P., Blanpain, O., & Lefebvre, A. (2023b). GAIA can model large marine dunes: Results from a sensitivity study in the southern North Sea. In *XXIXth Telemac-Mascaret user conference* (p. 190-197). October 12-13, 2023. Karlsruhe, Germany. https://hdl.handle.net/20.500.11970/112839

Durand, N., Tassi, P., Blanpain, O., & Lefebvre, A. (2024a). Meteorological conditions influence the migration of a marine dune field in the southern North Sea. *Journal of Geophysical Research: Earth Surface*. Accepted for publication

Durand, N., Tassi, P., Blanpain, O., & Lefebvre, A. (2024b). On the attraction of marine dunes to OWF fixed foundations. *Geomorphica*. Under review